Investigation of an Improved Acoustical Method for Determining Airtightness of Building Envelopes

Untersuchung eines verbesserten akustischen Verfahrens zur Bestimmung der Luftdichtheit von Gebäudehüllen

Von der Fakultät für Maschinenwesen der
Rheinisch-Westfälischen Technischen Hochschule Aachen

zur Erlangung des
akademischen Grades eines Doktors der Ingenieurwissenschaften
genehmigte Dissertation

vorgelegt von

Benedikt Kölsch

Berichter: Univ.-Prof. Dr.-Ing. Bernhard Hoffschmidt
Univ.-Prof. Dr.-Ing. habil. Wolfgang M. Willems

Tag der mündlichen Prüfung: 31.03.2022

Berichte aus dem Bauwesen

Benedikt Kölsch

Investigation of an Improved Acoustical Method for Determining Airtightness of Building Envelopes

Shaker Verlag
Düren 2022

Bibliographic information published by the Deutsche Nationalbibliothek
The Deutsche Nationalbibliothek lists this publication in the Deutsche Nationalbibliografie; detailed bibliographic data are available in the Internet at http://dnb.d-nb.de.

Zugl.: D 82 (Diss. RWTH Aachen University, 2022)

Printed in Germany.

ISBN 978-3-8440-8583-9
ISSN 0945-067X

Shaker Verlag GmbH • Am Langen Graben 15a • 52353 Düren
Phone: 0049/2421/99011-0 • Telefax: 0049/2421/99011-9
Internet: www.shaker.de • e-mail: info@shaker.de

Abstract

Unintended air infiltration in buildings is responsible for 30 to 50 % of the building stock energy demand. The fan pressurization method, also known as the blower-door test, is the most frequently used and standardized measurement method to evaluate a buildings' airtightness and determine the airflow through a building or a building element. While detection and quantification of individual leaks with smoke tracers or infrared thermography are challenging, time-consuming, and depend on the respective operator's experience, acoustic methods have the potential to localize and quantify leaks in building envelopes without the need for pressure or temperature difference between in and outside of the examined building.

In this thesis, two acoustic methods, coherence measurements and beamforming, are introduced to this field of application to estimate the leakage size and location of individual leaks in building elements. This work aims at finding if different leak sizes can be quantified and detected using these acoustic measurement methods. For an estimation of leakage size, acoustic and airflow measurements are compared in a laboratory test apparatus. Test walls representing a single characteristic air leakage path in the building envelope at a model scale and separate two chambers with speaker and microphones. Various types of wall structures with different slit geometry, wall thickness, and insulation materials are tested. The acoustic measurements are performed with a sound source placed in one chamber and ultrasonic microphones located in both chambers. The results of these measurements are compared to the airflow through the test wall measured using a flow nozzle. The results from laboratory measurements indicate a linear trend between acoustic coherence and leak size in the investigated range of several mm^2. Although the acoustic measurement uncertainty is still significant ($\approx \pm 50\,\%$), the acoustic method shows the potential to give an order of magnitude of leak sizes.

The findings are validated in a real building setup using various reproducible leaks constructed with cable ties wedged in a window gasket. The acoustic and airflow measurements in the building show results similar to the laboratory measurements. Further, the acoustic beamforming method ("acoustic camera") using a microphone array to detect leak locations and visualize them shows promising results. The same constructed leaks in a window gasket are detected. With decreasing leak size and sound pressure, detection frequency increases.

The thesis concludes that acoustic methods have the potential to detect and quantify the leaks in building envelopes without test preparations as for common methods.

Zusammenfassung

Ungewünschte Luft-Infiltration in Gebäuden ist für 30 bis 50 % des Energiebedarfs des Gebäudebestands verantwortlich. Der Blower-Door-Test ist die am häufigsten verwendete und standardisierte Messmethode zur Beurteilung der Luftdichtheit von Gebäuden und zur Bestimmung des Luftstroms durch ein Gebäude. Während die Detektion und Quantifizierung einzelner Leckagen mit Rauchgas oder Infrarot-Thermografie anspruchsvoll, zeitaufwendig und von der Erfahrung des jeweiligen Bedieners abhängig sind, haben akustische Methoden das Potenzial, Leckagen in der Gebäudehülle zu lokalisieren und zu quantifizieren, ohne dass eine Druck- oder Temperaturdifferenz zur Umgebung des Gebäudes erforderlich ist.

In dieser Arbeit werden zwei akustische Methoden (Kohärenzmessungen und Beamforming) in dieses Anwendungsgebiet eingeführt, um Leckgrößen und die Lage einzelner Lecks in Gebäudehüllen abzuschätzen. Ziel dieser Arbeit ist es herauszufinden, ob mit diesen akustischen Messverfahren unterschiedliche Leckgrößen detektiert und quantifiziert werden können. Zur Abschätzung der Leckgröße werden akustische und Differenzdruck-Messungen in einem Laborversuchsaufbau verglichen. Die Testwand repräsentiert einen modellhaften charakteristischen Luftleckagepfad in der Gebäudehülle und trennt zwei Kammern mit Lautsprecher und Mikrofonen. Getestet wurden verschiedene Wandaufbauten mit unterschiedlichen Schlitzgeometrien, Wandstärken und Dämmmaterialien. Die akustischen Messungen wurden mit einer Schallquelle in einer Kammer und Ultraschallmikrofonen in beiden Kammern durchgeführt und die Signalkohärenz ausgewertet. Die Ergebnisse der Kohärenz der akustischen Messungen wurden mit Differenzdruck-Messungen durch diese Testwand verglichen und zeigen einen linearen Trend der akustischen Kohärenz mit der Leckgröße im untersuchten Bereich weniger mm^2. Obwohl die Streuung der Messwerte noch signifikant ist ($\approx \pm 50\,\%$), zeigt die akustische Methode das Potenzial, Größen von Lecks abzuschätzen. Die Ergebnisse wurden an einem realen Gebäude unter Verwendung reproduzierbarer Lecks validiert, die mit Kabelbindern in einer Fensterdichtung erzeugt wurden. Die Messungen im Gebäude zeigen dabei mit den Labormessungen vergleichbare Ergebnisse. Zudem zeigten Messungen mit einem Mikrofonarray vielversprechende Resultate, die Leckagen in der Gebäudehülle zu erkennen und zu visualisieren. Dieselben sechs erzeugten Lecks in einer Fensterdichtung wurden detektiert. Mit abnehmender Größe der Leckage und des Schalldrucks nimmt die Frequenz der Detektion zu. Diese Arbeit zeigt, dass akustische Methoden das Potenzial haben, Lecks in der Gebäudehülle zu detektieren und ihre Größe abzuschätzen, ohne aufwändige Vorbereitungen zu treffen.

Contents

List of Figures

List of Tables

Nomenclature

Abbreviations and Acronyms

A/D	Analog-to-digital converter	–
ACH	Air change rate per hour	1/h
AHHRF	Alberta Home Heating Research Facility	–
ASHRAE	American Society of Heating, Refrigerating and Air-Conditioning Engineers	–
ASTM	American Society for Testing and Materials	–
DFT	Discrete Fourier transform	–
DIN	Deutsches Institut für Normung e.V. (German Institute for Standardization)	–
ELA	Equivalent leakage area	m^2
EMD	Empirical mode decomposition	–
EN	Europäischen Normen (European Standards)	–
EnEV	German Energieeinsparverordnung (energy saving regulation)	–
ESS	Exponential sine sweep	–
FFT	Fast Fourier transform	–
GHG	Greenhouse gas	–
HHT	Hilbert-Huang transform	–
IAQ	Indoor air quality	–
ILD	Interaural level difference	–
IMF	Intrinsic mode function	–
IRT	Infrared thermography	–
ISO	International Organization for Standardization	–
ITD	Interaural time difference	–
IWLS	Iterative weighted least square	–
KDE	Kernel density estimation	–
LBNL	Lawrence Berkeley National Laboratory	–
LSS	Linear sine sweep	–
MDF	Medium-density fiberboard	–
MLS	Maximum length sequence	–

NL	Normalized leakage	–
NRMSE	Normalized root mean square error	–
OLS	Ordinary least square	–
PDF	Probability density function	–
RMS	Root mean square	–
RMSE	Root mean square error	–
STFT	Short-time Fourier transform	–
WLOC	Weighted line of organic correlation	–

Greek Symbols

α	Heat transfer coefficient	$W/(m^2 \cdot K)$
β	Thermal expansion coefficient of air	$m/(m \cdot °C)$
Δ	Difference	–
λ	Wavelength	m
λ_c	Thermal conductivity	$W/(m \cdot K)$
μ	Dynamic viscosity	$Pa \cdot s$
∇^2	Laplacian operator	–
ω	Angular frequency	$1/s$
Φ	Heat loss	W
ϕ	Azimuth angle	rad
ϕ	Phase	rad
π	Archimedes' constant ($\pi \approx 3.14159$)	–
ρ	Fluid density	kg/m^3
ρ_o	Cross-correlation function	–
σ	Standard deviation	–
τ	Time delay	s
τ_i	Individual run times	s
θ	Polar angle	rad

Latin Symbols

$\hat{p}$	Pressure amplitude	m
$\hat{f}_h$	Probability density function	–

$\mathcal{F}$	Fourier transform	–
$\mathcal{H}$	Hilbert transform	–
A	Area	m^2
A	Flow coefficient forfully developed friciton losses	$\mathrm{Pa \cdot s/m^3}$
a	Amplitude	–
A_0	Fourier constant	–
a_f	Autocorrelation function	–
A_n	Fourier coefficient	–
A_S	Equivalent sound absorption area	m^2
B	Flow coefficient for entry, exit and turbulent flow losses	$\mathrm{Pa \cdot s^2/m^6}$
B_n	Fourier coefficient	–
C	Correction factor	dB
C	Flow coefficient	$\mathrm{m^3/(s \cdot Pa^n)}$
C	Tracer gas concentration	ppm
c	Specific heat capacity	$\mathrm{J/(kg \cdot K)}$
c	Speed of sound	$\mathrm{m/s}$
C_D	Discharge coefficient	–
c_j	Intrinsic mode function	–
C_{xy}	Coherence function	–
d	Crack thickness	m
d	Distance between the speaker and microphone	m
d	Thickness of wall layer	m
E	Elevation above sea level	m
E	Signal power	W
e	Euler's number ($e \approx 2.71828$)	–
e	Signal envelope	–
F	Tracer gas injection rate	$\mathrm{m^3/s}$
f	Calibration coefficient	$\mathrm{m^3(m/kg)^{1/2}}$
f	Frequency	Hz
G_{xx}	Auto-spectral density between time signal x and x	W/Hz
G_{xy}	Cross-spectral density between time signal x and y	W/Hz

G_{yy}	Auto-spectral density between time signal y and y	W/Hz
H	Building height	m
h	Bandwidth of probability density function	–
h	Difference between mean signal and initial signal	–
h	Impulse response	–
i	Imaginary number ($i = \sqrt{-1}$)	–
K	Flow coefficient	$\mathrm{m^3/(s \cdot Pa^n)}$
K	Uniform kernel	–
k	Wavenumber	1/m
K_1	Laminar flow coefficient	$\mathrm{m^3/(s \cdot Pa)}$
K_2	Turbulent flow coefficient	$\mathrm{m^3/(s \cdot Pa^{1/2})}$
L	Crack width	m
L	Level	dB
M	Number of microphones	–
m	Intensity attenuation coefficient	1/m
m	Mean value of upper and lower signal envelope	–
N	Number of bits	–
N	Number of measurement points	–
N	Proportion of tapered data	-
n	Air change rate per hour	1/h
n	Pressure exponent	–
n_C	Pressure exponent	–
Nu	Nusselt number	–
P	Pressure	Pa
p	Sound pressure	Pa
Q	Airflow	$\mathrm{m^3/h}$
q	Building air permeability	$\mathrm{m^3/(m^2 \cdot h)}$
R	Sound reduction index	dB
r	Residual function	–
r	Sweep rate	$\mathrm{1/s^2}$
R^2	Coefficient of determination	–
r_i	Geometrical distance between focus point and microphone position	m

Re	Reynolds number	–
S	Area of the common partition between two rooms	m^2
s	Linear sweep signal	–
s^2	Variance	–
T	Period	s
T	Temperature	K
t	Time	s
U	Thermal transmittance	$\mathrm{W/(m^2 \cdot K)}$
V	Volume	m^3
v_i	Weighting factor	–
w	Specific airflow	$\mathrm{m^3/(m^2 \cdot h)}$
w	Window function	-
w_i	Weighting factor	–
x	Focus point	–
x	Signal	–
x_i	Measurement coordinate which corresponds to $\ln(\Delta P_i)$	–
x_m	Spartial position of microphone	–
Y	Crack geometry factor	–
y_i	Measurement coordinate which corresponds to $\ln(Q_i)$	–
z	Analytical signal	–
z	Crack length	m

Superscripts

$*$	Fourier transform of $y(-t)$

Subscripts

0	Initial value
1	Corresponding to pressure measurement position 1
1	Sending room
2	Corresponding to pressure measurement position 2
2	Receiving room
20	Sound pressure level drop by 20 dB

30	Sound pressure level drop by 30 dB
60	Sound pressure level drop by 60 dB
ΔP	Pressure difference
a	Air
atm	Atmospheric
c	Center
cal	Calibration
$corr$	Corrected value
E	Envelope
ex	External
F	Floor
f	Frame
$hann$	Hanning window
i	Instantaneous
in	Internal
inv	Inverse
m	Microphone
max	Maximum
$meas$	Measured value
min	Minimum
out	Outside
p	Sound pressure
$pred$	Predicted value
Q	Airflow
ref	Reference
rev	Reverse
$reverb$	Reverberation
rms	Root mean square
S	Sampling
s	Set of data samples
sd	Overall sweep duration
t	Transmission
$tukey$	Tukey window
v	Ventilation

1 Introduction

1.1 Motivation

Within the last decades, the conservation of scarce energy resources and the associated environmental protection became a crucial topic in global media and politics. Besides the energy, industry, and transport sectors, the building sector is nowadays responsible for almost a third of the global final energy consumption. Moreover, the building sector accounts for an equally large share of global CO_2 emissions [1]. In the European Union, buildings are responsible for approximately 40 % of the total energy consumption and 36 % of the emitted greenhouse gases (GHG) [2].
The building sector in Germany is in 2018 directly responsible for GHG emissions of around 120 million t CO_2-equivalent per year. The German government addresses the goal to reduce these emissions to only 72 million t CO_2-equivalent by 2030 [3]. By the year 2050, Germany even aims that the building stock shall be nearly climate-neutral. The term "climate-neutral" is here defined as an 80 % reduction of the non-renewable primary energy demand compared to the year 2008 [4].
Other countries developed similar plans. For example, the Canadian government plans to reduce its greenhouse gas emissions by 40 % until the year 2030 and by 80 % until 2050 [5]. Because buildings are responsible for 17 % of Canada's current national GHG emissions, the reduction of building energy consumption has become a vital part of their energy policy as well.

The airflow through a building envelope is estimated to account for 30 to 50 % of the building's heating and cooling energy [6–11] and is, therefore, in addition to thermal transmittance, one of the significant sources for heat losses and their energy consumption [12]. According to Bell et al. [13], the energy consumption of ventilation-related heating requirements can be reduced by around 30 % if the buildings' air leakage is reduced. Further, Logue et al. [14] stated that an improvement of the airtightness of all homes in the US to current average retrofit performance levels would decrease the country's annual energy consumption by about 0.74 EJ or 206 TWh. If all homes would even be upgraded to the airtightness level of the upper 10 % of the tightest US homes, these energy savings would be doubled, and annual energy costs up to $22 bn could be saved. Thus, the knowledge of unintended infiltration in buildings is crucial.

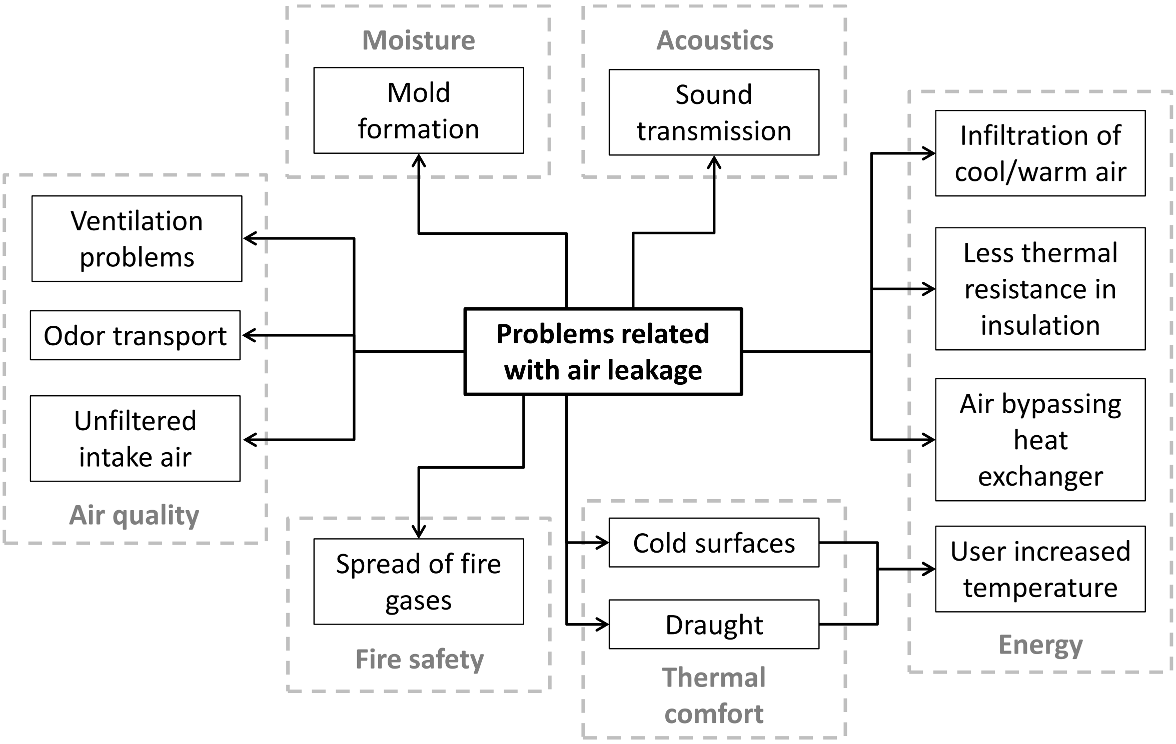

Figure 1.1: Problems related to building air leakage based on Ref. [15]

Fig. 1.1 summarizes the major problems related to air leakage, which are further explained in the following [15, 16]:

- **Energy**: The increase of infiltrating cool and warm air from outside leads to an increase of heating or cooling energy. Additionally, ventilation systems of buildings can only operate correctly in terms of heat recovery with airtight houses. The air should go entirely through the heat exchanger to provide sufficient fresh air with a minimum energy requirement [17].
- **Improved indoor air quality**: Sufficiently designed ventilation systems should ensure good indoor air quality. They reduce indoor emissions (e.g., from occupants or furniture) through a frequent air exchange and prevent containment intrusion from outside through filter systems. Air leakage may influence the efficiency of the ventilation systems.
- **Protection of sound and smell**: Particularly in large cities with a high impact of traffic and smog, a low building airtightness may significantly influence the sound transmission and odor from outside [18].

- **Improvement of thermal comfort**: Air leakage may create unwanted air motion inside buildings, and most humans react very sensitive to this airflow inside buildings. These draughts and cold surfaces can significantly reduce the thermal comfort of the inhabitants [19]. Additionally, thermal comfort can become a problem related to increased energy consumption because occupants may compensate for their experienced colder inside air temperature with an adjustment of the heating [20].
- **Fire Safety**: Fire inside buildings leads to an increase in temperature and toxic gas particles, which can be transported through leaks inside the building. Especially for multi-family homes and non-residential buildings, the spread of smoke and fire can be reduced within the building if the units are airtight.
- **Prevention of moisture and structural damage**: Warm and humid air can penetrate through leakages and condensate at cold surfaces inside the walls. This could lead to an increase in mold, fungus, and microbiological contaminants growth [21, 22]. Thus, it can become a potential source of indoor environmental pollution and is limited by airtight buildings. Particularly in wooden walls, up to 90 % of the damages are caused by moisture and temperature effects [23, 24]. Wilson et al. [25] calculated that the vapor transfer induced by air leakage is about ten times higher compared to diffusion. In colder climates, poorly insulated buildings can even lead to ice formation at exterior wall elements [18].
- **EnEV-Proof**: The requirements of energy saving regulation EnEV (German Energieeinsparverordnung) and other funding programs are easier to fulfill with an airtight house.

However, if only energy was taken into consideration, an airtight building would always be preferable. Nevertheless, if air infiltration is the only way of providing a proper dilution of indoor contaminants, a higher infiltration rate can be helpful in terms of indoor air quality (IAQ). Minimizing the energy costs and simultaneously providing sufficient IAQ for inhabitants is a complex optimization problem. Thus, an airtight building requires a properly designed ventilation system [18, 26].

The most frequently used technique to evaluate a building's airtightness and compare them among each other is the fan pressurization method (known as "blower door test"). This measurement method serves the purpose of measuring airtightness to meet requirements of specific energy performance standards, comparing relative airtightness of different buildings among each other, or determining the reduction of air permeability after refurbishments. It is necessary to identify leak locations and prioritize sealing of more substantial leaks to reduce air leakage in existing buildings. Additionally, the knowledge of leak locations can improve estimates of infiltration airflows [27]. The fan pressurization method only gives the overall leakage rate of one room or building. Quantification and identification of single leaks are challenging, time-consuming, and depend heavily on the respective operator's experience. Leak locations may be identified using, e.g., smoke sticks or anemometers in conjunction with a fan pressurization measurement, infrared thermography, or tracer gas. However, smoke sticks and anemometers require a pressure difference to detect leaks. The use of infrared thermography requires a temperature gradient across the building envelope in addition to a pressure difference.

Supplementary acoustic methods have the potential to identify and quantify single leaks in the building envelope. The non-destructive acoustic testing removes the need to move large quantities of air through the building envelope because the tests can be performed under naturally occurring low or no-flow conditions. In contrast to fan pressurization methods, acoustic methods do not rely on enclosed volumes. This would enable testing during the construction of the building.

1.2 Objectives and Scope

It is essential to identify and quantify single leaks in a building envelope to increase the effectiveness and decrease the costs of renovations. A fast, inexpensive, and objective measurement method of single leaks in buildings could encourage building owners to inspect their buildings and reduce barriers for renovation. Moreover, a higher rate of building renovations would contribute to national and international climate targets.

This thesis aims to investigate the potential of an improved acoustical method for the quantification and localization of single leaks in the building envelope. Here, experiments are conducted to demonstrate the feasibility and suitability of acoustic measurement techniques to evaluate the size of air leakages in building envelopes. Specifically, this goal is addressed by:

1. Evaluation and demonstration of acoustical measurement approaches under laboratory conditions to quantify single leak sizes.

2. Comparison of the acoustic method with the well-established fan pressurization method.

3. Investigation of the method's applicability at real buildings outside laboratory environments.

4. Investigation of the suitability of microphone arrays for leak localization in building envelopes.

This thesis emphasizes on the applicability of acoustic methods for measuring the airtightness of buildings. The transfer and implementation of this method into practical application is not within the scope of this thesis and remains open for future work.

In Chapter 2, the current state of the art of building envelope's airtightness in general and a brief review of experimental methods for measuring airtightness are introduced. This shall provide a background for this thesis. Moreover, Chapter 3 provides an overview of the necessary theory of acoustics and signal processing, which is required to follow the experiments in this work.

In Chapter 4, the results of preliminary laboratory experimental investigations are shown. These experiments paved the way for subsequent analyses of leak quantification in the following chapters. The experiments shown in Chapter 5 are done within a laboratory environment, where various wall and leak structures are investigated. Here, the well-established fan pressurization method is compared to the acoustic method within the same boundary conditions to quantify different leak sizes.

For a validation of this laboratory method in a real building application, the accuracy of the fan pressurization method is investigated in Chapter 6. To reduce the influence on measurement uncertainty, a regression method is introduced to reduce the impact of, e.g., wind on the measurement uncertainty. In Chapter 7, the acoustic method is compared to fan pressurization and tracer gas measurements in a real office building application.

Finally, in Chapter 8, an acoustic method using beamforming and microphone arrays is introduced. In addition to the investigation of leak quantification in the previous chapters, the potential of acoustic methods for leak detection in building envelopes is evaluated in this last chapter.

2 State of the Art

The following chapter is split up into two main sections. In the first section, the principles and terminologies of a building's airtightness are discussed. Within the second section, measuring methods to quantify airtightness and detect leaks in the building envelope are described.

2.1 Building Construction and Airtightness

When airtightness is examined, a compromise between having enough outdoor air supply and more leaks resulting in higher energy consumption must be found. Therefore, these impacts have to be discussed for building construction and design. In the first view, three different principles of incoming air will be described:

- Infiltration
- Natural Ventilation
- Mechanical Ventilation

Infiltration

The understanding of air infiltration is vital to assess a building's energy consumption and indoor environment. Liddament [28] defined air infiltration of buildings as follows:

> "Uncontrolled flow of air through penetrations in the building fabric caused by pressure differences generated across these openings by the action of wind and temperature."

In other words, infiltration is the natural air exchange through the building envelope. It is influenced by, e.g., the location and distribution of the leakage paths [8] and is enhanced by the wind blowing on a building, or the temperature differences between inside and outside, which creates stack pressures [29]. Stack pressure differences are

induced by air temperature gradients across the building envelope and height, which result in air buoyancy change and, therefore, in a pressure difference. In particular, for high-rise buildings, the stack effect is the driving force for infiltration [30]. The infiltration significantly influences the heating, cooling, and humidity load of buildings and is responsible for the indoor air pollutants' distribution. On the contrary, exfiltration is the airflow out of the building through the same openings. Usually, the air infiltration is measured to quantify airtightness in buildings.
The concept of airtightness refers to flow through unintentional openings in a building envelope and is an entirely passive process that depends on fortuitous leakage flow through these openings [31]. Some typical air leakage paths are described in more detail in Section 2.1.2. The intentional openings in buildings (e.g., open windows) are not considered part of the airtightness analysis [29]. Even though in this work mainly infiltration is considered, two other concepts of air exchange will be described shortly regarding completeness in the following paragraphs.

Natural Ventilation

The first one is natural ventilation, which describes the outdoor air intake through intentional openings (e.g., open windows or vents) [32]. The flow process of natural ventilation is mainly driven by wind and temperature [33, 34] as well as for infiltration. These intentionally placed openings are usually controllable apertures positioned at strategic places in the building envelope. Key factors influencing the airflow are the dimensions and positions of the openings and the occupant's behavior [31].

Mechanical Ventilation

Secondly, mechanical ventilation characterizes the intentional air intake by powered ventilation systems. Although these systems may diminish the influence of climatic parameters on the air changes, a correct design of mechanical air extract and supply still relies on the knowledge of the buildings' airtightness characteristics [31].

Historically the prediction of infiltration, natural ventilation, and air movements inside buildings was challenging. According to Cockroft et al. [35], this has several reasons:

1. The physical relationship of air moving through a building envelope is non-linear

2. The airflows through the building envelope are driven by several external forces

(e.g., wind) and are modified by the operation of building components (e.g., windows or doors)

3. The characteristic of the same building components can vary due to tolerances in manufacturing and installation

In the following sections, typical leakage paths in buildings, metrics for assessing and comparing air leakage through building envelopes by calculation methods, and different measurement methods are introduced. First of all, the thermal characteristics of building envelopes are defined.

2.1.1 Thermal Performance of Buildings

The energy performance of a building is mainly determined by its envelope's thermal properties, which became a critical factor in its design [36]. This thermal performance of buildings reflects a combination of different factors. However, the following paragraphs focus primarily on the assessment of heat losses through the building envelope.

The total heat loss Φ of a building can be approximated as the sum of transmission heat losses Φ_t and ventilation/infiltration heat losses Φ_v, whereby the heat loss due to phase change of moisture is neglected [12]:

$$\Phi = \Phi_t + \Phi_v \tag{2.1}$$

The transmission heat losses Φ_t can be expressed as:

$$\Phi_t = \Delta T \sum_{i=1}^{k} \mathrm{Nu}_i \; U_i \; A_{E,i} \tag{2.2}$$

ΔT is the difference between inside and outside temperature, k is the number of elements of the building envelope, Nu_i is the Nusselt number for the i-th element of the wall, $A_{E,i}$ is the area of the i-th element of the building envelope, and U_i is the averaged thermal transmittance of one element of the building envelope:

$$U_i = \frac{1}{\frac{1}{\alpha_{ex}} + \frac{1}{\alpha_{in}} + \sum_{j=1}^{m} \frac{d_j}{\lambda_{c,j}}} \tag{2.3}$$

The thermal transmittance is a function of the external α_{ex} and internal α_{in} heat transfer coefficients, the thickness d_j of the j-th layer of the i-th wall element, and the thermal conductivity $\lambda_{c,j}$ of the j-th layer of the i-th wall element.

Under the assumption that air exchange only exists between inside and outside, the heat loss due to ventilation or air infiltration Φ_v in Eq. (2.1) can be described as [37]:

$$\Phi_v = ACH \, \frac{V \, \rho_a \, c_a}{3600} \, \Delta T \tag{2.4}$$

where ACH (see Eq. (2.7)) is the air change rate, V is the building volume, ρ_a is the density of air, and c_a is the specific heat capacity of air at a constant pressure. Orme et al. [38] estimate that the heating loss due to air change accounts for 53 % of the estimated delivered space heating energy. Therefore, the air change rate and the airtightness of a building are vital for assessing the heat losses and calculating a building's energy performance. For more detailed information about heat losses in buildings, see Refs. [12, 37]. Which factors may influence the airtightness of buildings is specified in the following section.

2.1.2 Factors Influencing Airtightness of a Building

Leakage paths occur at the external envelope and between internal partitions of buildings. As soon as there is a pressure difference, air will flow through it. Therefore, an essential factor for a good airtightness of a building is a reliable air barrier system. Basic requirements of an air barrier system are [39]:

- **Air Impermeability**: The choice of air-impermeable raw materials for the air barrier system is essential.
- **Continuity**: Each assembly needs to be interconnected to prevent leaks between joint elements and components.
- **Structural Support**: An excellent structural support guarantees a proper resistance of the air barrier system against structural air pressure loads.
- **Durability**: Materials need to be selected to remain durable during the anticipated life of the building enclosure or have to be accessible for maintenance.

Besides these factors, many other factors affect a building's airtightness and its air barrier system, including the age of construction, the building type (e.g., single-family or multi-family), climate, and construction materials [18]. The knowledge of the leakage paths is a vital step for the evaluation of the building's airtightness. According to Lowe et al. [40, 41], one of the significant factors influencing a building envelope's airtightness is how the walls are constructed. Their findings exhibit that, e.g., wet plastered masonry walls are potentially several orders of magnitude more airtight than timber-framed masonry walls. Mélois et al. [42] also observed that wooden buildings are slightly less airtight than brick or concrete buildings.

A detailed summary of various studies concerning leakage paths can be found in Ref. [18]. Hereafter, the most crucial leakage paths of single-family, multi-family, and non-residential buildings are introduced.

Single-Family Homes

Single-family dwellings represent 64 % of the housing stock in Europe, which is the largest share of building types [43]. In addition to leakage directly through walls, the following building components contribute significantly to air leakage of single-family homes: windows, doors, flues, fireplaces, heating ducts, and the connection between the attic, basement, crawl space (if there is one), and garage [18]. Especially windows can contribute up to 22 % of the total leakage, whereby this value highly depends on the window type. According to Laverge et al. [44], secondary rooms like garages or attics should be considered because these rooms may bypass the insulation of the house and increase transmission losses. Some of these typical air leakage pathways are illustrated in Fig. 2.1.

Generally, for the evaluation of air leakage, the year of construction and the size of the dwellings are indicators that commonly reflect the level of airtightness that can be expected [18]. Chan et al. [45] observed that larger buildings tend to have larger overall leakage areas because of their larger surface areas. However, if the airflow through the envelope is normalized by the building size, these larger buildings tend to be tighter than smaller ones. As one explanation, the authors assumed that, on average, larger houses are owned by higher-income families and are, therefore, built with better materials and are more often maintained.

Li et al. [46] pointed out that the year of construction alone may not be sufficient for predicting airtightness. According to Sherman et al. [18] and Kraus et al. [47], the less influential factors are the location of the building, presence of heating ducts, basement construction type, or the envelope complexity.

Multi-Family Homes

Multi-family buildings often consist of multiple units, which makes the air leakage estimation more complex. The units share walls inside the building, and the building

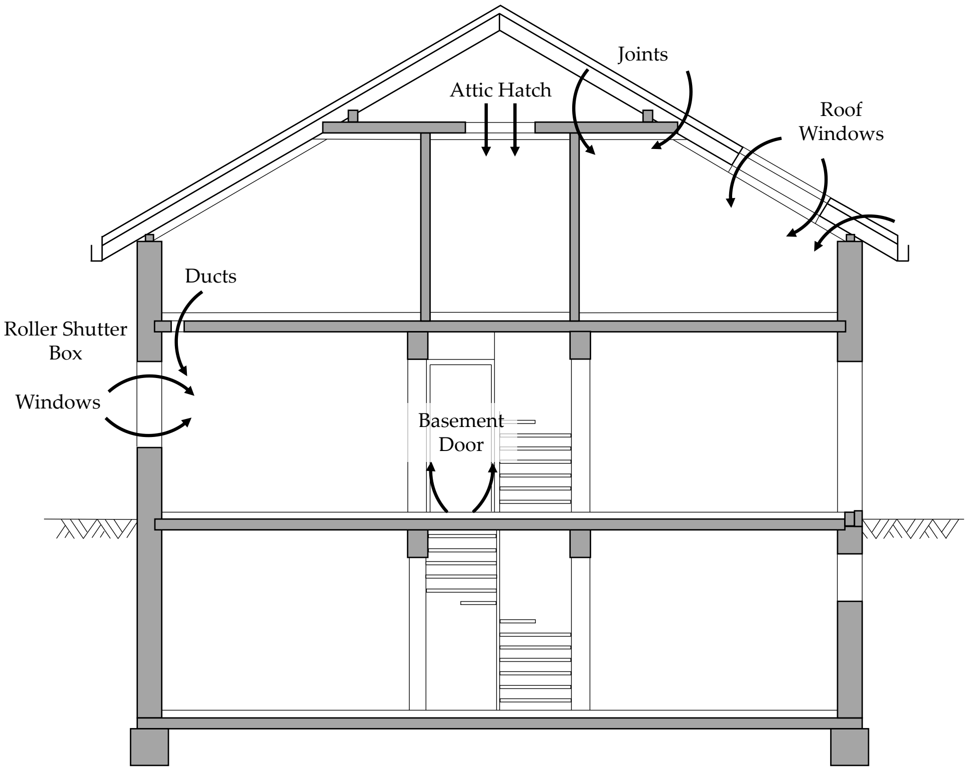

Figure 2.1: Typical air leakage pathways in single-family homes based on Ref. [48]

envelope is bigger compared to single-family houses. The complexity of these buildings makes testing more difficult, time-consuming, and labor-intensive. For low-rise multi-family homes, one can either test the envelope of the whole building, only single zones (e.g., floor by floor, unit by unit), or single components of the envelope [49]. In addition to potential leakage paths for single-family homes, already mentioned in the previous paragraph, dominant paths in multi-family buildings can be, e.g., connections to adjacent units, stairwell doors, garages chutes, or elevator shafts [18, 50].

Non-Residential Buildings

Air leakage in residential buildings has been investigated intensively in the past. However, due to its often higher complexity and size, less information is available for non-residential buildings. Moreover, the absence of suitable standardized testing protocols leads to less testing of these buildings [51, 52]. Furthermore, the testing of large non-residential buildings often requires a significantly larger investment in equipment. According to the American Society of Heating, Refrigerating and Air-Conditioning Engineers (ASHRAE) [32], the evaluation of internal partitions, elevators, stairs, shaft walls, and doors are essential for an air leakage evaluation of non-residential buildings. Especially automatic doors (sliding, swinging, or rotating) can be a significant source of incoming air in commercial buildings because they usually stay longer open than manual doors and allow air to infiltrate the building [30].

After explaining various building types and their complexity, different air permeability indicators will be introduced in the following paragraphs.

2.1.3 Indicators for Building Air Permeability

Different countries use various metrics to indicate the air permeability of a building. To be able to compare the performance of a building's airtightness, some common standard metrics are well established [53–55]:

- $Q_{\Delta P}$: The measured airflow at a specific pressure difference ΔP between inside and outside the building. ΔP should be high enough to be independent of weather conditions and low enough to be achievable for most houses. Often a pressure difference of 50 Pa is chosen. The index of Q indicates the chosen pressure difference in Pa at the measured airflow (e.g., Q_{50}).
- $w_{\Delta P}$: Specific airflow, which is the airflow rate divided by the net floor area A_F of the tested building:

$$w_{\Delta P} = \frac{Q_{\Delta P}}{A_F} \tag{2.5}$$

- $q_{\Delta P}$: Building air permeability at a specific pressure difference:

$$q_{\Delta P} = \frac{Q_{\Delta P}}{A_E} \tag{2.6}$$

  A_E is the area of the building envelope.
- $ACH_{\Delta P}$ or $n_{\Delta P}$: The air change rate per hour is defined as the airflow rate at a particular pressure difference divided by the internal house volume V:

$$ACH_{\Delta P} = \frac{Q_{\Delta P}}{V} \tag{2.7}$$

- $ELA_{\Delta P}$: The equivalent leakage area is seen as a measure of the total area of all different cracks in a building. It is calculated as the area of a sharp-edged hole (with a pressure exponent of 0.5, see Eq. (2.16)) that would result in the same airflow at a fixed reference pressure through the envelope of a building. The

$ELA_{\Delta P}$ can be defined as followed:

$$ELA_{\Delta P} = \frac{Q_{\Delta P}}{C_D} \sqrt{\frac{\rho_a}{2\,\Delta P}} \tag{2.8}$$

where ρ_a is the density of air, and C_D is a fixed discharge coefficient.

- NL: The normalized leakage NL can be a useful metric to compare the air leakage of buildings of different sizes. In most cases, the floor area A_F and the height of the building H can be easily measured:

$$NL = 1000 \left(\frac{ELA_4}{A_F}\right) \left(\frac{H}{2.5\,\mathrm{m}}\right)^{0.3} \tag{2.9}$$

Which metric is used depends on the application and country. The requirements on air change rates and airtightness according to energy regulatory are discussed in the following chapter.

2.1.4 Requirements on Air Tightness

Some countries require certain airtightness levels of houses, but these levels differ widely between them. According to their specific building codes and their condition variables, the airtightness requirements for several European countries are summarized in Table 2.1. These values are normalized to the air change rate at 50 Pa pressure difference (ACH_{50}) of houses with a typical volume of 300 m^3, a surface area of 250 m^2, and a pressure exponent of 2/3 (cf. Eq. (2.16)) [56]. This normalization enables a comparison between varying building standards and requirements of different countries.

Fig. 2.2 shows a map of all European countries which require or recommend airtightness testing. Typically, European countries with colder climates tend to require more demanding airtightness levels, whereby most eastern European countries are an exception. Countries in southern Europe with a less severe climate generally tend to overlook the issue of airtightness testing. Poza-Casado et al. [59] did a detailed review of regulations regarding building airtightness in Europe and North America.

Table 2.1: Requirements or recommendations of building airtightness of several selected European countries normalized to ACH_{50} based on Refs. [57–59]

Country	**Condition Variable**	**Requirements/ Recommendations for** ACH_{50}
Austria	Natural ventilation	3.0
Czech Republic	Natural ventilation	4.5
	Forced	1.5
	Forced + heat recovery	1.0
Denmark	Residential	6.5
Finland	Building heat loss reference	2.0
	Energy Performance Certificate	4.0
France	Single-family houses	4.3
	Other residential buildings	6.5
Germany	Mechanical ventilation	1.5
	Natural ventilation	3.0
Netherlands	Mechanical ventilation	2.0 − 3.0
	Natural ventilation	4.0 − 6.0
Norway	Residential	3.0
Spain	Ratio between volume and floor area	3.0 − 6.0
United Kingdom	Best practice natural ventilation	6.0
	Best practice mechanical ventilation	1.2
	Normal practice natural ventilation	8.4
	Normal practice mechanical ventilation	6.0

2.1.5 Calculation of Building Airtightness

The building air leakage can be represented by the measured airflow through the building envelope Q, which is a function of the pressure differences between the inside and the outside of the building ΔP. In order to avoid significant experimental errors, the pressure difference is typically measured at higher pressures. Subsequently, the high-pressure data has to be extrapolated to lower pressure levels to obtain airflows at pressures where buildings are typically exposed to. The identification of the most appropriate equation for curve-fitting and extrapolation is challenging [60]. In the past, several formulations have been developed to describe the relationship between

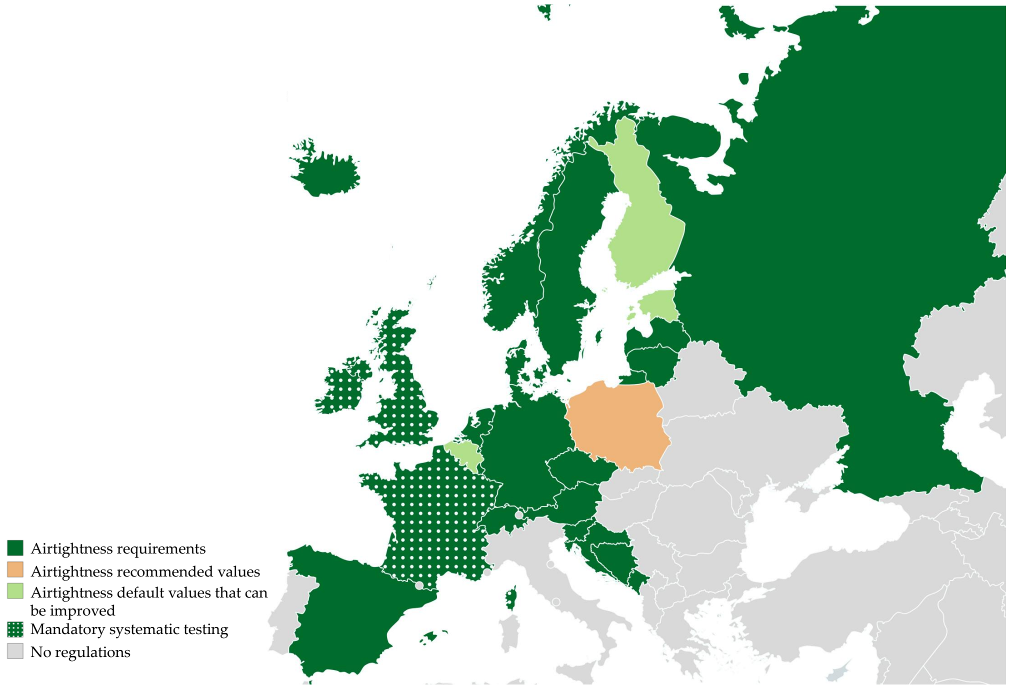

Figure 2.2: European airtightness regulatory context based on Ref. [59]

airflow and pressure difference through cracks [61–66], but two formulations have mainly been used to calculate building envelope leakage: the quadratic form [67] and the power-law form [18, 68]. Both forms are applied mainly by standards or infiltration models to extrapolate data from high-pressure differences to pressure ranges where natural infiltration occurs. In this section, these two calculation methods will be shortly introduced.

Quadratic Form

The following relationships between airflow and pressure are valid for long and fully developed laminar (2.10) and for short, sharp-edged (2.11) openings:

$$Q = K_1 \, \Delta P \tag{2.10}$$

$$Q = K_2 \, \sqrt{\Delta P} \tag{2.11}$$

Here, K_1 and K_2 are flow coefficients.

The flow patterns described in Eq. (2.10) are valid for low Reynolds Numbers (Re) and describe long openings where their length z is larger than their thickness d: $z/d > 1$. These openings are, e.g., ducted air vents or ventilation stacks (chimneys). On the contrary, Eq. (2.11) assumes that the leaks are very short and sharped-edged ($z/d \ll 1$). Here, the flow patterns are independent of Re (except very low Re). Examples of this opening type are sliding windows or air vents in windows [69–71].

Both flow equations can be combined and build the following quadratic formulation:

$$\Delta P = A\,Q + B\,Q^2 \tag{2.12}$$

where A is a flow coefficient for fully developed friction losses, and B is a flow coefficient for entry, exit, and turbulent flow losses. These coefficients can be derived from fluid mechanic principles, assuming, e.g., a flow between parallel plates [72]:

$$A = \frac{12\,\mu\,z}{L\,d^3} \tag{2.13}$$

$$B = \frac{\rho\,Y}{2\,d^3\,L^2} \tag{2.14}$$

where μ is the dynamic viscosity, z is the crack length, L is the crack width, d is the crack thickness, ρ is the fluid density, and Y is a factor that depends on the geometry of the crack. These coefficients may vary for different slit geometries (e.g., flow between parallel plates or short circular holes) [73] and can be estimated by applying a regression to experimental data [72].

For calculation of the flowrate Q, Eq. (2.12) can be expressed in a more useful form:

$$Q = \frac{-A + \sqrt{A^2 + 4\,B\,\Delta P}}{2\,B} \tag{2.15}$$

Etheridge [60, 74, 75] and Baker [72] suggest using this relationship to describe the flow because this formulation has a practical advantage at the extreme flows $Q \to 0$ and $Q \to \infty$. However, this approach is limited because it is based on a combination of fully developed laminar and turbulent flows, as well as entry and exit losses, and disregards an existence of a transition between the laminar and turbulent flow. In real applications, cracks in building envelopes often do not allow the airflow to form a fully developed flow profile due to its complex structure [76]. Hence, this formulation is not accurate for all types of cracks and pressure differences and often does not fit the measured data. Further, Walker et al. [77] have shown that this formulation is not suitable for a combination of series and parallel leaks as they occur in real buildings.

Power-Law Form

The empirical power-law has the following form:

$$Q = C\,\Delta P^n \tag{2.16}$$

C represents the flow coefficient, which can be a measure of the overall leakage size [77], and n is the pressure exponent, which characterizes the leakage shape. The pressure exponent is limited to values between 0.5 (turbulent flow) and 1.0 (laminar flow) but typically is in the vicinity of 2/3 for single-family houses [18, 78]. The typical value of $n = 2/3$ has been verified by a study of the Lawrence Berkeley National Laboratory (LBNL), where measurements of over 7000 single-family houses were analyzed [29]. The extreme cases of $n = 0.5$ and $n = 1.0$ correspond to the previously discussed Eqs. (2.10) and (2.11).
Moreover, Walker et al. [77] presented the following proportionality for flow coefficient C:

$$C \propto \frac{\rho^{n-1}}{\mu^{2n-1}} \tag{2.17}$$

For the evaluation of coefficient C at specific reference values, the ratio becomes:

$$\frac{C}{C_{ref}} = \left(\frac{\rho}{\rho_{ref}}\right)^{n-1} \left(\frac{\mu_{ref}}{\mu}\right)^{2n-1} \tag{2.18}$$

Using this format of expressing the flow coefficient shows that C gets independent of viscosity for turbulent orifice flows ($n = 0.5$) and of the fluid density for laminar flows ($n = 1.0$). Further, assuming that the viscosity is nearly linear dependent on the air temperature T_a for the relevant temperature range in buildings and air behaves like ideal gas in this temperature range, the equation can be reformulated to:

$$\frac{C}{C_{ref}} = \left(\frac{P}{P_{ref}}\right)^{n-1} \left(\frac{T_{ref}}{T_a}\right)^{3n-2} \tag{2.19}$$

It is possible to correct the flow coefficient to temperature and barometric pressure changes using this equation, thus ensuring comparability between measurements under different ambient conditions. As already mentioned above, the flow exponent n has a value of typically 2/3 in residential buildings. For this value, the flow coefficient C is independent of the ambient temperature, making this formulation easier to use than other formulations.

In summary, the power-law form is a reasonable model to describe the flow through a building envelope and through a network of cracks that can vary in size and shape and is in good agreement with measured data [18, 73]. The quadratic form has a more robust theoretical basis and is dimensionally homogeneous, unlike the power-law form [79]. However, Chiu et al. [80] recommended using the power-law form rather than the quadratic form because it is easier to use. On the one hand, it fits better to measurements with smaller cracks in the building envelope, and on the other hand, it provides a better balance for parallel and series networks of cracks.

2.2 Measuring Methods of Building Airtightness

2.2.1 Pressurization Methods

Fan Pressurization Method

The most prominent method of measuring airtightness is the fan pressurization method, also known as the "blower door" test or "DC pressurization" method. This method produces data, which are used to derive flow characteristics, such as n and C values (cf. Eq. (2.16)) of a building or its components.
A blower, usually placed in the front door, simultaneously moves air into a building while measuring the applied uniform and static pressure difference across the building envelope. Internal and external pressure taps measure the induced pressure difference. Usually, calibrated orifices in front of the blower are used to measure the airflow. An example of an experimental setup is shown in Fig. 2.3.

There are multiple methods for determining the airflow through a building envelope using the fan pressurization method. The simplest way to measure the airflow is a simple single-point measurement. Here, a building is either pressurized or depressurized with a pressure difference across the envelope of most often ±50 Pa, and simultaneously the airflow at 50 Pa pressure difference (Q_{50}) is measured. If required, the airflow under natural conditions at 4 Pa (Q_4) can thereafter be extrapolated from this data (assuming $n = 2/3$):

$$Q_4 = Q_{50}\left(\frac{4}{50}\right)^n \tag{2.20}$$

Because the pressure exponent is previously assumed and does not necessarily fit the actual building, this extrapolation procedure is likely to contain large errors if n differs in reality from the assumed value. Walker et al. [29] demonstrated that if the actual pressure exponent differs by only 0.1 compared to the assumed value, the extrapolation error would be 29 % if data from high pressures (at 50 Pa) were

Figure 2.3: Blower Door measurement system

extrapolated to the pressure range of interest (at, e.g., 4 Pa). If even the airflow at 1 Pa is interesting (which some models require), the error would increase to 48 %. Consequently, several international standards [53–55] require multiple measurements from 10 Pa up to 50 Pa or 60 Pa pressure difference (depending on which standard is used). Mostly, this measurement procedure is repeated twice for pressurization and depressurization tests. These measurements allow fitting the flow exponent n and flow coefficient C to the pressurized or depressurized measurement data, applying this rewritten linear form of the power-law (cf. Eq. (2.16)):

$$\ln(|Q|) = n \, \ln(|\Delta P|) + \ln(C) \tag{2.21}$$

After the determination of n and C, airflows at low pressures can be calculated.

According to Walker et al. [29], the most considerable uncertainty within the blower door measurements is attributable to the fact that the measured pressure range dramatically exceeds the pressure leaks are typically exposed to. The main advantage of using high pressures is that the higher the pressure differences are, the less important is the influence due to weather conditions. Moreover, the relative error due to the measurement devices is lower at higher pressures. However, the extrapolation error to lower pressures increases for larger pressure differences. For more information about uncertainties of blower door measurements, see Refs. [81–83].

At the same time, the system has some limitations. Finding individual leakage spots is cumbersome and requires experience and persistence. For the detection of these spots, additional equipment is needed, e.g., smoke generators (see Fig. 2.4) or infrared camera systems (see Section 2.2.2), which can additionally increase the overall costs of the inspection. Moreover, for buildings with significant air leakage or large buildings, one blower might not be sufficient to reach the required pressure differences.

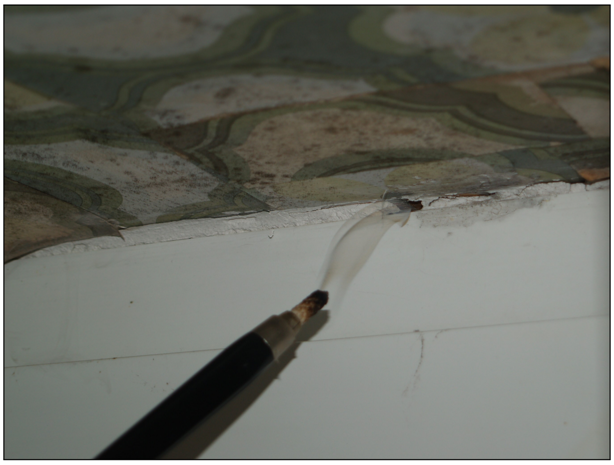

Figure 2.4: Leak detection using smoke sticks

In contrast to the steady fan pressurization method, the oscillation, decay, and pulse methods are called unsteady measurement methods. Whereas the airflow rate with the fan pressurization method is measured at time-consuming multiple steady pressure levels, the unsteady methods reflect the pressure response of a room or building with only one curve. These methods are shortly introduced in the following paragraphs.

Oscillation Method

With the oscillation or "AC pressurization" method, small sinusoidal pressure fluctuations (of order 1 Hz) are generated using a piston and cylinder assembly sealed in an exterior door of the building. These fluctuations are clearly distinguishable from naturally occurring pressures. The time-varying pressure response of the building is measured at the same frequency as the volume, whereas the amplitude and phase of the response are affected by the building's airtightness. From the phase change between the fluctuating piston volume pressure and the pressure across the envelope and from the change in pressure amplitude, the airflow through the building envelope can be calculated. For a detailed derivation of the equations, see Refs. [84–87]. The advantage of this method is the elimination of pressure fluctuations caused by the weather, which allows measurements at very low pressures.

Decay Method

In the decay method, the pressure inside a building enclosure is increased until it reaches a certain level. After an abrupt stop of supplied airflow, the leak rate is determined based on the pressure decay within a certain period of time [88–90]. The theoretical pressure profile of the decay method is shown in Fig. 2.5a. This measurement method is less time-consuming than the fan pressurization method because it requires the acquisition of only one parameter, the change of pressure difference. However, the sampling rate of the recording device needs to be higher, and the measurements are more sensitive to pressure-related deformations of the building envelope.

Pulse Method

The pulse method [91–95] can measure a building's airtightness at lower pressures than the fan pressurization method. Here, a known pressure volume of air is released rapidly into a building, which creates an instant pressure rise. This pressure rise quickly reaches a "quasi-steady" condition. Simultaneously, the pressure variations in the building and the pressure tank are monitored to establish a relationship between building air leakage and pressure gradient. This process is presented in Fig. 2.5b. Similar to the blower door test, multiple pressure levels are measured but dynamically and not at steady pressure points (typically between 1 to 10 Pa). The advantage of this method is that the building envelope is not penetrated during measurements, and the system is very small and portable. However, this method does not produce enough pressure to detect leaks in the envelope with supplementary methods like smoke tracers.

2.2.2 Thermographic Method

The technique of infrared thermography (IRT) is a non-contact, non-destructive technology used to determine building surface temperature. In contrast to the previously listed

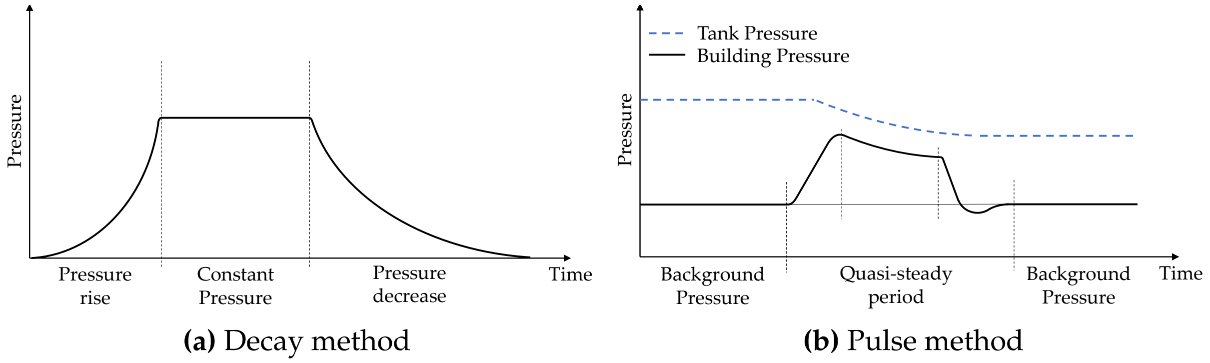

(a) Decay method **(b)** Pulse method

Figure 2.5: Pressure profile of a decay measurement based on Ref. [90] and pressure profiles of pulse test based on Ref. [93]

methods, which primarily quantify air leakage in buildings, the IRT method enables detecting leaks, thermal bridges, and insulation defects.

The measurement system maps the infrared radiation as a thermal image of the surface, which visualizes relative intensity as a function of the surface temperature, the surface physical properties (e.g., roughness and emissivity), surrounding conditions, and the measuring probe itself. This method is applied to buildings for several reasons, e.g., the evaluation of energy efficiency [96–99], the performance of building diagnosis [100–105], or the detection of moisture in building components [106–109].

Additionally, the thermographic method to detect thermal irregularities in the building envelope has been specified in the DIN EN 13187:1998 standard [110]. Irregularities in building envelope insulation lead to temperature gradients at the building surface. By analyzing the distribution of the building surface temperature, an infrared thermography system can detect defects in insulation and air leaks but requires expensive equipment (compared to other methods), a high level of expertise, and temperature differences between inside and outside.

The surface temperature and the air temperature near the surface are significantly influenced by air flows through the building envelope, which allows an identification of the most critical air leakage locations using IRT [7, 97, 100, 111–114]. Nevertheless, in most cases, these locations are only observable if a pressure difference across the building envelope is additionally applied. The magnitude of the temperature difference around a leak is a function of the shape/size of the leak, the temperature difference, and the pressure difference across the building envelope. The preferred temperature difference between inside and outside should be at least 5 K, but better 10 K [115]. This may require a rise of the indoor air temperature. A blower door device or natural wind pressure can be used to obtain a pressure difference. Whereas the installation of a blower door requires more effort, the approach using wind pressure does not guarantee stable conditions. According to Hart [116], a pressure difference of at least 10 Pa is desirable. IRT is used in some applications to detect air leaks in the building envelope, but it requires temperature increase in the building (in summer: overheating) and pressure difference. Leak detection is possible, but quantification of the airflow through single leaks is not possible.

2.2.3 Tracer Gas Methods

The tracer gas measurement method allows the measurement of the air exchange rate through the building envelope under actual conditions, like temperature and wind. This is an advantage over the fan pressurization method measuring the airflow in buildings at pressure ranges above the natural ventilation. At ambient pressure, this air exchange rate is the relevant measure to assess the building's energy consumption, indoor air quality, or propagation of gases and smell. Additionally, with this method, the air movement inside the building can be examined, which can be a vital factor for investigating the thermal comfort within occupied spaces and an essential design parameter for air distribution systems providing ventilation air inside buildings.

A suitable tracer gas should be detectable, non-reactive, non-toxic, relatively low concentrated in ambient air, and inexpensive [117]. Additionally, the tracer gas shall not react chemically with other materials or adsorb. Common tracer gases are inter alia SF_6, H_2, CO, CO_2, NO_2, or perfluorocarbons [118–120]. In this work, hydrogen (bottled forming gas: 5 % H_2 in N_2) has been used because it is more environmentally friendly than SF_6 and the detectors are small and handy.

The mass balance of tracer gas within a building can be described as [119]:

$$V\,\frac{dC}{dt} = F(t) - Q(t)\,C(t) \tag{2.22}$$

Here, V is the volume of the tested room, $C(t)$ is the tracer gas concentration, $F(t)$ is the tracer gas injection rate at time t, and $Q(t)$ is the airflow rate out of the volume. This mass balance is valid under the assumptions that no other tracer gas is existent, and the traces gas is mixed completely within the volume. In moderate climate zones, differences in air density due to temperature differences between indoor and outdoor are ignored [32].

The solution of Eq. (2.22) (with C_0 as concentration at $t = 0$) is given by:

$$C(t) = C_0\,e^{-n\cdot t} + e^{-n\cdot t}\int\limits_0^t e^{n\cdot u}\,\frac{F(u)}{V}du \tag{2.23}$$

For the assumption of a constant injection rate $F = const$, the solution presented in Eq. (2.23) is integrated further to:

$$C(t) = C_0\, e^{-n \cdot t} + \frac{F}{V}\left(1 - e^{-n \cdot t}\right) \tag{2.24}$$

n is the air change rate at natural pressure difference as defined in Eq. (2.7).
According to the ASTM E742 [121] and DIN EN ISO 12569:2018 [53] standards, there are three prevailing measurement techniques with tracer gas for determining the air exchange rate, depending on the specific application: the concentration decay, constant concentration, and constant injection method.
The most used technique for tracer gas measurements is the concentration decay method with an initial tracer gas concentration C_0 and no further injection over time ($F(t) = 0$). This method is the most frequently used method because it requires a minimum of equipment and is the least disruptive method [34]. For this method, a small amount of tracer is released into the room, whereby a proper mixing of tracer gas in the test volume is required. Mixing is the prevailing challenge of this method leading to errors if not performed thoroughly. This need for mixing limits the decay technique to investigate only small buildings.
After the injection is stopped ($F = 0$, cf. Eq. (2.24)), the decay of the concentration is monitored:

$$C(t) = C_0\, e^{-n \cdot t} \tag{2.25}$$

The typical method is to measure C periodically and apply a linear fit with the following form of Eq. (2.25):

$$\ln(C(t)) = \ln(C_0) - n \cdot t \tag{2.26}$$

From Eq. (2.26), the air change rate n can subsequently be calculated:

$$n = \frac{\ln\left(\frac{C_0}{C(t)}\right)}{t} \tag{2.27}$$

The air exchange rate n is the slope of the logarithmic Eq. (2.26) and in test determined with an applied linear fit. This is an advantage because only relative concentrations are needed. The result is independent of the initial concentration. The required measurement time in practical application is from a few minutes to hours. In order to determine n, measurements of the volume of the room as well as for the injection rate or injection volume are not needed. Due to its simplicity, the tracer gas concentration decay technique is used in this work for intercomparison of the acoustic methods.

The constant concentration method consists of maintaining a constant tracer gas concentration by measuring and controlling the tracer gas injection rate F to keep concentration C constant. The constant injection method uses a constant tracer gas injection flow and determines the resulting equilibrium concentration C. For more information about the application of the alternative constant concentration and constant injection method, see Refs. [32, 118, 119, 122–124].

2.2.4 Acoustic Methods

As in the previous sections discussed, localizing and quantifying leaks in the building enclosure is essential for assessing its thermal performance. However, conventional fan pressurization methods have significant drawbacks because they depend on weather conditions (such as wind or temperature), all intentional leaks have to be sealed before measurements, and locating and quantifying single leaks is cumbersome. Supplementary acoustic methods may have the potential to support current air leakage measurement methods to identify and quantify single leaks.

One possible acoustic approach has already been suggested in the ASTM E1186 [121] standard, based on the work of Keast et al. [125, 126] done in the 1970s. Among other methods like building pressurization, infrared scanning, and tracer gas detection, this standard recommends the use of sound detection, which is still rarely applied in buildings. The standard proposes simple tools, like a low-cost sound level meter and a vacuum cleaner as a sound source, to measure the sound transmission loss of building parts. However, the accuracy of measurement with these simple tools has not been studied yet.

Some related work has been done to quantify [127] and detect [128] holes in pipes with compressed air. Oldham et al. [129] modeled the acoustic and airflow performance of ventilation apertures, and Park et al. [130] investigated the acoustical performance of airtight windows.

Several other studies examined the sound transmission losses through the building envelope in both laboratory [131–134] and field testing [135–137] to quantify leakage sizes with some success. In addition to the range of audible sound, Graham [138] considered infrasonic impedance measurements for leakage determination, whereas other authors focused on the higher ultrasonic frequencies for localizing [139–142] and quantification [143] of air leakages in buildings. Ultrasonic frequencies have the advantage of being above the human auditory threshold of hearing, which may not disturb inhabitants in buildings during measurement. Additionally, ultrasonic wavelengths are in the same order of magnitude as potential leak sizes. Therefore, ultrasonic frequencies are considered in this work as well.

Some work has been recently done by evaluating microphone arrays and beamforming techniques for a comprehensive assessment of building façades. Raman et al. proposed the nearfield acoustic holography method to locate and quantify leaks in buildings and building components [144–147]. The technique of beamforming will be further introduced in this work in Chapter 8. In the following chapter, the basics of acoustics and signal processing are introduced.

3 Theory of Acoustics and Signal Processing

In this thesis, several acoustical approaches are assessed to quantify and locate leaks in building envelopes. The following chapter shall provide a brief theoretical background of the main principles of acoustics and signal processing necessary to follow the conducted experiments. For more detailed information about these topics, related literature is cited in this chapter.

3.1 Acoustic Fundamentals

3.1.1 Characteristics of Sound

First, some general characteristics of sound are defined. The term sound generally describes mechanical oscillations in an elastic medium.

A propagation of sound requires a matter which is solid, liquid, gaseous, or plasma-like or a matter with several phases (e.g., air with dust particles and water droplets). Requirements for the generation of sound are periodic or non-periodic processes, i.e., dynamic processes or fluctuations in physical quantities, parameters, and states in the macro and micro range [148].

Depending on the medium within the sound propagates, one can distinguish between:

- Solid medium → structure-borne sound
- Liquid medium → liquid-borne sound
- Gaseous medium → airborne sound

In a solid medium, waves can be propagated in complex forms because forces can be transmitted in the direction (tensile and compressive stresses) and transversely (shear stresses) of an element's deflection. In contrast to solid mediums, shear stresses cannot be transmitted in liquid and gaseous mediums. In fluids, like air, the sound is propagating only in longitudinal waves. In this work, predominantly airborne sound is considered. The propagation of airborne sound waves is based on the transmission of impulses as well as potential and kinetic energy between the air particles. The mathematical description of the processes is given by the three-dimensional sound wave equation, where the p is the sound pressure, and c is the speed of sound:

$$\nabla^2 p = \frac{1}{c^2}\frac{\partial^2 p}{\partial t^2} \tag{3.1}$$

with the Laplacian operator ∇^2 defined as:

$$\nabla^2 = \frac{\partial^2}{\partial x^2} + \frac{\partial^2}{\partial y^2} + \frac{\partial^2}{\partial z^2} \tag{3.2}$$

The sound wave equation is valid under the following assumptions: isentropic changes in state, fluid movements without friction and vortices, "stationary" fluids (no mean flow), no sources, and no external forces. For a detailed derivation of this formula, see Ref. [149].

Sound Pressure and Sound Pressure Level

The sound pressure is measured in Pa and is a scalar quantity. It describes the pressure of a sound wave oscillating above and below the atmospheric pressure p_{atm}. In the case of a simple harmonic oscillation of air particles (cf. Fig. 3.1), the sound pressure p can be described as a function of the pressure amplitude $\hat{p}$, time t, frequency f, and phase ϕ:

$$p(t) = \hat{p}\,\cos(2\,\pi\,f\,t + \phi) = \mathrm{Re}\left\{\hat{p}\,e^{i2\pi f t}\right\} \tag{3.3}$$

The frequency f will be further defined in the next paragraph.

Because the human ear responds across an extensive range of sound pressure, the more convenient logarithmic decibel scale (dB) is a preferred method of presenting acoustic quantities. The term "level" in combination with "sound pressure" indicates that the decibel scale is being used. For conversion to the decibel scale, a reference quantity is needed. The reference quantity p_{ref} in the case of sound pressure level calculation is often 20 µPa, which equals approximately the lower human threshold of hearing. This

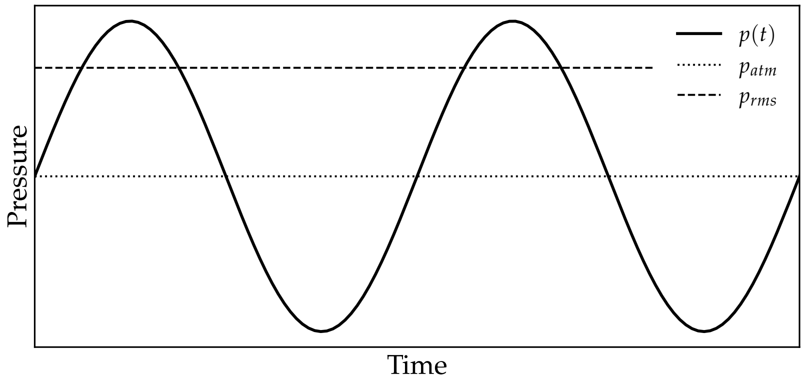

Figure 3.1: Harmonic oscillation of sound pressure in air

value is an internationally accepted reference value for most acoustic applications, but theoretically, any arbitrary value could be chosen as a reference. Therefore, the sound pressure level is given by:

$$L_p = 20\lg\left(\frac{p_{rms}}{p_{ref}}\right) \tag{3.4}$$

The required root mean square value (or effective value) of the sound pressure p_{rms} is defined as [150]:

$$p_{rms} = \sqrt{\frac{1}{T}\int_0^T p(t)^2\,dt} \tag{3.5}$$

Frequency and Wavelength

The frequency f of a vibrating object is defined as the number of oscillations (or cycles) completed in one second. The human audible frequency range extends from 16 Hz to about 20 kHz. Infrasound ($<$ 16 Hz) and ultrasound ($>$ 20 kHz) are frequency regions below and above the human threshold of hearing. In addition to the audible frequency range, particularly ultrasonic frequencies were investigated in this work.

The wavelength of sound is the distance between a minima or maxima of a harmonic disturbance propagating in a specific medium. The relationship between wavelength λ, speed of sound c, and frequency f can be described as follows:

$$\lambda = \frac{c}{f} = c\,T \tag{3.6}$$

T is the period length, which is inversely proportional to the frequency f.

The speed of sound c is defined as the magnitude of the phase speed of a freely propagating sound wave:

$$c = \sqrt{\frac{dp}{d\rho}} \tag{3.7}$$

According to Bergmann [151], the speed of sound in air can, for practical applications, further be approximated as:

$$c \approx c_0 \sqrt{1 + \beta \left(T_a - 273.15\right)} \approx 331.3 + 0.6 \left(T_a - 273.15\right) \tag{3.8}$$

Where c_0 is equivalent to the speed of sound at 0 °C and standard atmospheric pressure, β is the thermal expansion coefficient of air, and T_a is the ambient air temperature in K. This equation is valid as long as the wavelength is not in the same order as the free path between the molecules, thus until a frequency of roughly 10^8 Hz. Additionally, the effect of dispersion can be neglected within the considered frequency ranges in this thesis. In air, the speed of sound is approximately 344 m/s (at an ambient air temperature of 20 °C).

3.1.2 Sound Measurement

The previously described acoustic quantities are recorded by sensors and transformed into electrical signals. Microphones are sensors that are able to measure the superposition of the static barometric pressure with the dynamic pressure fluctuations in air and convert them to electrical signals. Sound measurement systems in liquids are called hydrophones, and systems measuring the structure-borne noise are accelerometers. In this work, only microphones for the measurement of airborne sound transmission are considered.

Depending on the microphone's construction, either the sound pressure or the sound pressure gradient is measured. If the microphone membrane is accessible from only one side, the membrane is moved according to the sound pressure, enabling a measurement of the sound pressure. On the other hand, if the sound pressure is able to access both sides of the membrane, the gradient can be measured. The membrane is excited as a function of the pressure difference between both sides. The pressure difference is induced by the time the soundwaves need to reach the backside of the membrane. Sound pressure microphones often have an omnidirectional recording characteristic; hence the recorded signal is independent of the direction of the incident soundwave. At the same time, pressure gradient microphones have a decrease in sensitivity with increasing incident angle. In this work, 1/4 in. sound pressure condenser microphones are used.

Within these condenser microphones, a membrane, together with a counter electrode, forms a capacitor. An incoming sound wave causes a displacement of the membrane, which changes the distance between the membrane and the counter electrode. This displacement leads to a measuring voltage proportional to the sound pressure. Typically, this sensitivity is for microphones with small capsule diameters of 1/4 in. between 2 and 10 mV/Pa and for medium capsule diameters of 1/2 in. between 30 and 50 mV/Pa. In addition to the directional characteristic, the linearity of the sensitivity with regard to the frequency content is of decisive importance. Ideally, all frequencies contained in a sound source are converted into the electrical signal with the same proportionality factor. Real microphones have an approximately linear behavior within a wide frequency range. Outside this range, the sensitivity decreases. The microphones used in this work have a sensitivity of 2.0 mV/Pa within a frequency range of 4 Hz to 100 kHz.

For more information about acoustic measurement techniques, see Refs. [152, 153]

3.2 Signal Processing

After a brief introduction of some fundamental terms and concepts of acoustic and sound propagation, the following section presents the mathematical and theoretical background of signal processing necessary to understand the experiments conducted in this work.

3.2.1 Fourier Series and Transform

One of the most fundamental concepts to determine the frequency content of a signal is the Fourier transform, which will be introduced here.

Fourier Series

According to Fourier's theorem, a periodic signal $x(t)$ can be represented by Fourier series as an infinite sum of sine and cosine functions [154]:

$$x(t) = A_0 + \sum_{n=1}^{\infty} \left[A_n \, \cos(\omega_n \, t) + B_n \, \sin(\omega_n \, t)\right] \tag{3.9}$$

with ω_n as the angular frequencies (harmonics) of the sines and cosines, which are multiples of the fundamental angular frequency ω_0:

$$\omega_n = n \, \omega_0 = 2 \, \pi \, f_0 \, n = 2 \, \pi \, \frac{n}{T} \tag{3.10}$$

f_0 is the fundamental frequency and defined as the lowest possible frequency of a sine or cosine function that fit exactly into one period T of $x(t)$.

A_n and B_n in Eq. (3.9) are the Fourier coefficients. They are defined as an integral of the product of $x(t)$ and a sine or cosine function over a duration of one period T (most commonly defined from $-T/2$ to $T/2$):

$$A_n = \frac{2}{T} \int\limits_{-T/2}^{T/2} x(t) \, \cos(\omega_n \, t) \, dt \tag{3.11}$$

$$B_n = \frac{2}{T} \int\limits_{-T/2}^{T/2} x(t) \, \sin(\omega_n \, t) \, dt \tag{3.12}$$

The term A_0 in Eq. (3.9) is a constant, which is practically the average value of signal $x(t)$ over period T:

$$A_0 = \frac{1}{T} \int\limits_{-T/2}^{T/2} x(t) \, dt \tag{3.13}$$

The Fourier series approximates a periodic function $x(t)$ as a sum of sine and cosine waves. Within the Fourier series, the Fourier coefficients A_n and B_n are real numbers and characterize the weight of the sine and cosine contributions. In a spectrum, these Fourier coefficients are simply plotted against the frequency.

Fourier Transform

The measurement of sound pressure takes place within the time domain and is therefore recorded as a time-dependent quantity. However, this time signal is often not directly interpretable. The Fourier transform converts the signal from the time into its frequency domain and shows the signal's frequency content. Although the Fourier transform is based on the previously described Fourier series, the Fourier transform differs in some ways. In contrast to the Fourier series, the Fourier transform is a complex and continuous function of frequency, whereas the Fourier series consists of discrete frequencies (which are multiples of the fundamental frequency). Additionally, negative and positive frequencies in a symmetrical spectrum are both equally important. For more information, see Refs. [155, 156].

By applying Euler's formula, the Fourier transform $X(\omega)$ of a continuous signal $x(t)$ can be demonstrated as follows:

$$X(\omega) = \mathcal{F}[x(t)] = \int\limits_{-\infty}^{\infty} x(t)\,[\cos(\omega\, t) - i\,\sin(\omega\, t)]\; dt = \int\limits_{-\infty}^{\infty} x(t)\, e^{-i\,\omega\, t}\, dt \tag{3.14}$$

Often, the polar expression of Eq. (3.14) is more useful because the function is directly divided into its magnitude and the exponential phase:

$$X(\omega) = |X(\omega)|\, e^{i\,\phi(\omega)} \tag{3.15}$$

Data Sampling

In actual measurements, continuous analog signals are converted to a digital sequence of measurement points, which is the "sampling process". According to the Nyquist–Shannon sampling theorem [157], a sampled signal adequately represents an analog signal if the sampling frequency f_S is higher or equals twice the highest desired frequency f_{max}: $f_S \geq 2 f_{max}$. A lower sampling frequency may lead to a loss of information and cause alias signals, leading to a wrong reconstruction of the sampled signal.

Additionally, the process of analog-digital converting leads to quantization errors because each measured quantity is rounded to the closest value that can be represented by the digital system. The accuracy of this process is influenced by the number of quantization levels, which is specified by the number of bits of the analog-digital converter. The distance between two displayable quantities is the measurement interval divided by $2^N - 1$ (with the number of bits N). The maximum quantization error is half of this distance. The analog-digital converters in this work have a resolution of 24 bits and 32 bits.

Discrete Fourier Transform

The Fourier transform is defined for continuous signals and signals that are unlimited in time. However, measured signals are not continuous. Because of the previously described sampling process, the signals contain a finite number of discrete frequency components; hence, the discrete Fourier transform (DFT) can be applied:

$$X(n\,\omega_0) = \Delta t \sum_{k=0}^{N-1} x_k \left[\cos\left(\frac{2\pi\,n\,k}{N-1}\right) - i\,\sin\left(\frac{2\pi\,n\,k}{N-1}\right)\right] = \Delta t \sum_{k=0}^{N-1} x_k\, e^{-\frac{i2\pi\,n\,k}{N-1}} \qquad (3.16)$$

The DFT requires a long computing time for large data sets; therefore, the fast Fourier transform (FFT), a faster algorithm, is used in this work. If the signal length is an exact power of two, the results from FFT are the same as the results from DFT, but with fewer operations and less processing time. The outcome of this calculation is again a two-sided spectrum in a complex format.

3.2.2 Auto- and Cross-Correlation

Correlation functions are beneficial to detect signals buried in noise or assess the similarity between signals. They form the basis for the analysis in this work. Therefore, these principles are shortly introduced here.

The autocorrelation function a_f describes the similarity between a time signal $x(t)$ at time t and the same signal with an additional time difference $t+\tau$ and is given by [154, 158]:

$$a_f(\tau) = \lim_{T\to\infty} \frac{1}{2T} \int\limits_{-T}^{T} x(t)\,x(t+\tau)\,dt = \lim_{T\to\infty} \frac{1}{2\pi\,T} \int\limits_{0}^{\infty} |X(\omega)|^2 \cos(\omega\,t)\,d\omega \qquad (3.17)$$

With $\tau = 0$, a_f becomes the square of $x(t)$, which is the largest possible value. This function may extract a signal which is covered in noise.

From the autocorrelation, the auto-spectral density can directly be derived, which is the

Fourier transform of the autocorrelation function a_f:

$$G_{xx} = \frac{2}{\pi} \int_{0}^{\infty} a_f(\tau)\, \cos(\omega\, \tau)\, d\tau = \frac{1}{2\pi\, T}\, |X(\omega)|^2 \tag{3.18}$$

Thus, through the Fourier transform of the autocorrelation, the frequency spectra of an unknown repetitive signal can be obtained, even if the signal is covered by accompanying noise [158].

In addition to the autocorrelation function, the cross-correlation function ρ_o measures the similarity of two different signals, $x(t)$ and $y(t+\tau)$, with a time difference between them. This cross-correlation function is defined as:

$$\rho_o(\tau) = \lim_{T\to\infty} \frac{1}{2T} \int_{-T}^{T} x(t)\, y(t+\tau)\, dt = \lim_{T\to\infty} \frac{1}{4\pi\, T} \int_{-\infty}^{\infty} X(\omega)\, Y^*(\omega)\, e^{i\,\omega\,\tau}\, d\omega \tag{3.19}$$

Similar to the calculation of the auto-spectral density, the cross-spectral density is calculated by taking the Fourier transform of the cross-correlation function [158]:

$$G_{xy}\,(\omega) = \frac{1}{\pi} \int_{-\infty}^{\infty} \rho_o(\tau)\, e^{-i\,\omega\,\tau}\, d\tau = \frac{1}{2\pi\, T}\, X(\omega)\, Y^*(\omega) \tag{3.20}$$

$X(\omega)$ and $Y^*(\omega)$ are here the Fourier transforms of $x(t)$ and $y(t)$. The superscript "*" indicates the Fourier transform of $y(-t)$:

$$\mathcal{F}(y(-t)) = Y^*(\omega) \tag{3.21}$$

3.2.3 Convolution

The principle of convolution is an important tool in Section 4.3 for a filter signal calculation and is therefore shortly described. The convolution between two functions $x(t)$ and $h(t)$ (given by $x(t) * h(t)$) is in the time domain defined by the convolution integral:

$$x(t) * h(t) = \int_{-\infty}^{\infty} x(\tau)\, h(t-\tau)\, d\tau \tag{3.22}$$

Sometimes the more convenient way to calculate the convolution is simply a multiplication in the frequency domain using the Fourier transform $X(f)$ and $H(f)$ of $x(t)$ and

$h(t)$:

$$\mathcal{F}(x(t) * h(t)) = X(f)\,H(f) \tag{3.23}$$

3.2.4 Hilbert-Huang Transform

In addition to the widely used and previously described Fourier transform, other methods are available to analyze the spectral content of a transient signal. Some signals in this work (see Section 4.2) are typical non-stationary signals. A high resolution in frequency and time may be crucial to obtain information about the signal behavior at specific time steps. Zhou et al. [159] compared different methods (e.g., fast Fourier transform, Wigner-Ville distribution, Wavelet transform, and Hilbert-Huang transform (HHT)) to identify the most appropriate time-frequency analysis method. They selected HHT as the most suitable method for analyzing frequency-modulated signals.

The fast Fourier transform can quickly calculate the frequency components of a signal, but it cannot guarantee a high resolution in frequency and time simultaneously. As described in Section 3.2.1, the Fourier transform decomposes a signal into a sum of sine and cosine functions with constant amplitude and frequency values. Therefore, these parameters remain stationary over the whole signal length regardless of abrupt changes in the original signal. Thus, the outputs of the Fourier transform are averaged over the whole signal length because calculations are made under the assumption of the stationary ability of the original signal.

The HHT enables a visualization of sudden changes in the original signal and has a good resolution in time and frequency simultaneously, but it requires more computing time [160].

Hilbert Transform

The HHT is based on the mathematical principle of a Hilbert transform. The Hilbert transform $\mathcal{H}[x(t)]$ of a function $x(t)$ is defined as [161]:

$$\mathcal{H}[x(t)] = y(t) = -\frac{1}{\pi} \lim_{\epsilon \to 0} \int_{\epsilon}^{\infty} \frac{x(t+\tau) - x(t-\tau)}{\tau}\, d\tau \tag{3.24}$$

Basically, this Hilbert transform is a convolution of the signal $x(t)$ with $1/t$ and can physically be interpreted as a frequency phase-shifted signal by $\pi/2$ while leaving the magnitude of the original signal $x(t)$ unchanged.

Together with the signal $x(t)$, its Hilbert transform $y(t)$ form the complex analytical signal $z(t)$ [160]:

$$z(t) = x(t) + i\,y(t) = a(t)\,e^{i\int f(t)\,2\pi\,dt} \tag{3.25}$$

The absolute value of the analytical signal $|z(t)|$ is frequently used to calculate the envelope of a signal $x(t)$ [154]. From the polar coordinate expression of the analytical signal $z(t)$, both the amplitude $a(t)$, and the instantaneous frequency $f_i(t)$, can be calculated:

$$a(t) = \sqrt{x^2(t) + y^2(t)} \tag{3.26}$$

$$f_i(t) = \frac{d\left(\arctan\left(\frac{y(t)}{x(t)}\right)\right)}{dt}\,\frac{1}{2\pi} \tag{3.27}$$

The “globally” defined frequency in the Fourier transform expresses the frequency of a sine or cosine function over the whole signal length. On the contrary, the here defined instantaneous frequency $f_i(t)$ is a “time-dependent” frequency. However, the instantaneous frequencies are only meaningful for signals with specific properties. Unfortunately, the instantaneous frequencies for most signals in real applications produce non-meaningful results, which is further discussed in Refs. [162, 163]. The recorded signal needs to be converted into various sub-signals, which meet specific requirements that enable interpreting the instantaneous frequencies. This process is the empirical mode decomposition.

Empirical Mode Decomposition

The empirical mode decomposition (EMD) is a fundamental part of the HHT [162]. Instead of describing a signal as a sum of sine and cosine functions (cf. FFT), the signal is decomposed into intrinsic mode functions (IMFs), which are modulated in frequency and amplitude. The original time signal $x(t)$ can then be described as the sum of the IMFs $c_j(t)$ and a residual $r(t)$:

$$x(t) = \sum_{j=1}^{n} c_j(t) + r(t) \tag{3.28}$$

The IMFs are able to determine the local instantaneous frequency at each position of the signal. An IMF has to fulfill the following requirements to determine meaningful instantaneous frequencies of the signal:

1. The number of zero-crossing and the number of extrema must be equal or should differ not more than one.

2. The mean value of the envelope defined by the maxima and the minima must be zero at any point.

Here, three steps are taken to obtain an IMF. First, all maxima and minima of the signal (Fig. 3.2a) must be identified and connected with two cubic splines to build the signal's upper ($e_{min}(t)$) and lower envelope ($e_{max}(t)$, Fig. 3.2b). Second, the mean value m_1 (Fig. 3.2c) of the upper and lower envelope has to be calculated for each step and subtracted from the initial signal to obtain the difference h_1 (Fig. 3.2d):

$$m_1(t) = \frac{e_{min}(t) + e_{max}(t)}{2} \tag{3.29}$$

$$h_1(t) = x(t) - m_1(t) \tag{3.30}$$

In the last step, the algorithm checks whether the new signal $h_1(t)$ corresponded to the previously described requirements of an IMF. If the requirements were not fulfilled, the first two steps are repeated with $h_1(t)$. If the new signal meets all requirements, the first IMF $c_1(t)$ is iteratively calculated. After that, a residual r_1 is obtained by subtracting the IMF from the original signal:

$$r_1(t) = x(t) - c_1(t) \tag{3.31}$$

Then, this residual signal is used as a new initial signal, and all steps of the previously described calculation are repeated to find subsequent IMFs. This process is stopped when a certain predefined threshold is reached or when the residual becomes non-oscillatory. In this work, the stopping criterion of this iteration process is selected according to Rilling et al. [164]. The number of IMFs depends on the original signal and is not automatically the same for all signals. Finally, the residual function $r(t)$ often shows the overall trend of the original signal.

The power of each IMF signal can be calculated using the following equation:

$$E(t) = \sum_{j=1}^{N} c_j^2(t) \tag{3.32}$$

Each IMF $c_j(t)$ is a signal on which the Hilbert transform [160] can be applied and which has a meaningful interpretation of the instantaneous frequency:

$$z_j(t) = c_j(t) + i\,y_j(t) = a_j(t)\,e^{i \int f_j(t)\,2\pi\,dt} \tag{3.33}$$

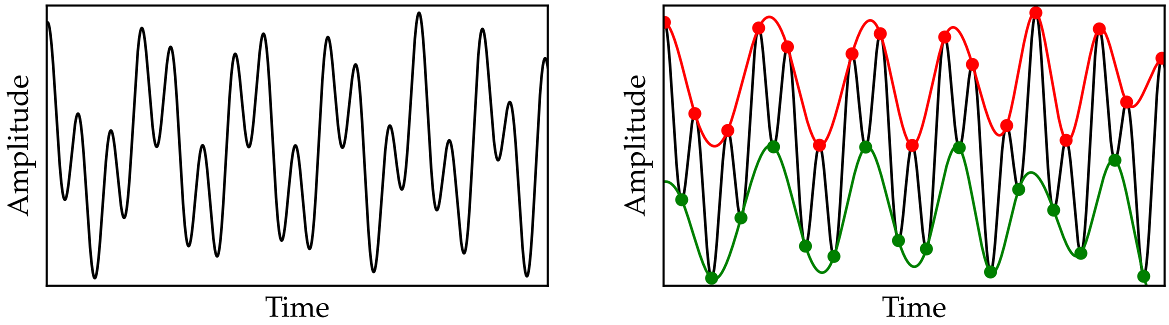

(a) Signal **(b)** Connection of maxima and minima

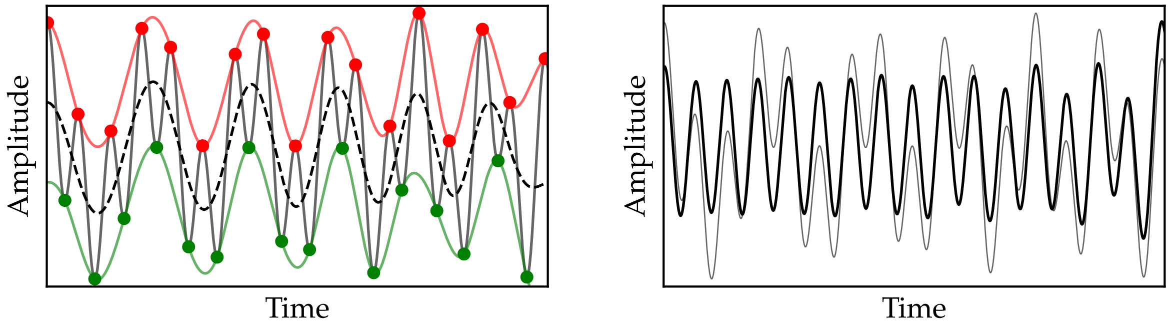

(c) Mean envelope m_1 (dashed) **(d)** Original signal and h_1 (bold)

Figure 3.2: First iteration of EMD

where $z_j(t)$ is the analytic signal associated with $c_j(t)$.

Finally, the original signal can be reassembled as the sum of the real part (Re) of the Hilbert transform of all individual IMFs:

$$x(t) = \mathrm{Re}\left\{ \sum_{j=1}^{\infty} a_j \, e^{i\, f_j \, 2\pi \, t} \right\} \tag{3.34}$$

This formulation permits the visualization of amplitude and instantaneous frequency as a function of time, which is the “Hilbert amplitude spectrum”.

3.2.5 Bandwidth Analysis

Sometimes, a high resolution in the frequency domain is not necessary. Details within large frequency intervals would not be very meaningful, so they would be quite random and vary widely between measurements. Further, results may be more reproducible within broader frequency bands. Moreover, broadband signals (e.g., white noise) are often used in room and building acoustics where spectral details are not always relevant.

For this reason, filters help to measure the frequency components of signals in broad sub-bands [149].
These filters are characterized by their bandwidth Δf, lower cut-off frequency f_{min}, upper cut-off frequency f_{max}, and the center frequency f_c. The bandwidth Δf is defined as the difference between the upper and lower cut-off frequency:

$$\Delta f = f_{max} - f_{min} \tag{3.35}$$

In acoustics, most commonly, filters with relative bandwidths are used. Here, the bandwidth is proportional to the center frequency of the filter. Therefore, the bandwidth increases with an increasing center frequency. For all filters with a relative bandwidth, the center frequency is defined as:

$$f_c = \sqrt{f_{min} f_{max}} \tag{3.36}$$

The most common relative filter types are octave-band and third-octave-band filters. Only third-octave-band filters are used in this work because of their higher spectral resolution compared to octave-band filters. The relationship between the center, upper cut-off, and lower cut-off frequencies for third-octave-band filters are defined as:

$$f_c = \sqrt[6]{2}\, f_{min} \tag{3.37}$$

$$f_{max} = \sqrt[3]{2}\, f_{min} \tag{3.38}$$

The band limits and center frequencies for octave and fractional-octave-band filters are further specified in the DIN EN 61260 standard [165].

3.2.6 Frequency Sweeps

A frequency swept signal changes its frequency with time. In this thesis, linear and exponential sweeps are applied. Thus, both are shortly introduced here.

Linear Sine Sweep

A linear sine sweep uses a linear frequency sweep function, in which the frequency increases linearly in time. With this sweep, a linear function is applied to ensure that all frequencies are equally distributed over a specified period of time [166]. The formulation for the linear sweep signal $s(t)$, which is valid in the interval of $0 \leq t \leq T$, can be described as follows:

$$s(t) = a\cos\Big(\phi_0 + 2\pi f_1 t + \pi r t^2\Big) \tag{3.39}$$

a is the signal amplitude, ϕ_0 the initial phase, and f_1 the start frequency. The sweep rate r, with f_2 equals the desired end frequency, and t_{sd} the overall sweep duration, is defined as:

$$r = \frac{f_2 - f_1}{t_{sd}} \tag{3.40}$$

In this specific implementation, $s(t)$ becomes 0 for $t < 0$ and $t > t_{sd}$. Fig. 3.3a shows an example of a linear sweep signal in the time domain.

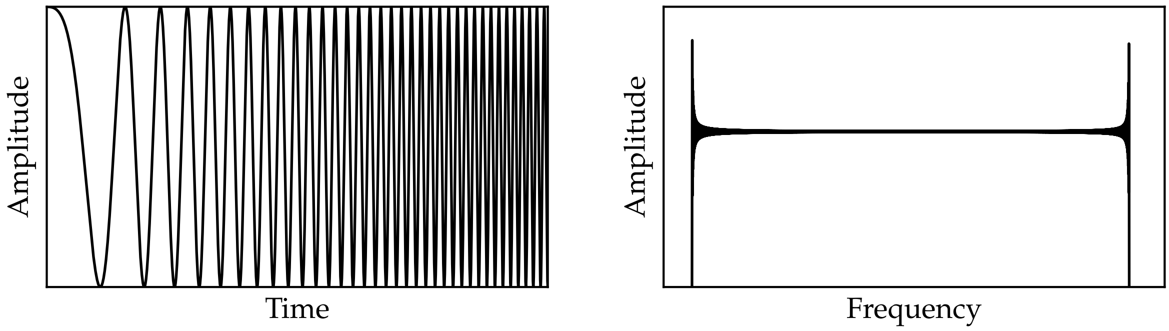

(a) Time domain

(b) Frequency domain

Figure 3.3: Linear sine sweep

If a Fourier transform is applied on a linear sweep with constant amplitude and sweep rate, all frequencies between the start and end frequency amplitude equally exist in the frequency spectrum and build a rectangular shape. In comparison, white noise has similar properties in the frequency spectrum. It exhibits a constant distribution of energy in the frequency spectrum [167]. Therefore, a frequency sweep with an infinite bandwidth would have a similar spectral shape. Although white noise is easy to implement, a frequency sweep tends to have a higher resolution and a better signal-to-noise ratio.

Fig. 3.3b illustrates the frequency spectrum of a linear sweep. In most parts of the sweep spectrum, the spectrum has a rectangular shape except at the beginning and end of the signal. There, oscillations called "Fresnel ripples" occur. No ripples would occur in a signal with infinite duration, but they appear because of a finite signal bandwidth, which generates artificial discontinuities at the ends of this signal in the frequency spectrum [168]. These discontinuities should be deleted to ensure that they do not lead to misinterpretation in evaluating the measured frequency spectrum.

According to Aldridge [166], the cosine tapered window (or Tukey window) w_{tukey} can be used to gradually taper the signal amplitude at the beginning and the end of the signal:

$$w_{tukey}[n] = \begin{cases} \frac{1}{2}\left[1 - \cos\left(\frac{\pi n}{N_1}\right)\right], & 0 \leq n \leq N_1 \\ 1, & N_1 < n < N - N_2 \\ \frac{1}{2}\left[1 - \cos\left(\frac{\pi(n-N+N_2)}{N_2}\right)\right], & N - N_2 \leq n \leq N \end{cases} \tag{3.41}$$

The parameters N_1 and N_2 express the proportion of the tapered data at the start and end of the sweep signal, whereas the signal remains constant in the interspace. In this work, N_1 and N_2 are both chosen to be 0.05, which promises to remove discontinuities but does not affect the signal bandwidth excessively. For $N_{1/2} \leq 0$, the Tukey window segues into a rectangular window, and for $N_{1/2} \geq 1$ the window segues into a Hanning window [169]. Fig. 3.4a shows an example of the shape of the resulting signal in the time domain. This signal adjustment is achieved by multiplying the original signal $s(t)$ with the window function w_{Tukey}.

This method of gradually induced tapering reduces the magnitude of oscillations at both ends of the spectrum, but it results in a slight reduction of spectral bandwidth; in this case, the reduction is approximately 4 %. Fig. 3.4b shows the spectrum of the tapered signal with no visible oscillations.

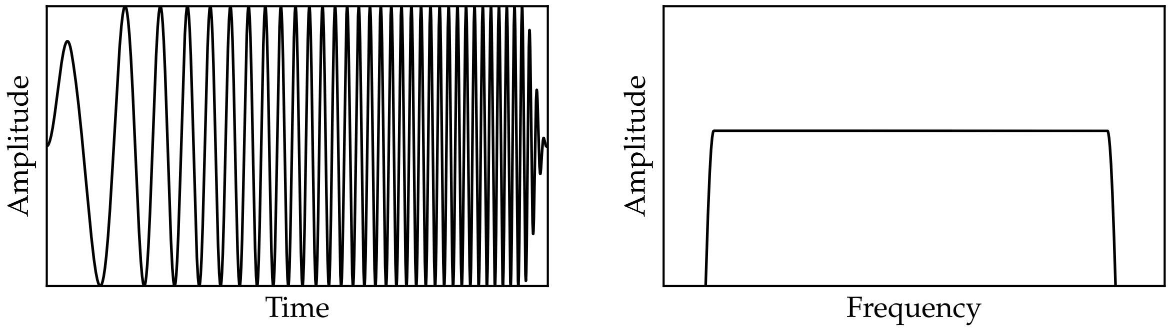

(a) Time domain **(b)** Frequency domain

Figure 3.4: Tapered linear sine sweep

Exponential Sine Sweep

In addition to the linear sine sweep, exponential sine sweeps are used to calculate the room impulse responses in this work (cf. Section 4.3). With the exponential sine sweep, the frequency function changes exponentially over time. This function is described by [170]:

$$s(t) = a \sin\left(\frac{2\pi f_1 t_{sd}}{\ln\left(\frac{f_2}{f_1}\right)}\left[\exp\left(\frac{\ln\left(\frac{f_2}{f_1}\right) t}{t_{sd}}\right) - 1\right]\right) \tag{3.42}$$

In Fig. 3.5, the time and frequency domains (with linear axes) are illustrated for an untapered (Figs. 3.5a and 3.5b) and a tapered (Figs. 3.5c and 3.5d) exponential sine sweep.

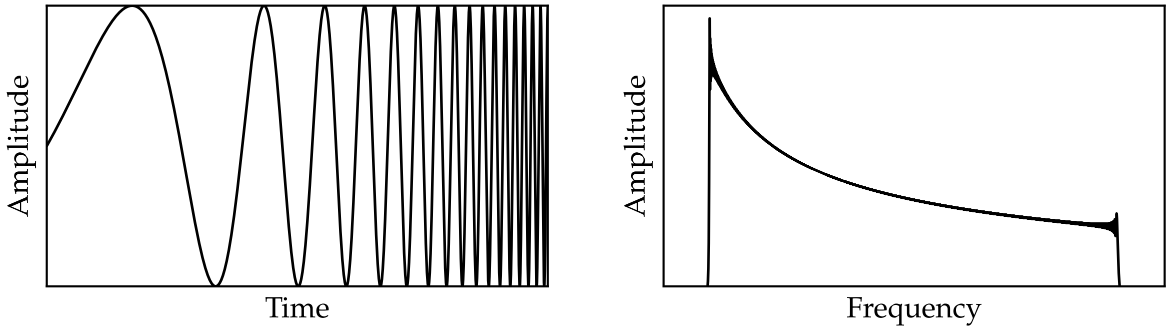

(a) Untapered time domain **(b)** Untapered frequency domain

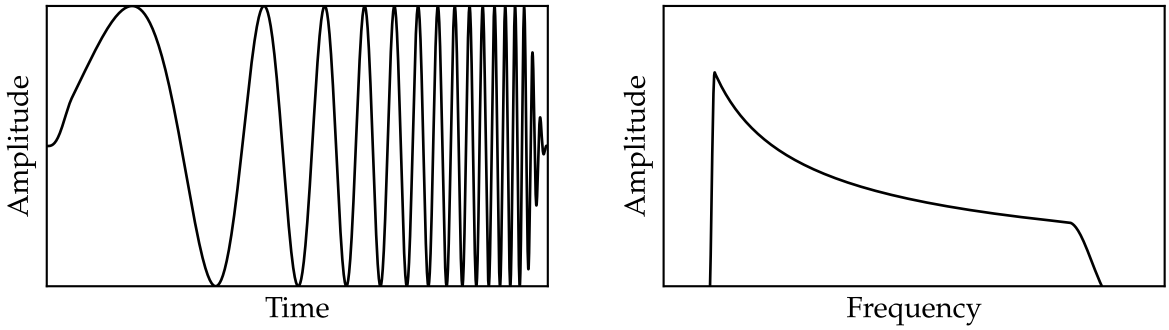

(c) Tapered time domain **(d)** Tapered frequency domain

Figure 3.5: Exponential sine sweep

4 Preliminary Laboratory Acoustic Investigations

The following chapter gives an overview of two laboratory experiments, which both aim to determine the size of small openings in artificial walls using different acoustic approaches.

4.1 Experimental Setup

4.1.1 Test Apparatus

A test chamber was constructed to compare different materials and leakage sizes under laboratory conditions wherein all measurements described in this chapter took place. This chamber consists of two equal-sized cells with the following dimensions for each cell: 30.0 cm × 43.5 cm × 31.0 cm and is schematically illustrated in Fig. 4.1. As test specimens, replaceable acrylic glass, as well as plywood walls, were used. Each barrier contains an orifice with a different diameter. These orifices simulate potential air leakages inside a wall. Except for these intentional openings, the walls were sealed airtight.

Major parts of this chapter are reproduced from:

B. Kölsch, A. Tiddens, J. Estevam Schmiedt, B. Schiricke, and B. Hoffschmidt, "Detection of Air Leakage in Building Envelopes Using Ultrasound Technology", in *Whole building air leakage*, ser. Selected technical papers ASTM International, T. A. Weston, K. Nelson, and K. Wissink, Eds., West Conshohocken, PA: ASTM International, 2019, pp. 160–183, ISBN: 978-0-8031-7675-1. DOI: `10.1520/STP161520180022`

B. Kölsch, B. Schiricke, J. Estevam Schmiedt, and B. Hoffschmidt, "Estimation of Air Leakage Sizes in Building Envelope using High-Frequency Acoustic Impulse Response Technique", in *Proceedings of the 40th AIVC Conference*, 2019, pp. 80–89

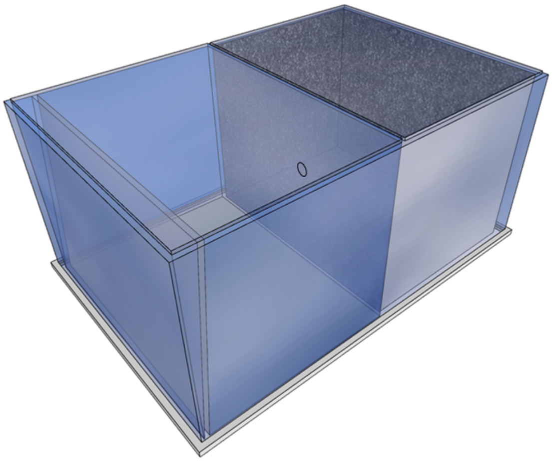

Figure 4.1: Acrylic glass test chamber

4.1.2 Measurement Equipment

An ultrasonic omnidirectional dynamic speaker (Avisoft - ultrasonic omnidirectional dynamic speaker vifa) with a frequency range of 1 to 120 kHz was placed in one cell. Two ultrasonic microphones were sited in the test chamber as well, one in each cell. The microphones (PCB Synotech - 378C01) are 1/4 in. condenser microphones with an even frequency response and a recommended frequency range of 0.004 to 100 kHz. Both, speaker and microphone remained stationary during measurements.
Data acquisition was performed using a USB wide dynamic range signal analyzer (Measurement Computing - DT 9847-3-1 USB Module), which has a sampling frequency of 216 kHz per channel and a resolution of 24 bits. An interface between the data logger and measurement computer and the signal generation and evaluation of the recorded signal was implemented in Python.

4.2 Linear Sweep Measurements

4.2.1 Methodology

For this experiment, acrylic glass walls were chosen as a barrier to separate the two chambers in the box. Different hole diameters between 4 to 10 mm in 2 mm steps were chosen.

Measurements were performed using a linear up-sweep, followed by a down-sweep, and a total swept frequency range from 20 to 100 kHz to cover a wide range of frequencies. In these experiments, particularly ultrasonic frequencies were chosen because the wavelengths of these frequencies are in the same range as potential hole diameters. One goal was to examine if it is possible to detect signal changes that correlate with the acoustic wavelengths, which are in the same order as potential leaks. A lower bound of 20 kHz was selected because ultrasound starts at this frequency. Additionally, from the upper bound of 100 kHz, the damping and absorption of ultrasound in the air become too dominant for practical applications. The duration of one sweep was 10 s; hence, it took 20 s to complete an entire measurement procedure. A signal length that is too short may have an unsatisfactory resolution and signal-to-noise ratio, but a longer signal would require too much processing time. The recorded signal was Fourier transformed to determine the corresponding frequency components. Between the measurements of various hole diameters, the wall with the orifice was exchanged accordingly.

A frequency sweep is an exceedingly transient signal. Thus, a high resolution in the frequency spectrum is crucial. The time signal was divided into small FFT-blocks to achieve this resolution. With a sampling frequency of 216 kHz and a total duration of the measurement of 20 s, the signal length equals 4.32 million data points. According to FFT requirements, the block length should be equal to the power of two; therefore, a block length of 8,192 (= 2^{13}) was selected. This length is equivalent to less than 2 % of the signal length and is a compromise between an appropriate length of the sequence and computing time. Furthermore, the FFT required a periodical signal to obtain ideal results, but the measurements are not periodic. Therefore, the signal time block was multiplied by a Hanning window function w_{hann} (Eq. (4.1)), which reduced the ends of the block gradually to zero and thus resulted in a continuous signal sequence [171].

$$w_{hann}[n] = \frac{1}{2}\left[1 - \cos\left(\frac{2\pi n}{N}\right)\right], \quad n = 1, 2, \ldots, N-1 \tag{4.1}$$

The applied window function weights the signal ends less, and signal information gets lost. Consequently, a moving window with an overlap of 95 % of the previous block was used in this analysis.

4.2.2 Results and Discussion

The results of the FFT analysis of the sound pressure level L_P for a linear frequency sweep with an airtight wall are shown in Fig. 4.2a. The measurement took place inside the previously described test chamber with a leak-proof wall separating the speaker and microphone. In addition to the frequency spectrum, the corresponding wavelengths are shown in the subsequent figures calculated using Eq. (3.6). By covering a swept frequency range between 20 and 100 kHz, the wavelengths are in a range between 17.2 and 3.4 mm, considering a room temperature of 23.5 °C during the measurements. An almost rectangular shape in the frequency spectrum is identifiable in the measurement plots. Because of the Tukey window function (see Eq. (3.41)), the bandwidth is slightly smaller here; the real rectangle in the frequency spectrum starts above 20 kHz and finishes below 100 kHz. The recorded swept frequency signal ends at approximately 100 kHz, but it does not fall back entirely to 0 dB. Although the generated signal is a pure sine wave, the speaker is incapable of producing pure sine waves without harmonic overtones, which are apparent above a frequency of 100 kHz.

In Fig. 4.2b, the same measurement is shown but without a separating wall inside the test chamber. In the frequency range between approximately 20 and 55 kHz, the sound pressure level is mostly higher compared to the measurement with a separating wall. Therefore, the damping effect of the wall appears to be the greatest in this part of the spectrum. The damping of the sound pressure level is roughly 6 dB in this range, which equals a reduction of the sound pressure by half, compared with the measurement shown in Fig. 4.2a. These two measurements function as references for subsequent tests. Additionally, significant periodic amplification and attenuation of specific frequencies occur in the frequency spectrum, but the spectrum's rectangular shape is still apparent from 20 and 100 kHz. In Fig. 4.2b, a decline of the overall frequency amplitude and stronger oscillations appear for frequencies larger than 55 kHz.

An explanation for these fluctuating frequencies might be the comb-filtering effect. This effect appears if sound waves with similar frequency and different phase positions are superimposed. In this case, the sound waves generated by the speaker and the sound wave reflected from the front side of the microphone might be superimposed, which is schematically shown in Fig. 4.3. Because of the linearity of the sound wave equations (see Eq. (3.1)), the sound pressures of both waves add up, and constructive as well as destructive interference occur as a function of the relative phase displacement. For instance, a frequency in which the incoming and reflecting waves exhibit a phase

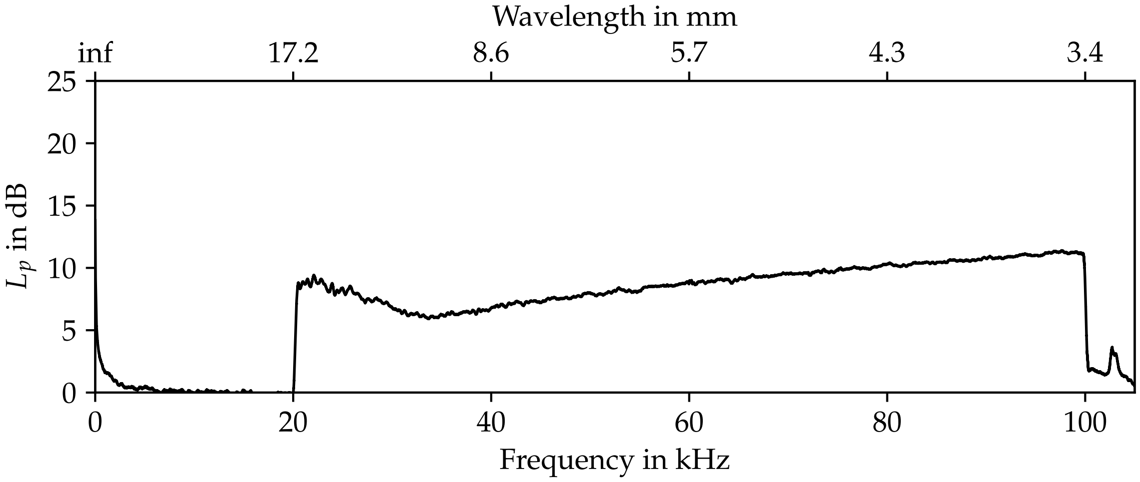

(a) With a separating wall

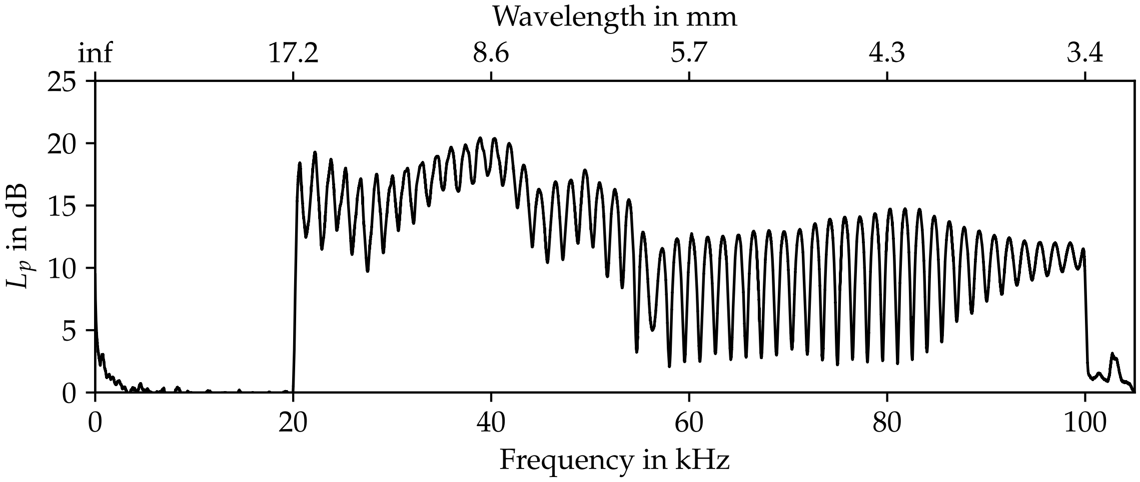

(b) Without a separating wall

Figure 4.2: Frequency spectrum of reference sweep measurements between 20 and 100 kHz in the test chamber

displacement of 180° would lead to a cancelation of the waves and consequently to a drop in the frequency spectrum. On the contrary, waves with the same phase intensify each other and increase the value in the frequency spectrum [153].

From the differences between the peaks Δf_{peak} in the frequency spectrum, the distance traveled by the waves can be calculated:

$$\Delta f_{peak} = \frac{c}{d} \tag{4.2}$$

In this case, d can be presumed as the distance between the speaker and microphone

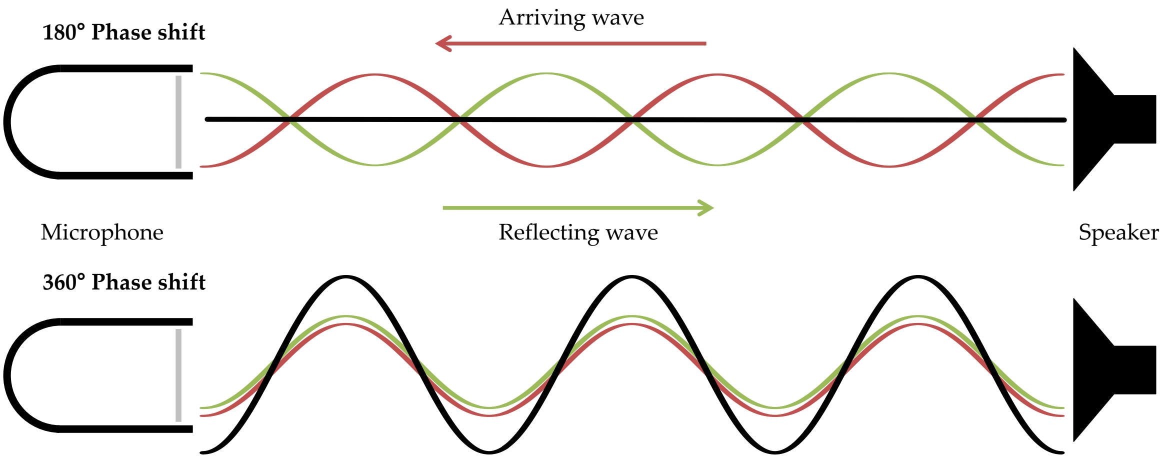

Figure 4.3: Destructive and constructive interference as reasons for the observed comb filter effect

and c as the velocity of sound in air. Therefore, if the comb-filtering effect is visible in the measurement results, additional information about the distance between the measuring devices can be obtained. With an increasing distance between the microphone and speaker, the amplitude of the oscillations in the sound field decreases, and the distances between the peaks in the frequency spectrum get smaller. The distance between the frequency peaks Δf_{peak} in this measurement equals approximately 1.5 kHz, which, according to Eq. (4.2), would lead to a distance between the microphone and speaker of roughly 0.23 m. This value is in agreement with the distance between the speaker and microphone tip in the measurement setup.

Next, the experiments are performed with separating walls and different sizes of openings. Figs. 4.4 and 4.5 show measurements with diameters of the hole inside the separating wall from 10 mm down to 4 mm with 2 mm steps between them. The vertical dashed red lines indicate the frequency at which the hole's diameter and the wavelength are identical.

The comb-filtering effect seems to be more visible for large hole diameters (10 and 8 mm). Furthermore, with increasing hole diameter, a weak correlation between the range of the maximum oscillation peaks in the frequency spectrum and the location of the hole diameter (vertical dashed lines) can be seen. At smaller holes diameters (6 and 4 mm), oscillations in the lower frequency part of the spectrum are still visible but considerably smaller. For these smaller hole diameters, the location of the predominant oscillations does not match the location of the hole diameters anymore, but a distinction between these measurements and the measurement of a leak-proof wall in Fig. 4.2a remains possible. Oscillations at lower frequency components still appear and decrease with smaller leakage sizes.

The characteristics of condenser microphones change with the wavelength of the received signal. For higher frequencies, the wavelengths become smaller and reach the order of magnitude of the microphone diaphragm at some point. In these measurements, condenser microphones are used with a diaphragm diameter of 0.25 in. ($\approx$ 6.4 mm). At this point, pressure maxima and minima at the microphone diaphragm surface may cause local counter-movements of the diaphragm and partial damping of the frequencies. A wavelength of 6.4 mm is equivalent to approximately 54.5 kHz, and hence, to the frequency at which the decline of oscillations appears.

In summary, the presence of a leak could be detected, but the determination of its size becomes more challenging for smaller leaks within this measurement setup. According to the intensity of amplification and attenuation of the frequencies, it is not yet possible to make more than an estimation of the hole size.

The problem of the here applied Fourier transform is that it displays the frequency content of a signal as a mean function over the signal duration. However, the information about the frequency components at specific time steps is lost here. Due to the non-stationary characteristic of this signal and possible changes of the spectrum at specific time steps, the simultaneous time and frequency information of the signal may be interesting. To address this issue, the short-time Fourier transform (STFT) can be used. The STFT divides a signal into multiple sub-signals. Applying the FFT on these parts of the original leads to a better localization of the frequency components along the time axis. The final resolution of time and frequency depends on the length of the sub-signals. Long sub-signals lead to a high frequency resolution, and short sub-signals enable a better time resolution. However, the STFT cannot obtain a high resolution in time and frequency simultaneously. A high resolution of the frequency components leads to a bad resolution in time and vice versa, which is the uncertainty principle [172]. On the contrary, the previously described HHT algorithm (see Section 3.2.4) overcomes this problem by defining the instantaneous frequency by iteratively calculating the intrinsic mode functions (IMFs). This HHT is applied to measurements with holes in the separating wall inside the test chamber. The measurement period was extended to 28 s to obtain a better time resolution for these measurements, and a single up-sweep (20 to 100 kHz) was used. These frequency swept signals have the lowest frequency components at the beginning and the highest components at the end of the signal. This analysis aims to find possible changes in the frequency spectrum at specific time steps according to the hole size, which might not be visible in a simple Fourier transformed spectrum.

Fig. 4.6 shows the results of the empirical mode decomposition (see Section 3.2.4) for a single frequency sweep and a hole diameter in the separating wall of 10 mm. Fig. 4.6a

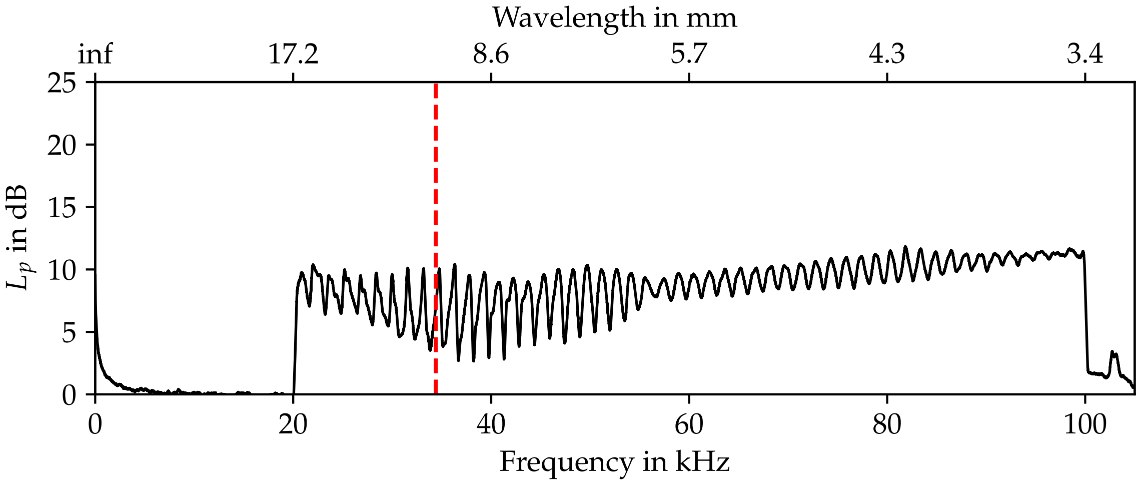

(a) 10 mm hole size

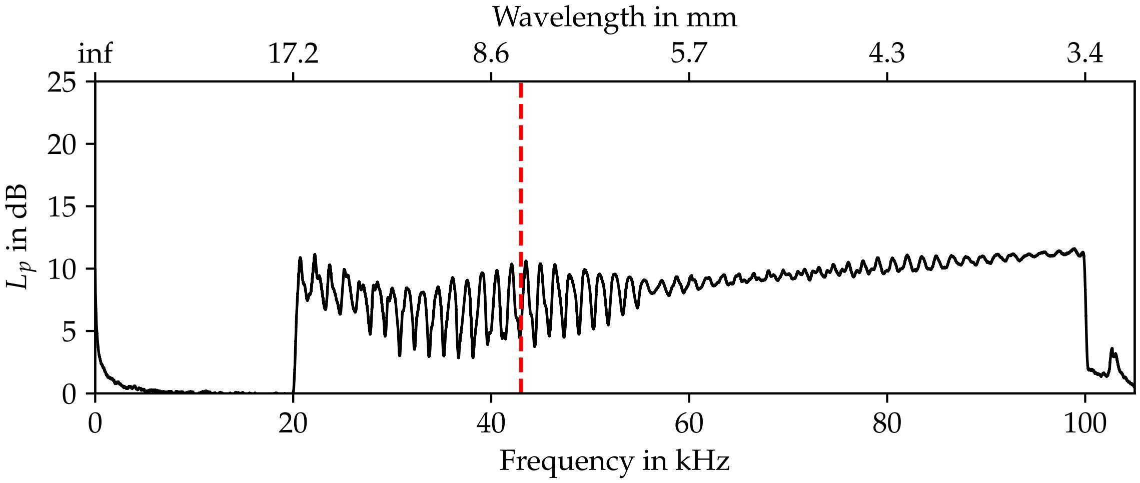

(b) 8 mm hole size

Figure 4.4: Frequency spectrum of sweep measurements in the test chamber and a separating wall with large hole diameters of 10 and 8 mm between 20 and 100 kHz in the test chamber

shows the original recorded signal, and the first four corresponding intrinsic mode functions (IMFs) are plotted below. In total, the original signal is decomposed into 20 IMFs. Here, only the first four calculated IMFs are shown to demonstrate the process. The sum of all IMFs and a residual together result in the original signal (see Eq. (3.28)).

The first IMF (Fig. 4.6b) predominantly displays the signal part in the last 3/4 of the frequency sweep, which can be associated with higher frequencies. Between second 5 and 13, oscillations observed in the frequency spectrum (Fig. 4.4a) are evident in the time signal as well. Whereas the subsequent IMFs primarily show low-frequency

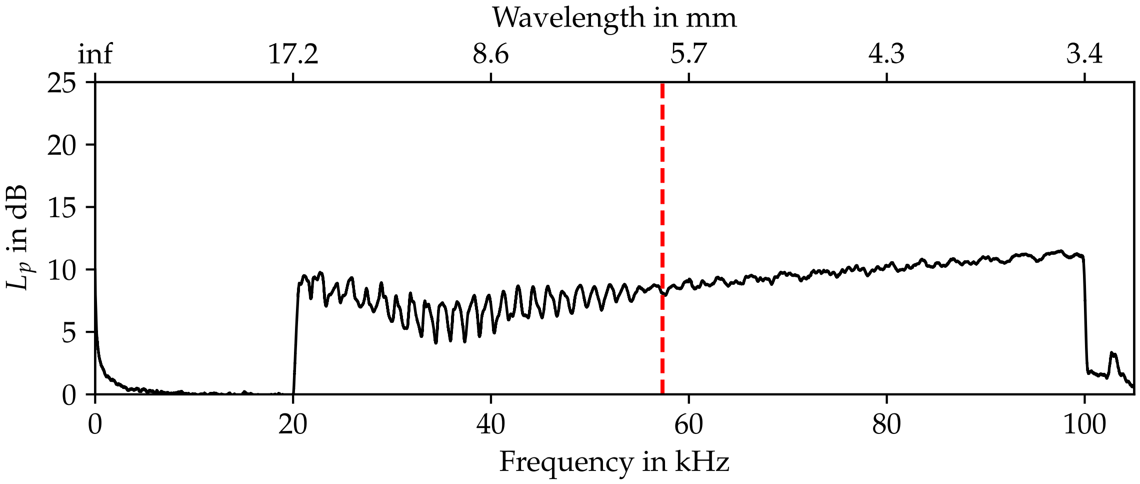

(a) 6 mm hole size

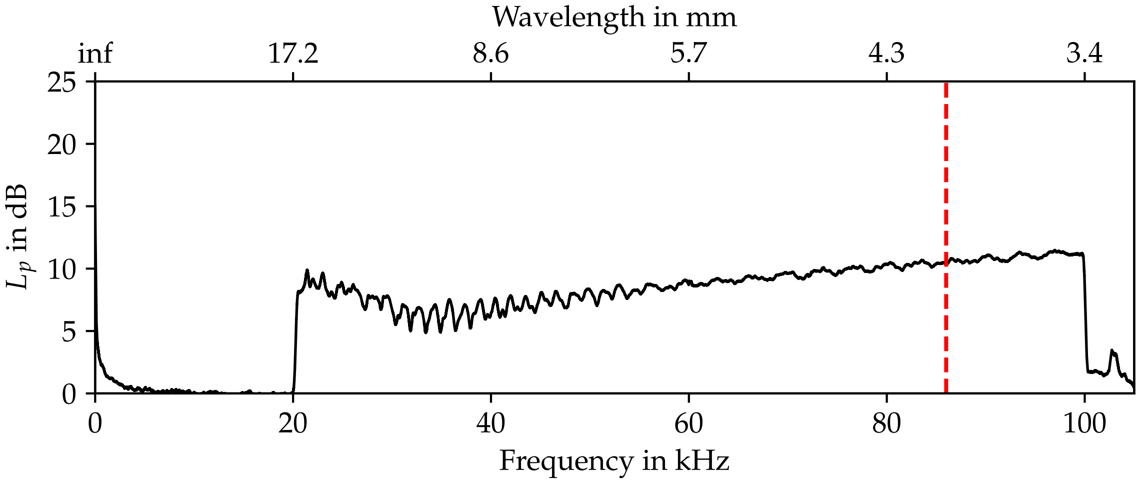

(b) 4 mm hole size

Figure 4.5: Frequency spectrum of sweep measurements in the test chamber and a separating wall with small hole diameters of 6 and 4 mm between 20 and 100 kHz in the test chamber

components. These IMFs are the basis for the Hilbert spectral analysis.

In Fig. 4.7, the Hilbert spectrum for the measurement with a hole diameter of 10 mm is shown. The magnitude of the frequencies at a specific time equals the power (see Eq. (3.32)) of this signal, which is calculated from the IMFs shown in Fig. 4.6. This power of the first four IMFs is displayed at the bottom part of the plot in blue, orange, green and red for different IMFs. The other calculated IMFs are not considered in Fig. 4.7 because their power is close to zero. On the left side of the spectrum, the weighted instantaneous frequencies (see Eq. (3.27)) are shown. The calculated instantaneous

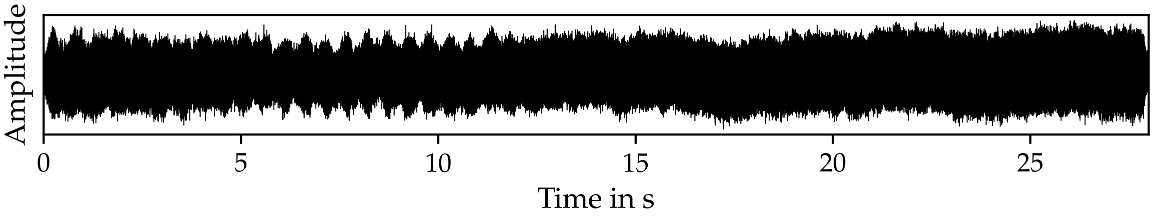

(a) Original signal

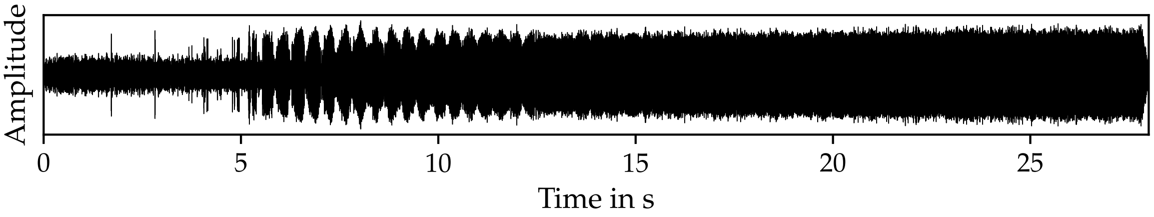

(b) IMF No.1

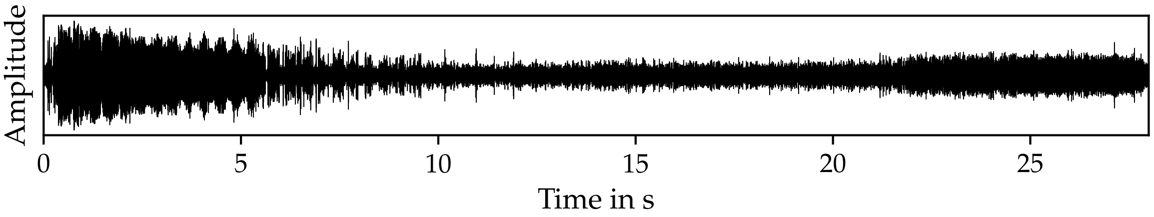

(c) IMF No.2

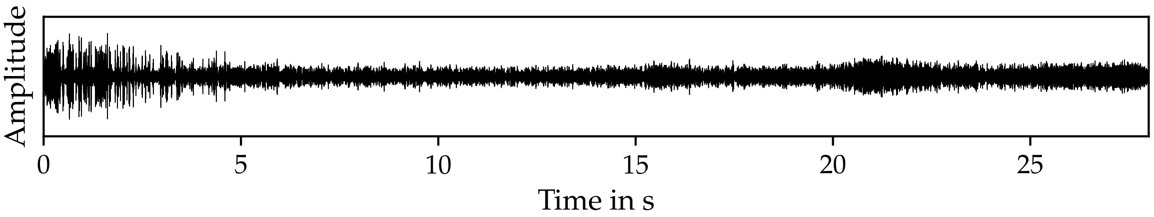

(d) IMF No.3

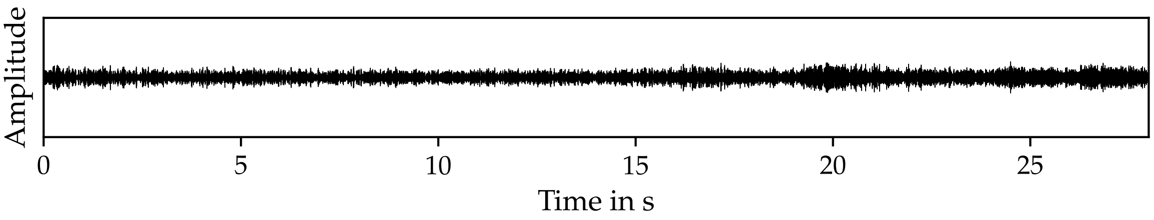

(e) IMF No.4

Figure 4.6: The recorded time signal and an example of the first four calculated intrinsic mode functions (IMFs) at a hole diameter of 10 mm

frequencies from each IMF are weighted with their respective signal power to display the proportion of a specific frequency component on the whole spectrum.

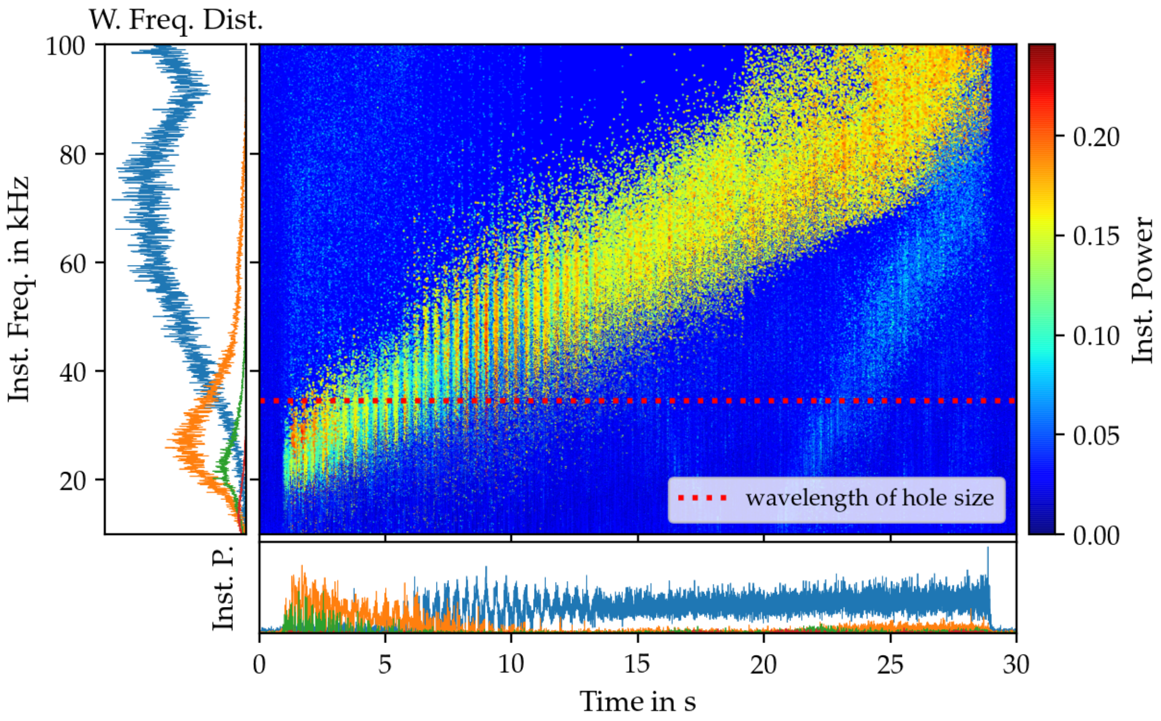

Figure 4.7: Hilbert spectrum of sweep measurement between 20 and 100 kHz with a separating wall and a hole size of 10 mm

The Hilbert spectrum shows the magnitude of the instantaneous frequency components over time as an overlay of the IMFs (according to Eq. (3.34)). All bright areas represent higher amplitude values of the frequencies at this specific time step. Here, the frequency sweep from low frequency (20 kHz) to high frequency (100 kHz) is clearly identifiable. Furthermore, the attenuation and amplification of frequencies at specific time steps between 5 and 13 s and their corresponding frequencies of approximately 20 to 60 kHz are apparent in the spectrum and at the time axis throughout this measurement period. From second 20 until the end of the measurement period, a weak short sweep between 20 to 60 kHz is visible in the spectrum, which arises from the second IMF (in orange). These are most likely the harmonics of the original signal.

Fig. 4.8 visualize the Hilbert spectrum of measurements with the smallest hole diameter of 4 mm in the separating wall. This enables a comparison of the two measurement setups with the smallest and the largest investigated holes. In this spectrum, the only visible difference compared to the measurements with a 10 mm diameter hole is the absence of these characteristic oscillations.

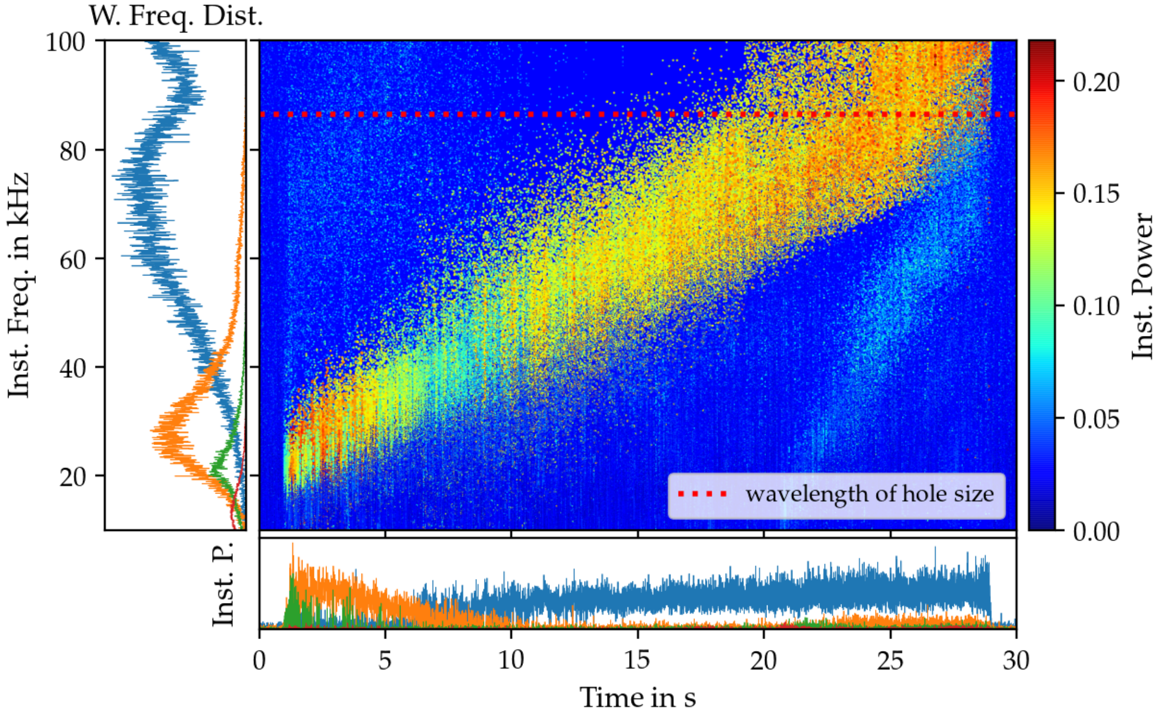

Figure 4.8: Hilbert spectrum of sweep measurement between 20 and 100 kHz with a separating wall and a hole size of 4 mm

In summary, the HHT enables a better knowledge about the frequency contents of transient signals, like frequency sweeps. In both the FFT and HHT, characteristic attenuation and amplification in the time and frequency domain are visible, which increase with increasing hole diameter. However, this effect is found under laboratory conditions and may not be strong enough to be found in a real building investigation to characterize air leakage sizes. Therefore, the next section describes another approach using high-frequency impulse response measurements to characterize the sound transmission within the same measurement setup.

4.3 Impulse Response Measurements

The objective of the following measurements is to identify to what extent different leak sizes in different materials of the wall can be determined by measuring the impulse responses in two rooms of the test chamber. For this reason, acrylic glass and plywood walls with orifice diameters of 4 , 6 , 8 or 10 mm are investigated as separating walls. The frequency-dependent sound insulation of different walls between both chambers is determined to examine the sound transmission through these different wall materials with various leak sizes.

4.3.1 Methodology

The sound insulation between two rooms can be determined using the sound reduction index R [173]:

$$R = \Delta L_P + C = \Delta L_P + 10\lg\left(\frac{S}{A_S}\right) \approx \Delta L_P + 10\lg\left(\frac{S}{0.161\,\frac{V}{t_{reverb}}}\right) \tag{4.3}$$

Here, ΔL_P is the measured sound pressure level difference in dB between two rooms. The sound reduction index can usually not be directly determined by measuring only the sound pressure level difference. In the receiving room, the measured sound pressure is superimposed by reflected sound waves of the surrounding surfaces [174]. This fact is considered by the term C of the equation. Here, S is the area of the common partition, and A_S is the equivalent absorption area of the receiving room. The equivalent absorption area can be approximated using Sabine's empirical formula, where V is the volume of the receiving room and t_{reverb} is the reverberation time, which has to be measured in the receiving room. The reverberation time is the time it takes to reduce the energy density to the one-millionth of the original sound or, respectively, the time it takes for the sound pressure level to drop by 60 dB after the abrupt ending of a generated test signal [152]. It should be noted that the constant 0.161 in Eq. (4.3) has the unit s/m.

In practice, this formula (Eq. (4.3)) is usually acceptable and a sufficient approximation of the sound reduction index if rooms are small and the considered frequencies low. However, in this work, higher frequencies are considered as well. Hence, this formula is adapted (based on Ref. [175]), and the air absorption is taken into account using the intensity attenuation coefficient m, which is indicated be the index A in the following:

$$R_A = \Delta L_P + C_A \approx \Delta L_P + 10\lg\left(\frac{S}{V\left(\frac{0.161}{t_{reverb}} - 4m\right)}\right) \tag{4.4}$$

The attenuation coefficient depends on the frequency, the ambient atmospheric temperature, and the relative humidity and is calculated according to the ISO 9613-1 standard [176] and Wenmaekers et al. [177]. This coefficient increases with increasing ambient temperature and frequency.

Measurement Procedure

The calculation of the sound reduction index R_A (Eq. (4.4)) requires a measurement of the sound pressure level difference ΔL_P and of coefficient C_A. According to the DIN EN ISO 18233 standard [178], the sound pressure level difference between two rooms can be calculated using the ratio of the integrated and squared impulse response $h(t)$ of the sending (index 1) and receiving room (index 2):

$$\Delta L_P = 10\lg\left(\frac{\int_0^\infty h_1^2(t)\,dt}{\int_0^\infty h_2^2(t)\,dt}\right) \tag{4.5}$$

Assuming the acoustics of a room is a linear and time-invariant system, the entire information of the room transfer function is contained in the room impulse response. Unfortunately, the system is not entirely linear in reality because a measured impulse response contains artifacts caused by noise and the non-linear behavior of, e.g., amplifiers or transducers. A method based on Farina [179, 180] is applied in this chapter to overcome this problem. Here, an exponential sine sweep with constant amplitude is used as an excitation signal (see Eq. (3.42)). The excitation signal was generated using a Python script and was then recorded in the sending, as well as in the receiving room (see Fig. 4.9).

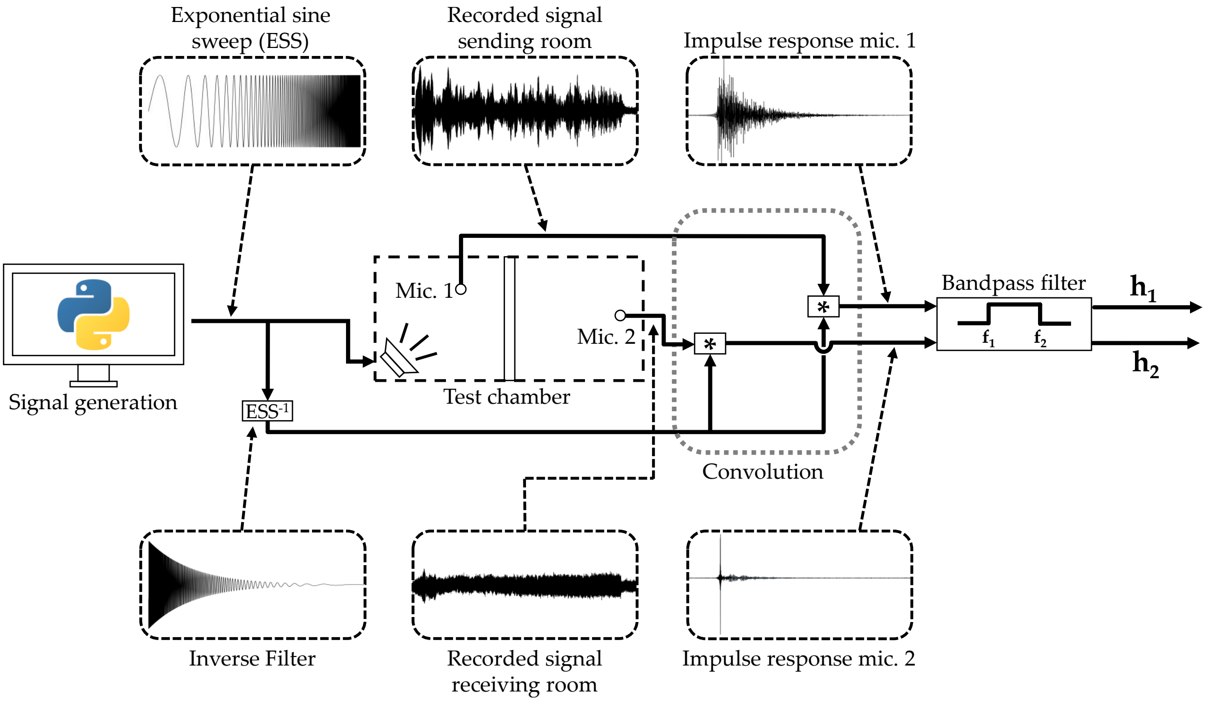

Figure 4.9: Measurement procedure of impulse response measurements

The recorded signal $y(t)$ has to be convolved with an inverse filter signal to obtain the desired impulse response $h(t)$:

$$h(t) = y(t) * ESS_{inv} \tag{4.6}$$

In practice, the inverse filter signal ESS_{inv} is the reversed time signal $s_{rev}(t)$ of the exponential sine sweep with modulated amplitude to compensate for the exponentially changing sweep energy. This inverse filter can be described as:

$$ESS_{inv} = s_{rev}(t)\, e^{-\frac{t \ln\left(\frac{f_2}{f_1}\right)}{T}} \tag{4.7}$$

In this equation, f_1 is the start frequency of the sweep, f_2 is the end frequency, and T the duration of the sweep.

In contrast to other methods employed to measure the impulse response (e.g., the maximum length sequence (MLS) method [178, 181] or the linear sine sweep (LSS) method [182]), this ESS convolution process results in a sum of time-shifted higher harmonic impulse responses in addition to the desired linear response. This accumulation of harmonic distortion responses in the measured signal can be entirely separated from the actual linear room impulse response using a window function in the time domain. In other established measurement methods, e.g., the MLS method, these distortions are mixed with the desired impulse response and severely affect the signal quality [179]. For a more detailed description, see Ref. [183]. Fig. 4.10 shows an example of the separated harmonics on the left side of the major room impulse response, which are filtered out using a window function.

Moreover, the signal-to-noise ratio and the repeatability of measurements (also air and temperature fluctuations) are better than those of other methods. Additionally, the use of an exponential sweep enables the user to consider only relevant frequency bands. In this case, a frequency range of 1 to 100 kHz is chosen. All frequency-dependent parameters are finally band filtered and evaluated within a third-octave-band.

Next, the missing parameters for the second part of Eq. (4.4) have to be identified. The area of the common partition S and the room volume of the receiving room V are only geometrical parameters and constants. The reverberation time t_{reverb} is frequency-dependent and has been measured in the receiving room according to the DIN EN ISO 3382-2 standard [184]. In this procedure, the impulse response was measured in the receiving room for an acrylic glass and a plywood wall, similarly to the method illustrated in Fig. 4.9, in order to calculate the reverberation time. After the impulse response is 1/3 octave filtered, decay curves are determined for each frequency band by

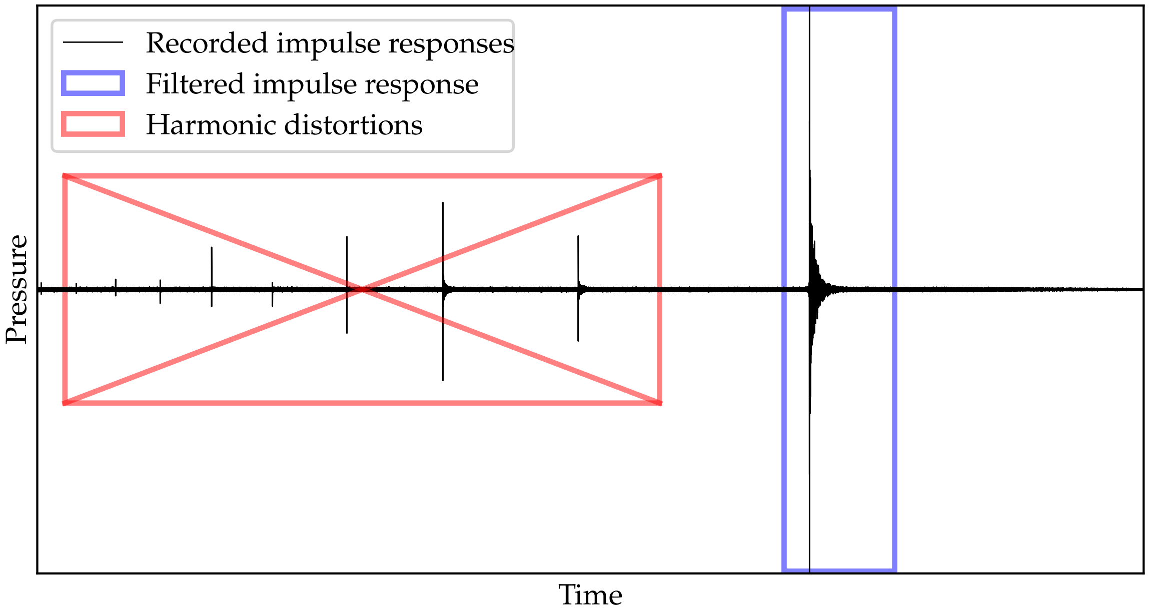

Figure 4.10: Schematic illustration of detection of non-linearities in the measured room impulse signal

calculating the backward integration of the squared impulse responses. Subsequently, the sound level can be calculated from the integrated squared impulse responses, and it is possible to determine the time the sound pressure level takes to drop by 60 dB, which is the reverberation time $t_{reverb\,60}$. This process is illustrated in Fig. 4.11.

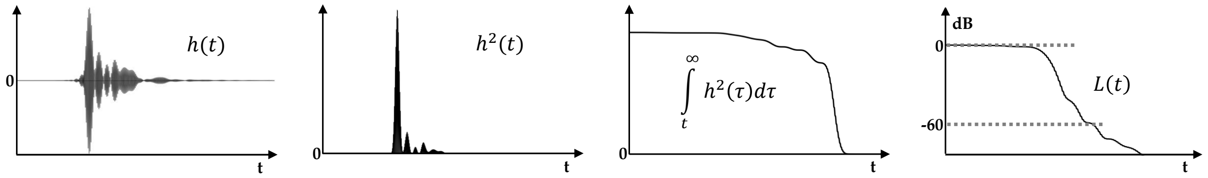

(a) **(b)** **(c)** **(d)**

Figure 4.11: Measurement process of reverberation time: a) Measured impulse response in the receiving room, b) Squared impulse response, c) Backward integration of the squared impulse response, d) Estimation of reverberation time from sound level $L(t)$ drop

4.3.2 Results and Discussion

In this section, the measurement of the sound reduction indexes between the two rooms, as well as the required reverberation times in the receiving room are explained and the results are presented in the following.

Reverberation Time

The measured values of the reverberation time $t_{reverb\,60}$ in the receiving room for a separation wall of acrylic glass and plywood are shown in Fig. 4.12. As stated above, $t_{reverb\,60}$ is the time span until the sound pressure level in a room decreases by 60 dB. In practice, the $t_{reverb\,60}$ is often not measured directly because background noise would distort the measurement. Here, the measurements of the $t_{reverb\,30}$ and $t_{reverb\,20}$ are taken and subsequently extrapolated to the required $t_{reverb\,60}$ value.
It can be seen that the reverberation time using the acrylic glass wall is higher than the reverberation time using the plywood wall for every frequency. The difference is mainly significant for lower frequencies. For high frequencies, the differences are marginal. The lower reverberation times for a plywood wall indicate that a wooden wall absorbs more sound energy, hence less sound is reflected from the walls compared to a stiff acrylic glass wall.

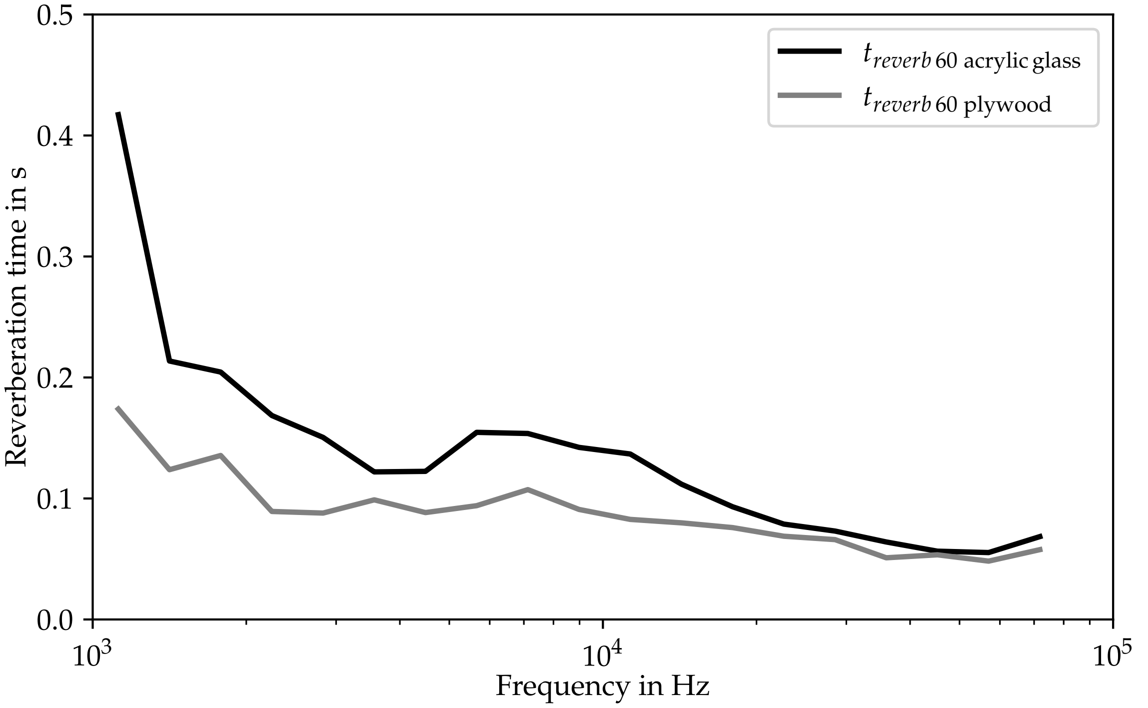

Figure 4.12: Reverberation times $t_{reverb\,60}$ in receiving room for acrylic glass and plywood

Fig. 4.13 shows the calculated coefficients C and C_A, which are the second part of the sound reduction index in Eqs. (4.3) and (4.4). In contrast to C, C_A considers the damping of the sound waves in air. The black lines are the values for acrylic glass and the gray ones for plywood. For lower frequency values (< 4 kHz), the damping factor does practically not affect C. At higher frequencies, it becomes increasingly important. However, since higher frequencies are considered in this study as well, it is not sufficient to neglect the damping factor. For all following calculations of R, C_A has therefore been used.

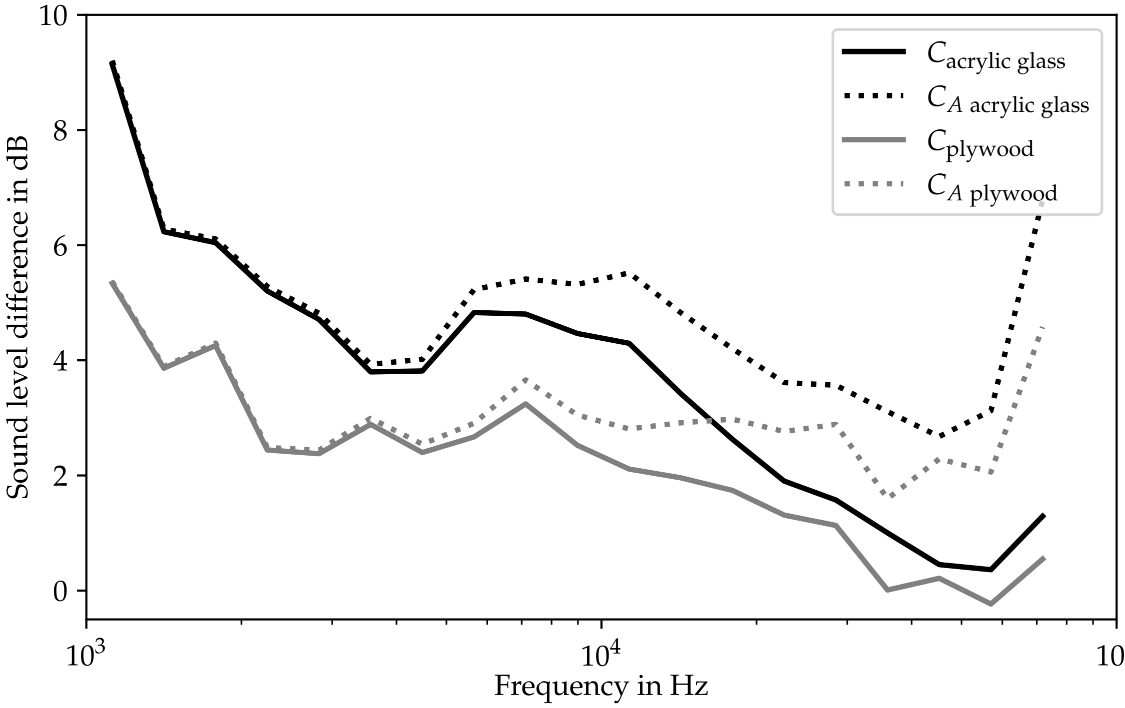

Figure 4.13: Factors C and C_A of the acrylic glass and the plywood wall at an ambient temperature of 24.3 °C and a relative humidity of 23.0 %

Sound Reduction Index

Figs. 4.14 to 4.17 show the sound reduction indexes R for acrylic glass and plywood walls. The index indicates the sound transmission and absorption characteristics for these different wall materials at each frequency. In the upper part of each figure, four measured R-values as a function of frequency are illustrated. The solid lines are the measurements taken with a hole in the wall (4, 6, 8 or 10 mm). The same measurements are also performed with both wall materials under leak-proof conditions (dotted lines) to compare the reduction of R to a reference value. These reference measurements are identical in all the following figures.

In the same figures, the frequency dependence of the difference in R between the reference measurement and the measurement for each hole size is shown. This enables the identification of frequencies, where the output signal is predominantly affected by the hole size. If ΔR is negative, the sound reduction index of the (measurement of a) wall with a hole is lower than the same leak-proof wall. A lower sound reduction index indicates that more sound energy is transmitted at these frequencies.

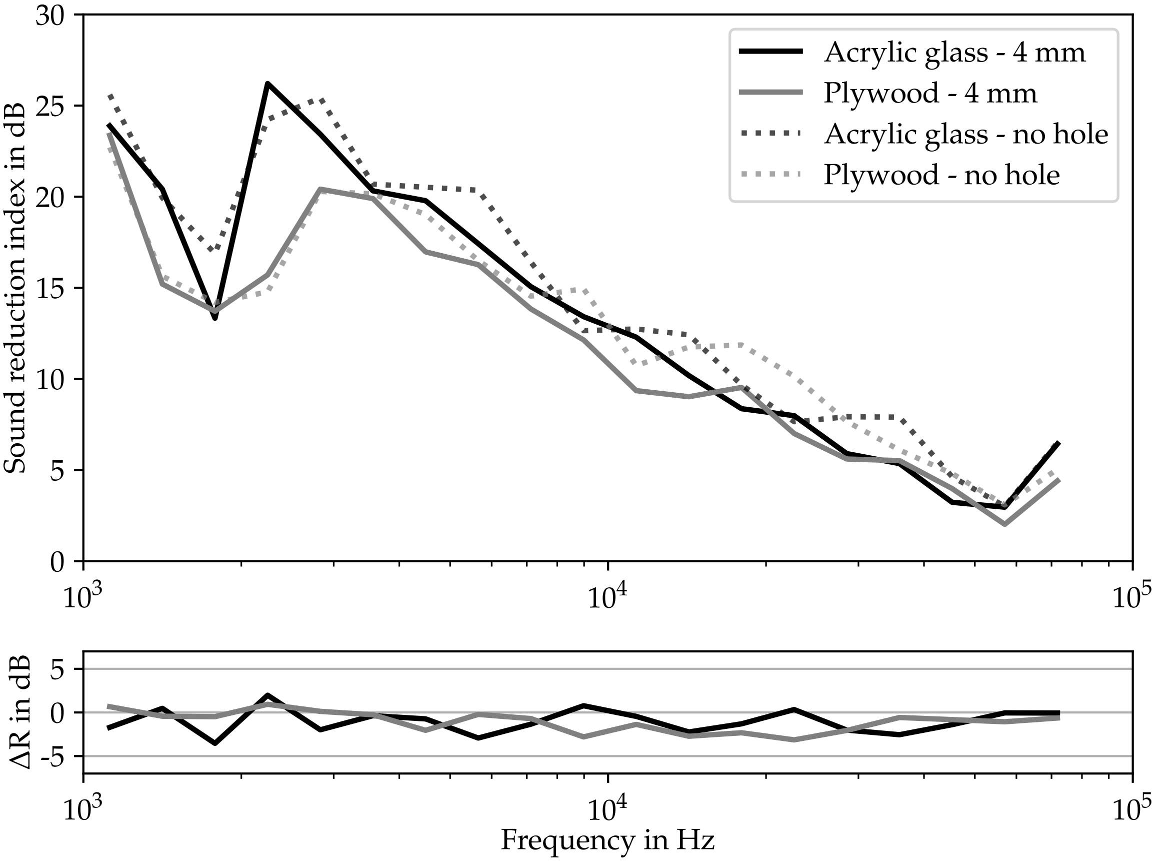

Figure 4.14: Sound reduction index R for measurements at walls with no holes (dotted lines), walls with a 4 mm hole (solid lines in the upper graph), and differences of R from these two measurements (lower graph)

The sound reduction index for plywood walls with no holes and frequencies below 7.5 kHz is significantly lower than the same measurement with acrylic glass. The R-values for none of these two materials are dominant over a broad frequency band for higher frequencies. Moreover, all following measurements show a sudden drop of the sound reduction index at a frequency of around 1.7 kHz, probably caused by resonance.

The difference in sound reduction between measurements on walls with a hole and those with no hole grows with increasing hole diameter. This fact is presented in Table 4.1, where the mean differences of the sound reduction index are presented.

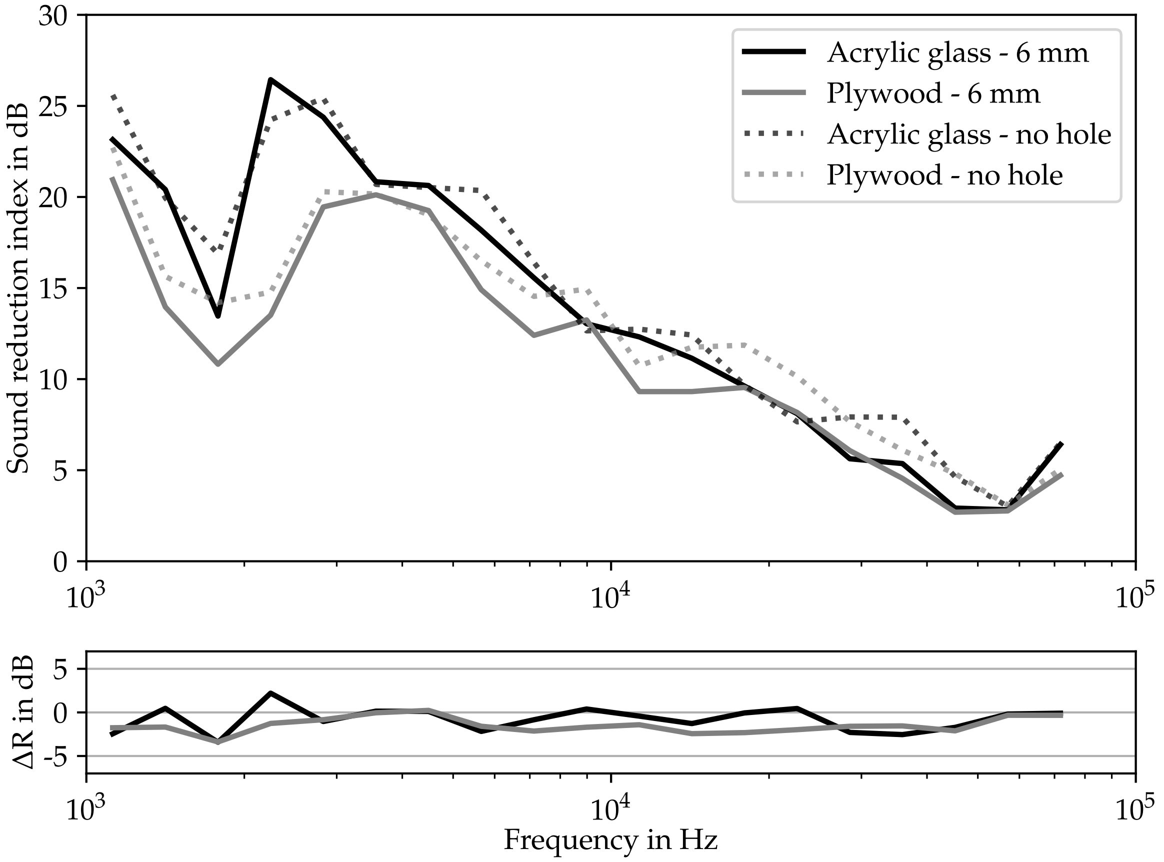

Figure 4.15: Sound reduction index R for measurements at walls with no holes (dotted lines), walls with a 6 mm hole (solid lines in the upper graph), and differences of R from these two measurements (lower graph)

Table 4.1: Mean sound reduction index differences

Hole size	4 mm	6 mm	8 mm	10 mm
Acrylic Glass	-1.01	-1.10	-1.22	-1.39
Plywood	-1.05	-1.29	-1.48	-2.08

On average, over all frequencies, the sound reduction index decreases with increasing hole size. The differences are more considerable for the plywood walls compared to acrylic glass walls. This indicates that sound reduction and hole size may be correlated. A direct link between a specific frequency and the hole size could not be observed in these measurements.

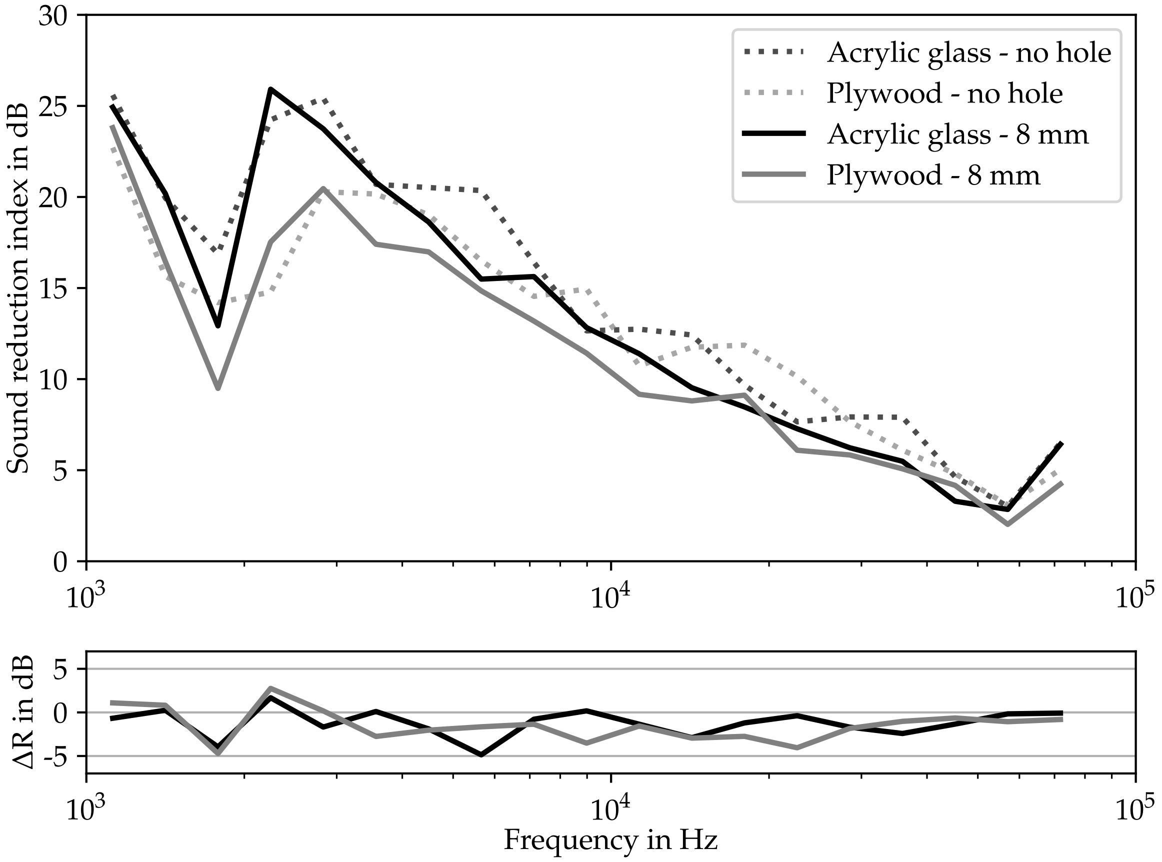

Figure 4.16: Sound reduction index R for measurements at walls with no holes (dotted lines), walls with an 8 mm hole (solid lines in the upper graph), and differences of R from these two measurements (lower graph)

4.4 Summary

In the first part of this chapter, a method is proposed using linear sine sweeps over a broad frequency range to investigate the size of different air leakage spots in an acrylic glass wall within a laboratory test chamber. The Fourier transform and the Hilbert-Huang transform are applied to visualize the spectral contents of recorded time signals for the different leakage sizes. Based on these data, it is observed that the leakage size could affect the appearance of the comb-filtering effect in the acoustic near field. It is shown that signal components pass through the openings at which frequencies corresponded to wavelengths in the range of large leakage diameters. Accordingly, the order of magnitude of leakage sizes may be deduced. For smaller diameters, the detection of leakages is still possible, but an accurate determination of the size is difficult because the dimension of the microphone diaphragm appears to limit the detection range. This effect is visible in a laboratory environment, but a reliable interpretation of this effect in a real building application is questionable.

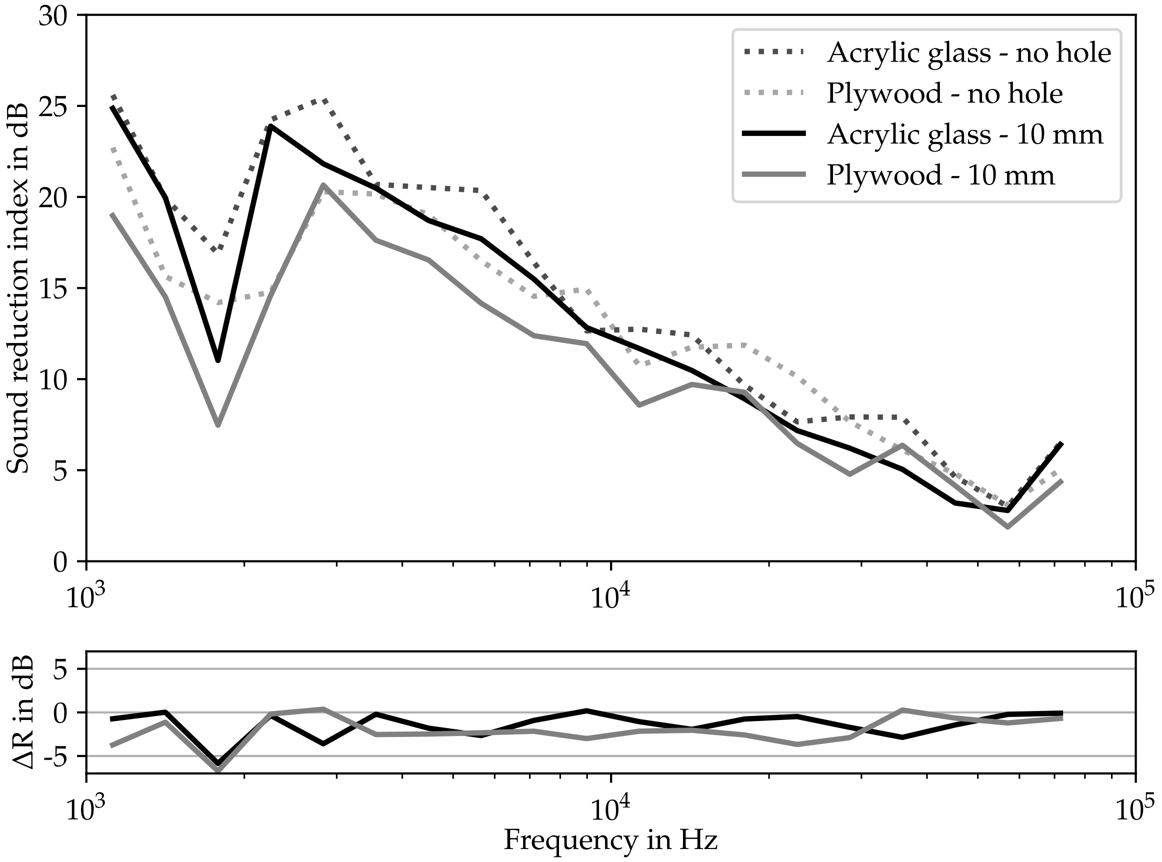

Figure 4.17: Sound reduction index R for measurements at walls with no holes (dotted lines), walls with a 10 mm hole (solid lines in the upper graph), and differences of R from these two measurements (lower graph)

In the second part of this chapter, impulse responses over a wide frequency range are used to determine the sound reduction indexes for an acrylic glass and a plywood wall with various hole sizes. It is possible to differentiate between leak-proof walls and walls with a hole. Furthermore, a distinction between different leakage sizes is possible. This technique may have the potential to locally determine leak sizes in walls, particularly if measurements are compared with nearby leak-proof wall parts as a reference. However, a distinct allocation of acoustic parameters to the various hole sizes is only hardly possible.

5 Laboratory Comparison of Airflow and Acoustic Measurements

In this chapter, an experimental setup is introduced to compare acoustic measurement procedures with conventional airflow measurements. This laboratory experiment uses a laboratory test box with well-controlled artificial leaks of known dimensions.

5.1 Methodology

5.1.1 Laboratory Test Box

In this experimental test setup, a wooden test box is chosen, which is shown in Fig. 5.1. The box is made of medium-density fiberboard (MDF), has a total length of 2.5 m, and a height and depth of 0.6 m. It consists of two chambers with a length of each chamber of 1.1 m. The chambers are separated from each other with a test section, where different leaks can be inserted. Artificial walls were constructed that incorporated leaks of various geometries and were installed in the test section of the apparatus. These two separated chambers ensure a controlled environment on both sides of these artificial walls. For all measurements, the box was closed and air sealed with a lid on top.

Major parts of this chapter are reproduced from:

B. Kölsch, I. S. Walker, B. Schiricke, W. W. Delp, and B. Hoffschmidt, "Quantification of Air Leakage Paths: A Comparison of Airflow and Acoustic Measurements", *The International Journal of Ventilation*, 2021, DOI: `10.1080/14733315.2021.1966576`

B. Kölsch, I. S. Walker, W. W. Delp, B. Schiricke, and B. Hoffschmidt, "Comparison of Airflow and Acoustic Measurements for Evaluation of Building Air Leakage Paths in a Laboratory Test Apparatus", in *Proceedings of the 41st AIVC - ASHRAE IAQ 2020 joint conference*, 2022

(a) Top view into the box with two chambers and space between two tight reference walls **(b)** Side view with the connections of the blower and pressure taps

Figure 5.1: Laboratory test box

5.1.2 Investigated Wall Structures

In this experiment, 43 different configurations of wall leaks are studied to simulate realistic leakage scenarios for individual leaks on a model scale. The following parameters are modified between measurements:

- The number of walls: a single wooden wall with a slit in the upper part of the wall or two walls with slits and an air gap between them (see Figs. 5.2a and 5.2b). The slit has a fixed length of 180 mm for all configurations.
- Different distances between the double-wall constructions: 100 and 150 mm (see Figs. 5.2b and 5.2c). These distances are in the magnitude of typical wall thicknesses.
- Measurements with and without insulating material (glass wool) in between two walls (see Fig. 5.2d).
- Connection of the slits at a double-wall with a channel (see Fig. 5.2e).
- Non-parallel leakage paths, where the slit is in one wall at the top and in the other at the bottom. Here, measurements have been performed with and without a channel between the slits (see Figs. 5.2f and 5.2g).
- Variation of the slit height: 5.00, 1.00, 0.40 and 0.25 mm (see Fig. 5.2h).
- Blank wall panels without openings for reference purposes.

38 of the total 43 investigated configurations are walls with deliberate openings (shown in Fig. 5.2), and 5 configurations are different types of walls with no openings for reference purposes, corresponding to Figs. 5.2a to 5.2d.

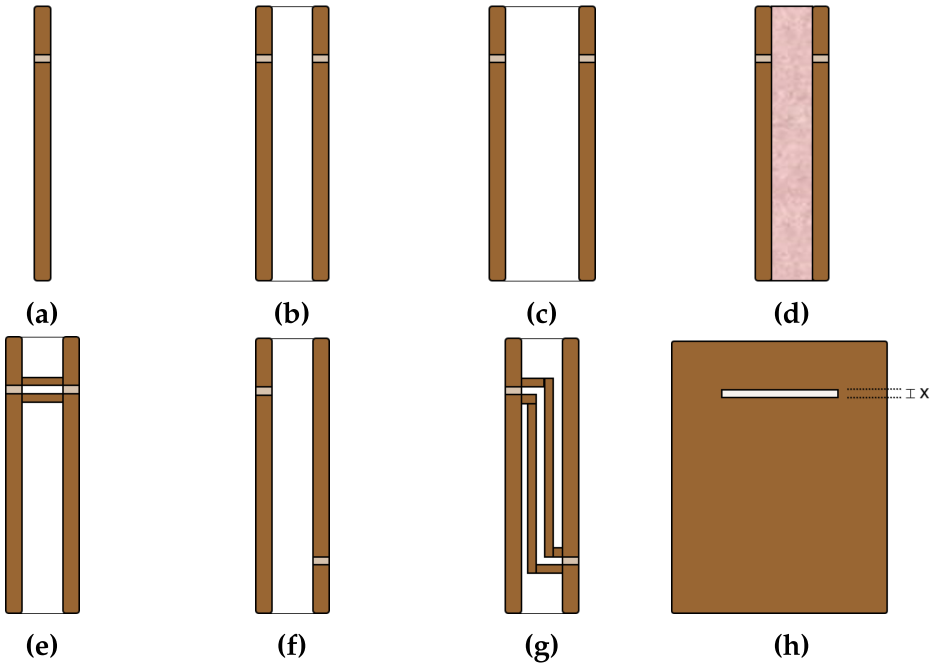

Figure 5.2: Schematic illustration of configurations and investigated parameters for the 38 artificial wall leaks

5.1.3 Pressure Difference and Airflow Measurements

Multi-point air leakage tests were performed to characterize the test wall leakage, similar to the ASTM E779 [54] or DIN EN ISO 9972 [53] fan pressurization standard for whole buildings or single rooms. The blower is connected to one of the two chambers and is shown in Fig. 5.3a. This pressurized chamber is sealed, and the second chamber is open to ambient conditions. The airflow of this blower is controlled with a manual valve and a blower speed controller. In this experiment, only pressurization and no depressurized tests were performed. The results of depressurization measurements are expected to be the same because the leak configurations remain rigid and symmetrical during the tests and, therefore, will not change between pressurized and depressurized tests. The airflow is measured with a Venturi airflow meter installed between the blower and box and is shown in Fig. 5.3b. A Venturi airflow meter consists of a cylinder at the entrance, a convergent section, a throat, and a divergent section, as illustrated in Fig. 5.3c. According to Bernoulli's principle, the contraction of the pipe diameter results in an increase of fluid velocity and a decrease of the static pressure along a streamline.

From the measurement of this static pressure difference (ΔP_{1-2}), the airflow (Q) through the tube can be calculated using Bernoulli's principle and continuity equation [185].

(a) Blower with manual valve

(b) Venturi airflow meter with pressure taps

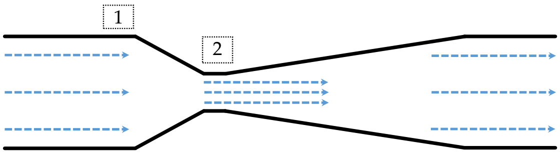

(c) Schematic illustration of the streamlines

Figure 5.3: Blower and Venturi airflow meter

This correlation is described in Eq. (5.1), where A_1 and A_2 are the cross-sectional areas at the positions where the pressure measurements are taken, and ρ is the density of air. The positions of the pressure measurement taps 1 and 2 are shown in Figs. 5.3b and 5.3c.

$$Q = A_1 \sqrt{\frac{2}{\rho\left(\left(\frac{A_1}{A_2}\right)^2 - 1\right)}} \cdot \sqrt{\Delta P_{1-2}} = f_{cal}\sqrt{\Delta P_{1-2}} \tag{5.1}$$

Due to the broad range of different leak sizes and, therefore, magnitudes of airflows through the leaks, two different airflow meters were used. These airflow meters have different geometries and are calibrated to measure different magnitudes of airflow. The calibration coefficients f_{cal} for the two different airflow meters used in this work are 0.1591 and 0.8096. The first meter is chosen for low flows up until $4.5\,\mathrm{m^3/h}$ and the second one is chosen for larger flows above this value.

The pressure in the pressurized chamber was measured using a flush-wall pressure tap on the chamber's inner wall. Copper tubing is used to connect the pressure tap location to a differential pressure gauge. Due to the open second chamber to ambient conditions, the pressure difference between both chambers can easily be determined. A second pressure measurement location is inside the double-wall structures (see Figs. 5.2b to 5.2g) to monitor the pressure difference inside the wall structure as well. With the measurement of pressure difference across the test walls and the airflow through the walls, the pressure exponent n and flow coefficient C of the power-law formulation (see Eq. (2.16)) can be obtained for each leak configuration using a least squares fit to the pressure-flow relationship. This description is later used in Section 5.2.1.

The temperatures in both chambers were roughly the same (±0.4 °C) during the measurements; therefore, a temperature correction of the airflow through the flowmeter, which is required in ASTM E779 [54] and DIN EN 12114 [186], was not necessary.

5.1.4 Acoustic Measurements

The acoustic measurements in the laboratory setup were performed with a speaker placed together with one microphone in one chamber and another microphone in the other chamber. For these measurements, both chambers are sealed to ambient conditions. All measurements were taken at zero pressure difference and zero airflow. The only intended sound source was the speaker in one of the two chambers. The microphones and the signal analyzer are the same already described in Chapter 4. The speaker is an omnidirectional ultrasonic dynamic speaker with an even frequency range of 1 to 120 kHz. The signal which was sent by the speaker is a white noise signal, which enables an analysis of a broad frequency range. The frequency range for these experiments was chosen between 1 and 40 kHz. An interface between the data logger and the measurement computer, as well as the signal generation, was implemented in Python.

The relationship between the signal which is emitted in one chamber and the signal received in the other chamber can be described using the frequency-dependent coherence function $C_{xy}(f)$. The coherence function is a measure of the linear dependency between two discrete time signals. It describes the fraction of an output signal from an input signal at a specific frequency. This can be characterized by the following equation:

$$C_{xy}(f) = \frac{|G_{xy}(f)|^2}{G_{xx}(f)\,G_{yy}(f)} \tag{5.2}$$

The coherence is calculated by dividing the squared magnitude of the cross-spectral density $G_{xy}(f)$ (see Eq. (3.20)) between x and y with the product of the auto-spectral density of signals x ($G_{xx}(f)$) and y ($G_{yy}(f)$) (see Eq. (3.18)). This function is always between 1 and 0, with a value at 1, indicating a perfect correlation and at 0 a total independence between both signals at a specific frequency [158, 161, 187]. The experiments described in this chapter intend to examine the ability to use the coherence function to estimate the size of building envelope leaks.

5.2 Results and Discussion

5.2.1 Pressure Difference and Airflow Measurements

For each of the 38 investigated leak configurations, multiple airflow and pressure difference measurements were performed to get a full pressure-flow characteristic for each leak. Fig. 5.4 shows an example of measurements for four selected leak configurations. In the example, a double-wall construction with a 100 mm distance between both walls, no insulation between these walls, and a connecting canal between both parallel slits is shown (see Fig. 5.2e). The solid lines show the power-law fit to Eq. (2.16) to the measured data (dots). The measured data in Fig. 5.4 include measurement uncertainties (standard deviation) in airflow and pressure difference, but for the majority of these values, the error bars are smaller than the size of the displayed dots.

The airflow through the largest slit with a cross-sectional area of 9.0 cm^2 (blue) is, as might be expected, the largest. Much smaller is the airflow through slits with a cross-sectional area of 0.7 cm^2 (green) and 0.4 cm^2 (magenta), but even at these small flows, a distinction between both leaks is still possible. In these examples, the leaks have the following pressure exponents: $n_{9.0\,\mathrm{cm}^2} = 0.55$, $n_{1.8\,\mathrm{cm}^2} = 0.64$, $n_{0.7\,\mathrm{cm}^2} = 0.71$, and $n_{0.4\,\mathrm{cm}^2} = 0.76$. The three black vertical dotted lines indicate the predicted airflows through these leaks at 50, 10 and 4 Pa pressure difference. 50 Pa pressure difference is a frequently used value for comparing blower door measurements of real buildings for compliance with building regulations [53], whereas a 10 Pa pressure difference is used in the Canadian CGSB 149.10 standard [55] to calculate, for instance, the equivalent leakage area. At 4 Pa pressure difference or less, natural infiltration usually occurs in buildings, which is an essential metric in indoor air quality applications [188] and building energy simulations [189]. This is also the reference pressure in French guidelines [190] and most often used when converting to equivalent leakage area (e.g., in the ASTM test method).

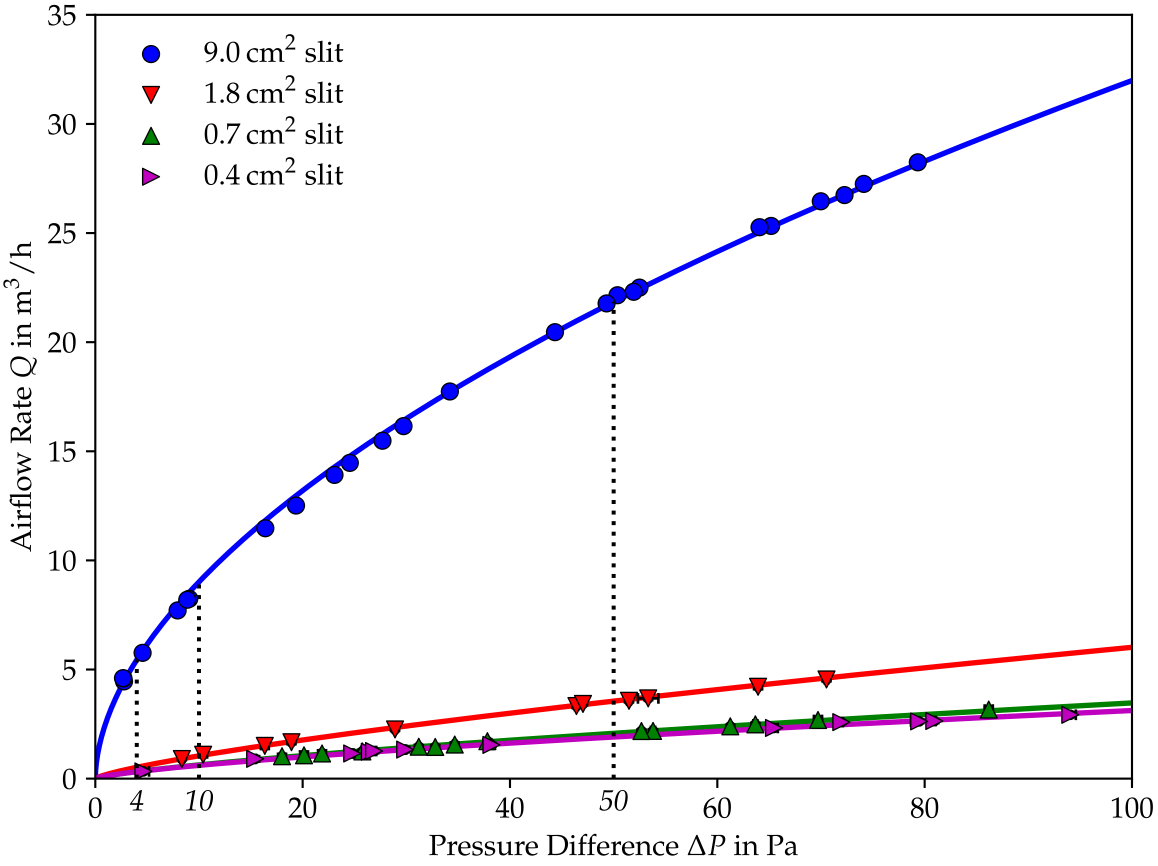

Figure 5.4: Airflow-pressure measurements of laboratory test apparatus and power-law fit for a double-wall construction with 100 mm distance between the walls, no insulation and connection between the slits (see Fig. 5.2e) for four different slit sizes

5.2.2 Acoustic Measurements

The mean coherence value of a wall with no slits is subtracted from the mean value of the same wall with a specific slit for each of the acoustic measurements to reduce the impact of sound transmitted through the wall structure, the impact of background noise, and to focus more on the sound transmitted through the openings. This characteristic is determined for each different wall structure (e.g., single or double walls). The coherence function is calculated for all 38 investigated leak configurations. An example of the measured coherence function (with no airflow) is shown in Fig. 5.5 for the same leak configurations shown previously in Fig. 5.4.

Fig. 5.5 also includes the coherence function for the double-wall with no slits (100 mm distance between the walls and no insulation material between the walls) as the black bottom line. This line shows how sound is transmitted through the wall, even though the wall has no deliberate airflow paths. The dotted horizontal lines in Fig. 5.5 indicate the mean value of the coherence functions over the whole considered frequency spectrum of the leak configurations with the same color. This value increases with increasing slit size. While there are some changes with frequency, there are no clear trends, and the different test configurations have different results. This indicates that it is reasonable to use a single coherence value averaged over the entire frequency range. Therefore, the mean coherence values are used when assessing the test results for all configurations.

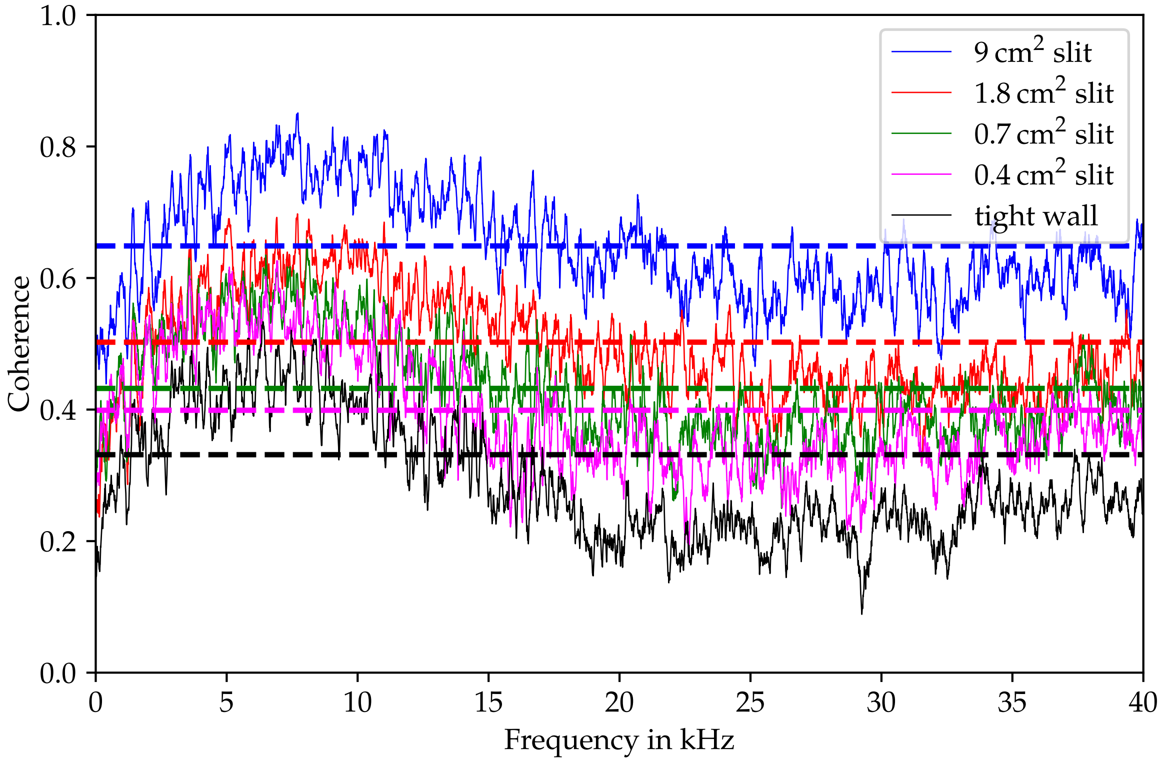

Figure 5.5: Coherence functions for a double-wall construction with a 100 mm distance between the walls, no insulation and a connection between the slits (see Fig. 5.2e) for four different slit sizes, and a tight double-wall, with dashed lines indicating the mean values

Fig. 5.6 shows the differences between the coherence of a slit size with a height of 1 mm (cross-sectional area: 1.8 cm^2) and an airtight wall for four different wall configurations. The following leak configurations are displayed (see Figs. 5.2a to 5.2d):

- One wall (Fig. 5.6a)
- Two walls with a 100 mm distance (Fig. 5.6b)
- Two walls with a 150 mm distance (Fig. 5.6c)
- Two walls with a 100 mm distance and additional insulation in between (Fig. 5.6d)

Even though the slit size is the same, the mean magnitudes, as well as the frequency responses, are different for each of these different leak configurations.

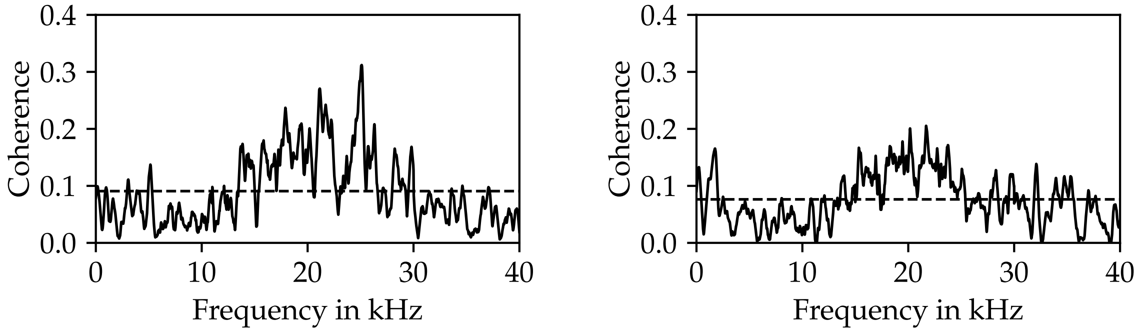

(a) One wall

(b) 100 mm double-wall

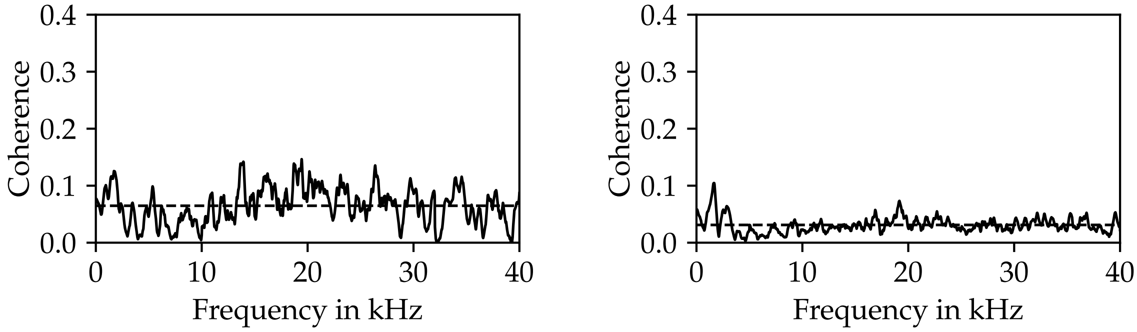

(c) 150 mm double-wall

(d) Insulated double-wall

Figure 5.6: Differences between the coherence of four different wall configurations and the coherence of the same tight wall constructions for the largest slit size of a cross-sectional area of 1.8 cm^2, with dashed lines indicating the mean values

The top left configuration with only one wall separating the two chambers has the highest mean magnitude of all four displayed configurations, with its highest peak at around 25 kHz. The largest frequency responses are between around 15 and 30 kHz, which is still visible at the double-wall construction with a 100 mm distance between them. However, this second displayed configuration has a lower mean magnitude compared to the single wall construction. Furthermore, the shape of the frequency response is similar for both double-wall constructions without insulation between 30 and 40 kHz. The last configuration with insulation material between both walls has the lowest mean magnitude of the coherence differences. The insulation material seems to attenuate the frequency components over the whole considered frequency range. Here, no single distinct frequency is visible. These results indicate that there is the potential to identify types of leaks from their sonic signature, which will have to be further investigated in future work.

As already described in Section 5.2.1, the airflow at the pressure difference at 50, 10 and 4 Pa is a crucial parameter for assessing a building's airtightness. Therefore, a prediction of these values using acoustic methods would be beneficial. In Figs. 5.7 to 5.9, the differences between the mean coherence functions of walls with artificial leaks and the same airtight wall constructions ΔC_{xy} are plotted against the respective airflow rates of the same constructions at 50 (Fig. 5.7), 10 (Fig. 5.8), and 4 Pa (Fig. 5.9) pressure difference. The airflow rates at these pressure values are extracted from the airflow measurements (as illustrated in Fig. 5.4) by interpolation along the fitted curves.

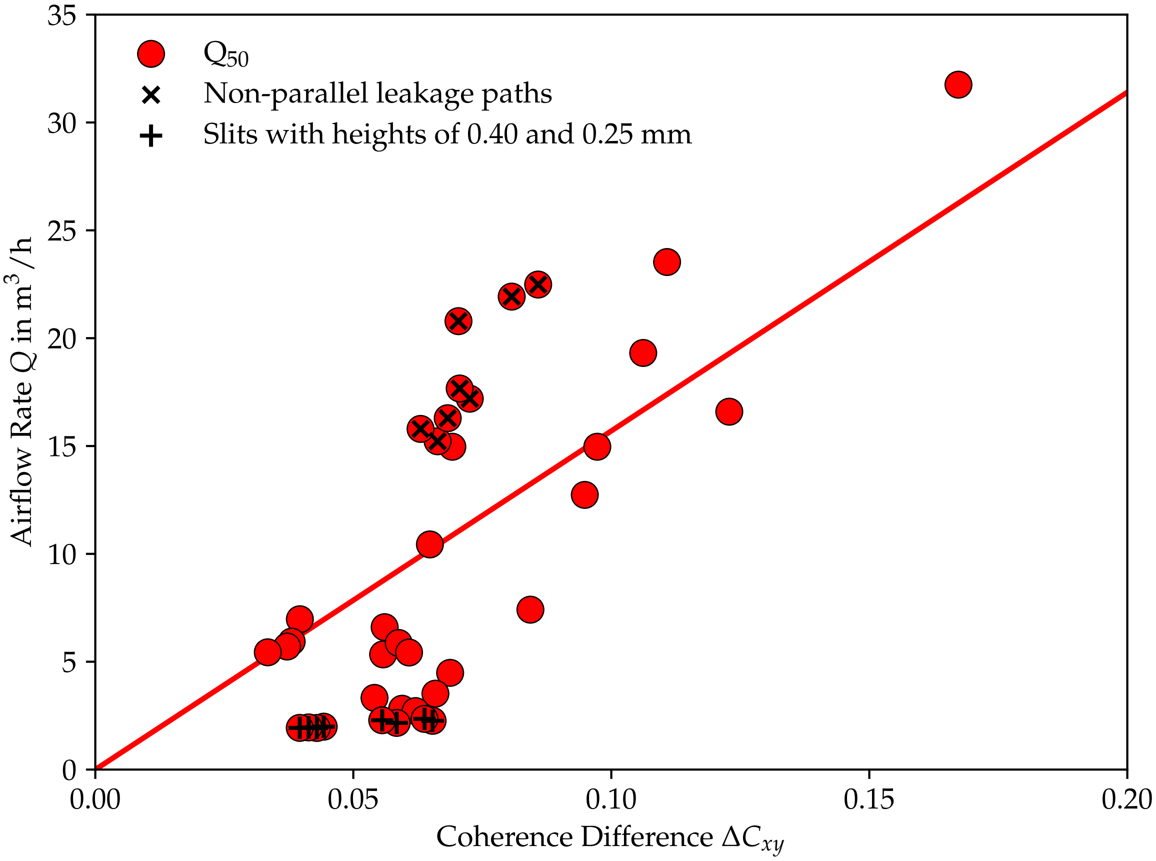

Figure 5.7: Correlation between mean coherence difference and different airflow rates at 50 Pa pressure difference for all investigated leakage configurations

Figs. 5.7 to 5.9 show an observable trend between the mean coherence difference (ΔC_{xy}) and airflow for a given pressure difference. This indicates that the mean coherence difference can be used to predict air leakage. These values of the mean coherence difference function are related to the airflow to investigate this trend using the following Eq. (5.3) for each of the three pressures in Figs. 5.7 to 5.9:

$$Q = K \, \Delta C_{xy} \, \Delta P^{n_c} \tag{5.3}$$

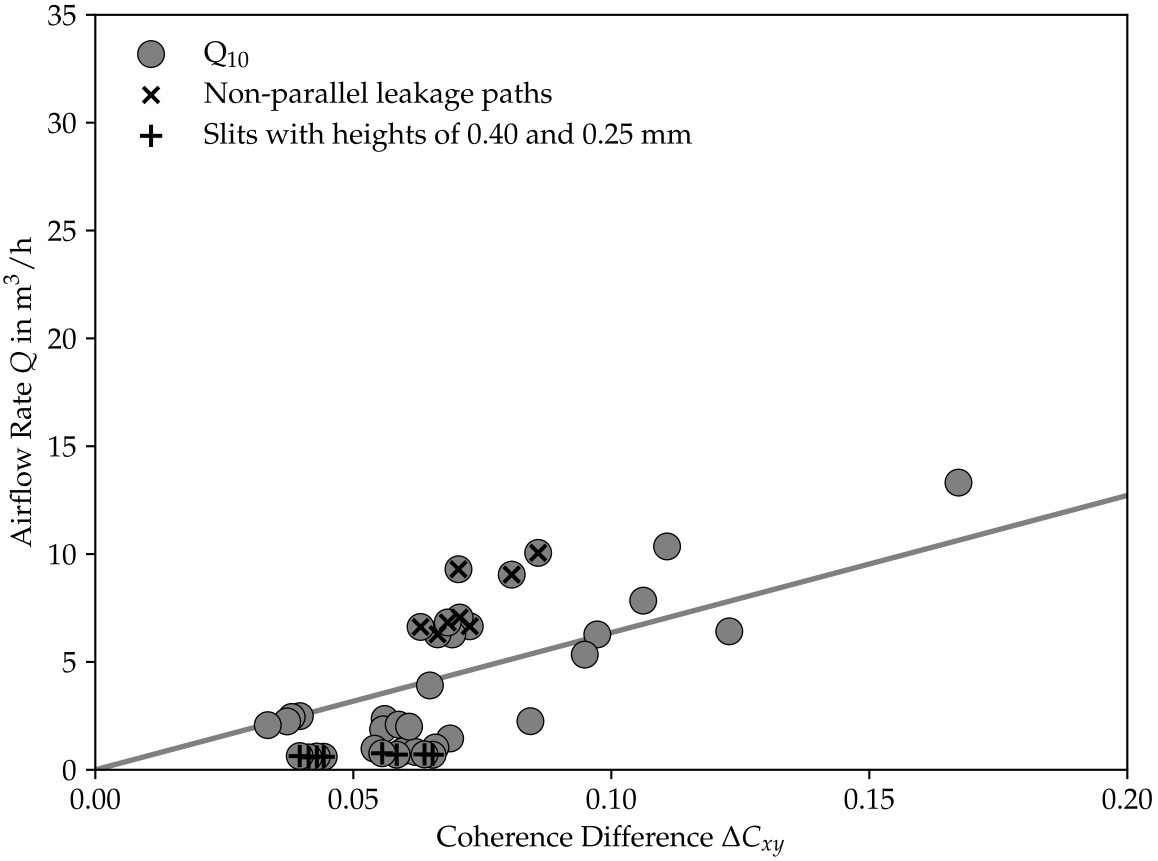

Figure 5.8: Correlation between mean coherence difference and different airflow rates at 10 Pa pressure difference for all investigated leakage configurations

Where ΔP is equal to each of the three reference pressures (50, 10 and 4 Pa) and coefficient K and pressure exponent n_C are determined using an optimizer at each pressure. The optimizer uses least squares to fit Eq. (5.3) to the data. For each pressure case, the pressure exponent n_C is close to 1. Fig. 5.10 shows the fitted n_C and K values for the three investigated pressure differences. The fitted coefficients K indicate a non-linear relationship between K and the pressure difference.

The lines in Figs. 5.7 to 5.9 show the resulting flow-coherence relationship. From these figures, it can also be observed that different leak configurations can have similar coherence differences but a quite different airflow. Further spectral analysis may be combined with the coherence to improve the acoustic estimates of leakage and airflow in future work. For example, a possible weighting of certain dominant frequency bands, instead of taking a mean value over the whole frequency range, may have the potential to increase the prediction accuracy.

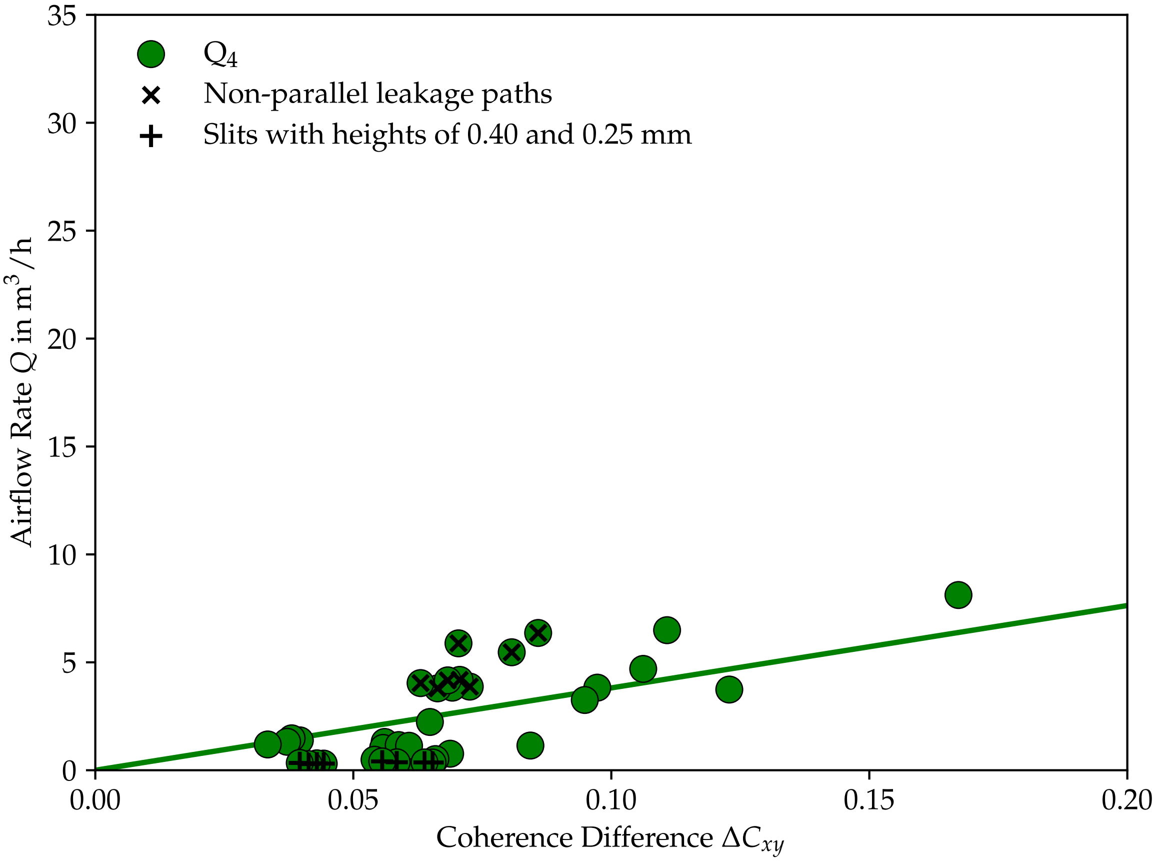

Figure 5.9: Correlation between mean coherence difference and different airflow rates at 4 Pa pressure difference for all investigated leakage configurations

Additionally, two prominent leak configurations are highlighted in Figs. 5.7 to 5.9 to indicate some significant outliers from this general trend. Firstly, all non-parallel leakage paths (see Figs. 5.2f and 5.2g) are highlighted with an additional "x" on the dots in Figs. 5.7 to 5.9. These are all grouped in the top left part of the figures. For all configurations with non-parallel leakage paths (with and without a connecting channel), only slits with heights of 5 and 1 mm are manufactured. Here, the acoustic measurement procedure generally underestimates the actual leak size. One explanation might be that sound waves are attenuated due to reflection inside the structure. Therefore, this acoustic method might be less suitable for quantifying airflows in constructions with large non-parallel airflow paths.

Secondly, the leak configurations containing only the smallest slits with heights of only 0.4 and 0.25 mm (see Fig. 5.2h) are highlighted with an additional "+" on the dots. These are all grouped in the bottom part of Figs. 5.7 to 5.9. Even though the measured airflow through these leaks does not differ significantly (e.g., for different distances in the double-wall configurations), there is a variation in the coherence difference for this group of artificial leaks. Therefore, the influence of the sound transmission through the

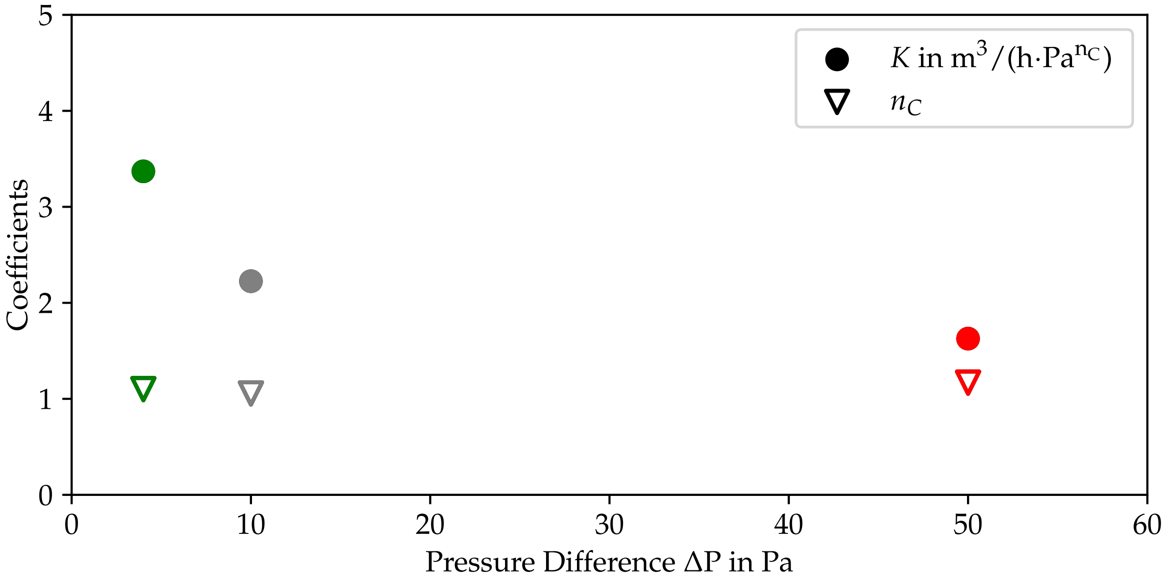

Figure 5.10: Fit of coefficient K and exponent n_C for the investigated pressure differences in the laboratory tests, the colors correspond to Figs. 5.7 to 5.9

wall structure itself seems to dominate these measurements compared to the sound transmission through these tiny leaks. This makes it hard to detect these small leaks correctly using this method.
However, the acoustic parameter may not serve the purpose of precisely predict the airflow, but it may have the potential to give an estimate.

In order to assess the accuracy of the prediction of airflow rates with the relationship introduced in Eq. (5.3), the absolute root mean square error (RMSE) and a normalized root mean square error (NRMSE) between the measured (*meas*) airflow rates and the predicted (*pred*) function are calculated (see Eqs. (5.4) and (5.5)). The NRMSE is normalized by the predicted flow rate of the airflow at the specific pressure differences to be able to compare this error for different scales.

$$RMSE = \sqrt{\frac{\sum_{i=1}^{N} \left(Q_{i,meas} - Q_{i,pred}\right)^2}{N}} \tag{5.4}$$

$$NRMSE = \sqrt{\frac{\sum_{i=1}^{N} \left(\frac{Q_{i,meas}-Q_{i,pred}}{Q_{i,pred}}\right)^2}{N}} \tag{5.5}$$

These errors for flow rate predictions at 50, 10 and 4 Pa pressure difference are shown in Table 5.1. The absolute RMSE decreases with predicting airflow rates at lower pressure differences, whereas the NRMSE decreases with airflow rates at increasing pressure differences. The NRMSE indicates errors greater than ±50 % for the prediction of airflow rates with the acoustic method.

Table 5.1: RMS and NRMS errors for flow predictions

	Q_{50}	Q_{10}	Q_4
RMS errors in m^3/h	5.42	2.48	2.44
NRMS errors	0.53	0.59	0.63

5.3 Summary

In this chapter, an acoustic method is proposed for quantifying the air leakage of multiple artificial leaks and wall constructions in a laboratory test apparatus. This test apparatus consists of two chambers, separated by the test walls. An omnidirectional speaker is placed in one chamber and the acoustic coherence is calculated with the recorded signals in both chambers. This acoustic method is compared with pressurization measurements under the same boundary conditions. Within this laboratory test setup, a linear trend is shown between the mean acoustic coherence difference and the airflow rate at three characteristic pressure differences (50, 10 and 4 Pa), which pass through a single leak. Therefore, the acoustic approach is able to give an estimate of the magnitude of airflow within this laboratory setup. Additional spectral analysis and a discussion of more complex leakage paths may improve this estimation in future work. In the next step, this method needs to be validated outside the laboratory environment in a real building. However, the influence of external factors (e.g., wind) on the fan pressurization measurement conducted here is neglected in the laboratory tests. Before comparing this acoustic testing procedure to fan pressurization methods in a real building, the influence of external factors on the determination of these air leakage metrics will be discussed in the following chapter.

6 Improving Air Leakage Prediction of Fan Pressurization Measurements

The airtightness of building envelopes is typically ascertained by the fan pressurization method, which is already described in Section 2.2.1. The following chapter describes a method that enables a more reliable prediction of the airflow and, therefore, gives a better input value for a future comparison with acoustic parameters.

The pressure range across the building envelope during fan pressurization measurements dramatically exceeds the pressures, leaks in a building are exposed to under regular operation. At these higher pressure differences (usually $\geq$ 50 Pa), relative impacts due to ambient disturbances (like wind) and uncertainty of the measurement devices are usually lower compared to pressures where natural infiltration occurs (< 4 Pa). The determination of infiltration at these low pressures may not be interesting to fulfill energy performance standards (e.g., passive house) or used in building standards to compare the relative airtightness of different buildings, but is essential for building energy calculations [189] or indoor air quality assessments [188]. However, a subsequent interpolation of the measured pressures and an extrapolation from high to low pressure where natural infiltration occurs may contain a significant uncertainty [191]. Therefore, the most precise measurements at high pressure are the least accurate ones [29, 192].
Although measurement uncertainties may significantly influence the prediction of airflow rates at low pressures, the current standards do not necessitate the acquisition

---

Major parts of this chapter are reproduced from:

B. Kölsch, and I. S. Walker, "Improving Air Leakage Prediction of Buildings using the Fan Pressurization Method with the Weighted Line of Organic Correlation", *Building and Environment*, vol. 181, p. 107 157, 2020, ISSN: 0360-1323. DOI: `10.1016/j.buildenv.2020.107157`

B. Kölsch and I. S. Walker, "Reducing Wind Sensitivity for Blower Door Testing, in *Proceedings of the 41st AIVC - ASHRAE IAQ 2020 joint conference*", 2022

of uncertainties of the measured values. The importance of considering uncertainties in fan pressurization measurements was already discussed by Persily et al. [193] in 1985 and Herrlin et al. [194] in 1988. Geissler [82] performed simulations about the estimation of errors of blower door measurements. Sherman et al. [195] analyzed in 1995 the errors of extrapolation to low pressures using the ordinary least square (OLS) regression method. Recent studies also confirmed that the uncertainty of fan pressurization measurements could not be neglected [196]. Furthermore, Carrié et al. [197] recently highlighted, in particular, the influence of wind fluctuations on the uncertainty of building airtightness pressurization tests.
In addition to the conventionally used OLS regression method, Delmotte et al. [198] discussed in 2011 the applicability of a weighted least squares regression, and Okuyama et al. [199] introduced in 2012 an iterative weighted least square (IWLS) regression approach. In 2017, Delmotte [200] suggested the weighted line of organic correlation (WLOC) as an improved non-iterative regressing method, which takes measurement uncertainties into account.

In this chapter, the OLS and WLOC regression methods are applied to a large dataset of almost 7500 blower door measurements in six different single-story, single-family houses. The goal is to identify the uncertainties in the prediction of the pressure exponent and flow coefficient of the power-law (Eq. (2.16)) using both regression techniques. In addition to the work done by Prignon et al. [201, 202], this chapter investigates a statistical analysis of a larger data set of blower door measurements.

6.1 Methodology

6.1.1 Test Site and Measurement Equipment

In this chapter, a data set of fan pressurization measurements is used, which was recorded at the Alberta Home Heating Research Facility (AHHRF). This facility consists of six unoccupied houses, which are each of different construction. These houses were located south of Edmonton, Alberta, Canada, and were used to test different heating and ventilation strategies. Each of these six houses is a single-story construction with a floor area of 6.7 by 7.3 m, a wall height of 2.4 m, and a full basement. For more detailed information about this test facility and data source, see Refs. [29, 203]. The measurement campaign itself was not part of this thesis.
Repeated fan pressurization measurements were performed at each of these six houses.

These repetitions allow an investigation of how external factors (like the presence and strength of wind) may affect the measurement results when the building construction and, therefore, the airtightness remains constant. All tests were automated, which prevents additional uncertainties due to equipment installation and operator errors, and enables recording a large data set. A total of almost 7500 fan pressurization tests were performed, where each test contains between 20 and 100 measurements of pressure difference and airflow rate, which enables to obtain a complete flow-pressure difference characteristic for each test. The covered pressure range lies between 1 and 100 Pa, for both pressurization and depressurization, which is a broader range than required by the ASTM E779 [54] or DIN EN ISO 9972 [53] standard. The houses were operated in 109 different test configurations, e.g., pressurization and depressurization tests, open and closed flues, windows, or passive vents. Prior to this analysis, the data set is filtered to remove erroneous files, where, e.g., no standard deviation or offset pressure is recorded. This filtering results in 7402 sets of measurements from the original 7500 sets being selected.

Because wind (and stack) pressures vary over the building envelope, the testing procedure would ideally measure the indoor-outdoor pressure difference at each leak location. However, this approach is impractical. For this study, indoor-outdoor pressure differences are taken from pressure taps on each wall of the test building connected to a pressure averaging manifold. This averaging of multiple pressure taps is intended to reduce uncertainties and biases due to wind speed and direction [204] and follows the guidance in standardized testing [54]. Despite the use of multiple pressure taps, some test uncertainty due to varying wind direction during a test can be expected. Wind direction is measured during these tests, but the additional analysis of wind direction effects is beyond the scope of this thesis, and it should be noted that wind direction effects will also scale with wind speed, with the effect of wind direction variability being more significant at higher wind speeds. In most field measurements, only one pressure tap is used to record outside pressure data and may result in higher sensitivities to wind than presented here. Each measured envelope pressure consisted of about 150 individual measurements over a period of 15 s. The mean and standard deviations of the pressure measurements at each station are recorded. These standard deviations are used as an uncertainty estimate for each pressure station and are an essential input to the WLOC analysis.

In contrast to the required measurement procedure in most standards, where offset pressures have to be recorded at the beginning and end of each measurement series, for this study, every pressure difference data point has been corrected by a reference pressure at zero-flow rate for this point in this analysis. For this purpose, a damper closed the fan opening for each offset pressure measurement because this opening may affect the pressure distribution throughout the building.

The airflow rates Q are measured using a laminar element flowmeter, which is connected to the outside with a flexible duct. All flow rates are corrected with indoor and outdoor air temperatures according to the ASTM E779 [54] standard. As with the pressure difference measurements, the airflows are taken over a period of 15 s, at a sampling rate of about ten samples per second. Both the mean $\Delta P_{flowmeter}$ and standard deviation ($\sigma_{\Delta P\,flowmeter}$) are recorded from the pressure measurements across the laminar element flowmeter. Due to the linear behavior of the flowmeter, the respective standard deviation of the airflow (σ_Q) is determined by the following equation:

$$\sigma_Q = \sigma_{\Delta P\,flowmeter} \frac{Q}{\Delta P_{flowmeter}} \tag{6.1}$$

In this data set, a wide range of weather conditions are covered with outside temperatures between −40 °C and 30 °C, and wind speeds of up to 10 m/s. The wind speed, wind direction, and ambient temperature data were gathered from a meteorological station next to the test site.

6.1.2 Regression Methods

As already described in detail in Section 2.1.5, the relationship between the airflow rate Q and the pressure difference ΔP across the building envelope can be predicted using the power-law formulation (see Eq. (2.16)). Eq. (2.21) shows the linear expression of this power-law formulation. A regression is applied to this linear form of the power-law, where n is the slope, and $\ln(C)$ is the intercept of this regression. In the following paragraphs, the OLS and the WLOC regression techniques, which are compared in this chapter, are introduced.

Ordinary Least Square Method

In current standards [53, 54], the ordinary least square (OLS) method is used for determining the flow coefficient C and pressure exponent n. In this case, $x_i = \ln(\Delta P_i)$ is the independent, and $y_i = \ln(Q_i)$ is the dependent variable (with $1 \leq i \leq N$). The OLS method minimizes the airflow rate residuals, which are geometrically the distances in the y-direction between the fitted line and the measured values [205]. The pressure exponent and flow coefficient of the power-law formulation (Eq. (2.16)) can directly be determined using the following formulas:

$$n = \frac{\sum\limits_{i=1}^{N}\left(x_i - \sum\limits_{i=1}^{N}\frac{x_i}{N}\right)\left(y_i - \sum\limits_{i=1}^{N}\frac{y_i}{N}\right)}{\sum\limits_{i=1}^{N}\left(x_i - \sum\limits_{i=1}^{N}\frac{x_i}{N}\right)} \tag{6.2}$$

$$C = \exp\left(\sum_{i=1}^{N}\frac{y_i}{N} - n\sum_{i=1}^{N}\frac{x_i}{N}\right) \tag{6.3}$$

Here, the assumption is made that values in the y-direction are equally uncertain, and the uncertainties in the x-direction, which correspond to the pressure difference measurements, are not taken into account [206]. These assumptions are, however, not valid for measurements in real buildings. Imperfect knowledge of the uncertainties may lead to a shifting and rotation of the linear regression line of the power-law. The fractional error is usually more significant for lower pressure points (e.g., 4 and 10 Pa) than for higher pressure points and may lead, therefore, to uncertain predictions of flows at these pressures [200].

Weighted Line of Organic Correlation

In contrast to OLS, the weighted line of organic correlation (WLOC) minimizes the sum of the product of the measured values and the weighted horizontal as well as vertical differences and the predicted line [200]. Consequently, measurement points with higher uncertainty are less significant in the calculation of the regression line. This is an important characteristic, mainly if airflows at low pressures shall be predicted. Unlike the before mentioned iterative weighted least square (IWLS) regression approach [199], pressure exponent and flow coefficient can be calculated without iteration:

$$n = \frac{\sqrt{\sum\limits_{i=1}^{N} v_i\,w_i \sum\limits_{i=1}^{N} v_i\,w_i\,y_i^2 - \left(\sum\limits_{i=1}^{N} v_i\,w_i\,y_i\right)^2}}{\sqrt{\sum\limits_{i=1}^{N} v_i\,w_i \sum\limits_{i=1}^{N} v_i\,w_i\,x_i^2 - \left(\sum\limits_{i=1}^{N} v_i\,w_i\,x_i\right)^2}} \tag{6.4}$$

$$C = \exp\left(\frac{\sum\limits_{i=1}^{N} v_i\,w_i\,y_i - n\sum\limits_{i=1}^{N} v_i\,w_i\,x_i}{\sum\limits_{i=1}^{N} v_i\,w_i}\right) \tag{6.5}$$

In Eqs. (6.4) and (6.5), v_i and w_i are the weights of each measurement point $x_i = \ln(\Delta P_i)$ and $y_i = \ln(Q_i)$. These weights are defined by Delmotte [200] as the reciprocal value of the measured standard deviation at each pressure level:

$$v_i = \frac{1}{\sigma(x_i)} \tag{6.6}$$

$$w_i = \frac{1}{\sigma(y_i)} \tag{6.7}$$

Thus, lower variability in the measured data gives it more significant weight in the analysis, and therefore, these points are more important in the fitting.

In Fig. 6.1, an example of a typical blower door measurement with twelve different pressure differences and their corresponding airflow rates is shown. This specific example is just one out of the 7402 considered measurement series in this work to demonstrate the difference between the fitting of OLS and WLOC (a depressurization test of a masonry structure with an open 150 mm diameter furnace flue). The measured standard deviations for each point are displayed as well. For the same measurement series, both previously described regression methods are applied, and the resulting power-law functions are plotted on a linear scale. The ordinary least square fitting (blue line) tries to find an appropriate fit for all pressure differences equally. In contrast, the weighted line of organic correlation (red line) considerably improves the fit for data points with low measurement uncertainty. Data with more significant errors are less important in the fitting. In this specific case, WLOC shows a significantly better fitting for measurement data points, particularly above a 25 Pa pressure difference.

6.1.3 Probability Density Functions

The results for each of the 109 configurations have been taken, and the distributions of calculated n and C for both WLOC and OLS have been investigated for multiple measurements to determine the potential improvement using WLOC. This comparison is achieved by analyzing Probability Density Functions (PDFs) for each leakage configuration. The area under the PDF curve between two points equals the probability of getting a value between these two points. Therefore, not the value of the function is essential but the integral. Here, the PDFs are calculated using the kernel density estimation (KDE) algorithm, which allows estimating an unknown continuous density function from a set of N discrete 1D data samples $x_{s,i}$, with $1 \leq i \leq N$ [207]. The use of KDE has a significant advantage of directly evaluating the data without previously applying a model to it [208]. Compared to the commonly used histogram as an estimation of a dataset's density, the shape of the kernel density estimation is continuous and seems

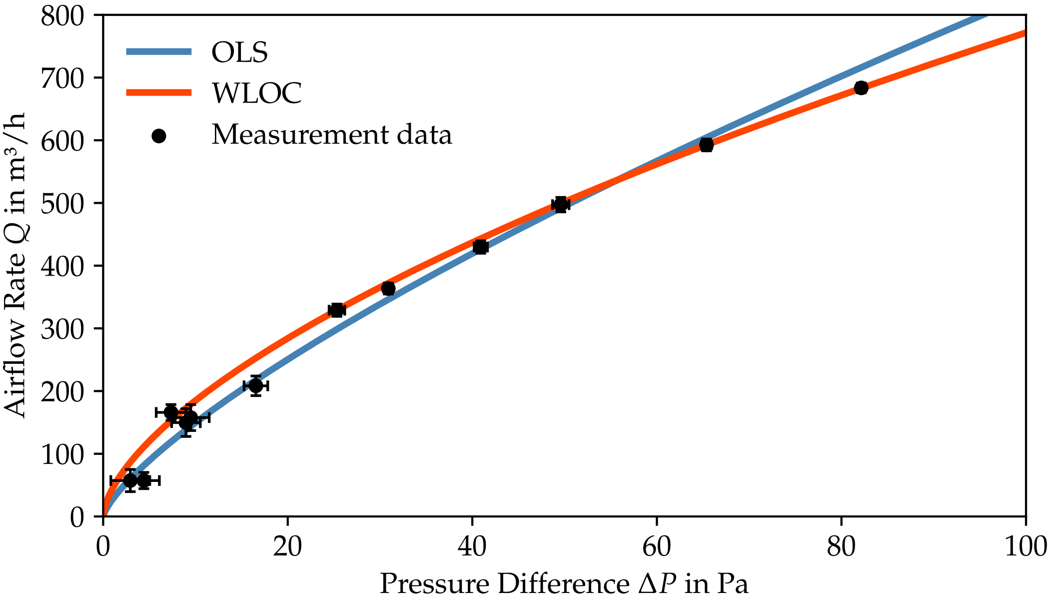

Figure 6.1: Linear display of a comparison between OLS and WLOC fitting method for one blower door measurement series

to be a reasonable estimation of the "true" PDF [209]. According to Sheather [210], the bias of kernel density estimation is one order better compared to a histogram estimator. The approximated PDF $\hat{f}_h(x_s)$ is computed as (cf. [211]):

$$\hat{f}_h(x_s) = \frac{1}{N\,h} \sum_{i=1}^{N} K\left(\frac{x_s - x_{s,i}}{h}\right) \tag{6.8}$$

Each observed sample is first replaced with a uniform kernel K, which is here based on the normal Gaussian distribution, which is the most frequently used kernel [209]:

$$K(x) = \frac{1}{\sqrt{2\pi}}\,\mathrm{e}^{-\frac{x^2}{2}} \tag{6.9}$$

A summation of these curves and a subsequent normalization to obtain an area of one under the final curve leads to an approximated PDF. The parameter h in Eq. (6.8) is the bandwidth, which adjusts the smoothness of the PDF and is calculated as recommended by Silverman [208]:

$$h = 1.06\,\sigma\,N^{-\frac{1}{5}} \tag{6.10}$$

where σ is the standard deviation of the investigated samples and N is the sample size. The narrower the distribution of the results (i.e., lower variance), the less sensitive the analysis is to experimental variation (primary from wind), and the lower the uncertainty is for any given test in predicting the correct leakage.

In order to assess the variance s^2 of predicted values for OLS and WLOC, the variance of the data set is calculated according to the following formula:

$$s^2 = \frac{\sum_{i=1}^{N} \left(x_i - \frac{\sum_{i=1}^{N} x_i}{N} \right)^2}{N-1} \tag{6.11}$$

A higher variance indicates, the data set has a more significant variability, and data points are widely spread around the mean.

6.2 Results and Discussion

Results are presented here in terms of PDFs of predictions of pressure exponent n and flow coefficient C for different leak configurations. The variability in other metrics that are commonly used has also been examined: the building envelope flow and the equivalent leakage area at both 4 and 10 Pa reference pressures.

6.2.1 Pressure Exponent and Flow Coefficient

The PDFs are calculated for all 109 configurations, and example figures are provided for illustration purposes. Each example is for one single leak configuration. The small vertical lines next to the x-Axis indicate the predicted values of n and C for a complete series of measurements using the OLS (blue line) and WLOC (red line) regression method, respectively. The global maximum of the PDFs can be interpreted as the mode and is here the expected true value of n and C for the respective data set and regression technique.

The results are broken down into five different fundamental cases:

1. Equal expected values and higher variances for OLS:

In this case, both regression methods predict approximately the same values of n and C, but the PDFs of the OLS regression have a significantly higher variance.

An example is shown in Fig. 6.2. In this specific configuration, the OLS regression method predicts the pressure exponent values over a broad range, here between 0.55 and 0.78 (small blue vertical lines next to the x-Axis). The distribution of calculated pressure exponent values using the WLOC regression method is here limited between 0.57 and 0.69 (small red vertical lines). Even though the highest density (indicated with dashed vertical lines) of calculated pressure exponents and flow coefficients for both regression methods has roughly the same value ($n = 0.6$), the probability of getting close to this value with one single measurement, which is often done in field testing, is much higher using WLOC regression. For this specific configuration, the variance using the WLOC regressing technique is reduced by 67 % for the pressure exponent and by 52 % for the flow coefficient.

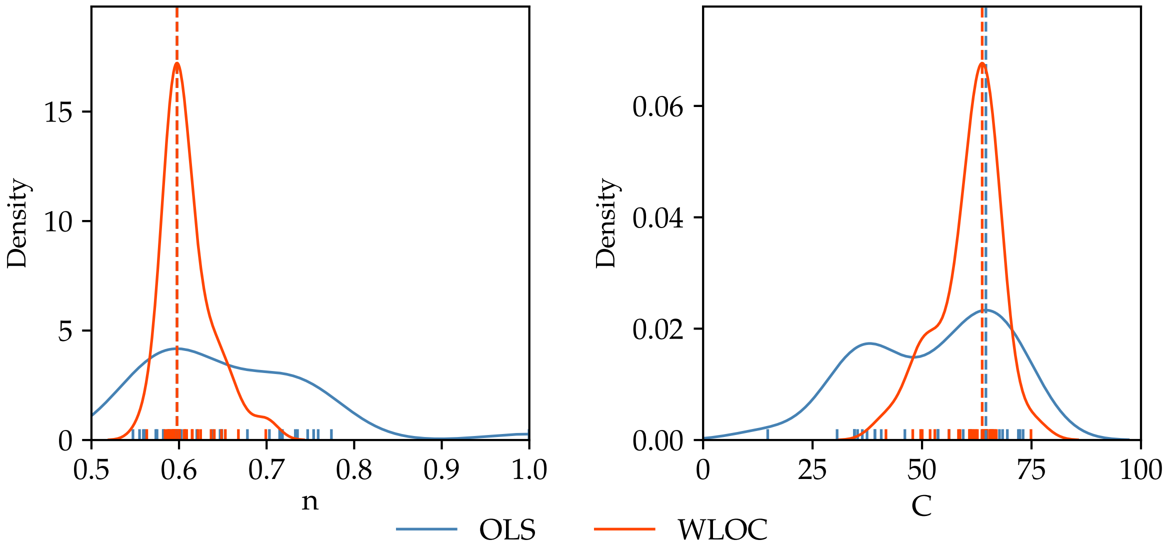

Figure 6.2: PDF of calculation of n and C using OLS and WLOC fitting method, with a higher variance of OLS and approximately the same mean values

2. Different expected values and higher variances for OLS:

The estimation of the expected values differs significantly for both regression techniques. In addition, the PDFs of the OLS regression method have a higher variance. Most of the investigated leak configurations fall into this case. In the displayed configuration (see Fig. 6.3), the point of the highest density of the predicted pressure exponent n differs by approximately 0.11 ($n_{OLS} = 0.76$, $n_{WLOC} = 0.65$). In most cases, a higher prediction of n simultaneously results in a lower prediction of C because C and n tend to be highly correlated [83]. The variance of n is reduced by 75 % and the variance of C by 61 % using WLOC in the displayed configuration. Thus, even with multiple fan pressurization measurement series, the probability of getting close to the correct values for n and C is challenging using OLS.

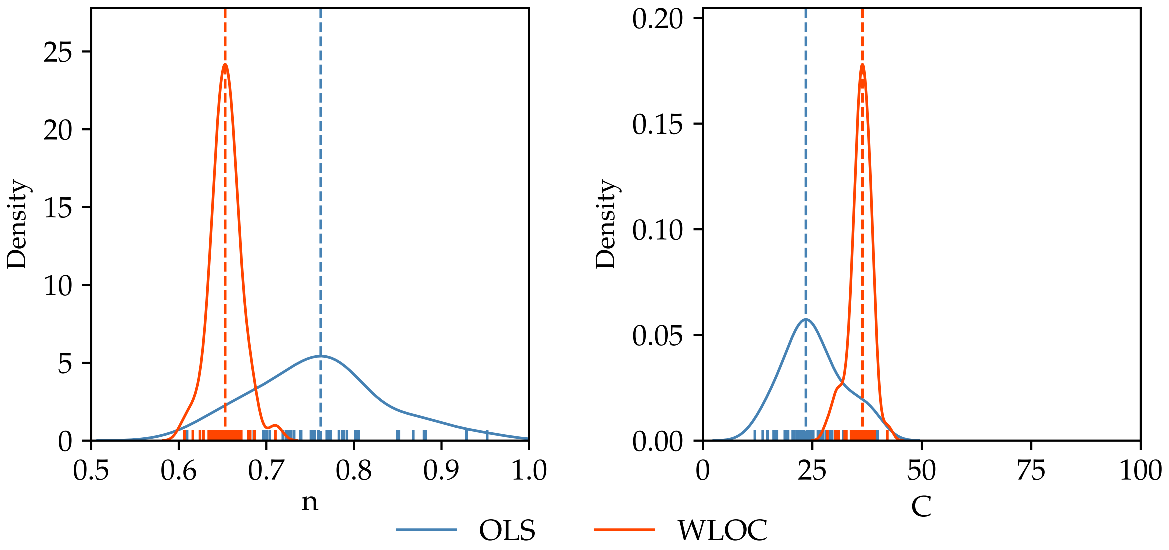

Figure 6.3: PDF of calculation of n and C using OLS and WLOC fitting method, with a higher variance of OLS and different mean values

3. Equal expected values and equal variances:

In the third case, the shapes of the PDFs of pressure exponent and flow coefficient with both fitting methods are approximately the same. Here, both regression methods predict n and C with an almost equal probability. An example is shown in Fig. 6.4, where $n = 0.67$ for both regression methods. In this case, the choice of regression method is of no importance because the performance of both is the same.

4. Different expected values and equal variances:

The shapes of the PDFs classified as case 4 are similar and, therefore, the variances are similar for both regression techniques. However, the expected values are considerably different (see Fig. 6.5, where $n_{OLS} = 0.66$, $n_{WLOC} = 0.61$). Here, it is not clearly evident which value of n or C can be interpreted as the true value for this configuration. Only a few leak configurations fall into this category.

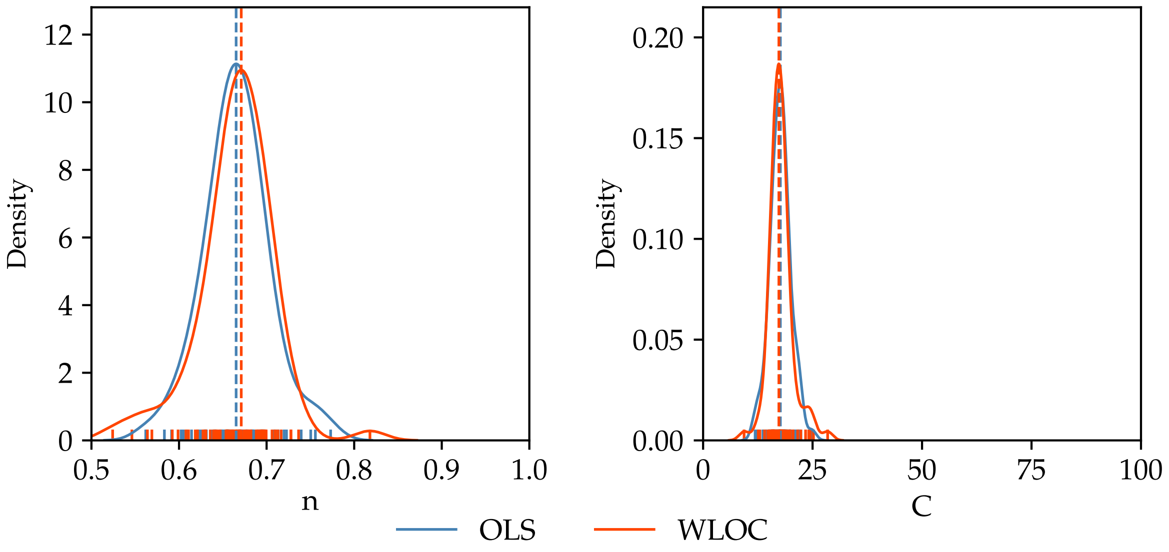

Figure 6.4: PDF of calculation of n and C using OLS and WLOC fitting method, with approximately the same variances and the same mean values

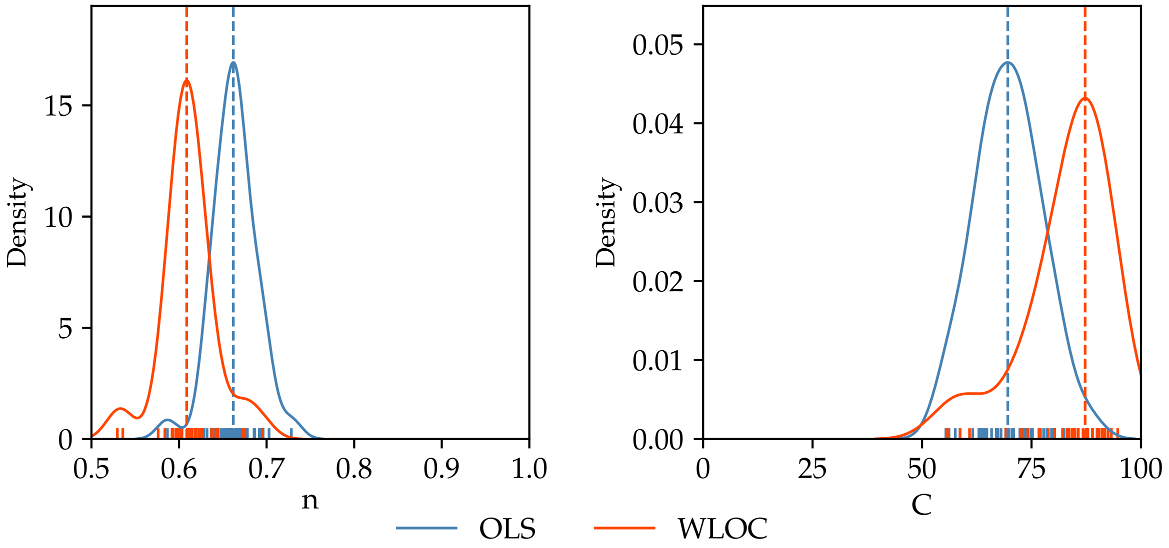

Figure 6.5: PDF of calculation of n and C using OLS and WLOC fitting method, with approximately the same variances and different mean values

5. Equal expected values and higher variances for WLOC:

This case is the opposite of case 1. Both regression methods predict values of n and C, which are very close to each other, but WLOC has a higher variance this time. In the example displayed in Fig. 6.6, the values for n are $n_{OLS} = 0.69$ and $n_{WLOC} = 0.70$. At leak configurations that fit in case 5, the WLOC regression method seems to perform worse than the OLS method. However, the number of configurations allocated to this case is far lower than the number of configurations in cases 1 or 2. Additionally, the number of measurements per leak configuration and thus, the number of data samples used to calculate the PDF is considerably lower for the configurations in case 5. Therefore, the reliability of these PDFs might be lower.

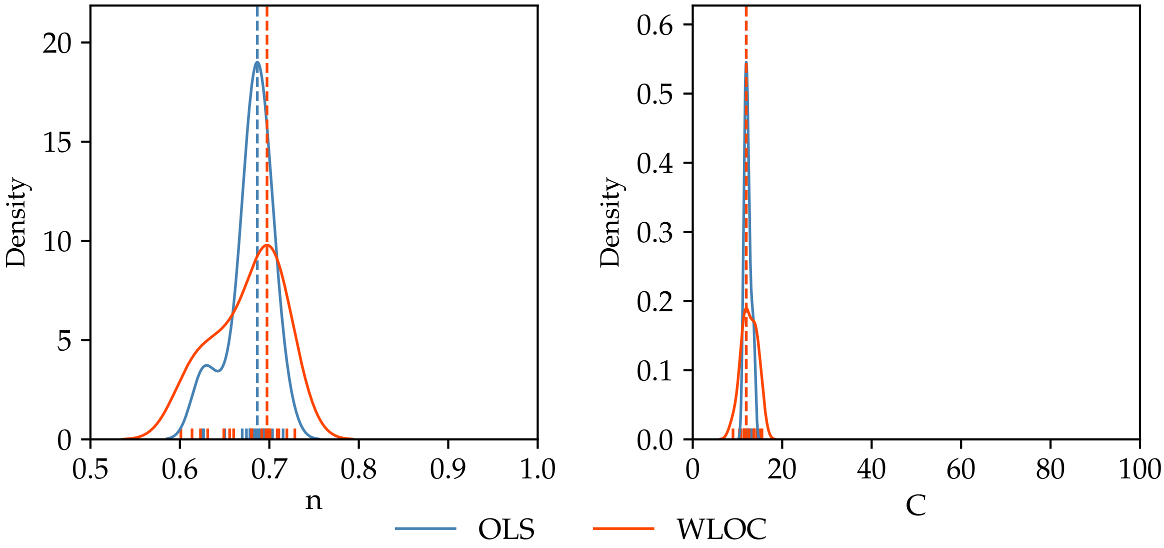

Figure 6.6: PDF of calculation of n and C using OLS and WLOC fitting method, with a higher variance of WLOC and approximately the same mean value

There is no specific case where the prediction of both regression curves is significantly different and where the variances of the PDFs of WLOC are higher.

The effectiveness of the WLOC approach depends on how often tests fall into these different categories. For this data set of 7402 sets of measurements with 109 different test configurations, 17.4 % can be allocated to case 1, 40.5 % to case 2, 15.6 % to case 3, 7.3 % to case 4, and 12.8 % to case 5. Only 6.4 % of the investigated tests cannot explicitly be allocated to one of these cases. The most popular case (case 2) has both a lower variance for WLOC and differences in predicted leakage parameters, C and n. This is an interesting result because a lower variance for WLOC might be expected but not necessarily a change in the predicted value. Combining cases 2 and 4 shows that about half the tests show changes in predicted value between the two approaches. The example for case 5 shows that even when WLOC has a higher variance, it is not as high as the higher variance result for OLS. In most of the investigated leak configurations, the variance of WLOC is lower compared to OLS, and the expected value is different.

In 73.5 % of all investigated configurations, the WLOC regression technique shows that lower weighting to data with higher variability is better than or at least as good as the conventionally used OLS regression. Overall, the WLOC substantially reduces the variances in the test results on average for all 7402 tests by 32 % for pressure exponent n and by 22 % for flow coefficient C.

6.2.2 Airflow Rate and Equivalent Leakage Area

In addition to the test-to-test uncertainty, there may be biases introduced by testing at different wind speeds [204]. Here, the airflow rates and the equivalent leakage areas (see Eq. (2.8)) are shown for one specific example: a masonry structure with an open 150 mm diameter furnace flue in depressurization. This example has been chosen because it contains a large amount of 65 tests.

To better observe the sensitivity of testing bias to wind, the results of the 65 repeated tests with 20 different pressure stations at each measurement for this configuration are binned every 1 m/s of wind speed. The vertical errors bars show the standard deviation of the measurements within each bin. This process reveals any biases due to testing at different wind speeds. The results are plotted as differences between the calculated value (using the power-law) and a reference value. This reference value has been chosen as the value with the lowest corresponding wind speed in the data set and can be seen as a benchmark to the other measurements at higher wind speeds because the influence of wind is the smallest. These reference cases at low wind speeds have also been used in previous studies, e.g., Ref. [29]. A good fit, and thus a reasonable estimation of airflow rates or ELAs at low pressures, is therefore characterized by a small difference between the estimated value and the reference value.

For this analysis, airflow rates and ELAs at 4 and 10 Pa pressure difference have been chosen. Airflow rates at 4 Pa pressure differences are relevant for users because it is a typical metric for energy simulations [189] or indoor air quality applications [188]. Additionally, the airflow at 4 Pa is an important value in French guidelines [190]. The ELA at 4 Pa pressure difference is part of the ASTM E779 standard [54] and is at 10 Pa pressure difference part of the Canadian CGSB 149.10 standard [55].

In Fig. 6.7, the average relative airflow rate is plotted as a function of the mean wind speed during the measurement, evaluated at 4 and 10 Pa pressure difference. Fig. 6.7a shows the absolute difference between the actual airflow, and the reference airflow and Fig. 6.7b shows the fractional difference in %.

For mean wind speeds up to 2 m/s, both regression techniques appear to be equally good. For mean winds speed of more than 2 m/s, the difference between the reference value and the calculated values increases, particularly for OLS up to 6 m/s. This increase in uncertainty at higher wind speeds has been recognized in the DIN EN ISO 9972 test method [53] that states that above a meteorological wind speed of 6 m/s, it is unlikely to obtain satisfactory pressure difference measurements. At the last bin, between 6 m/s and 7 m/s, the OLS seems to obtain better values again (compared to the previous bin). However, this last bin needs to be treated with caution because it contains only one single measurement. All other bins include far more than one measurement and are therefore more reliable.

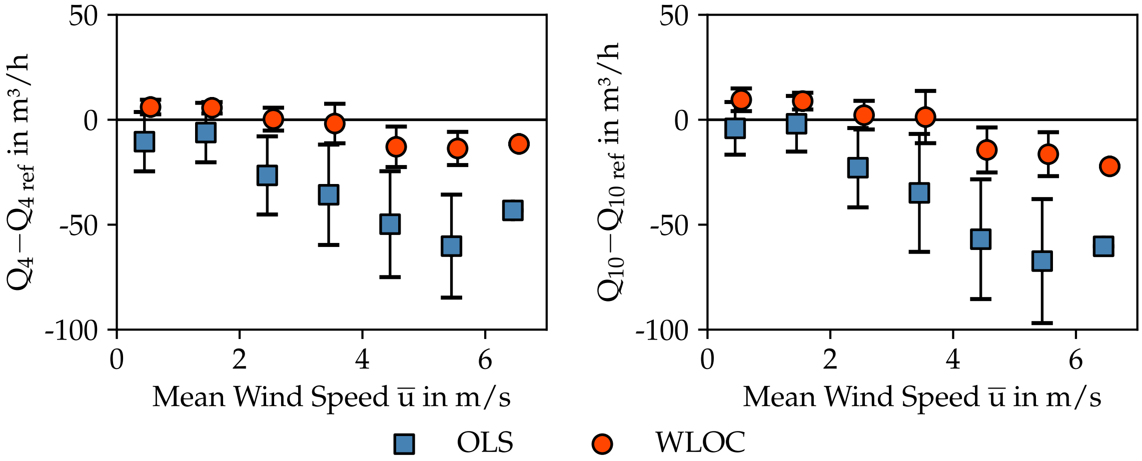

(a) Absolute difference

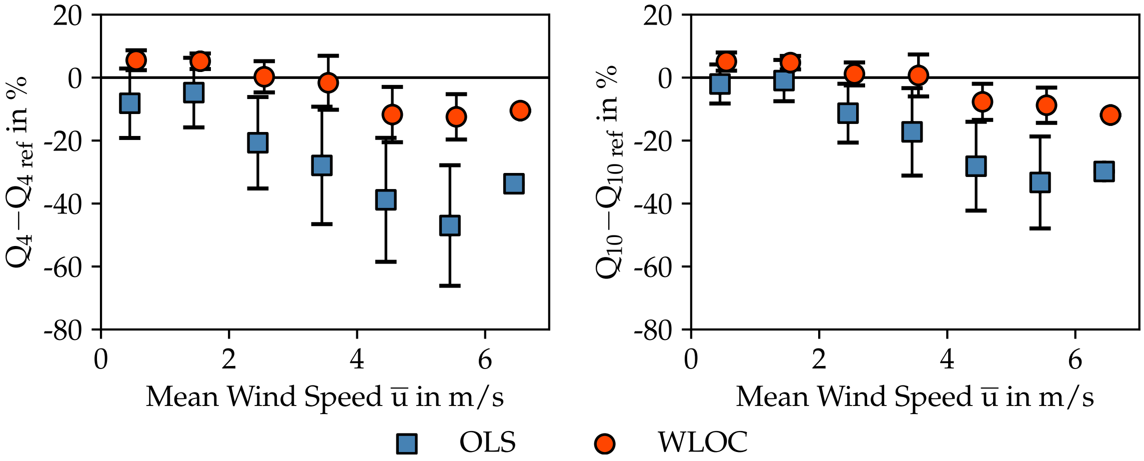

(b) Percentage difference

Figure 6.7: Average relative airflow rate as a function of the mean wind speed at 4 Pa (left) and 10 Pa (right) pressure difference binned every 1 m/s of wind speed.

Fig. 6.8 illustrates the average relative ELAs at 4 and 10 Pa pressure difference, again in absolute (Fig. 6.8a) and fractional differences (Fig. 6.8b). Here, the differences between the calculated values and the reference value increase much more with the mean wind speed for OLS. In contrast to the relative airflow rate, the error of predicted ELAs seems to increase with decreasing pressure. The error for extrapolation up to 4 Pa is in this specific configuration for OLS higher than for 10 Pa. The error for WLOC seems to remain more or less the same. Again, the last bin contains only one value.

In general, Figs. 6.7 and 6.8 show that OLS has much higher wind-induced biases, and

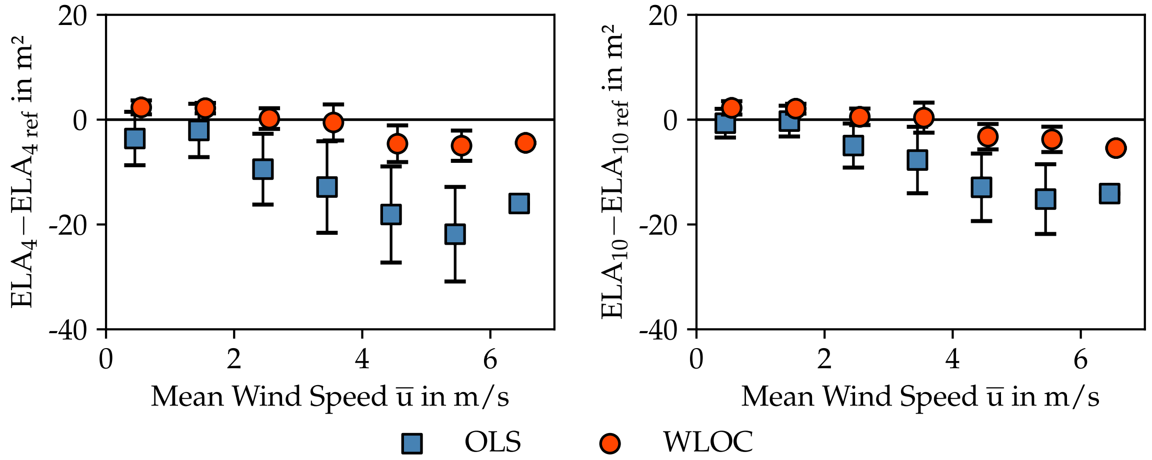

(a) Absolute difference

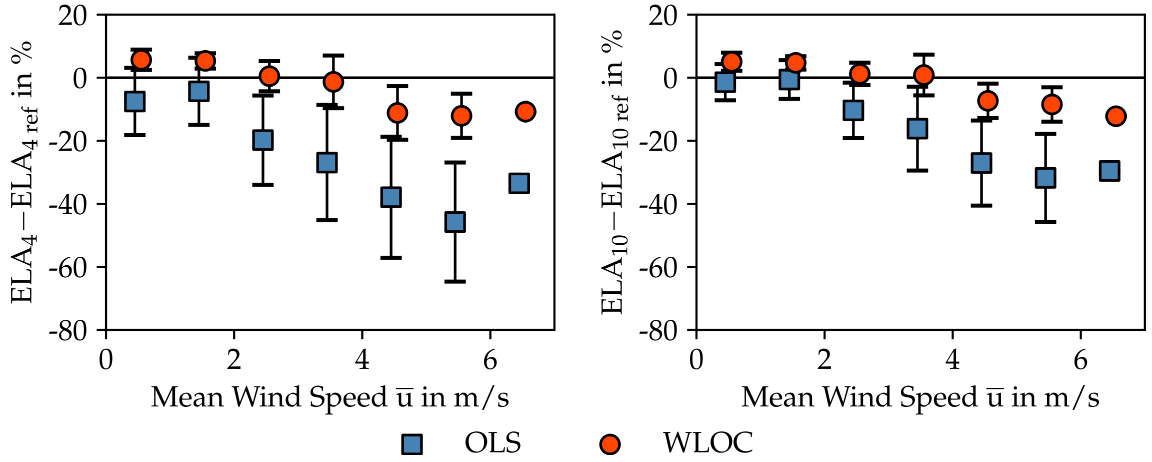

(b) Percentage difference

Figure 6.8: Average relative equivalent leakage area as a function of the mean wind speed at 4 Pa (left) and 10 Pa (right) pressure difference binned every 1 m/s of wind speed.

these biases toughly increase with wind speed. Even though standards (e.g., Ref. [53]) allow fan pressurization measurements up to 6 m/s, these findings show that the extrapolation error of OLS is much higher in this range compared to WLOC.

Furthermore, the mean absolute and root mean square (RMS) errors between the predicted and reference value are displayed in Table 6.1 for this example configuration. All errors are calculated for the airflows and equivalent leakage areas at 4 and 10 Pa as well as for OLS and WLOC. These numbers confirm that the prediction errors for WLOC are lower. The reduction of the mean absolute and RMS prediction errors from WLOC to OLS for values evaluated at 4 Pa is between 72 and 75 % and for values at 10 Pa between 63 and 68 %. Therefore, the relative difference between the prediction error of WLOC and OLS increases with the decreasing pressure differences for this dataset.

Table 6.1: Mean absolute and RMS errors between predicted and reference value for the example dataset

	Q_4 in m^3/h	Q_{10} in m^3/h	ELA_4 in cm^2	ELA_{10} in cm^2
Mean abs. error OLS	27.22	27.32	27.19	16.92
Mean abs. error WLOC	7.20	9.61	7.42	6.20
RMS error OLS	35.93	37.80	36.06	23.50
RMS error WLOC	9.07	11.99	9.23	7.73

In Table 6.2, the mean absolute and RMS errors are displayed as fractions of the reference value. When represented as fractions, a better comparison between configurations with different overall air flows and leakage areas is possible, and biases toward the leakier configurations are eliminated.

Table 6.2: Mean absolute and RMS errors between predicted and reference value for the example dataset in %

	Q_4 in %	Q_{10} in %	ELA_4 in %	ELA_{10} in %
Mean abs. error OLS	21.23	13.51	20.51	12.77
Mean abs. error WLOC	6.57	5.14	6.49	5.03
RMS error OLS	28.03	18.69	27.20	17.74
RMS error WLOC	8.25	6.41	8.08	6.27

The above analysis for the example configuration was repeated for all 109 test configurations in the dataset. The results for all configurations are summarized in Table 6.3. In comparison to the example dataset in Table 6.2, the overall errors are smaller here. The reason for this is that over all 109 considered leak configurations, the differences between the predictions of WLOC and OLS are smaller than for the example dataset. Nevertheless, the differences between both fitting techniques are still significant: about a 41 % error reduction for 4 Pa results and 33 % for 10 Pa results. Roughly 91 % of all considered configurations show similar results where WLOC was superior in estimating the airflow rates and equivalent leakage areas at low pressures compared to OLS.

Table 6.3: Mean absolute and RMS errors between predicted and reference value for the whole dataset in %

	Q_4 in %	Q_{10} in %	ELA_4 in %	ELA_{10} in %
Mean abs. error OLS	13.48	9.40	13.17	9.00
Mean abs. error WLOC	8.05	6.32	7.93	6.18
RMS error OLS	17.76	12.20	17.31	11.66
RMS error WLOC	10.30	7.97	10.12	7.76

6.3 Summary

WLOC reduces the variances for pressure exponent n and flow coefficient C, typically by 32 and 22 %, respectively, compared to the OLS regression method, averaged over 7402 fan pressurization tests. Additionally, the results show a far better prediction (by about 40 % for Q_4 and ELA_4) of the airflow rate and equivalent leakage area at low pressures using the WLOC regression technique, particularly under the increasing influence of wind on the measurements and standards. In more than 90 % of all considered configurations, the WLOC was superior in estimating the airflow rates and equivalent leakage areas at low pressures compared to OLS. Therefore, the use of this analysis technique is encouraged and should be adopted in building measurements. One caveat is that each pressure station needs to record the uncertainty (variance or standards deviation) at each point in addition to the mean. Given modern test equipment and test automation, this should not be too much of a barrier.

In the following chapter, the applicability of the acoustic method introduced in Chapter 5 will be investigated and compared with the fan pressurization method using the WLOC regression in a real building.

7 Real Building Application

The goal of the measurements presented in the following chapter is to verify the laboratory results (see Chapter 5) in a real building environment. For this reason, several leaks are artificially created in a window frame, and the airflow rate through these leaks is measured at different pressure levels using the fan pressurization method. Additionally, air exchange rates without pressurization are determined with a tracer gas method. The results are again compared with acoustic measurement within the same experimental setup.

7.1 Methodology

7.1.1 Test Site and Investigated Leaks

The test site is a small office at ground level with a window façade (one wall) as part of the building envelope (DLR Cologne, Building 3e west wing orientation north). In this window façade, a single leak of six different sizes is artificially constructed and tested. A varying number of cable ties are wedged at the same place of one window frame to simulate a damaged window gasket and to create leaks in a reproducible setup. Six combinations using two sizes of cable ties are used to achieve this: a larger tie (top row of Fig. 7.1) with a width and thickness of 8.0 × 1.5 mm and a smaller one (bottom row of Fig. 7.1) with a width and thickness of 3.0 × 1.0 mm width and thickness, respectively. The ties are clamped onto a small piece of wood to ensure they remain in place during the measurements. Fig. 7.2 shows how the cable ties were inserted in the window frame. To measure the flow through the deliberate window leaks only, a solid wooden frame

---

Major parts of this chapter are reproduced from:

B. Kölsch, I. S. Walker, B. Schiricke, W. W. Delp, and B. Hoffschmidt, "Quantification of Air Leakage Paths: A Comparison of Airflow and Acoustic Measurements", *The International Journal of Ventilation*, 2021, DOI: `10.1080/14733315.2021.1966576` (dimensions: 1.55 m × 2.12 m × 0.15 m, see Fig. 7.3) fits precisely over the window containing the leaks. This frame is covered with an airtight foil (proclima-INTELLO polypropylene foil) and sealed (with proclima-TESCON VANA duct tape) to create a closed control volume around the window.

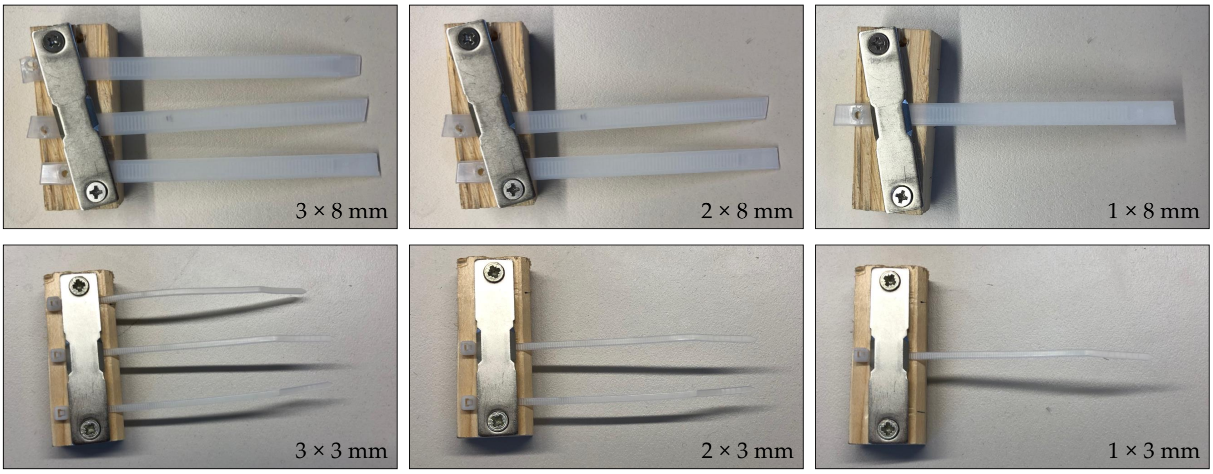

Figure 7.1: The two types of cable ties used to create reproducible artificial leaks in the window frame and the approximated cross-sectional areas of the leak in the window gasket. Top row: large cable ties with an 8 mm width, bottom row: small cable ties with a 3 mm width

Figure 7.2: Insertion of cable ties in the window frame

7.1.2 Pressure Difference and Airflow Measurements

A duct (diameter: 0.16 m, length: 2.42 m) with a controllable fan (ebm-papst - axial fan 6314/2TDHP) and a Venturi airflow meter (Electro mation-EMVMD 160) are connected to the frame (Fig. 7.3). Similar to the method described in Section 5.1.3, the pressure difference across the calibrated airflow meter is measured and converted to the airflow rate afterward.

A pressure tap is connected to the wooden frame to measure the static pressure inside the frame, and a second static pressure measurement is taken inside the room next to an open window outside the frame. This measurement position is chosen because the static pressure is expected to be similar to the pressure outside next to the leak, but the influence of wind on the pressure measurement is lower. From these two pressure measuring stations, the static pressure difference across the window is calculated simultaneously to the airflow measurements. Temperature measurements (in °C) are taken inside (T_{in}) and outside (T_{out}) the room, and corrections for the air density are applied to readings from the flow measurement system (Q) according to:

$$Q_{corr} = Q_{meas} \left(\frac{\rho_{in}}{\rho_{out}} \right) \tag{7.1}$$

Here, Q_{corr} is the corrected airflow. The inside and outside air densities $\rho_{in/out}$ are determined following the ASTM E779 standard [54]:

$$\rho_{in/out} = 1.2041 \left(1 - \frac{0.0065\,E}{293} \right)^{5.2553} \left(\frac{293}{T_{in/out} + 273} \right) \tag{7.2}$$

E is the elevation above sea level, which is 53 m for this test site. It should be noted that the inside and outside air densities are corrected to standard conditions at 20 °C ($\approx$ 293 K) for temperature and 1.2041 kg/m^3 for air density. The zero-flow pressure offset before and after each measurement is recorded, and their average is subtracted from the measured pressures.

7.1.3 Tracer Gas Measurements

In addition to the pressure difference and airflow measurements, tracer gas measurements using the concentration decay method with forming gas (5 % H_2 in N_2) are performed to measure air changes without pressurization through the considered window.

In the first step, the hydrogen is released from a gas pressure regulator into the sealed wooden frame with a manual valve. For these measurements, the duct containing the Venturi airflow meter is removed, and the remaining hole is sealed. No pressure is applied during the measurements. However, an influence of wind-induced pressure from outside on the window leaks is still possible.

Figure 7.3: Experimental setup for pressure difference and airflow measurements at an office building window

A hydrogen gas measurement device (Sewerin Ex-Tec GM4, electrochemical cell detector) is placed inside the wooden frame to monitor the concentration decay inside the control volume. This sensor works with a built-in electrochemical sensor and includes the data logger. The measurement range of this sensor for hydrogen is between 40 and 10 000 ppm with a resolution of 20 ppm. The preferred range of H_2 concentration in this application is between 100 and 1000 ppm. A fan is placed inside the wooden frame, providing air mixing inside the wooden frame.
Finally, the concentration decay is measured over a period of typically 10 min and a sampling interval of 5 s, which provides a sufficient data quality for evaluation of the air change rate according to Eq. (2.27).

7.1.4 Acoustic Measurements

The goal of this measurement setup is to determine the acoustic coherence, which was investigated in Chapter 5, in a real building application. For this reason, a pair of high and mid/low-frequency omnidirectional speakers are placed in the middle of the office room (see Fig. 7.4a). The high-frequency speaker (Avisoft - ultrasonic omnidirectional dynamic speaker vifa) has an even frequency range of 15 to 120 kHz, and the low-frequency dodecahedron speaker (Infra Q-Sources Qohm) has an even frequency range of 0.05 to 16 kHz. During the tests, it was recognized that this speaker is capable of emitting signals up to 40 kHz, even though not guaranteed by its manufacturer. The emitted signal is a broadband white noise, recorded with a sampling frequency of 192 kHz. Thus, according to the Nyquist–Shannon sampling theorem [157], frequencies up to 96 kHz can be analyzed. One microphone records the emitted signal inside the room next to the speakers (as a reference), and a second microphone is placed outside the window (see Fig. 7.4b). The microphones are the same as used in the laboratory measurements in Chapter 4.

(a) Omnidirectional speaker setup **(b)** Microphone outside the building

Figure 7.4: Measurement setup of a high-frequency (top), a mid/low-frequency (bottom) omnidirectional dodecahedron speaker, and microphone outside the office building

7.2 Results and Discussion

7.2.1 Pressure Difference and Airflow Measurements

The results of all measurements for all six different willfully constructed leaks on the window with the wooden frame at multiple pressure levels are shown in Fig. 7.5. The three blue lines in the upper part of the plot indicate the fit according to the power-law (cf. Eq. (2.16)) for the larger cable ties with a width of 8 mm. In the lower part of the plot, the three green lines show the measurement fit for the smaller cable ties with a 3 mm width (see Section 7.1.1). Here, a clear distinction between all six measurements and leak configurations is possible. However, there is significantly higher uncertainty in the flow measurements for the three smallest leak configurations with a smaller airflow (in green). Again, the black dotted vertical lines indicate the differential pressure levels at 4, 10 and 50 Pa, chosen for the subsequent analysis. As for the laboratory measurements (in Chapter 5), the resulting airflow rates at these pressure levels are determined for the intersection point with the fitted curve. The airflow rates without any deliberate leak through the window are investigated as well, but no airflow was measurable, indicating a tight window.

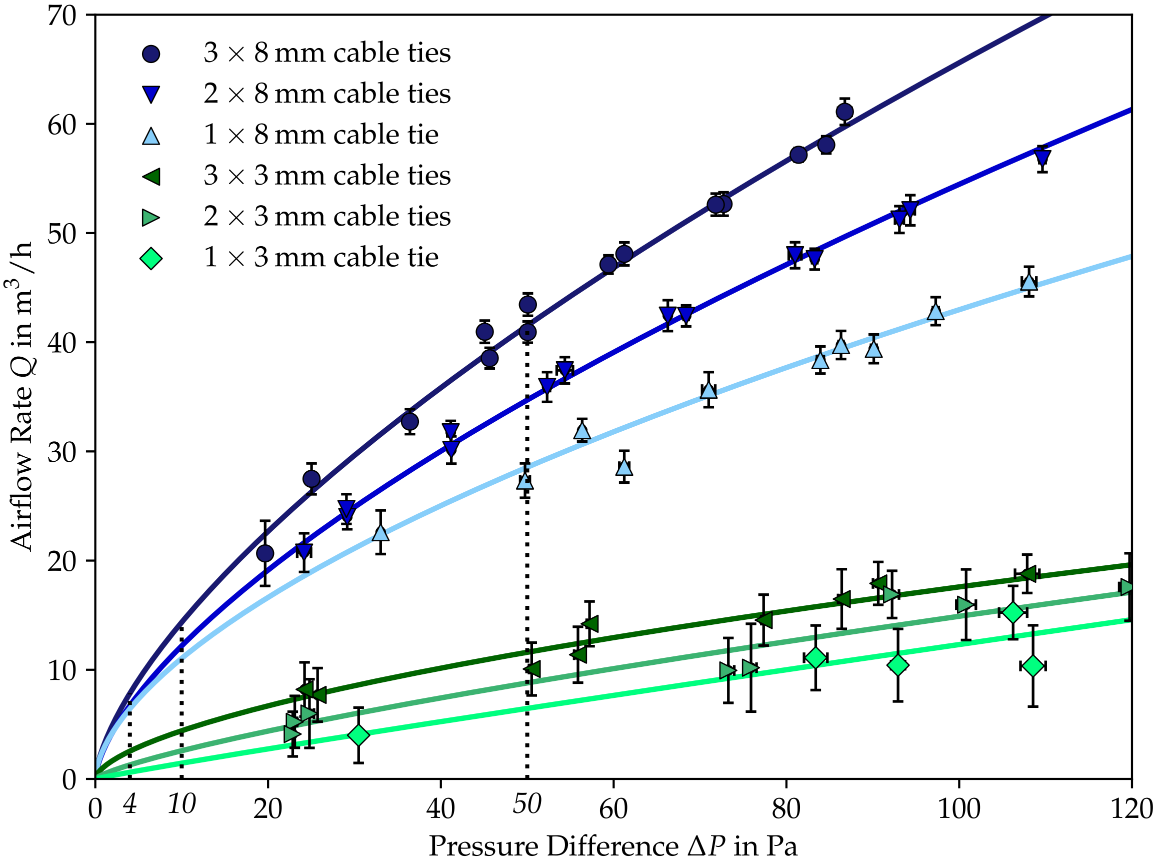

Figure 7.5: Airflow-pressure measurements of constructed leaks with cable ties wedged in the window frame

7.2.2 Air Change Rate Measurements with Tracer Gas Method

Air change rate measurements are performed with the tracer gas method for the same six different constructed leak configurations. Fig. 7.6 shows the concentration measurement of the largest leak size (3 × 8 mm) as an example. Fig. 7.6a visualizes the H_2 concentration decay over a period of 10.7 min. In Fig. 7.6b, this logarithmic concentration decay is illustrated. The slope is derived from the slope of the linear least squares fit (dashed red line) to this measured dataset.

Fig. 7.7 shows the mean air changes per hour (ACH) on the left axis for all six investigated leak configurations. Three measurements are performed for each of the configurations from which the mean value and standard deviation are calculated. The largest leak (3 × 8 mm) shows the highest measurement error, which results from an outlier of one of this three considered measurements.

A decrease in the air change rate is clearly visible with a decreasing constructed slit size. The airflow at natural pressure difference Q is presented on the right axis, which is calculated from the air change rate and the frame volume V_f according to Eq. (2.7).

7.2.3 Acoustic Measurements

The coherence functions of both recorded acoustic signals from the microphones inside and outside the office room are calculated. Similar to the laboratory testing, measurements are made with the window closed and no artificial leaks to measure the sound transmission through the window and façade to be subtracted from the leak coherence measurements. Fig. 7.8 shows the coherence function for the window without any artificial leak as a function of the frequency. The thin blue line is the calculated function, and the thicker black line is a calculated moving average value for better visualization with less noise. In this measurement, notably lower frequencies ($< 10\,\text{kHz}$) appear to be coherent between both signals. At higher ultrasonic frequencies ($> 20\,\text{kHz}$), the coherence of inside and outside measurement is close to zero.

These results show how signal energy through the window is transmitted, even though the window is airtight, and this measured coherence will be subtracted from measurements with added leaks.

Fig. 7.9 shows the measured coherence for the deliberately added leaks without the no leak results in Fig. 7.8 subtracted. The thin lines (in red) represent the calculated coherence values, and the bold black line the moving averages of the same function.

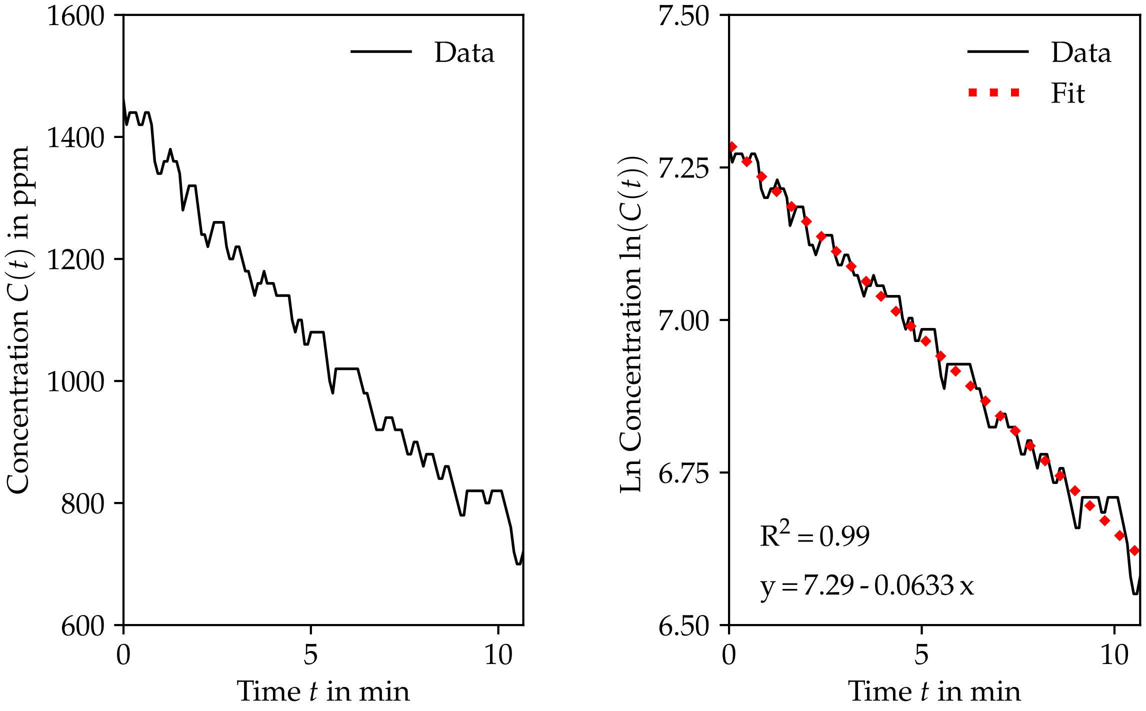

(a) Measured concentration decay **(b)** Logarithmic concentration decay

Figure 7.6: Example of H_2 concentration decay measurement with three large cable ties (3×8 mm) wedged in the window gasket

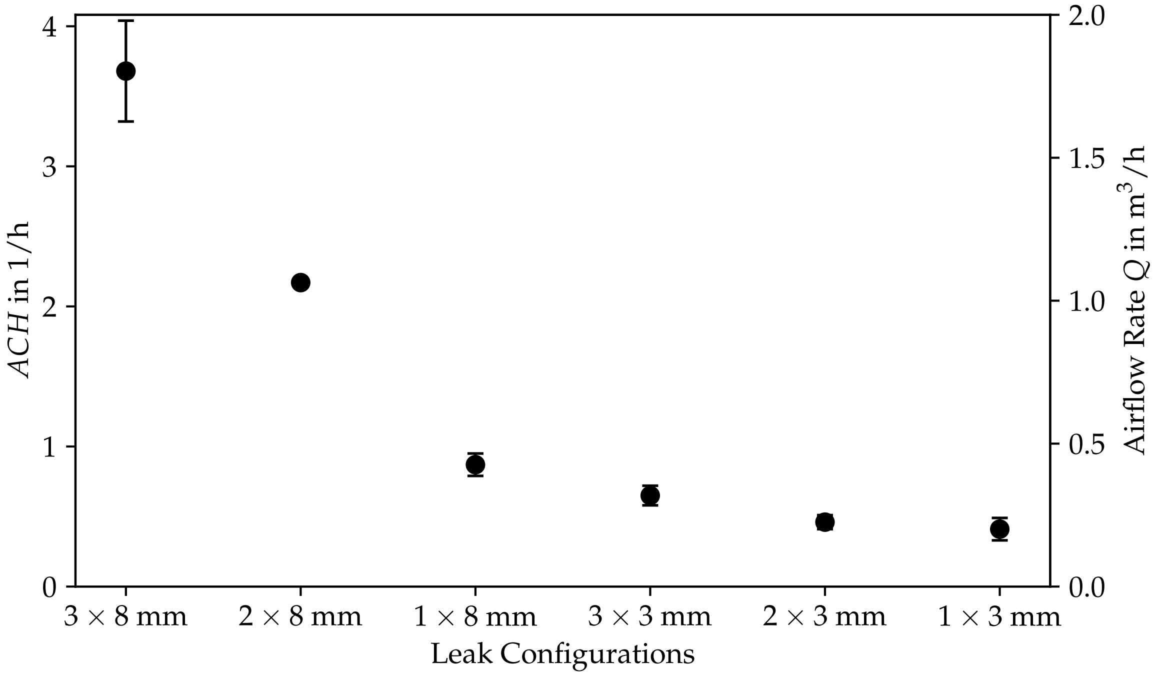

Figure 7.7: Air change rates (left axis) and air supply rates Q (right axis) for the six investigated leak configurations on the office window with constructed leaks

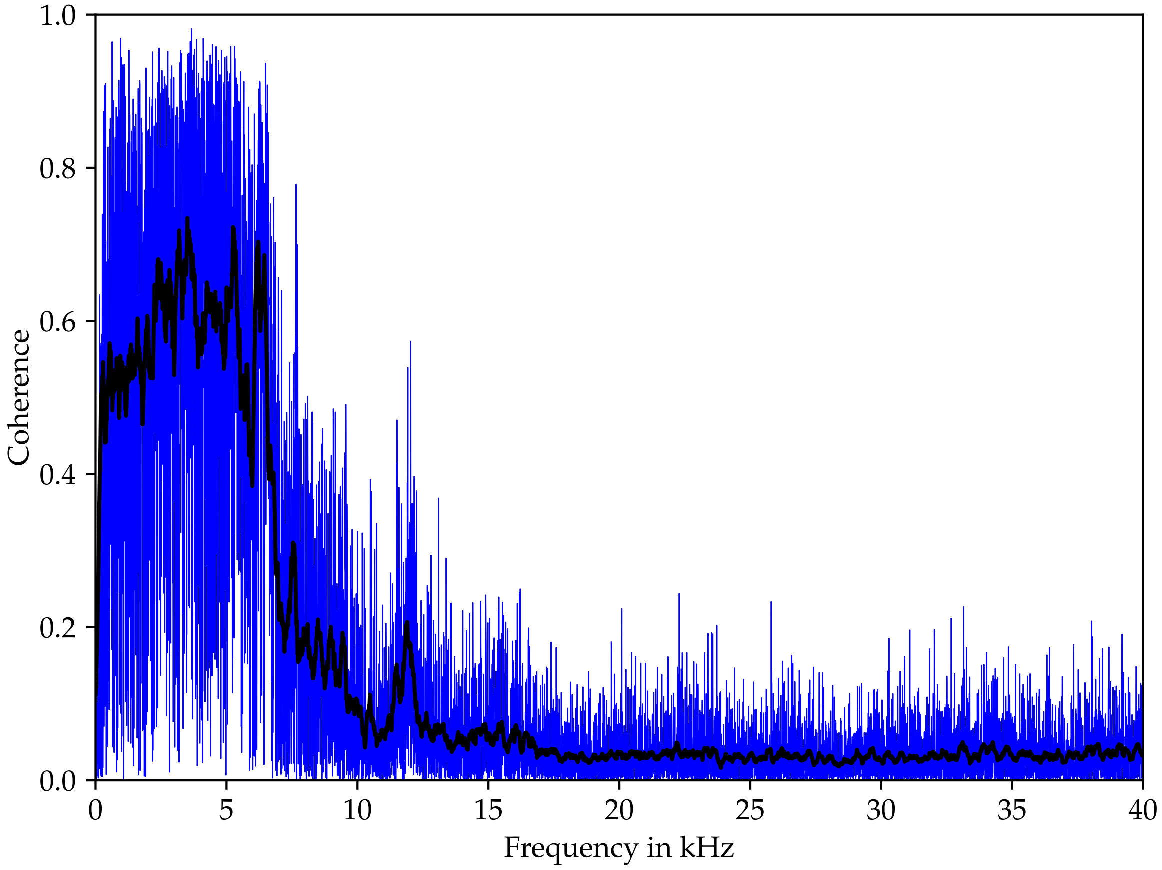

Figure 7.8: Coherence of building measurement without any constructed leak, with the black line indicating the moving average

These measurements exhibit a clear contrast compared to the measurements without added leaks (cf. Fig. 7.8). In addition to the already transmitted frequencies (< 10 kHz) from the window itself, responses at higher frequencies can be observed that are caused by openings in the window.

The largest opening, where three large cable ties have been wedged in the window frame (3×8 mm), shows a relatively strong coherence (sometimes more than 0.6) for frequencies up to 35 kHz. As well as the change in frequency response, the magnitude of the coherence function decreases with decreasing opening size. For smaller openings, specific frequencies appear to dominate. For the four smaller leaks, the response below 10 kHz is very close to that for the window with no leaks.

Next, the coherent frequencies from the test with no leaks, as shown in Fig. 7.8, are subtracted from the measurements containing openings to exhibit sound transmission at frequencies only affected by the openings. These results are shown in Fig. 7.10. The frequencies can be interpreted as frequencies of dominant sound transmission depending on the size of the specific leaks. These results show some of the same

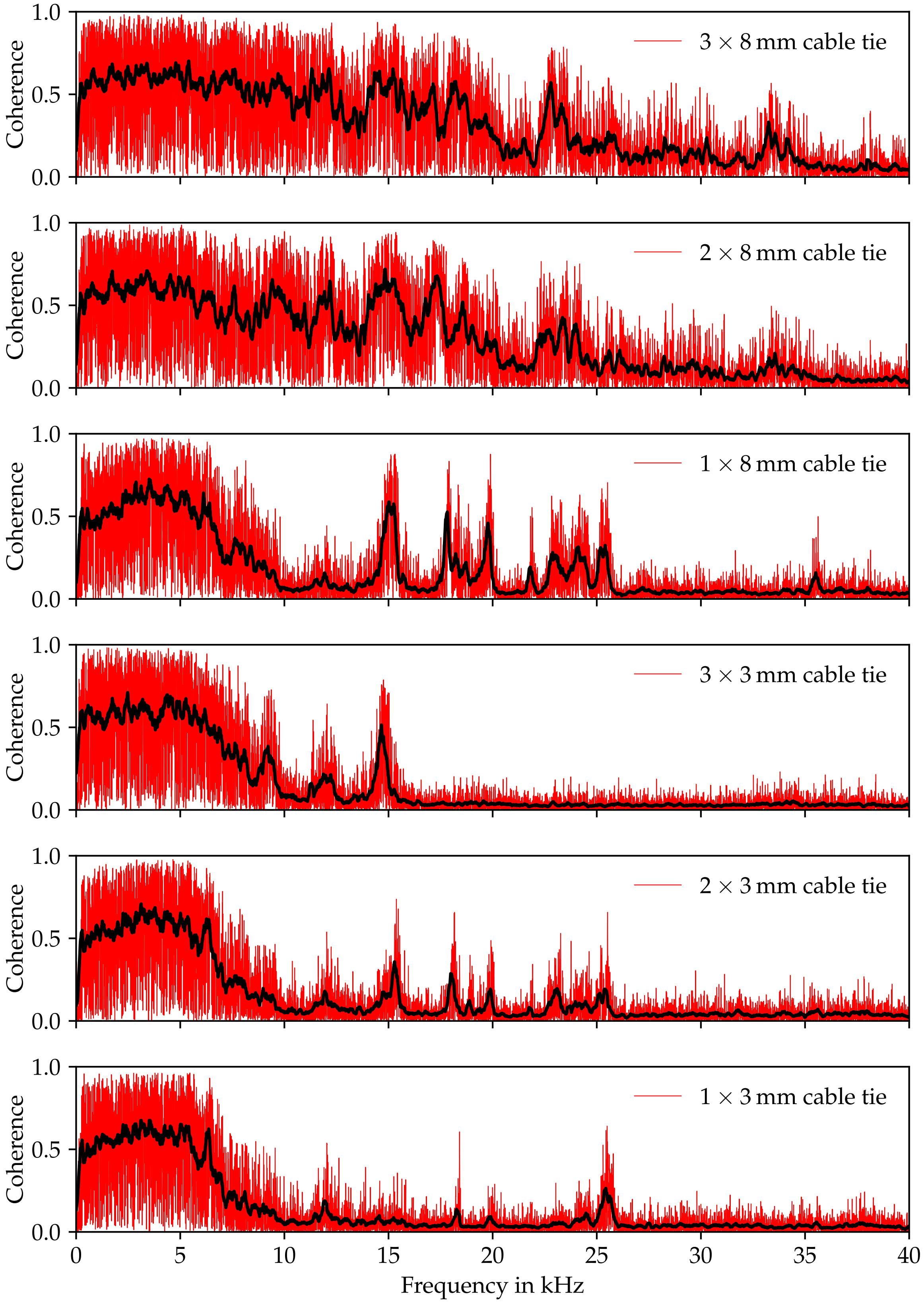

Figure 7.9: Coherence of building measurements with constructed window leaks of 8 and 3 mm cable tie width, with the black line indicating the moving average

trends as the laboratory tests: an increasing magnitude of coherence difference with increased leak size for the 8 mm tests. However, the results using the 3 mm cable ties are less clear. With most of the response below 10 kHz removed, characteristic frequency spikes are observed above that frequency. A spike at about 15 kHz is observed for the 1 × 8 mm, 3 × 3 mm and 2 × 3 mm cases. 1 × 8 mm and 2 × 3 mm cases also show similar responses at higher frequencies between 15 and 25 kHz. These are absent from the 3 × 3 mm case. Finally, the 1 × 3 mm case does not show the same sub-25 kHz responses of the other cases and has a strong response just above 25 kHz. While these results do not show any particular characteristic trends, they indicate that spectral analyses may help characterize other aspects of leaks beyond their scalar size, such as determining the pressure exponent n_C.

In the last step, the mean difference of measured leak coherence and the reference measurement over the chosen frequency range is defined as a measure of the leak size and plotted against the airflow rates at 50 (red), 10 (black), and 43 Pa (green) pressure difference. This comparison between acoustic and airflow metrics is shown in Fig. 7.11. The airflow values are taken from the measurements shown in Fig. 7.5.

The lines in Fig. 7.11 are the relationships introduced in Eq. (5.3), with optimized K and n_C values for the airflow rates at the respective pressure differences (Q_{50}, Q_{10}, and Q_4) and the mean differences of the calculated coherence within this considered frequency range. Similar to the laboratory experiments, these correlations between airflow and acoustic parameters show a general trend that with increasing leak size, the mean difference of the coherence measurements increases as well. These findings are similar to the laboratory measurements described in Chapter 5. Therefore, this measurement procedure has the potential to measure single leaks.

The three dots above each line (Q_{50}, Q_{10}, and Q_4) correspond to the leaks with the larger cable tie (8.0 mm width), and the three dots below each line correspond to the leaks with the smaller ones (3.0 mm width). Similar to changes in airflow path and leak configuration in the earlier laboratory measurements, the substantial increase in airflow rate between these two types of cable ties, which is visible in Fig. 7.5 between the group of green and blue lines, is not directly represented by the acoustic measurements. The increase in the mean coherence difference between these groups of leaks is much smaller. This would lead to an overestimation of the leak size for the small leak configurations and an underestimation of the leak size for larger leaks if one would only consider the acoustic measurements. Nevertheless, a prediction of an order of magnitude might be possible. As with the laboratory testing, the different window leaks had different spectral properties (as shown in Fig. 7.10), and this shows some potential for future spectral analyses to improve the relationship between acoustic coherence measurements

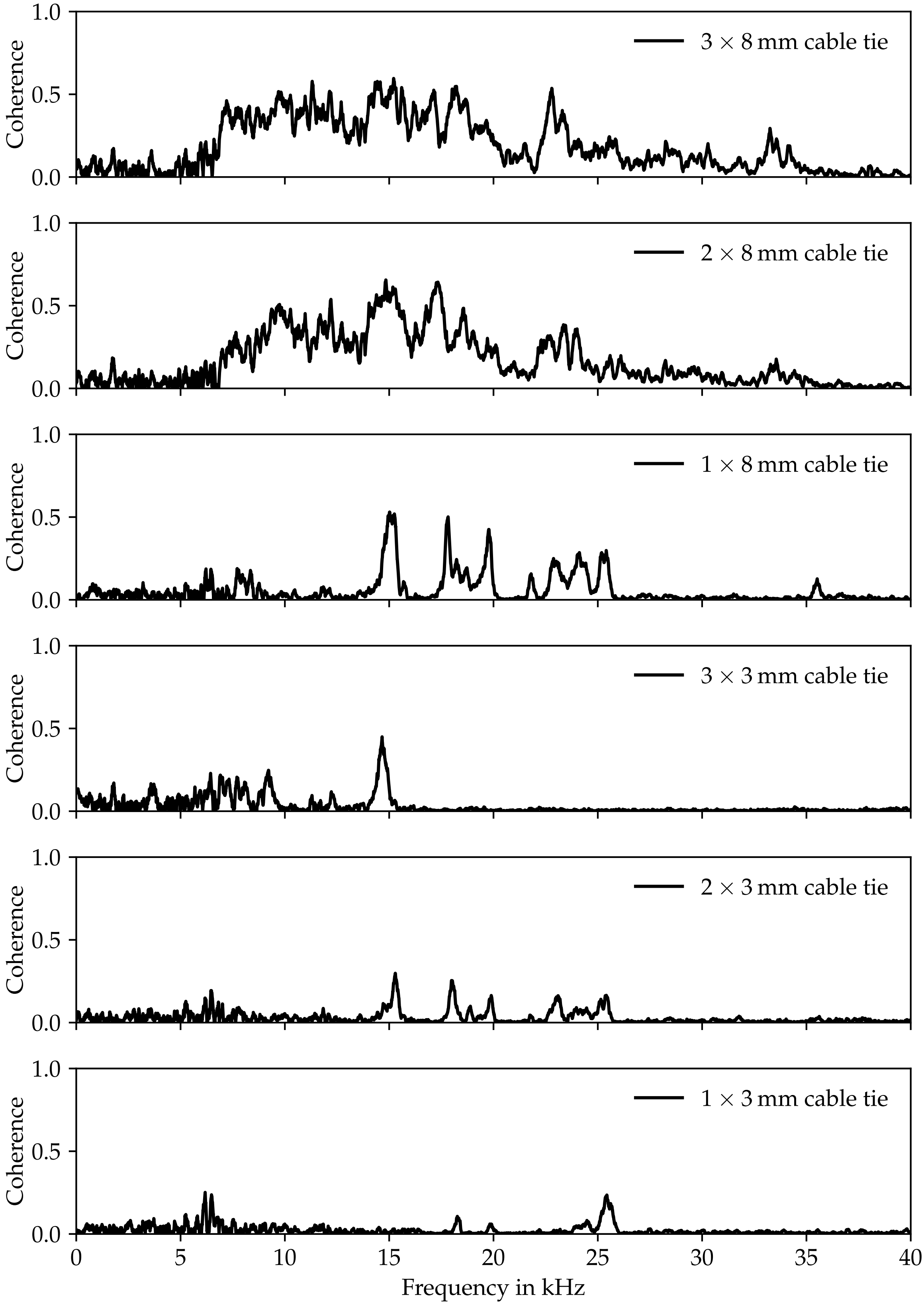

Figure 7.10: Moving average of difference between the coherence of building measurements with constructed window leaks of 8 and 3 mm cable tie width and tight window

and predicted air leakage.

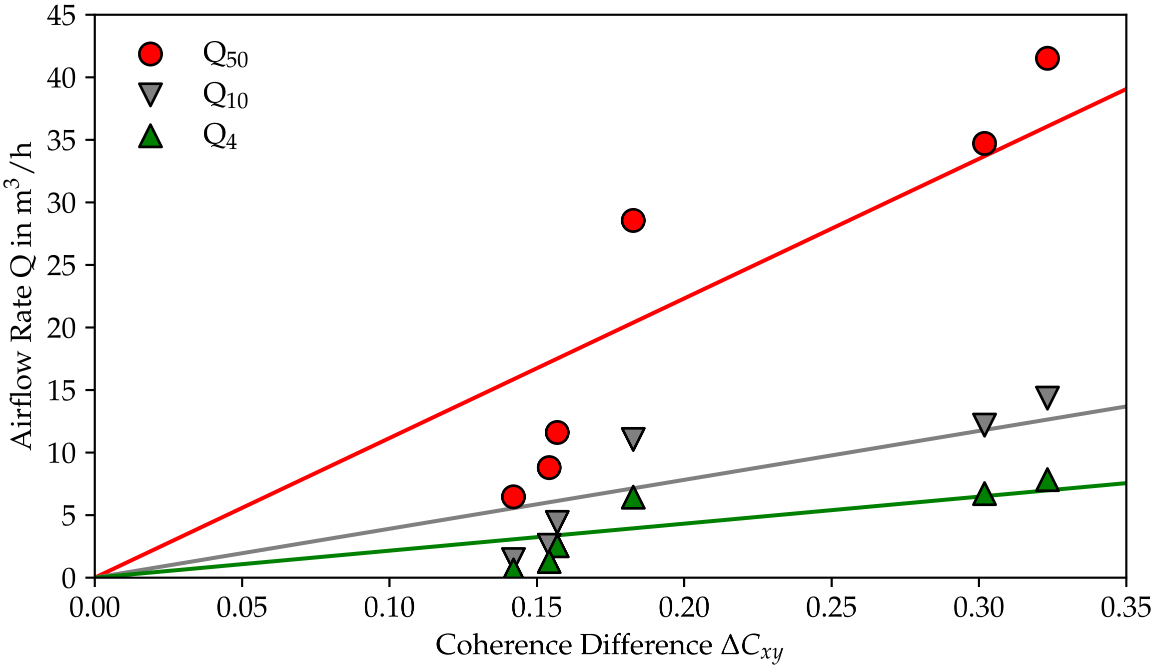

Figure 7.11: Correlation of flow rate and mean coherence difference for constructed leaks in window frame

The fitted K and n_C values for the three investigated pressure differences are finally illustrated in Fig. 7.12 for the building tests. As for the laboratory tests (in Chapter 5), these fitted coefficients for n_C are close to 1, and the fitted coefficients for K indicate a non-linear relationship between this coefficient and the pressure difference. The coefficients K at 50 and 10 Pa are in the same magnitude as for the laboratory tests. However, the K value at 4 Pa is a bit higher. The uncertainties in the flow measurements are, particularly at low pressures and flows, higher for the building measurements than the laboratory measurement, which could explain this deviation.

In addition to the pressurization measurements, acoustic measurements are compared to tracer gas measurements under natural pressure differences. For this reason, the mean coherence differences, which were already compared with the airflow measurements in Fig. 7.11, are plotted against the air changes per hour (ACH) and the derived flow rates in Fig. 7.13. Again, the correlation shows the trend that with increasing mean coherence differences, the airflow rate increases as well. Except for the measurement with the largest investigated leak (3 × 3 mm cable tie), the relationship between airflow rate and mean coherence difference seems to be linear again and, therefore, agrees with the findings from the fan pressurization measurements. Figs. 7.7 and 7.13 show that the

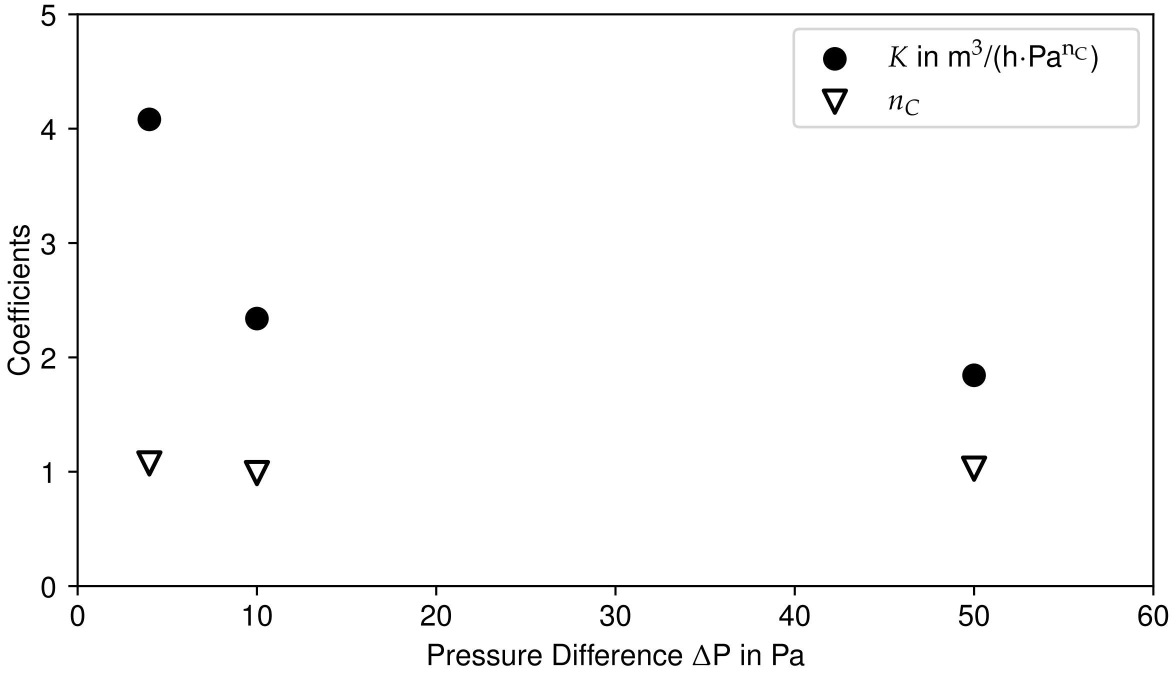

Figure 7.12: Fit of coefficient K and exponent n_C for the investigated pressure differences in the building tests

measurement uncertainty for this measurement at the largest leak is much higher than for the other smaller leaks, which could be an explanation for this outlier.

7.3 Summary

In this chapter, the acoustic method, previously introduced in a laboratory environment, is applied in a real building application. Fan pressurization and acoustic measurements are again performed within the same experimental setups. Reproducible leaks were created in a building enclosure by clamping six different combinations of cable ties into a window gasket. A combination of omnidirectional speakers was placed inside an office and the coherence was calculated with measurements inside the building and next to the leak outside the building.

The linear trend of increasing mean coherence difference with an increasing leakage size, which is already observed in the laboratory test apparatus, is again found in this real building application. A prediction of an order of magnitude with the acoustic approach might be possible. A more sophisticated analysis of the frequency spectra of the different leaks can be a promising next step. Additionally, tracer gas measurements were performed within this setup, indicating a similar linear trend under natural

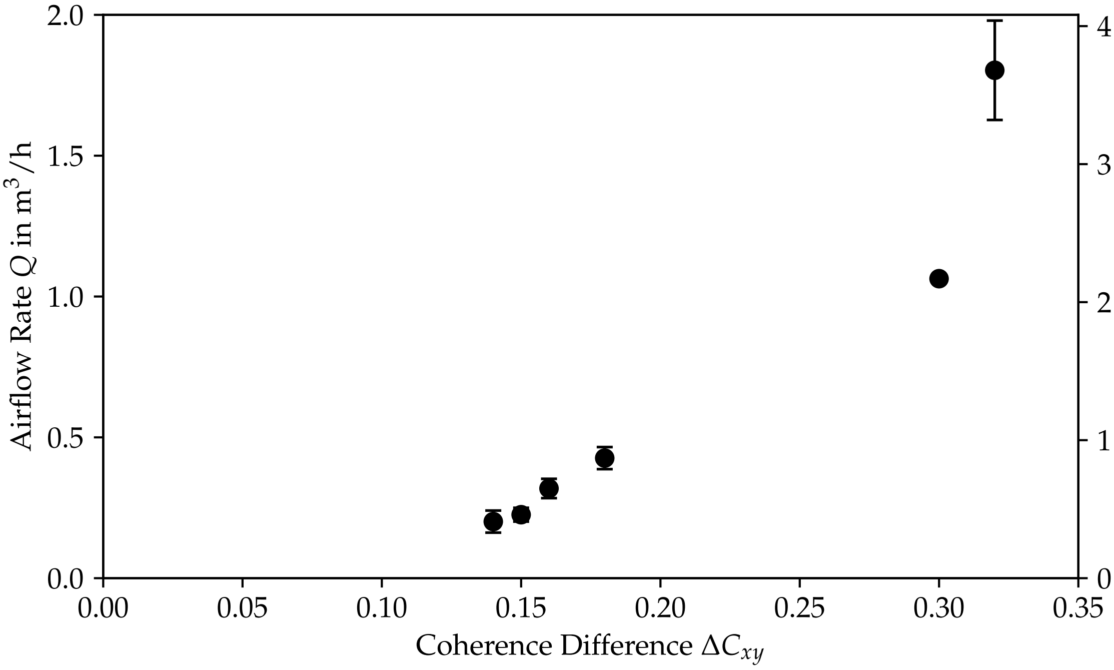

Figure 7.13: Correlation of flow rate under natural conditions (left axis), ACH (right axis), and mean coherence difference for tracer gas measurements in the window frame

pressure conditions.

A limitation of this measurement concept is the need for a reference measurement at an airtight part of the wall in addition to the measurement at a leak. Therefore, a fundamental distinction between airtight and non-airtight parts of the building is crucial prior to a possible quantification of single leaks. The following chapter introduced a method using microphone arrays, which enables the detection of leaks in building envelopes using acoustics.

8 Acoustic Detection and Localization of Leaks in Building Envelopes

In addition to the quantification of leaks in the building envelope, it is crucial to identify leak locations. The knowledge of leak locations enables prioritizing sealing of more substantial leaks to reduce air leakage and associated energy loss in new and existing buildings. The acoustic methods (and other: fan pressurization, tracer gas) applied in the previous chapters are not able to discriminate more than one leak location in building envelopes. In this chapter, an acoustic beamforming method is proposed using a microphone ring array to detect sound sources and visualize them. The objective of this investigation is to identify the potential of this technique for an application to building envelopes. The results shown in this chapter shall demonstrate if small openings in a building enclosure can be localized using a microphone array by detecting the transmitted sound through them with the corresponding sophisticated signal analysis.

8.1 Fundamentals

The physical background of sound source localization is already realized by humans and animals to estimate the direction and distance of surrounding sound sources. The interaural time difference (ITD) of sound in combination with the interaural level differences (ILD) between two ears enable humans to locate and differentiate different sound sources [212]. The theoretical knowledge for transforming this phenomenon into

---

Major parts of this chapter are reproduced from:

B. Kölsch, B. Schiricke, E. Lüpfert, and B. Hoffschmidt, "Detection of Air Leakage in Building Envelopes using Microphone Arrays", in *Proceedings of the 41st AIVC - ASHRAE IAQ 2020 joint conference*, 2022 a technical application using microphone arrays is known for decades (e.g., Ref. [213]). However, only within the last twenty years, the necessary computing power got available to process multiple microphone signals simultaneously, making this principle usable for practical applications.

There are a few different microphones array measurement techniques for the identification or localization of sound sources. The most common one is the beamforming technique, besides others such as the acoustic holography [214] and the inverse boundary element method [215]. Today, these techniques of sound source localization are commonly used in the automotive, railroad, or aerospace sector to detect significant noise and sound sources of vehicles and reduce them. In addition to work done by Raman et al. [144, 145] on buildings, this thesis investigates much smaller leaks and higher frequencies.

Generally, beamforming is a technique of signal processing that enables an array of microphones to separate sound sources from different directions [216]. In this work, these microphones are arranged as a ring on a flat surface, and a digital camera is placed in the center of the array that delivers an additional visible image of the object to be examined.

The measuring principle is based on the fact that the microphone array focuses on different measuring points on the measured object. During the analysis, the time signals from the individual microphones of the array are superimposed with a time delay which equals the time the sound wave takes from the measured focus point to the microphone. These time-corrected signals from all microphones are summed, which results in a time signal assigned to the respective focus point. If the origin of a noise component is found at that point, the result is a positive interference for all microphone signals after the corresponding time shift and, therefore, a maximum power output. However, if the viewing angle does not match the sound waves' angle of incidence, partial cancelation is the result since their signals are no longer fully time-corrected and sometimes overlap destructively. Therefore, noise sources outside the focus direction of the acoustic camera are reduced.

The method results in what is called an "acoustic camera" because the result of a scan process over a range of viewing angles produces an image of the most intensive constructive interferences of the acoustic waves. The advantage for a wide range of applications is the visual result, which is typically overlaid on a visible image of the same scene.

8.1.1 Delay-and-Sum Beamforming

The most straightforward calculation is the delay-and-sum beamforming in the time domain. Here, every time function at each current focus point $\vec{x}$ can be reconstructed as [217]:

$$\hat{f}(\vec{x},t) = \frac{1}{M}\sum_{i=1}^{M} w_i f_i(t - \Delta\tau_i) \tag{8.1}$$

M is the number of microphones in the chosen array, and w_i refers to an optional weighting factor that is applied before the spectral transformation of the time signal to reduce the influence of leakage and smearing effects. However, for a standard ring array used in this measurement, this weighting factor is set to 1. Further, $f_i(t)$ are the time signals of the sound pressure recorded at each individual microphone, and $\Delta\tau_i$ are the time delays for each microphone signal:

$$\Delta\tau_i = |\tau_i - \min(\tau_i)| \tag{8.2}$$

These time delays $\Delta\tau_i$ are calculated by subtracting the minimum run times over all microphones between the sound source and the microphone from their individual run times τ_i. For a calculation of these time delays, the distance between the microphone array and focus plane is required. A wrong distance leads to a focusing error of the system. This erroneous focus reduces the accuracy of the evaluation of the calculated sound pressure levels, especially for non-stationary signals. The magnitude of this error depends on the frequency and chosen array geometry.
The run times are calculated from the speed of sound c and the geometrical distance $\vec{r}_i$ between the calculated focus point $\vec{x}$ and the spatial position of the i-th microphone $\vec{x}_{m,i}$:

$$\tau_i = \frac{|\vec{r}_i|}{c} \tag{8.3}$$

$$\vec{r}_i = |\vec{x}_{m,i} - \vec{x}| \tag{8.4}$$

The effective sound pressure $\hat{p}_{rms}(\vec{x})$ at the calculated focus point can finally be calculated as:

$$\hat{p}_{rms}(\vec{x}) \approx \hat{p}_{rms}(\vec{x},n) = \sqrt{\frac{1}{n}\sum_{k=0}^{n-1} \hat{f}^2(\vec{x},t_k)} \tag{8.5}$$

In Eq. (8.5), n is the total number of corresponding discrete time samples and t_k the time value at the sample index k. This fundamental principle of delay-and-sum calculation is illustrated in Fig. 8.1 for a simplified array of four microphones.

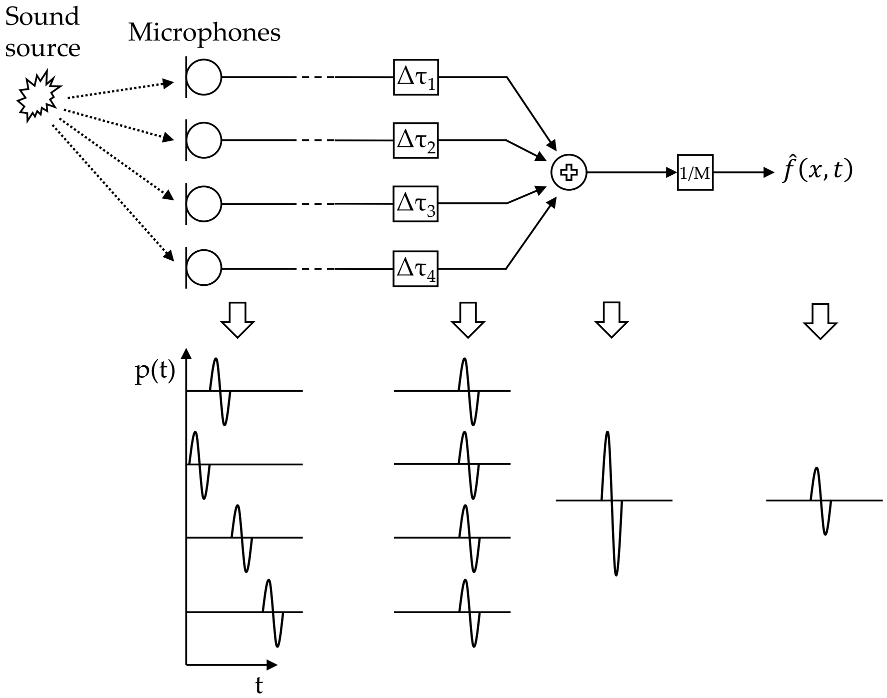

Figure 8.1: Basic principle of delay-and-sum calculation in the time domain with a simplified microphone array, based on [217]

During the signal analysis, the focus point is scanned on a defined grid. For each focus point, there are individual sound pressure values from the microphone array signals that can be assigned to the pixels of the optical camera image. The sound sources can now be visualized by superimposing acoustic values and the optical camera image.

The possible frequency range to be examined depends on the following factors: a lower cut-off frequency is limited by the size of the array; the larger the array, the lower its cut-off frequency. The upper cut-off frequency, however, is determined by the signal sampling frequency f_s and the distances between the microphones. If the distance between the microphones is larger than half of the analyzed wavelength λ, sound sources might not be located correctly.

The delay-and-sum beamforming can be performed in the frequency domain as well. For more information, see Ref. [217].

8.1.2 Microphone Array Sensitivity

The degree to which other sound sources outside the focus direction are suppressed depends on the chosen array geometry and size. This effect can be evaluated by the beam pattern of an array. A beam pattern plot evaluates the magnitude of an array output as a function of the incoming viewing angle of sound waves with regard to the focus direction.

The array sensitivity is often characterized by a single frequency wave from an arbitrary incident angle [218]. According to Teutsch [219], the pressure function of a three-dimensional single frequency plane wave from a point source recorded by a single sensor of the array is a solution of Eq. (3.1) and can be expressed as:

$$p_m(t) = e^{i(2\pi f - \vec{k}\vec{x}_m)} \tag{8.6}$$

p_m is the plane wave signal of one sensor and differs between the microphones with different time delays. In this equation, $\vec{x}_m$ is the position of the microphone, and $\vec{k}$ is the wavenumber vector of the incoming plane wave, with $k = \|\vec{k}\| = 2\pi f / c$. $\vec{k}$ is with spherical coordinates defined as:

$$\vec{k} = k \begin{bmatrix} \sin(\theta)\cos(\phi) \\ \sin(\theta)\sin(\phi) \\ \cos(\theta) \end{bmatrix} \tag{8.7}$$

The wavenumber vector gives the direction and magnitude of the arriving plane wave. In this spherical coordinate system, θ is the polar angle, and ϕ is the azimuth angle, which is shown in Fig. 8.2.

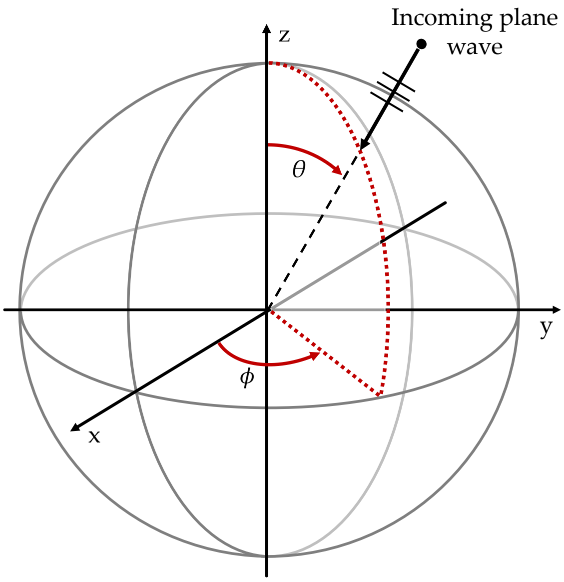

Figure 8.2: Definition of the spherical coordinate system

The beam patterns of an array depend on the number M and position $\vec{x}_m$ of microphones within the array the frequency f and can be calculated using the following equation [218, 219]:

$$W(\vec{k}) = \sum_{m=0}^{M-1} e^{i(\vec{k}\vec{x}_m)} \tag{8.8}$$

8.2 Methodology

8.2.1 Measurement Equipment and Experimental Setup

In the following experiments, a microphone ring array with 48 equally spaced microphones and a diameter of 0.75 m (GFaI tech - ACPro 48) was placed outside the office building to examine a window façade. The window façade was the same as described in Chapter 7. The ring array selected in this work has a lower sensitivity regarding the accuracy of the focal distance compared to other array geometries [220]. The array remained stationary during the measurements, and the focal distance between the microphone array and object was measured with a measuring tape.

The recommended frequency range of this array lies between 164 Hz and 20 kHz. According to the manufacturer, if the sound source localization is more important than the absolute value of the sound pressure level, measurements up to 60 kHz are feasible. In the center of the array, a video camera (Intel RealSense Depth Camera D435) is located to record an optical image (1920 × 1080 pixels) of the outer building envelope. The measurement setup of the array in front of the investigated window is displayed in Fig. 8.3. A relevant part of the setup is a pair of speakers (same configuration as described in Section 7.1.4), which was placed inside the building in the middle of the office (Fig. 7.4a). The sound waves produced by the speaker system penetrate through the leaks in the façade in order to be detected as individual sound sources by the acoustic camera system in its scanning procedure. A computer-generated broadband white noise was emitted at a level of 90 dB over a duration of 6 s via the D/A converter described in Chapter 4. One of the previously described ultrasonic microphones (Chapter 4) was placed inside the office room next to the speakers (distance between speaker and microphone: 0.6 m) to record the emitted sound inside the building as a reference signal for subsequent analysis. The data recorder (mcdRec Data Recorder to record up to 168 time-synchronized analog channels) recorded all microphone signals with a sampling frequency f_s of 192 kHz and digitized with 32-bit. The calculation of beamforming took place within the software NoiseImage (GFaI tech [221]).

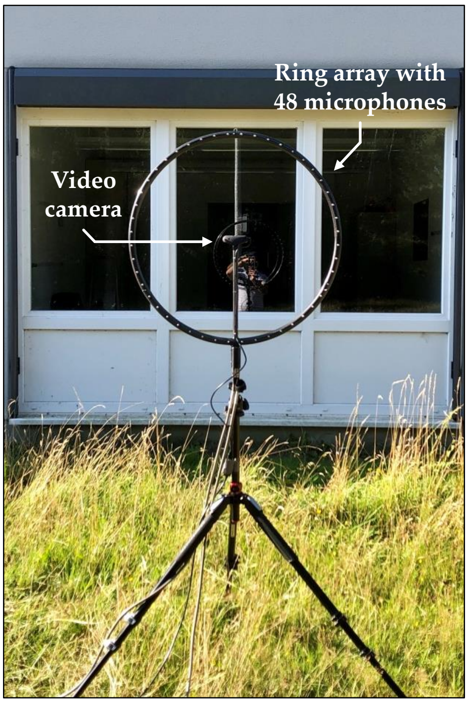

Figure 8.3: Setup with the microphone ring array and video camera in front of the building façade

8.2.2 Array Directivity

Directivity beam patterns of this two-dimensional ring array are illustrated for three frequencies (1250, 6300 and 12 500 Hz) in Figs. 8.4 to 8.6. These three frequencies illustrate the differences in the directivity for the chosen array at a low, mid, and high frequency. For this modeling, it is assumed that microphones are point-like and have individually perfect spherical directivity. The calculation of the beam patterns and visualization of all acoustic images was enabled in Python.

Figs. 8.4a, 8.5a and 8.6a show the directivity as a function of the two viewing angles θ and ϕ (see Section 8.1.2). The cross-section is displayed in Figs. 8.4b, 8.5b and 8.6b. The main lobe in the center corresponds to the array's focus direction. The side lobes do not correspond to the focus direction. The figures show to what extent sound sources outside the focus direction are reduced. The array's spatial resolution, and therefore the ability to separate sound sources, is determined by the width of the main lobe [222]. These calculations for this array show that the resolution increases with increasing frequency. The ratio between main and side lobes determines the contrast or dynamic range. These side lobes should be as low as possible. In order to take advantage of the properties at different frequencies, broadband noise is applied for these measurements.

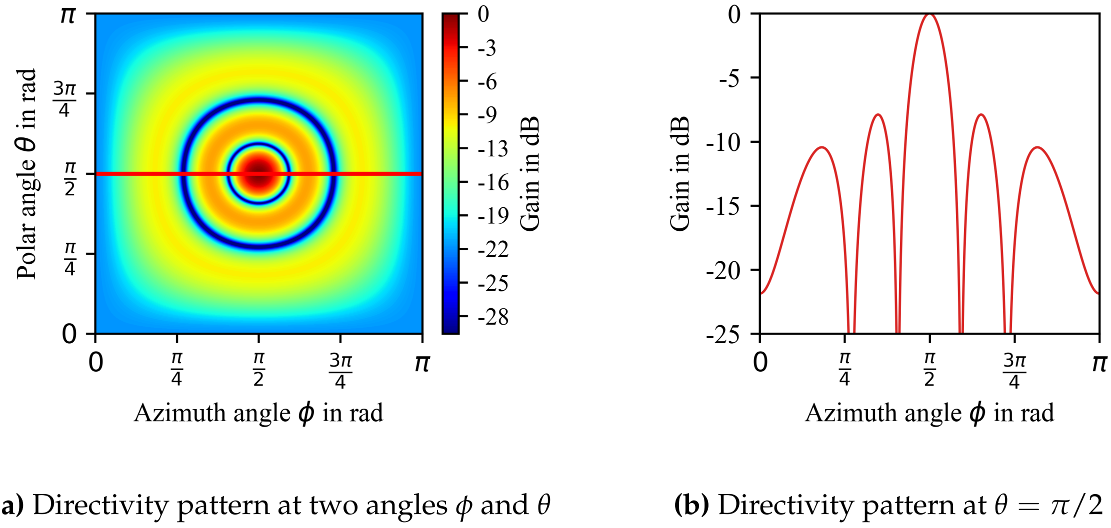

(a) Directivity pattern at two angles ϕ and θ **(b)** Directivity pattern at $\theta = \pi/2$

Figure 8.4: Modeled sensitivity of the used microphone ring array at 1250 Hz

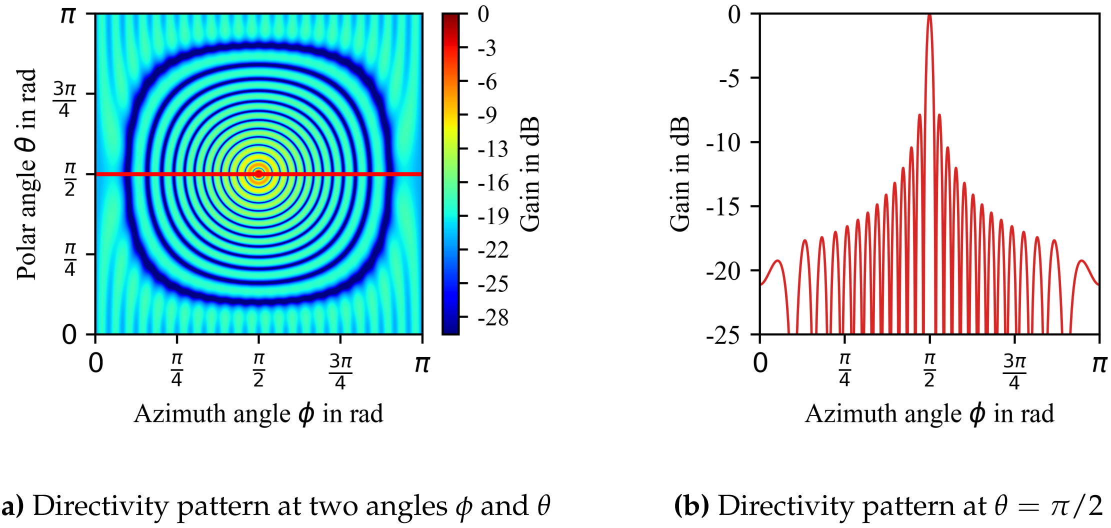

(a) Directivity pattern at two angles ϕ and θ **(b)** Directivity pattern at $\theta = \pi/2$

Figure 8.5: Modeled sensitivity of the used microphone ring array at 6300 Hz

8.2.3 Testing Procedure

As the sound source was placed inside the building and the microphones were placed outside, other disturbing sound sources (traffic, construction works, planes) are contained in the recorded signals, which is a significant difference to measurements under laboratory conditions. This may mask the intentional sound sources from the building leaks. The building test site, already described in Section 8.2.1, is located next to a street, a large construction site, and in the approach flight path of a large airport. Therefore, numerous external sound sources can potentially disturb acoustic measurements outside.

In order to assess the impact of disturbing and unwanted sound sources in relation to

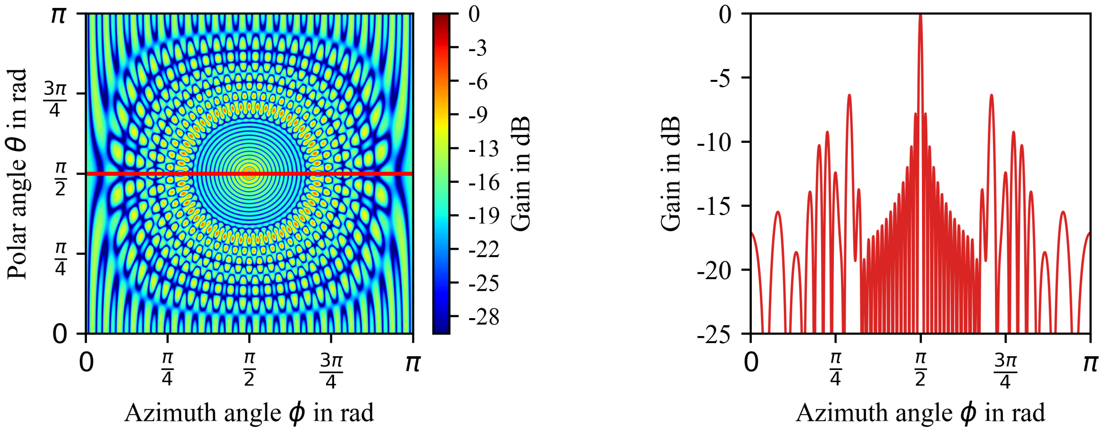

(a) Directivity pattern at two angles ϕ and θ

(b) Directivity pattern at $\theta = \pi/2$

Figure 8.6: Modeled sensitivity of the used microphone ring array at 12 500 Hz

the acoustic signal generated inside the building, first measurements are conducted with a tilted window. Producing a much larger opening and associating signal level than the small leaks described in the final setup makes localization using a microphone array much easier with the presence of unwanted noise at the test site. For these measurements, the microphone array was located at a distance of 3.7 m in front of the window façade.

Additionally, acoustic measurements were performed for the six different artificial constructed leaks using various combinations of cable ties (same as in Chapter 7) with this microphone array. To improve the spatial resolution and the potential visibility of these leaks, the distance between the window façade and microphone array for these experiments was decreased to 2.3 m.

8.3 Results and Discussion

8.3.1 External Sound Source Reduction

The following figures show the recorded spectra and the analyzed frequency bands as gray areas at the top. This spectrum is the mean of all 48 recorded microphone signals. The images below show the camera image of the examined window façade with the superimposed results of the beamforming analysis of the microphone signals recorded from the white noise emitted inside the building. Each pixel of the visible image is

a focus point for the acoustic analysis where an effective sound pressure level (see Eq. (3.37)) can be assigned. The pictures in Fig. 8.7 represent the measurement with a tilted window (left window). They show the acoustic images for the localization of significant sound sources within selected third-octave frequency bands. The chosen frequency bands are almost equally distributed over the investigated spectrum, from the lowest center frequency f_{c1} of 400 Hz up to the highest center frequency f_{c6} of 20 kHz. The acoustical images show only the pixels with effective sound pressure levels which are in the upper 3 dB within the considered frequency band to avoid the detection of side lobes in the picture. The absolute values of this upper 3 dB range can be taken from the color scale next to the image. From the low-frequency band Δf_1 to the highest frequency band Δf_6, the degree of localization increases because the array's spatial resolution increases with frequency, as predicted in the beampattern simulation.
In Fig. 8.7, especially at the high-frequency bands (Δf_5 and Δf_6), the sound source can be assigned to the area where the window is open. However, another prominent sound source is identified at the very right part of the picture. The sound source is only visible at the edge of the picture, which indicates that this second sound source is outside the captured visible image. In the lowest frequency band ($f_{c1} = 400\,\mathrm{Hz}$), the tilted window cannot be detected at all within the chosen upper 3 dB sound pressure level. In the following bands (Δf_2 to Δf_4), the sound source at the window can partially be detected, but the disturbing unwanted noise dominates the result. This bears the risk of detecting the wrong sound sources when a building enclosure is examined.

For an assessment of filtering unwanted noise outside the building, the reference microphone signal next to the speaker inside the building is used as a reference signal. Based on the correlation analysis [223–225], the aim is to display only sources that significantly correlate with the recorded reference signal. For this reason, the cross-correlation function (Section 3.2.2) is automatically calculated between the reference signal inside and each microphone of the array outside the building within the software NoiseImage. This enables to filter out and reduce the impact of noise on the measurement results.
Fig. 8.8 shows the same measurements as Fig. 8.7, but with the noise-filtered results. In all displayed frequency bands, the previously disturbing sound sources are successfully eliminated, but the displayed resulting signal levels are significantly lower than in Fig. 8.7. The sound source through the tilted window is now clearly visible, and the influence of unwanted sound sources or noise is reduced. All subsequent analyses use this signal filtering with the reference signal in order to reduce noise impact from the environment.

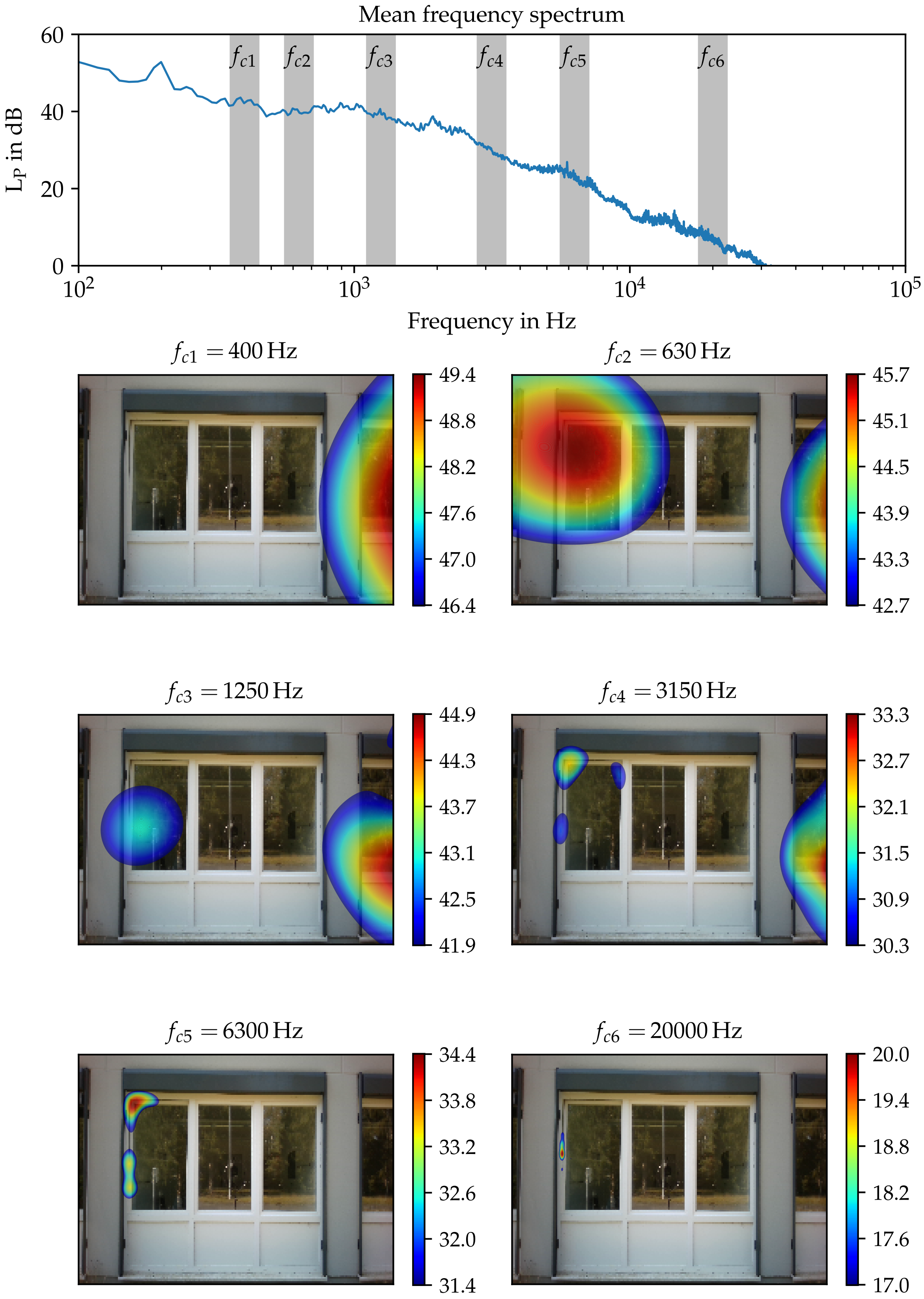

Figure 8.7: Unfiltered acoustical images showing the maximum 3 dB in six different frequency bands with a tilted window (left window) and with influence of external disturbing sound source, color scale in dB

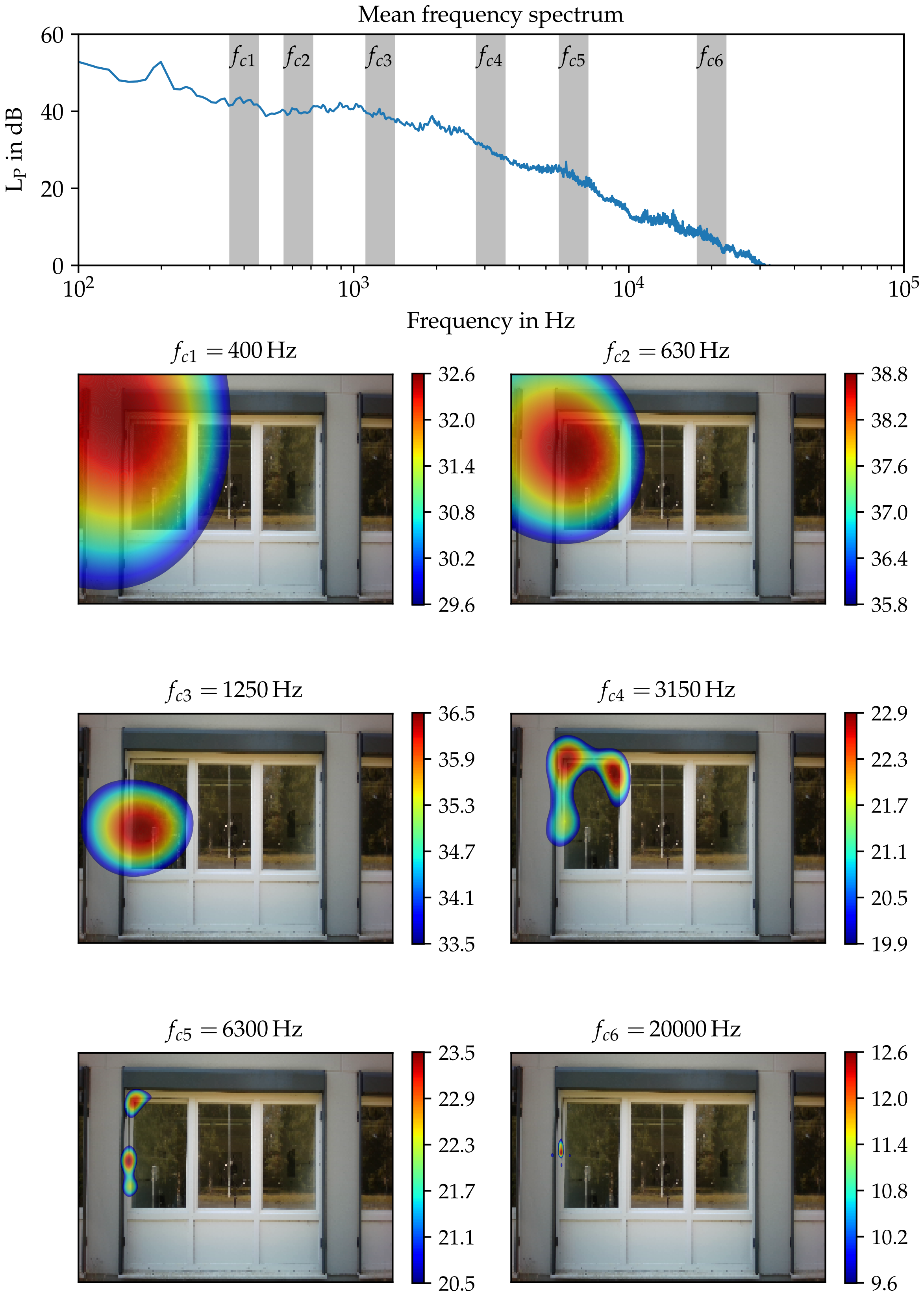

Figure 8.8: Filtered acoustical images showing the maximum 3 dB in six different frequency bands with a tilted window (left window) and with influence of external disturbing sound source, color scale in dB

8.3.2 Building Façade Measurements

After a successful reduction of unwanted external sound sources, the following paragraphs describe the potential detectability of the same constructed cable tie leaks, introduced in Chapter 7. All constructed leaks are created in the right part of the middle window.
Fig. 8.9 shows images for selected frequency bands of a measurement with the largest constructed leak (3×8 mm cable tie) in the window gasket, which is clearly detected in all six selected third-octave frequency bands. The directional characteristic increases with increasing frequency. At the frequency band with $f_{c5} = 12.5\,\mathrm{kHz}$, the sound source, which was identified as one single point source at lower frequencies, is displayed as two separate smaller sources. Due to the construction of this leak with three clamped cable ties in the window gasket, the leak consists of two larger openings at the top and bottom of the cable tie row and two smaller openings between the ties. Because the resolution increases with higher frequencies, the two larger openings may be detected as two separate openings at 12.5 kHz. The highest chosen frequency band ($f_{c6} = 20\,\mathrm{kHz}$) also indicates the smaller openings between the ties.

In the spectrum of Fig. 8.9, a significant spike can be detected at a frequency of approximately 5 kHz, indicating a sudden increase in the sound pressure level. Based on this observation, the acoustical image of a frequency band with $f_c = 5\,\mathrm{kHz}$ is presented in Fig. 8.10. In the acoustical image, a number of sound sources are equally distributed on the element underneath the window, and the constructed leak in the window gasket is now masked. The façade element below the window is made of thin plastic sheets in window frames. It can be assumed that the elements are vibrating at a resonance that masks the measurement at the leak. This resonance is visible in all subsequently investigated leaks as well, which shows that it is beneficial to analyze always multiple frequency bands (here: white noise) to increase the potential of correctly identifying possible leaks in the building enclosure. Except for this specific frequency band, the largest constructed cable tie leak is visible in almost all frequency bands in the entire spectrum.

Figs. 8.11 to 8.15 show the acoustic images of selected frequency bands of the other constructed leak sizes (from large to small). The second-largest artificial constructed leak in Fig. 8.11 with a cable tie leak combination of 2×8 mm is visible almost across the entire spectrum as well. The difference compared to the largest leak in Fig. 8.9 is a lower maximum sound pressure level of approximately 2 dB, which is significant.

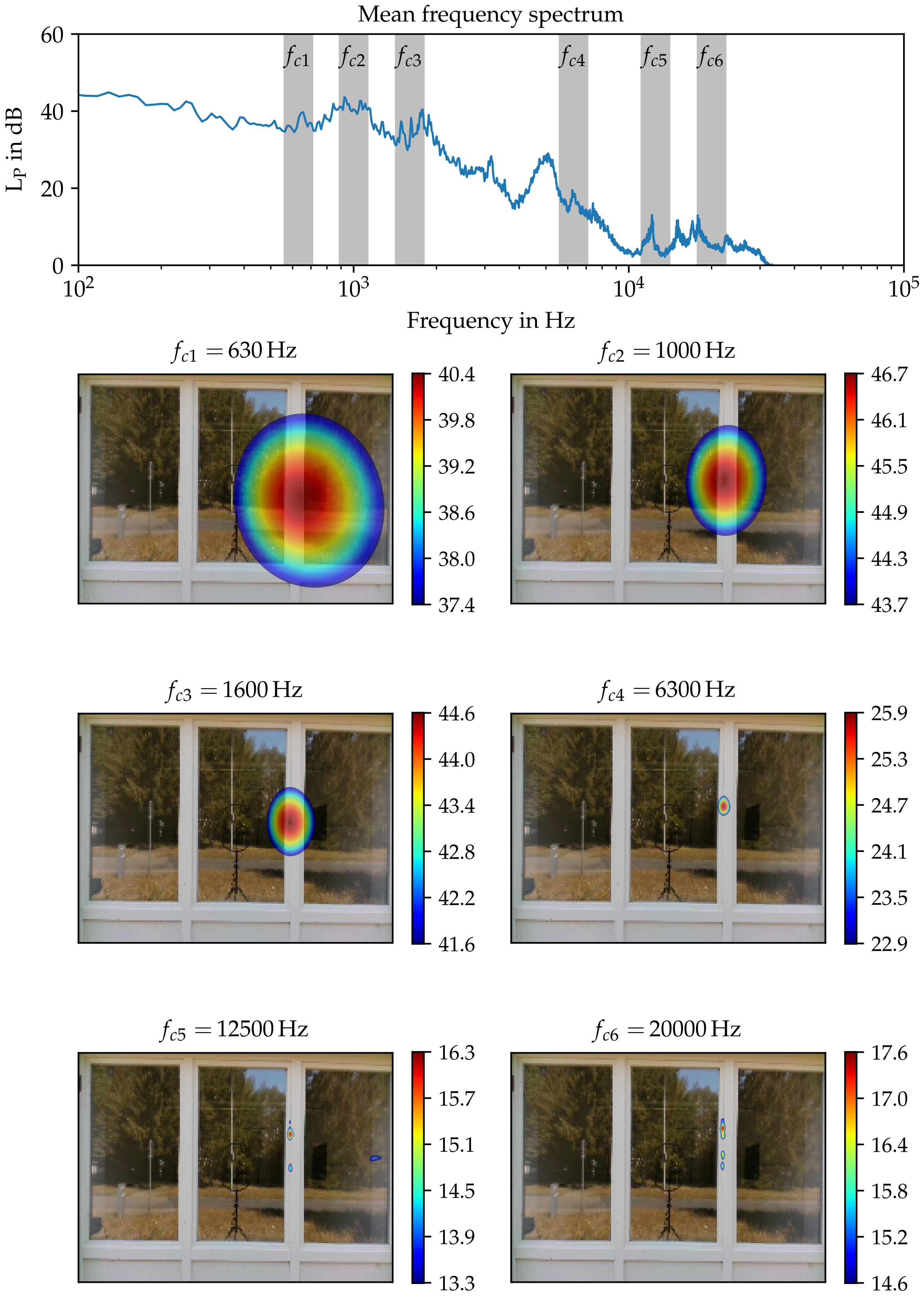

Figure 8.9: Filtered acoustical images showing the maximum 3 dB at six different frequency bands with a cable tie leak combination of 3×8 mm, color scale in dB

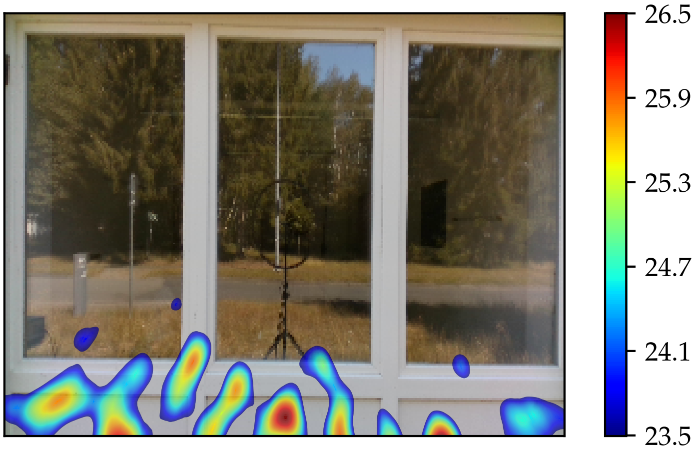

Figure 8.10: Resonance in the filtered acoustical image showing the maximum 3 dB at the frequency band with $f_c = 5000\,\mathrm{Hz}$ and a cable tie leak combination of $3\times 8\,\mathrm{mm}$, color scale in dB

In contrast to the measurements shown with large artificial constructed leaks in Figs. 8.9 and 8.11, where the location of the leak can be observed almost in the entire frequency spectrum, in Figs. 8.12 and 8.13, the constructed leak is only visible at frequency bands above 16 kHz. The smaller the leaks, the lower gets the relevant signal level to be detected (see color bars). Due to the increased directivity of sound at higher frequencies, the detected sound sources are getting very small. Therefore, all Figs. 8.12 to 8.15 show the maximum recorded 5 dB instead of the previously shown 3 dB to increase the visibility at these high frequencies.

The measurements of the smallest artificial constructed leaks are shown in Figs. 8.14 and 8.15. Overall, the maximum detectable sound pressure level decreases with decreasing leak size. Additionally, the small leaks are only detectable at the highest analyzed frequency band of $f_c = 25\,\mathrm{kHz}$. This indicates a relationship between the leak size and the analyzed frequency.

8.4 Summary

In this chapter, several experiments assess the detectability of the previously tested artificial constructed leaks in a window façade using a microphone ring array with 48

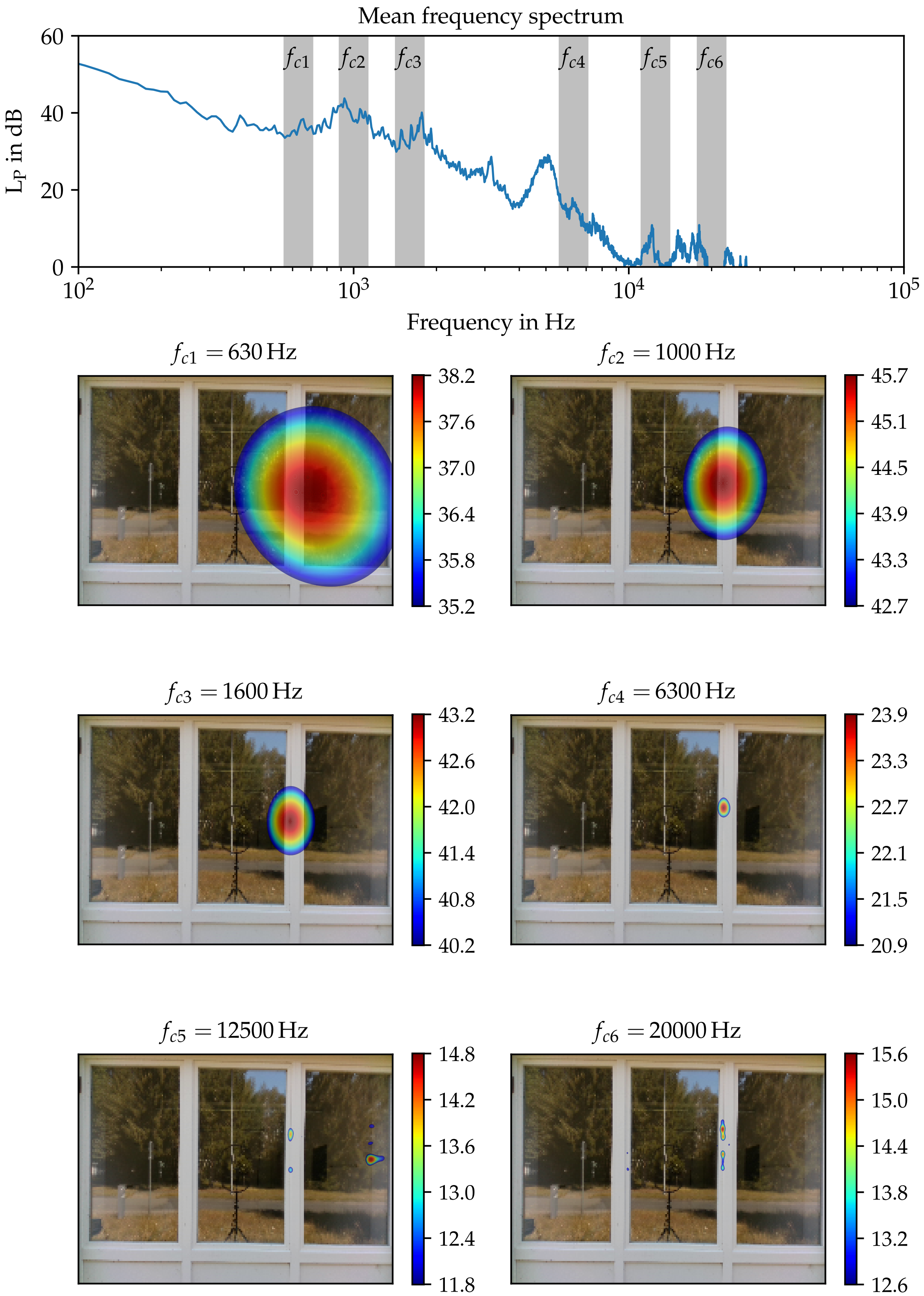

Figure 8.11: Filtered acoustical images showing the maximum 3 dB at six different frequency bands with a cable tie leak combination of 2×8 mm, color scale in dB

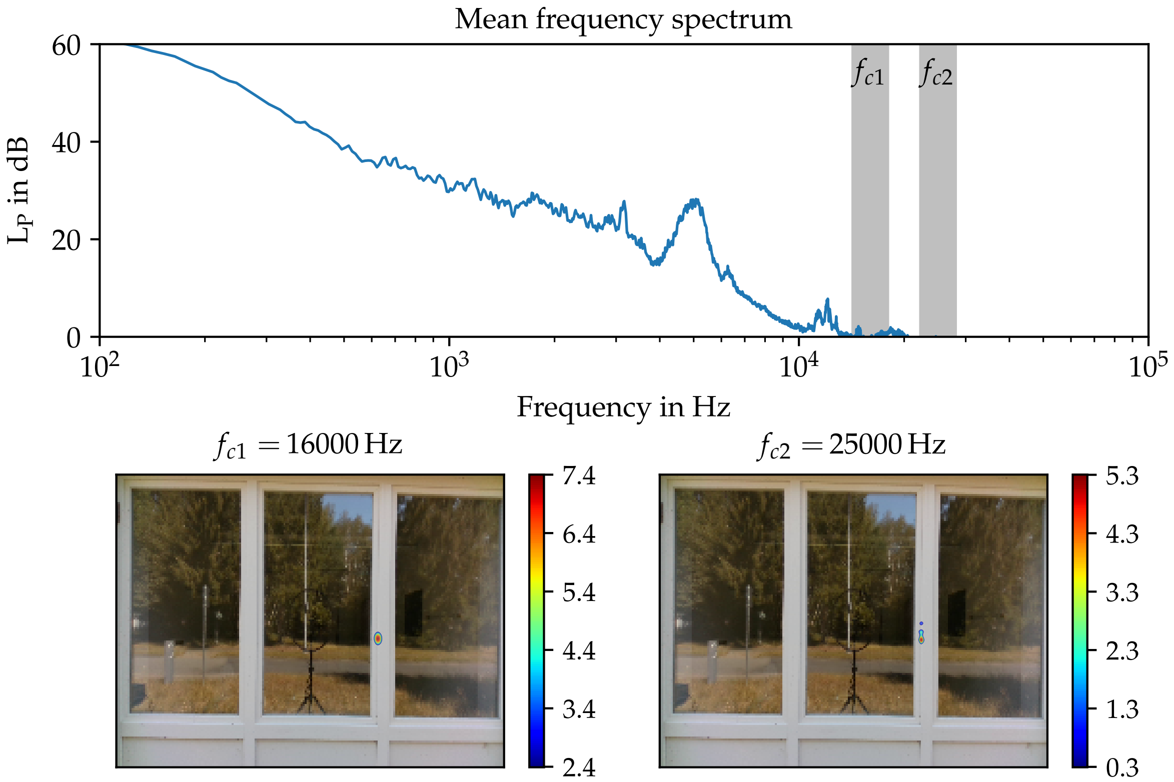

Figure 8.12: Filtered acoustical images showing the maximum 5 dB at two different frequency bands with a cable tie leak combination of 1×8 mm (no signal at lower frequency bands), color scale in dB

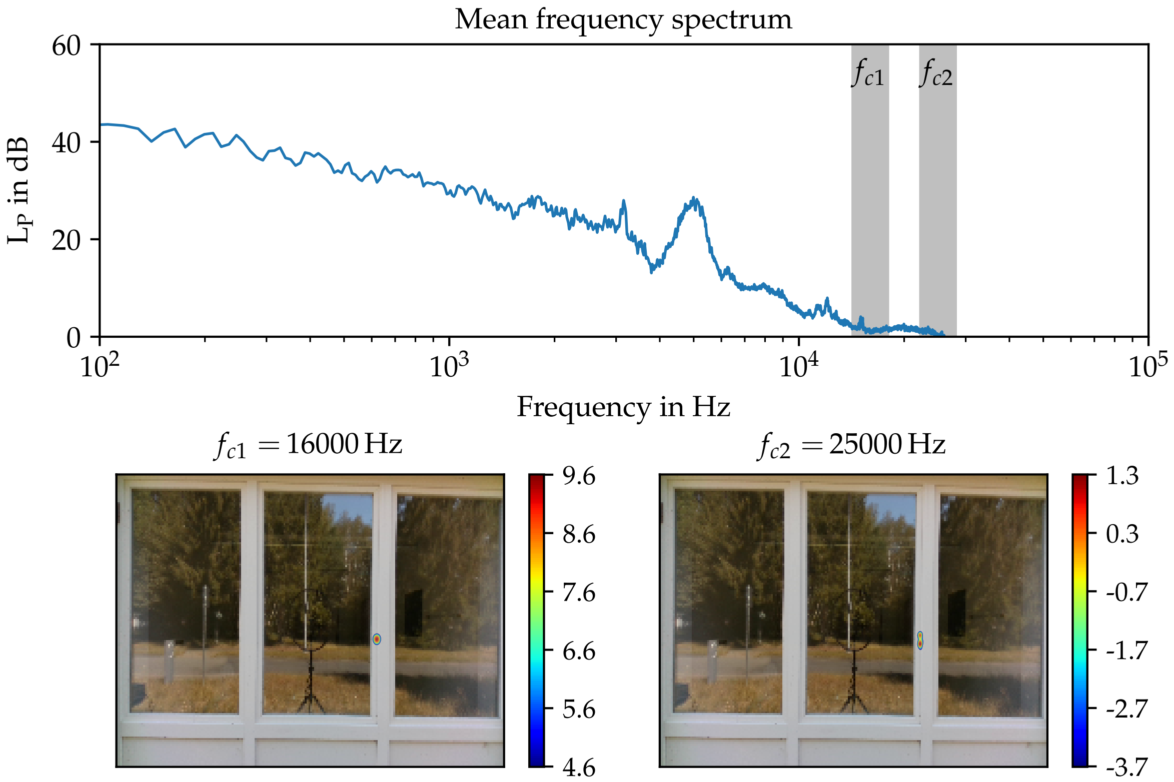

Figure 8.13: Filtered acoustical images showing the maximum 5 dB at two different frequency bands with a cable tie leak combination of 3×3 mm (no signal at lower frequency bands), color scale in dB

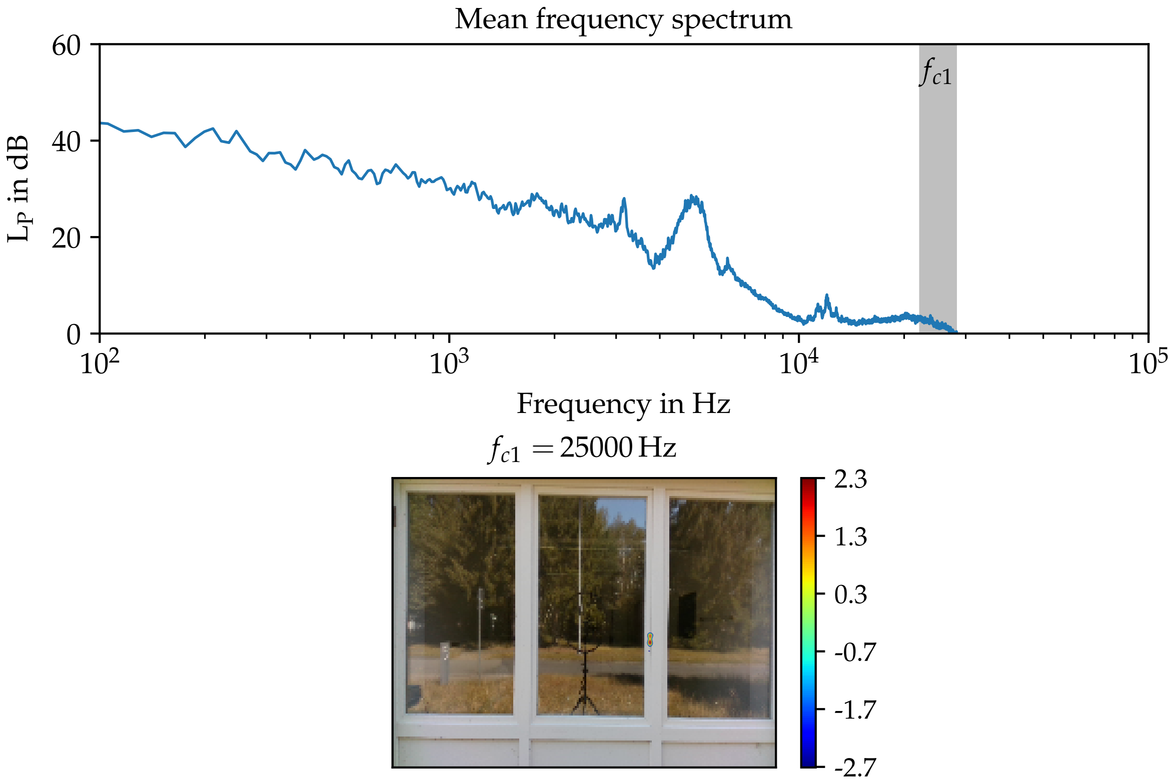

Figure 8.14: Filtered acoustical image showing the maximum 5 dB at one frequency band with a cable tie leak combination of 2×3 mm (no signal at lower frequency bands), color scale in dB

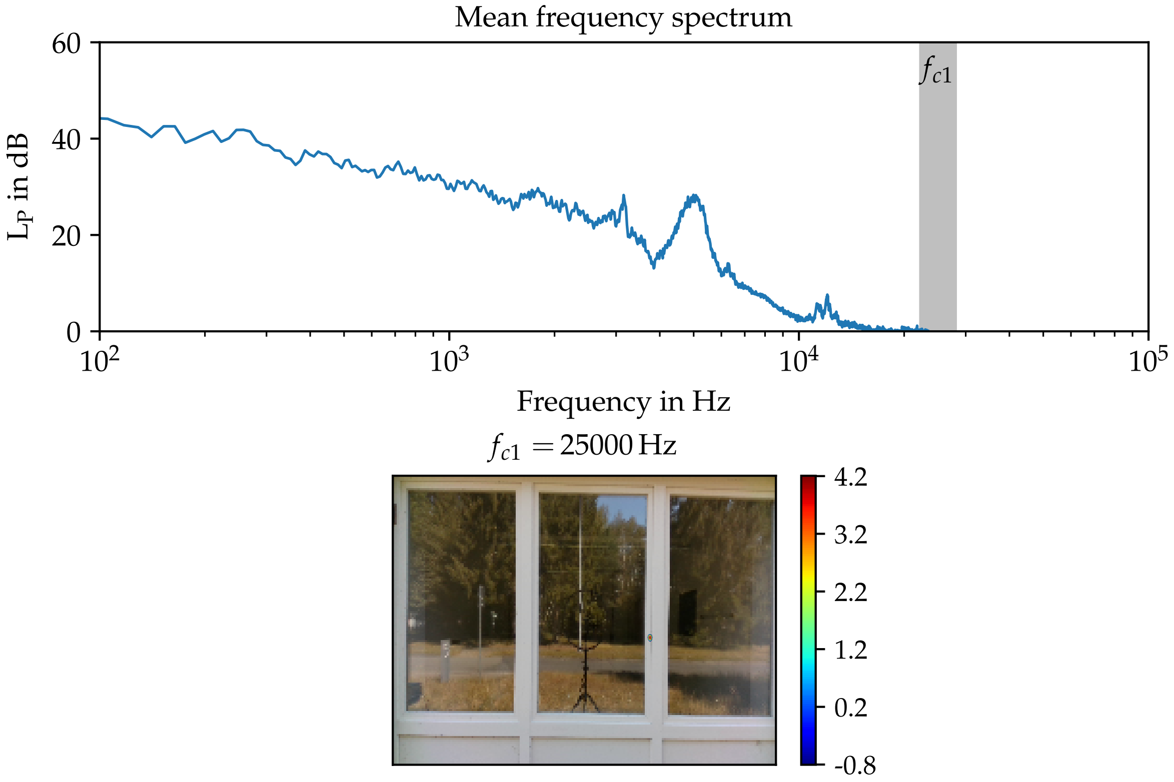

Figure 8.15: Filtered acoustical image showing the maximum 5 dB at one frequency band with a cable tie leak combination of 1×3 mm (no signal at lower frequency bands), color scale in dB

microphones. A broadband white noise sound source is placed inside the building, and the microphone array outside the building aims to detect sound transmitted through these leaky spots in the building envelope.

A significant problem of conducting acoustic measurement at buildings outside the laboratory environment is the presence of unwanted, disturbing noises (from traffic or construction works). Therefore, a filtering method based on the additional reference microphone signal from inside the building is successfully applied, which reduces the impact of such noise on the recorded signals outside and improves the quality of the results.

The six different configurations of cable ties of constructed leaks simulate different degrees of a non-airtight window. The location of all investigated leak sizes is determined with acoustic beamforming, particularly at frequencies $> 16\,\mathrm{kHz}$. It is observed that with a decreasing leak size, the corresponding frequency bands, in which the leaks can be detected, increases. Additionally, the maximum detectable sound pressure level at these frequencies decreases with decreasing leak sizes.

9 Summary, Conclusions and Future Perspective

9.1 Summary and Conclusions

Measurement of the building envelope's air leakage is a crucial parameter for not only heating and cooling energy consumption but is also vital for occupants' well-being and the building's structural integrity. Although the overall evaluation of a building's airtightness is common practice using the fan pressurization method, it is still cumbersome to detect individual leaks in a building envelope and quantify the size of these leaks with current measurement methods. Therefore, the primary goals of this work include assessing the potential of acoustical measurement methods for leak detection and quantification.

In the first part of this work, preliminary acoustic investigations are introduced. Within a small laboratory test setup, two chambers are separated with an interchangeable artificial wall. This wall is either made of acrylic glass or plywood and contains holes with diameters between 4 and 10 mm. One chamber is equipped with a loudspeaker, both with microphones. The microphone signal's response to linear and exponential broadband frequency sweeps in combination with these holes is studied. A distinction between these holes by analyzing the received acoustic spectrum is possible, but accurate quantification is difficult. Although these measurements do not entirely meet the requirements of a sufficient leak quantification, they pave the way for subsequent investigations.

To obtain a better quantitative measure of the leak size, the acoustic measurement results are compared to airflow measurements, similar to fan pressurization in a building, within a more advanced laboratory test apparatus. In contrast to the test chamber used in the previous experiments, more complex leak configurations and more realistic wall constructions are tested together with a broadband white noise signal. Here, the acoustic and airflow measurements through these constructed leaks are conducted within the same boundary conditions. The results promise to estimate the airflow through multiple artificial leaks and wall constructions using the mean acoustic coherence difference. This demonstrates a possible application in real buildings.

However, the airflow measurements through these artificial leaks, used as a quantity to validate the acoustic measurements in laboratory environments, are susceptible to uncertainties induced by external conditions in real buildings (e.g., changing wind conditions during the tests). With the analysis of an extensive data set of almost 7500 fan pressurization measurements (provided by the Lawrence Berkeley National Laboratory), the new method of the weighted line of organic correlation is identified to improve the repeatability of airflow measurement in buildings even under windy conditions. Therefore, the use of this analysis technique is encouraged and should be adopted by building test standards.

In a next step, this comparison between airflow and acoustic measurements in a laboratory test apparatus is validated in a real building application. For this reason, different artificial openings are created in the gasket of an office window using multiple combinations of cable ties. In addition to the airflow measurements, the mean acoustic coherence difference is compared to tracer gas measurements in the building to obtain more reliable air exchange rates at low pressure difference buildings are usually exposed to. Within the laboratory and the building setups, the acoustic approach estimates the magnitude of airflow, which passes through a leak (with investigated leak sizes in the order of several mm^2). From the test results, it is concluded that the mean acoustic coherence difference changes with the size of leaks. A linear trend of increasing mean coherence difference with increasing leak size indicates the potential for this acoustic technique as a practical building diagnostic even though the uncertainties are still significant (around ±50 %).

In addition to a potential quantification of air leaks in building envelopes, a microphone array combined with a white noise sound source and beamforming evaluation ("acoustic camera") is applied to locate even small leaks in a building envelope, where the sound passes through. The technique is tested on the example of the same office window with cable ties wedged in the gasket to construct reproducible leaks. Noise from the surroundings is canceled by implementing the signal of a reference microphone near the sound source inside the room. It is possible to detect all six constructed leaks in a window gasket, down to the smallest leak with one cable tie with a width of 3 mm. Frequency and maximum detectable sound pressure level are found to depend on the leak size. The smaller the leak is, the higher is the frequency band in which the leak is detected even though at a lower sound pressure level. The attractive advantages of the applied microphone array technique are detecting different leaks simultaneously on images of the building, in a short time, and with low preparation effort.

9.2 Future Perspective

The findings of this thesis show that the size of leaks, respectively the related airflow rates, in building envelopes can be estimated with the acoustic methods in comparison with the conducted airflow and tracer gas measurements. Different tested leaks show different spectral properties, which is a potential for future investigation to reduce the uncertainty in quantifying leaks. Even though there is still significant uncertainty in quantification, acoustic methods are promising to differentiate between different leak sizes and enable a prioritized sealing of the leaks.

Additionally, acoustic camera results indicate a better detectability of smaller leaks at higher investigated frequency bands. The method is successfully tested but still requires further development towards quantitative results. In a next development step, the relationship between frequency, sound pressure level, and leak size needs to be further studied.

A limitation of the concept of using a single microphone outside the building to quantify the leakage size is that an acoustic reference measurement of an airtight part of the building envelope is still necessary to correct the measurement with the respective wall structure. Because air leaks, at least at the investigated straight passages, can be detected using a microphone array, it is possible to distinguish between airtight and non-airtight parts of the envelope. For quantification of these leaks, calibrating measurements with a single microphone could be taken at airtight and non-airtight locations.

The proposed testing procedures have been tested for relatively simple leaks in a gasket of an office window. More complex and longer leakage paths may limit the application of this approach. Therefore, more complex leaks need to be investigated in real buildings to assess further the chances and limitations of the acoustic approaches to leak detection and quantification in future work.

This proposed acoustic method does not aim to replace well-established methods like the blower door test but is a promising approach for finding and quantifying significant leaks with far less preparation time, which makes it cost-effective. Moreover, this method does not need any temperature or pressure difference for the localization or quantification of leaks. Although the transition to practical application needs elaboration, this work shows the potential of leak detection and quantification in buildings using acoustic methods.

Acknowledgments

The present thesis was created as part of my work as a doctoral student at the DLR Institute of Solar Research in Jülich. I want to take this opportunity to thank many people for their essential help and support in completing this work.

First and foremost, I would like to thank my doctoral supervisor Univ.-Prof. Dr.-Ing. Bernhard Hoffschmidt, who placed a lot of trust in me, created an extremely pleasant working atmosphere and asked the relevant questions during our meetings. Also, I want to thank Univ.-Prof. Dr.-Ing. habil. Wolfgang Willems for acting as the second examiner and let me present and discuss parts of my research.

Further, my special thanks are attributed to Dr.-Ing. Björn Schiricke and Dr.-Ing. Arne Tiddens for supervising my work during the four years, their endless motivational support, numerous discussions, and critical feedback.

Additionally, I am thankful to Univ.-Prof. Dr.-Ing. Robert Pitz-Paal and Univ.-Prof. Dr. rer. nat. Christian Sattler for showing great interest in my work and giving me helpful advice during our periodic scientific discussions.

A very special thanks goes to my doctoral student colleagues in the project *Gtom*: Dhruvkumar Patel and Philip Gorzalka. It was a pleasure to share my office with you and to further develop the building topic in the institute together.

Additionally, my thanks goes to my colleague Dr.-Ing. Eckhard Lüpfert for his considerable improvement of this manuscript through his conscientious proofreading and feedback. Moreover, many thanks go to the current and former colleagues from my working group for their fruitful discussions and warm welcome at the beginning of my work: Luis Armando Blanco Bohorquez, Dr. rer. nat. Jacob Estevam Schmiedt, Dr.-Ing. Nicole Janotte, Dr.-Ing. Johannes Pernpeintner, and Dr.-Ing. Silvan Siegrist. I am thankful to many other colleagues with whom I worked at DLR, organized lectures at the university, and had countless lunches together: Aiko Bernehed, Juan Pablo Rincon Duarte, Dr.-Ing. Johannes Grobbel, Philipp Holzemer-Zerhusen, Gkiokchan Moumin, Matthias Offergeld, Mathias Pein, Tim Schlichting, and Dr.-Ing Josua Vieten. In particular, I am thankful to Kristina Blume for having a great time while sharing a car every day from Aachen to Jülich. You all considerably brightened my work experience, and

you became more friends than colleagues.

I would further like to thank my student Amine El Khallouki for his great work and help in moving this thesis forward.

Also, I would like to thank all technical, administrative, and managing staff for their excellent work at our institute, especially Sven Dathe and Volkmar Dohmen for their help with my experimental setups.

As a doctoral student, I had the chance to spend three months on a research visit at the Lawrence Berkeley National Laboratory (LBNL) in California, USA. This was an outstanding experience! In particular, I am very thankful to Dr. Iain Walker for his warm welcome, supervision and dedication to sharing his expertise. Also, I would like to thank Dr. Woody Delp for his support with my experiments and for creating a great working environment. Further, I am very thankful to my wonderful international colleagues and friends from Berkeley: Bea Andrés, Dr. Laura Carnieletto, Dr. Shimeng Hao, Dr. Wooyoung Jung, Haoran Li, Dr. Jeetika Malik, Ranjith Narasimhamurthy, Théo Picard, Dr. Handi Chandra Putra, Lorenzo Teso, and Dr. Haoran Zhao. You made these months unique!

I also want to thank my national and international colleagues with whom I had great discussions about the topics of acoustics, building physics, and airtightness: Dr. Virginia Gori, Dr. Valerie Leprince, Dr. Martin Prignon, and Bernd Virnich.

A big thanks go to my good friends Bastin, Benjamin, Dimitri, Frederic, Jan, Lars, Malte, Marvin, Nicolai, and all my other friends I do not mention here. You always supported me and allowed me to get away from work when I needed to.

Throughout my whole life, I was unconditionally supported in every step by my parents, Ursula and Gregor, my brother Niklas, and my sister Hannah. I am deeply grateful for this privilege!

From the bottom of my heart, I am grateful to Katharina. You are a remarkable person, and I am incredibly thankful for all your invaluable daily support and having you in my life!

Publications and Student Theses

Journal Publications

B. Kölsch, I. S. Walker, B. Schiricke, W. W. Delp, and B. Hoffschmidt, "Quantification of Air Leakage Paths: A Comparison of Airflow and Acoustic Measurements", *The International Journal of Ventilation*, 2021, DOI: `10.1080/14733315.2021.1966576`

B. Kölsch, and I. S. Walker, "Improving Air Leakage Prediction of Buildings using the Fan Pressurization Method with the Weighted Line of Organic Correlation", *Building and Environment*, vol. 181, p. 107 157, 2020, ISSN: 0360-1323. DOI: `10.1016/j.buildenv.2020.107157`

B. Kölsch, A. Tiddens, J. Estevam Schmiedt, B. Schiricke, and B. Hoffschmidt, "Detection of Air Leakage in Building Envelopes Using Ultrasound Technology", in *Whole building air leakage*, ser. Selected technical papers ASTM International, T. A. Weston, K. Nelson, and K. Wissink, Eds., West Conshohocken, PA: ASTM International, 2019, pp. 160–183, ISBN: 978-0-8031-7675-1. DOI: `10.1520/STP161520180022`

Peer-reviewed Conference Publications

B. Kölsch, B. Schiricke, E. Lüpfert, and B. Hoffschmidt, "Detection of Air Leakage in Building Envelopes using Microphone Arrays", in *Proceedings of the 41st AIVC - ASHRAE IAQ 2020 joint conference*, 2022

B. Kölsch, and I. S. Walker, “Reducing Wind Sensitivity for Blower Door Testing”, in *Proceedings of the 41st AIVC - ASHRAE IAQ 2020 joint conference*, 2022

B. Kölsch, I. S. Walker, W. W. Delp, B. Schiricke, and B. Hoffschmidt, “Comparison of Airflow and Acoustic Measurements for Evaluation of Building Air Leakage Paths in a Laboratory Test Apparatus”, in *Proceedings of the 41st AIVC - ASHRAE IAQ 2020 joint conference*, 2022

Further Conference Contributions

B. Kölsch, “Comparison of Airflow and Acoustic Measurements for Evaluation of Building Air Leakage Paths in a Laboratory Test Apparatus”, in *AIVC Webinar - Better Quantifying and Locating Building Leakages*, 2020

B. Kölsch, B. Schiricke, J. Estevam Schmiedt, and B. Hoffschmidt, “Estimation of Air Leakage Sizes in Building Envelope using High-Frequency Acoustic Impulse Response Technique”, in *Proceedings of the 40th AIVC Conference*, 2019, pp. 80–89

Patents

A. Tiddens, S. Siegrist, D. Patel, J. Estevam Schmiedt, and **B. Kölsch**, “Verfahren zur berührungslosen Bestimmung von Wärmedurchgangskoeffizienten an Wänden eines Raumes sowie System zur Bestimmung von Wärmedurchgangskoeffizienten an Wänden eines Raumes”, DE 10 2018 218 096 B4, 2020

A. Tiddens, B. Schiricke, **B. Kölsch**, S. Siegrist, and D. Patel, “Verfahren und Vorrichtung zur Identifizierung eines Fensters sowie zur Bestimmung einer Rauminnentemperatur durch ein Fenster hindurch”, DE 10 2018 210 928 B3, 2019

Supervised Student Theses

A. El Khallouki, “Entwicklung eines Akustikprüfstandes zur Bestimmung der Luftdichtheit von Gebäudehüllen”, Master’s Thesis, HAW Hamburg, 2019

J. Kniprath, “Simulation eines geschlossenen Gasturbinenprozesses für verschiedene Arbeitsmedien”, Master’s Thesis, RWTH Aachen University, 2018

Bibliography

[1] International Energy Agency, *Technology Roadmap: Energy-efficient Buildings - Heating and Cooling Equipment*, OECD Publishing, Ed., Paris, France, 2011. [Online]. Available: `www.iea.org`.

[2] European Parliament, *Directive 2010/31/EU of the european parliament and of the council on the energy performance of buildings (recast)*, 2010.

[3] Federal Ministry for Economic Affairs and Energy, *Klimaschutzprogramm 2030 der Bundesregierung zur Umsetzung des Klimaschutzplans 2050*, 2019.

[4] V. Bürger, T. Hesse, B. Köhler, A. Palzer, and P. Engelmann, "German Energiewende—different visions for a (nearly) climate neutral building sector in 2050", *Energy Efficiency*, vol. 12, no. 1, pp. 73–87, 2019, ISSN: 1570-646X. DOI: `10.1007/s12053-018-9660-6`.

[5] Environment and Climate Change Canada, *Pan-Canadian Framework on Clean Growth and Climate Change: Canada's plan to address climate change and grow the economy*, Gatineau, Quebec, 2016.

[6] S. J. Emmerich, T. McDowell, and W. Anis, *Investigation of the Impact of Commercial Building Envelope Airtightness on HVAC Energy Use*, 2005.

[7] T. Kalamees, "Air tightness and air leakages of new lightweight single-family detached houses in Estonia", *Building and Environment*, vol. 42, no. 6, pp. 2369–2377, 2007, ISSN: 0360-1323. DOI: `10.1016/j.buildenv.2006.06.001`.

[8] J. Jokisalo, J. Kurnitski, M. Korpi, T. Kalamees, and J. Vinha, "Building leakage, infiltration, and energy performance analyses for Finnish detached houses", *Building and Environment*, vol. 44, no. 2, pp. 377–387, 2009, ISSN: 0360-1323. DOI: `10.1016/j.buildenv.2008.03.014`.

[9] W. R. Chan, J. Joh, and M. H. Sherman, *Analysis of Air Leakage Measurements from Residential Diagnostics Database*, Berkeley, CA, 2012.

[10] G. Han, J. Srebric, and E. Enache-Pommer, "Different modeling strategies of infiltration rates for an office building to improve accuracy of building energy simulations", *Energy and Buildings*, vol. 86, pp. 288–295, 2015, ISSN: 03787788. DOI: `10.1016/j.enbuild.2014.10.028`.

[11] B. Jones, P. Das, Z. Chalabi, M. Davies, I. Hamilton, R. Lowe, A. Mavrogianni, D. Robinson, and J. Taylor, "Assessing uncertainty in housing stock infiltration rates and associated heat loss: English and UK case studies", *Building and Environment*, vol. 92, pp. 644–656, 2015, ISSN: 0360-1323. DOI: `10.1016/j.buildenv.2015.05.033`.

[12] K. Pietrzyk, "Thermal Performance of a Building Envelope - A Probabilistic Approach", *Journal of Building Physics*, vol. 34, no. 1, pp. 77–96, 2010, ISSN: 1744-2591. DOI: `10.1177/1744259109339652`.

[13] M. Bell and R. Lowe, "Energy efficient modernisation of housing: a UK case study", *Energy and Buildings*, vol. 32, no. 3, pp. 267–280, 2000, ISSN: 03787788. DOI: `10.1016/S0378-7788(00)00053-0`.

[14] J. M. Logue, M. H. Sherman, I. S. Walker, and B. C. Singer, "Energy impacts of envelope tightening and mechanical ventilation for the U.S. residential sector", *Energy and Buildings*, vol. 65, pp. 281–291, 2013, ISSN: 03787788. DOI: `10.1016/j.enbuild.2013.06.008`.

[15] A. Berge, "Analysis of Methods to Calculate Air Infiltration for Use in Energy Calculations", Master's thesis, Chalmers University of Technology, Göteborg, 2011.

[16] U. Jung, J. Baier, W. Bauer, N. Endres, F. Flesche, M. Giebeler, C. Hartung, M. Hellerforth, D. Markfort, and F. Mayr, *Handbuch Energieberatung: Recht und Technik in der Praxis-für Energieberater, Bauingenieure und Architekten*. Bundesanzeiger, 2013, ISBN: 3846201901.

[17] W. Borsboom, W. Kornaat, P. van Beek, N.-J. Bink, and T. Lanooy, "Commission and performance contracting of ventilation systems in practice. Determination, analyses and consequences for practitioners and contractors", in *Proceedings of the 40th AIVC Conference*, 2019.

[18] M. H. Sherman and W. R. Chan, "Building air tightness: Research and practice", *Building Ventilation: the state of the Art*, pp. 137–162, 2006.

[19] L. Rodrigues, R. Tubelo, A. Vega Pasos, J. C. S. Gonçalves, C. Wood, and M. Gillott, "Quantifying airtightness in Brazilian residential buildings with focus on its contribution to thermal comfort", *Building Research & Information*, pp. 1–22, 2020, ISSN: 0961-3218. DOI: `10.1080/09613218.2020.1825064`.

[20] V. Tam, L. Almeida, and K. Le, "Energy-Related Occupant Behaviour and Its Implications in Energy Use: A Chronological Review", *Sustainability*, vol. 10, no. 8, p. 2635, 2018. DOI: `10.3390/su10082635`.

[21] A. TenWolde, "Ventilation, humidity, and condensation in manufactured houses during winter", *ASHRAE Transactions*, vol. 100, no. 1, 1994.

[22] H. Hens, *Building Physics Heat, Air and Moisture: Fundamentals and Engineering Methods with Examples and Exercises*, 3rd ed. Berlin: Wilhelm Ernst & Sohn, 2017.

[23] R. A. Zabel and J. J. Morrell, *Wood Microbiology: Decay and Its Prevention*. San Diego, CA: Academic Press, Inc., 1992.

[24] M. Nofal and K. Kumaran, "Biological damage function models for durability assessments of wood and wood-based products in building envelopes", *European Journal of Wood and Wood Products*, vol. 69, no. 4, pp. 619–631, 2011, ISSN: 0018-3768. DOI: `10.1007/s00107-010-0508-9`.

[25] A. G. Wilson and E. S. Nowak, "Condensation between the panes of double windows", *ASHRAE Transactions*, vol. 65, pp. 551–570, 1960.

[26] W. R. Chan, J. Joh, and M. H. Sherman, "Analysis of air leakage measurements of US houses", *Energy and Buildings*, vol. 66, pp. 616–625, 2013, ISSN: 03787788. DOI: `10.1016/j.enbuild.2013.07.047`.

[27] I. S. Walker and D. J. Wilson, "Field Validation of Algebraic Equations for Stack and Wind Driven Air Infiltration Calculations", *HVAC&R Research*, vol. 4, pp. 119–139, 1998.

[28] M. W. Liddament, *Air Infiltration Calculation Techniques - An Application Guide*. Coventry, UK, 1986.

[29] I. S. Walker, M. H. Sherman, J. Joh, and W. R. Chan, "Applying Large Datasets to Developing a Better Understanding of Air Leakage Measurement in Homes", *International Journal of Ventilation*, vol. 11, no. 4, pp. 323–338, 2013. DOI: `10.1080/14733315.2013.11683991`.

[30] C. Younes, C. A. Shdid, and G. Bitsuamlak, "Air infiltration through building envelopes: A review", *Journal of Building Physics*, vol. 35, no. 3, pp. 267–302, 2012, ISSN: 1744-2591. DOI: `10.1177/1744259111423085`.

[31] P. S. Charlesworth, *Air Exchange Rate and Airtightness Measurement Techniques - An Applications Guide*, Air Infiltration and Ventilation Centre, Ed., Coventry, UK, 1988.

[32] ASHRAE, Ed., *2001 ASHRAE Handbook: Fundamentals*. Atlanta, 2001, ISBN: 1-883413-87-7.

[33] J. B. Dick, “The Fundamentals of Natural Ventilation of Houses”, *Journal of the Institution of Heating and Ventilating Engineers*, vol. 18, no. 179, pp. 123–134, 1950.

[34] M. W. Liddament, *A Guide to Energy Efficient Ventiltion*, Coventry, UK, 1996.

[35] J. P. Cockroft and P. Robertson, “Ventilation of an Enclosure Through a Single Opening”, *Building and Environment*, no. 11, pp. 29–35, 1976, ISSN: 0360-1323.

[36] G. Bauwens and S. Roels, “Characterizing Thermal Performance of Buildings Using Dynamic Model Identification”, in *Proceedings of the Thermal Performance of the Exterior Envelopes of Whole Buildings XII International Conference*, 2013.

[37] W. M. Willems, Ed., *Lehrbuch der Bauphysik: Schall - Wärme - Feuchte - Licht - Brand - Klima*, 8th ed. Wiesbaden: Springer Vieweg, 2017, ISBN: 978-3-658-16073-9. DOI: `10.1007/978-3-658-16074-6`.

[38] M. Orme, “Estimates of the energy impact of ventilation and associated financial expenditures”, *Energy and Buildings*, vol. 33, no. 3, pp. 199–205, 2001, ISSN: 03787788. DOI: `10.1016/S0378-7788(00)00082-7`.

[39] W. Anis, “Airtight Buildings: Past, Present and Future”, *ASHRAE Journal*, vol. 57, no. 11, 2015.

[40] R. J. Lowe, S. R. Curwell, M. Bell, and A. Ahmad, “Airtightness in masonry dwellings: Laboratory and field experience†”, *Building Services Engineering Research and Technology*, vol. 15, no. 3, pp. 149–155, 1994, ISSN: 0143-6244. DOI: `10.1177/014362449401500304`.

[41] R. J. Lowe, D. Johnston, and M. Bell, “Airtightness in UK Dwellings: A Review of Some Recent Measurements”, in *Proceedings of the 2nd International Buildings and the Environment Conference*, 1997.

[42] A. B. Mélois, B. Moujalled, G. Guyot, and V. Leprince, “Improving building envelope knowledge from analysis of 219,000 certified on-site air leakage measurements in France”, *Building and Environment*, vol. 159, 2019, ISSN: 0360-1323. DOI: `10.1016/j.buildenv.2019.05.023`.

[43] K. Dol and M. Haffner, *Housing Statistics in the European Union*, Delft, 2010.

[44] J. Laverge, M. Delghust, N. den van Bossche, and A. Janssens, “Airtightness Assessment of Single Family Houses in Belgium”, *International Journal of Ventilation*, vol. 12, no. 4, pp. 379–390, 2014. DOI: `10.1080/14733315.2014.11684031`.

[45] W. R. Chan, P. N. Price, M. D. Sohn, and A. J. Gadgil, *Analysis of U.S. Residential Air Leakage Database: Report Number 53367*, Lawrence Berkeley National Laboratory, Ed., Berkeley, CA, 2003.

[46] Y. Ji, L. Duanmu, Y. Liu, and H. Dong, "Air infiltration rate of typical zones of public buildings under natural conditions", *Sustainable Cities and Society*, vol. 61, 2020, ISSN: 22106707. DOI: `10.1016/j.scs.2020.102290`.

[47] M. Kraus and P. Charvátová, "Location as a Determinative Factor of Building Airtightness", *Procedia Engineering*, vol. 161, pp. 1532–1537, 2016, ISSN: 18777058. DOI: `10.1016/j.proeng.2016.08.622`.

[48] K. Schild and W. M. Willems, *Wärmeschutz: Grundlagen - Berechnung - Bewertung*, 2nd ed. Wiesbaden: Springer Fachmedien Wiesbaden, 2013, ISBN: 978-3-658-02570-0. DOI: `10.1007/978-3-658-02571-7`.

[49] E. L. Hult, D. J. Dickerhoff, and P. N. Price, *Measurement Methods to Determine Air Leakage Between Adjacent Zones*, Berkeley, CA, 2012.

[50] J. Fernández-Agüera, S. Domínguez-Amarillo, J. J. Sendra, and R. Suárez, "An approach to modelling envelope airtightness in multi-family social housing in Mediterranean Europe based on the situation in Spain", *Energy and Buildings*, vol. 128, pp. 236–253, 2016, ISSN: 03787788. DOI: `10.1016/j.enbuild.2016.06.074`.

[51] M. Bartko, C. Banister, A. Wills, B. Kemery, M. Voutari, J. Berquist, and I. Macdonald, "Commercial Buildings Air Leakage Testing and Comparison of Results", in *Whole building air leakage*, ser. Selected technical papers ASTM International, T. A. Weston, K. Nelson, and K. Wissink, Eds., West Conshohocken, PA: ASTM International, 2019, pp. 184–190, ISBN: 978-0-8031-7675-1. DOI: `10.1520/STP161520180026`.

[52] K. Knight, C. Carson, and G. Proskiw, "Target Airtightness Rates for Large Buildings, What Is Possible, What Is Probable, and What Is Prophetic", in *Whole building air leakage*, ser. Selected technical papers ASTM International, T. A. Weston, K. Nelson, and K. Wissink, Eds., West Conshohocken, PA: ASTM International, 2019, pp. 291–300, ISBN: 978-0-8031-7675-1. DOI: `10.1520/STP161520180121`.

[53] Deutsches Institut für Normung e.V., *DIN EN ISO 12569:2018: Thermal performance of buildings and materials - Determination of specific airflow rate in buildings - Tracer gas dilution method*, Berlin, 2018.

[54] ASTM International, *ASTM E779-19: Standard Test Method for Determining Air Leakage Rate by Fan Pressurization*, West Conshohocken, PA, 2019.

[55] Canadian General Standards Board, *CAN/CGSB, 149.10-2019: Determination of the Airtightness of Building Envelopes by the Fan Depressurization Method*, Gatineau, 2019.

[56] M. J. Limb, "A Review of International Ventilation, Airtightness, Thermal Insulation and Indoor Air Quality Criteria", *AIVC Technical Note 55*, 2001.

[57] A. Meiss and J. Feijó-Muñoz, "The energy impact of infiltration: a study on buildings located in north central Spain", *Energy Efficiency*, vol. 8, no. 1, pp. 51–64, 2015, ISSN: 1570-646X. DOI: `10.1007/s12053-014-9270-x`.

[58] V. E. M. Cardoso, P. F. Pereira, N. M. M. Ramos, and R. M. S. F. Almeida, "The Impacts of Air Leakage Paths and Airtightness Levels on Air Change Rates", *Buildings*, vol. 10, no. 3, p. 55, 2020. DOI: `10.3390/buildings10030055`.

[59] I. Poza-Casado, V. E. Cardoso, R. M. Almeida, A. Meiss, N. M. Ramos, and M. Á. Padilla-Marcos, "Residential buildings airtightness frameworks: A review on the main databases and setups in Europe and North America", *Building and Environment*, vol. 183, p. 107 221, 2020, ISSN: 0360-1323. DOI: `10.1016/j.buildenv.2020.107221`.

[60] D. W. Etheridge, "Air leakage characteristics of houses - a new approach", *Building Services Engineering Research and Technology*, vol. 5, no. 1, pp. 32–36, 1984, ISSN: 0143-6244. DOI: `10.1177/014362448400500105`.

[61] F. Kreith and R. Eisenstadt, "Pressure Drop and Flow Characteristics of Short Capillary Tubes at Low Reynolds Numbers", *ASME Transactions*, vol. 79, pp. 1070–1078, 1947.

[62] H. Honma, "Ventilation of dwellings and its disturbances", *Technical notice at the Royal Institute of Technology Stockholm*, vol. 3, 1975.

[63] B. A. Fleury, A. Y. Gadilhe, P. Niard, and J. L. Chazelas, "Air flow through building slits and components", in *Proceedings of the 11th AIVC Conference*, 1990.

[64] M. R. Mokhtarzadeh-Dehghan, A. J. Ward-Smith, and R. N. Walker, "A study of laminar air flow through cracks by numerical solution of the differential equations", *International Journal for Numerical Methods in Fluids*, vol. 14, no. 12, pp. 1485–1496, 1992, ISSN: 0271-2091. DOI: `10.1002/fld.1650141209`.

[65] K. Siren, "A modification of the power-law equation to account for large scale wind turbulence", in *Proceedings of the 18th AIVC Conference*, 1997.

[66] T. Baracu, V. Badescu, C. Teodosiu, M. Degeratu, M. Patrascu, and C. Streche, "Consideration of a new extended power law of air infiltration through the building's envelope providing estimations of the leakage area", *Energy and Buildings*, vol. 149, pp. 400–423, 2017, ISSN: 03787788. DOI: `10.1016/j.enbuild.2017.04.055`.

[67] D. W. Etheridge, "The Rule of The Power Law - An Alternative View", *Air Infiltration Review*, vol. 8, no. 4, 1987.

[68] M. W. Liddament, "Power Law Rules - OK?", *Air Infiltration Review*, vol. 8, no. 4, 1987.

[69] D. W. Etheridge, "Natural Ventilation through Large Openings - Measurements at Model Scale and Envelope Flow Theory", *International Journal of Ventilation*, vol. 2, no. 4, pp. 325–342, 2004. DOI: `10.1080/14733315.2004.11683676`.

[70] Y.-H. Chiu and D. W. Etheridge, "External flow effects on the discharge coefficients of two types of ventilation opening", *Journal of Wind Engineering and Industrial Aerodynamics*, vol. 95, no. 4, pp. 225–252, 2007, ISSN: 01676105. DOI: `10.1016/j.jweia.2006.06.013`.

[71] D. W. Etheridge, *Natural Ventilation of Buildings: Theory, Measurement and Design*. Chichester, UK: John Wiley & Sons, Inc, 2012, ISBN: 978-0-470-66035-5.

[72] P. H. Baker, S. Sharples, and I. C. Ward, "Air flow through cracks", *Building and Environment*, vol. 22, no. 4, pp. 293–304, 1987, ISSN: 0360-1323.

[73] M. Sherman, "A Power-Law Formulation of Laminar Flow in Short Pipes", *Journal of Fluids Engineering*, vol. 114, no. 4, pp. 601–605, 1992, ISSN: 0098-2202. DOI: `10.1115/1.2910073`.

[74] D. W. Etheridge, "Crack flow equations and scale effect", *Building and Environment*, vol. 12, no. 3, pp. 181–189, 1977, ISSN: 0360-1323. DOI: `10.1016/0360-1323(77)90016-6`.

[75] ——, "A note on crack flow equations for ventilation modelling", *Building and Environment*, vol. 33, no. 5, pp. 325–328, 1998, ISSN: 0360-1323. DOI: `10.1016/S0360-1323(97)00072-3`.

[76] L. P. Hopkins and B. Hansford, "Air flow through cracks", *Building Services Engineer*, vol. 42, pp. 123–131, 1974.

[77] I. S. Walker, D. J. Wilson, and M. H. Sherman, "A comparison of the power law to quadratic formulations for air infiltration calculations", *Energy and Buildings*, vol. 27, no. 3, pp. 293–299, 1998, ISSN: 03787788. DOI: `10.1016/S0378-7788(97)00047-9`.

[78] J. Feijó-Muñoz, C. Pardal, V. Echarri, J. Fernández-Agüera, R. Assiego de Larriva, M. Montesdeoca Calderín, I. Poza-Casado, M. Á. Padilla-Marcos, and A. Meiss, "Energy impact of the air infiltration in residential buildings in the Mediterranean area of Spain and the Canary islands", *Energy and Buildings*, vol. 188-189, pp. 226–238, 2019, ISSN: 03787788. DOI: `10.1016/j.enbuild.2019.02.023`.

[79] H.-G. Kula and S. Sharples, "Air Flow Through Smooth and Rough Cracks", in *Proceedings of the 15th AIVC Conference*, 1994.

[80] Y.-H. Chiu and D. W. Etheridge, "Calculations and Notes on the Quadratic and Power Law Equations for Modelling Infiltration", *International Journal of Ventilation*, vol. 1, no. 1, pp. 65–77, 2002. DOI: `10.1080/14733315.2002.11683623`.

[81] A. Geißler, "Genauigkeit von Luftdichtheitsmessungen", in *Proceedings of the 4th EUZ BlowerDoor-Symposium*, 1999, pp. 14–20.

[82] A. Geissler, "Error Estimation of Blower Door Measurements by Computer Simulation", in *Proceedings of the 8th International Conference on Indoor Air Quality and Climate*, 1999, pp. 827–832.

[83] M. H. Sherman and L. Palmiter, "Uncertainty in fan pressurization measurements", *Airflow Performance Conference 10/93 LBL-32115*, 1995.

[84] M. H. Sherman, D. T. Grimsrud, and R. C. Sonderegger, "Low pressure leakage function of a building", in *Proceedings of the ASHRAE/DOE Conference*, 1979.

[85] J. Dewsbury, "AC pressurisation: Fourier analysis and the effect of compressibility of air", *Building Services Engineering Research and Technology*, vol. 17, no. 2, pp. 73–77, 1996, ISSN: 0143-6244. DOI: `10.1177/014362449601700203`.

[86] ——, "AC pressurisation: Analysis by non-linear optimisation", *Building Services Engineering Research and Technology*, vol. 17, no. 2, pp. 65–71, 1996, ISSN: 0143-6244. DOI: `10.1177/014362449601700202`.

[87] S. Sharples and Thompson D., "Experimental study of crack flow with varying pressure differentials", in *Proceedings of the 17th AIVC Conference*, 1996.

[88] T. Nishioka, Q. Chen, N. Arai, K. Fujiwara, N. Umemiya, and R. Okura, "Unsteady pressurization method to measure the airtightness of the building envelope", in *Research in Building Physics: Proceedings of the Second International Conference on Building Physics*, J. Carmeliet, H. Hens, and G. Vermeir, Eds., CRC Press LLC, 2003, pp. 771–776.

[89] B. Mattsson and J. Claesson, "A Transient Pressurization Method for Measurements of Airtightness", *Journal of Building Physics*, vol. 31, no. 1, pp. 35–53, 2007, ISSN: 1744-2591. DOI: `10.1177/1744259107079021`.

[90] E. B. Moller, T. V. Rasmussen, and A. Nicolajsen, "A Simplified Method Using Compressed Air to Determine Air Leakage", in *Proceedings of the Thermal Performance of the Exterior Envelopes of Whole Buildings XI International Conference*, 2010.

[91] P. S. Carey and D. W. Etheridge, "Leakage measurements using unsteady techniques with particular reference to large buildings", *Building Services Engineering Research and Technology*, vol. 22, no. 2, pp. 69–82, 2001, ISSN: 0143-6244. DOI: `10.1191/014362401701524136`.

[92] E. W. Cooper, D. W. Etheridge, and S. J. Smith, "Determining the adventitious leakage of buildings at low pressure. Part 2: pulse technique", *Building Services Engineering Research and Technology*, vol. 28, no. 1, pp. 81–96, 2007, ISSN: 0143-6244. DOI: `10.1177/0143624406072331`.

[93] E. Cooper, X. Zheng, C. Wood, M. Gillot, D. Tetlow, S. Riffat, and L. de Simon, "Field trialling of a pulse airtightness tester in a range of UK homes", *International Journal of Ventilation*, vol. 18, no. 1, pp. 1–18, 2019. DOI: `10.1080/14733315.2016.1252155`.

[94] X. Zheng, J. Mazzon, I. Wallis, and C. Wood, "Experimental study of enclosure airtightness of an outdoor chamber using the pulse technique and blower door method under various leakage and wind conditions", in *Proceedings of the 39th AIVC Conference*, 2018.

[95] C. Wood, X. Zheng, A. V. Pasos, Y.-S. Hsu, and L. Smith, "An extended pressure range comparison of the blower door and novel pulse method for measuring the airtightness of two outdoor chambers with different levels of airtightness", in *Proceedings of the 39th AIVC Conference*, 2018.

[96] F. Asdrubali, G. Baldinelli, and F. Bianchi, "A quantitative methodology to evaluate thermal bridges in buildings", *Applied Energy*, vol. 97, pp. 365–373, 2012. DOI: `10.1016/j.apenergy.2011.12.054`.

[97] T. Taylor, J. Counsell, and S. Gill, "Energy efficiency is more than skin deep: Improving construction quality control in new-build housing using thermography", *Energy and Buildings*, vol. 66, pp. 222–231, 2013, ISSN: 03787788. DOI: `10.1016/j.enbuild.2013.07.051`.

[98] D. Katunsky, A. Korjenic, J. Katunska, M. Lopusniak, S. Korjenic, and S. Doroudiani, "Analysis of thermal energy demand and saving in industrial buildings: A case study in Slovakia", *Building and Environment*, vol. 67, pp. 138–146, 2013, ISSN: 0360-1323. DOI: `10.1016/j.buildenv.2013.05.014`.

[99] D. González-Aguilera, S. Lagüela, P. Rodríguez-Gonzálvez, and D. Hernández-López, "Image-based thermographic modeling for assessing energy efficiency of buildings façades", *Energy and Buildings*, vol. 65, pp. 29–36, 2013, ISSN: 03787788. DOI: `10.1016/j.enbuild.2013.05.040`.

[100] C. A. Balaras and A. A. Argiriou, “Infrared thermography for building diagnostics”, *Energy and Buildings*, vol. 34, no. 2, pp. 171–183, 2002, ISSN: 03787788. DOI: `10.1016/S0378-7788(01)00105-0`.

[101] E. Barreira and V. P. de Freitas, “Evaluation of building materials using infrared thermography”, *Construction and Building Materials*, vol. 21, no. 1, pp. 218–224, 2007, ISSN: 09500618. DOI: `10.1016/j.conbuildmat.2005.06.049`.

[102] S. S. de Freitas, V. P. de Freitas, and E. Barreira, “Detection of façade plaster detachments using infrared thermography – A nondestructive technique”, *Construction and Building Materials*, vol. 70, pp. 80–87, 2014, ISSN: 09500618. DOI: `10.1016/j.conbuildmat.2014.07.094`.

[103] A. Menezes, M. Glória Gomes, and I. Flores-Colen, “In-situ assessment of physical performance and degradation analysis of rendering walls”, *Construction and Building Materials*, vol. 75, pp. 283–292, 2015, ISSN: 09500618. DOI: `10.1016/j.conbuildmat.2014.11.039`.

[104] M. Fox, D. Coley, S. Goodhew, and P. de Wilde, “Time-lapse thermography for building defect detection”, *Energy and Buildings*, vol. 92, pp. 95–106, 2015, ISSN: 03787788. DOI: `10.1016/j.enbuild.2015.01.021`.

[105] E. Lucchi, “Applications of the infrared thermography in the energy audit of buildings: A review”, *Renewable and Sustainable Energy Reviews*, vol. 82, pp. 3077–3090, 2018, ISSN: 13640321. DOI: `10.1016/j.rser.2017.10.031`.

[106] N. P. Avdelidis, A. Moropoulou, and P. Theoulakis, “Detection of water deposits and movement in porous materials by infrared imaging”, *Infrared Physics & Technology*, vol. 44, no. 3, pp. 183–190, 2003, ISSN: 13504495. DOI: `10.1016/S1350-4495(02)00212-8`.

[107] E. Grinzato, G. Cadelano, and P. Bison, “Moisture map by IR thermography”, *Journal of Modern Optics*, vol. 57, no. 18, pp. 1770–1778, 2010, ISSN: 0950-0340. DOI: `10.1080/09500341003731597`.

[108] E. Edis, I. Flores-Colen, and J. de Brito, “Passive thermographic detection of moisture problems in façades with adhered ceramic cladding”, *Construction and Building Materials*, vol. 51, pp. 187–197, 2014, ISSN: 09500618. DOI: `10.1016/j.conbuildmat.2013.10.085`.

[109] E. Barreira, R. Almeida, and J. Delgado, “Infrared thermography for assessing moisture related phenomena in building components”, *Construction and Building Materials*, vol. 110, pp. 251–269, 2016, ISSN: 09500618. DOI: `10.1016/j.conbuildmat.2016.02.026`.

[110] Deutsches Institut für Normung e.V., *DIN EN 13187:1998: Thermal Performance of buildings - Qualitative detection of thermal irregularities in building envelopes - Infrared method*, Berlin, 1999.

[111] D. J. Titman, "Applications of thermography in non-destructive testing of structures", *NDT & E International*, vol. 34, no. 2, pp. 149–154, 2001, ISSN: 0963-8695. DOI: `10.1016/S0963-8695(00)00039-6`.

[112] S. Martin Ocaña, I. Cañas Guerrero, and I. González Requena, "Thermographic survey of two rural buildings in Spain", *Energy and Buildings*, vol. 36, no. 6, pp. 515–523, 2004, ISSN: 03787788. DOI: `10.1016/j.enbuild.2003.12.012`.

[113] E. Barreira, R. M. Almeida, and M. Moreira, "An infrared thermography passive approach to assess the effect of leakage points in buildings", *Energy and Buildings*, vol. 140, pp. 224–235, 2017, ISSN: 03787788. DOI: `10.1016/j.enbuild.2017.02.009`.

[114] C. Lerma, E. Barreira, and R. M. Almeida, "A discussion concerning active infrared thermography in the evaluation of buildings air infiltration", *Energy and Buildings*, vol. 168, pp. 56–66, 2018, ISSN: 03787788. DOI: `10.1016/j.enbuild.2018.02.050`.

[115] P. Wahlgren and E. Sikander, "Methods and Materials for an Airtight Building", in *Proceedings of the Thermal Performance of the Exterior Envelopes of Whole Buildings XI International Conference*, 2010.

[116] J. M. Hart, *A practical guide to infra-red thermography for building surveys*, Garston, Watford, 1991.

[117] C. M. Hunt, "Air Infiltration: A Review of Some Existing Measurement Techniques and Data", in *Building Air Change Rate and Infiltration Measurements*, H. R. Trechsel, Ed., 100 Barr Harbor Drive, PO Box C700, West Conshohocken, PA 19428-2959: ASTM International, 1980, pp. 3–23, ISBN: 978-0-8031-0607-9. DOI: `10.1520/STP27521S`.

[118] R. N. Dietz and E. A. Cote, "Air infiltration measurements in a home using a convenient perfluorocarbon tracer technique", *Environment International*, vol. 8, no. 1-6, pp. 419–433, 1982, ISSN: 0160-4120.

[119] A. K. Persily, *Tracer Gas Technique for Studying Building Air Exchange*, U.S. Deartment of Commerce, Ed., Gaithersburg, 1988.

[120] C. J. Ghazi and J. S. Marshall, "A CO2 tracer-gas method for local air leakage detection and characterization", *Flow Measurement and Instrumentation*, vol. 38, pp. 72–81, 2014, ISSN: 09555986. DOI: `10.1016/j.flowmeasinst.2014.05.015`.

[121] ASTM International, *ASTM E1186 − 17: Air Leakage Site Detection in Building Envelopes and Air Barrier Systems*, West Conshohocken, PA, 2017.

[122] R. Kumar, A. D. Ireson, and H. W. Orr, "An automated air infiltration measuring system using SF6 tracer gas in constant concentration and decay methods", *ASHRAE Transactions*, vol. 85, no. 2, pp. 385–395, 1979.

[123] R. C. Fortmann, N. L. Nagda, and H. E. Rector, "Comparison of methods for the measurement of air change rates and interzonal airflows to two test residences", in *Air Change Rate and Airtightness in Buildings*, M. H. Sherman, Ed., 100 Barr Harbor Drive, PO Box C700, West Conshohocken, PA 19428-2959: ASTM International, 1990, pp. 104–118, ISBN: 978-0-8031-1451-7.

[124] I. S. Walker and T. W. Forest, "Field measurements of ventilation rates in attics", *Building and Environment*, vol. 30, no. 3, pp. 333–347, 1995, ISSN: 0360-1323. DOI: `10.1016/0360-1323(94)00053-U`.

[125] D. N. Keast, *Acoustic Location of Infiltration Openings in Buildings: Final Report*, Bolt Beranek and Newman Inc., Ed., New York, 1978.

[126] D. N. Keast and P. Hsien-Sheng, "The Use of Sound to Locate Infiltration Openings in Buildings", in *Proceedings of the ASHRAE/DOE Conference*, 1979.

[127] S. Dudić, I. Ignjatović, D. Šešlija, V. Blagojević, and M. Stojiljković, "Leakage quantification of compressed air using ultrasound and infrared thermography", *Measurement*, vol. 45, no. 7, pp. 1689–1694, 2012, ISSN: 02632241. DOI: `10.1016/j.measurement.2012.04.019`.

[128] M. H. F. de Salis, N. V. Movchan, and D. J. Oldham, "Characterizing holes in duct walls using resonance frequencies", *The Journal of the Acoustical Society of America*, vol. 111, no. 6, pp. 2583–2593, 2002. DOI: `10.1121/1.1470506`.

[129] D. J. Oldham, J. Kang, and M. W. Brocklesby, "Modelling the Acoustical and Airflow Performance of Simple Lined Ventilation Apertures", *Building Acoustics*, vol. 12, no. 4, pp. 277–292, 2005, ISSN: 1351-010X. DOI: `10.1260/135101005775219139`.

[130] H. K. Park and H. Kim, "Acoustic insulation performance of improved airtight windows", *Construction and Building Materials*, vol. 93, pp. 542–550, 2015, ISSN: 09500618. DOI: `10.1016/j.conbuildmat.2015.05.058`.

[131] G. Benedetto and E. Brosio, *A relation between transmission loss and air infiltration characteristics in windows*, Turin, Italy, 1981.

[132] T. Sonoda and F. Peterson, "A sonic method for building air-leakage measurements", *Applied Energy*, vol. 22, no. 3, pp. 205–224, 1986. DOI: `10.1016/0306-2619(86)90003-6`.

[133] M. Ringger and P. Hartmann, "Evaluation of an Acoustical Method for Detecting Air Leaks", *Air Infiltration Review*, vol. 11, no. 1, pp. 6–9, 1989.

[134] O. A. Hassan, "An alternative method for evaluating the air tightness of building components", *Building and Environment*, vol. 67, pp. 82–86, 2013, ISSN: 0360-1323. DOI: `10.1016/j.buildenv.2013.05.007`.

[135] V. Iordache and T. Catalina, "Acoustic approach for building air permeability estimation", *Building and Environment*, vol. 57, pp. 18–27, 2012, ISSN: 0360-1323. DOI: `10.1016/j.buildenv.2012.04.008`.

[136] K. Varshney, J. E. Rosa, I. Shapiro, and D. Scott, "Air-Infiltration Measurements in Buildings Using Sound Transmission Loss Through Small Apertures", *International Journal of Green Energy*, vol. 10, no. 5, pp. 482–493, 2013, ISSN: 1543-5075. DOI: `10.1080/15435075.2012.675603`.

[137] U. Berardi and S. Pouyan, "Exploring acoustical approaches for pre-screening the airtightness of building enclosures", in *Proceedings of the177th Meeting of the Acoustical Society of America*, 2019.

[138] R. W. Graham, "Infrasonic Impedance Measurements of Buildings for Air Leakage Determination", Master Thesis, Syracuse University, Syracuse, NY, 1977.

[139] P. Holstein, M. Barth, and C. Probst, "Acoustic methods for leak detection and airtightness testing", in *Proceedings of the 19th World Conference of Nondestructive Testing*, 2016.

[140] P. Holstein, A. Raabe, N. Bader, A. Tharandt, M. Barth, and H.-J. Münch, "Energetische Probleme und akustische Verfahren", in *Denkmal und Energie 2017*, B. Weller and S. Horn, Eds., Wiesbaden: Springer Fachmedien Wiesbaden, 2017, pp. 189–199, ISBN: 978-3-658-16453-9. DOI: `10.1007/978-3-658-16454-6-14`.

[141] N. Bader, P. Holstein, K. Eckert, H.-J. Münch, L. Holtkamp, and T. d. van Eschut, "Akustisches Verfahren zur Dichtheitsprüfung", in *Denkmal und Energie 2018*, B. Weller and S. Horn, Eds., Wiesbaden: Springer Fachmedien Wiesbaden, 2018, pp. 285–295, ISBN: 978-3-658-19671-4. DOI: `10.1007/978-3-658-19672-1-22`.

[142] P. Holstein, N. Bader, S. Moeck, H.-J. Münch, D. Döbler, and A. Jahnke, "Akustische Verfahren zur Ermittlung der Luftdichtheit von Bestandsgebäuden", in *Denkmal und Energie 2020*, B. Weller and L. Scheuring, Eds., Wiesbaden: Springer Fachmedien Wiesbaden, 2020, pp. 111–123, ISBN: 978-3-658-28752-8. DOI: `10.1007/978-3-658-28753-5-8`.

[143] P. Holstein, A. Raabe, M. Barth, N. Bader, and S. Zur Horst-Meyer, Eds., *Potenzial akustischer Methoden zum Einsparen von Energie*, 2015.

[144] G. Raman, M. Prakash, R. Ramachandran, H. Patel, and K. Chelliah, “Remote Detection of Building Air Infiltration Using a Compact Microphone Array and Advanced Beamforming Methods”, in *Proceedings of the BeBeC, 5th Berlin Beamforming Conference*, Gesellschaft zur Förderung Angewandter Informatik, Ed., 2014.

[145] G. Raman, K. Chelliah, M. Prakash, and R. T. Muehleisen, “Detection and quantification of building air infiltration using remote acoustic methods”, in *Proceedings of 43rd International Congress on Noise Control Engineering*, The Australian Acoustical Society, Ed., 2014.

[146] K. Chelliah, G. G. Raman, and R. T. Muehleisen, “Enhanced nearfield acoustic holography for larger distances of reconstructions using fixed parameter Tikhonov regularization”, *The Journal of the Acoustical Society of America*, vol. 140, no. 1, p. 114, 2016. DOI: `10.1121/1.4954757`.

[147] K. Chelliah, G. Raman, and R. T. Muehleisen, “An experimental comparison of various methods of nearfield acoustic holography”, *Journal of Sound and Vibration*, vol. 403, pp. 21–37, 2017, ISSN: 0022460X. DOI: `10.1016/j.jsv.2017.05.015`.

[148] Deutsches Institut für Normung e.V., *DIN 1320:2009-12: Acoustics - Terminology*, Berlin, 2009.

[149] M. Möser, *Technische Akustik*, 6th ed. Berlin: Springer-Verlag, 2005, ISBN: 3-540-22510-2.

[150] W. M. Willems, K. Schild, and D. Stricker, *Formeln und Tabellen Bauphysik: Wärmeschutz – Feuchteschutz – Klima – Akustik – Brandschutz*, 4th ed. Wiesbaden: Springer Fachmedien Wiesbaden, 2016, ISBN: 978-3-658-16049-4. DOI: `10.1007/978-3-658-16050-0`.

[151] L. Bergmann, *Der Ultraschall und seine Anwendung in Wissenschaft und Technik*, 5th ed. Stuttgart: Hirzel-Verlag, 1949.

[152] G. Müller and M. Möser, Eds., *Taschenbuch der Technischen Akustik*, 3rd ed. Berlin: Springer-Verlag, 2004.

[153] S. Weinzierl, Ed., *Handbuch der Audiotechnik*. Berlin, Heidelberg: Springer-Verlag, 2008, ISBN: 978-3-540-34300-4. DOI: `10.1007/978-3-540-34301-1`.

[154] T. D. Rossing, Ed., *Springer Handbook of Acoustics*. New York: Springer Science, 2007, ISBN: 978-0-387-30446-5.

[155] W. M. Hartmann, *Signals, Sound, and Sensation*, 1st ed., ser. Modern Acoustics and Signal Processing. AIP-Press, 1998, ISBN: 978-1-56396-283-7.

[156] W. Schenk, F. Kremer, G. Beddies, T. Franke, P. Galvosas, and P. Rieger, *Physikalisches Praktikum*, 14th ed. Wiesbaden: Springer Spektrum, 2014, ISBN: 978-3-658-00665-5. DOI: `10.1007/978-3-658-00666-2`.

[157] C. E. Shannon, "Communication in the Presence of Noise", *Proceedings of the IRE*, vol. 37, no. 1, pp. 10–21, 1949, ISSN: 0096-8390. DOI: `10.1109/JRPROC.1949.232969`.

[158] W. J. Witteman, *Detection and Signal Processing*, 1st ed. Berlin, Heidelberg: Springer Berlin Heidelberg, 2006, vol. 22, ISBN: 978-3-540-29599-0. DOI: `10.1007/978-3-540-29600-3`.

[159] J. L. Zhou and F. Wang, "Chirp Signal Time-Frequency Analysis Characteristic Comparison", *Applied Mechanics and Materials*, vol. 226-228, pp. 568–571, 2012. DOI: `10.4028/www.scientific.net/AMM.226-228.568`.

[160] N. E. Huang and S. S. P. Shen, *Hilbert-Huang Transform and Its Applications*. Singapore: World Scientific Publishing Co. Pte. Ltd, 2005, vol. 5, ISBN: 978-981-256-376-7. DOI: `10.1142/5862`.

[161] J. S. Bendat and A. G. Piersol, *Random Data: Analysis and Measurement Procedures*, 4th ed. Hoboken, New Jersey: John Wiley & Sons, Inc, 2010, ISBN: 978-0-470-24877-5.

[162] N. E. Huang, Z. Shen, S. R. Long, M. C. Wu, H. H. Shih, Q. Zheng, N.-C. Yen, C. C. Tung, and H. H. Liu, "The empirical mode decomposition and the Hilbert spectrum for nonlinear and non-stationary time series analysis", in *Proceedings of the Roayal Society: Mathematical, Physical and Engineering Sciences*, 1998. DOI: `10.1098/rspa.1998.0193`.

[163] N. E. Huang, Z. Wu, S. R. Long, K. C. Arnold, X. Chen, and K. Blank, "On Instantaneous Frequency", *Advances in Adaptive Data Analysis*, vol. 01, no. 02, pp. 177–229, 2009, ISSN: 1793-5369. DOI: `10.1142/S1793536909000096`.

[164] G. Rilling, P. Flandrin, and P. Goncalves, "On empirical mode decomposition and its algorithms", in *Proceedings of the IEEE-EURASIP Workshop on Nonlinear Signal and Image Processing*, 2003, pp. 8–11.

[165] Deutsches Institut für Normung e.V., *DIN EN 61260:2014-10: Electroacoustics - Octave-band and fractional-octave-band filters*, Berlin, 2014.

[166] D. F. Aldridge, "Mathematics of Linear Sweeps", *Canadian Journal of Exploration Geophysics*, vol. 28, no. 1, pp. 62–68, 1992.

[167] F. A. Everest and K. C. Pohlmann, *Master Handbook of Acoustics*, 6th ed. New York City: McGraw-Hill Education., 2015, ISBN: 978-0-07-184103-0.

[168] T. M. Dantas, R. Costa-Felix, and J. C. Machado, “Nonlinear frequency modulated excitation signal and modified compressing filter for improved range resolution and side lobe level of ultrasound echoes”, *Applied Acoustics*, vol. 130, pp. 238–246, 2018, ISSN: 0003682X. DOI: `10.1016/j.apacoust.2017.10.008`.

[169] P. Bloomfield, *Fourier Analysis of Time Series: An Introduction*, 2nd ed. New York: John Wiley & Sons, Inc, 2013, ISBN: 978-0-471-88948-9.

[170] I. H. Chan, *Swept Sine Chirps for Measuring Impulse Response*, Sunnyvale, CA, 2010.

[171] F. J. Harris, “On the use of windows for harmonic analysis with the discrete Fourier transform”, *Proceedings of the IEEE*, vol. 66, no. 1, pp. 51–83, 1978, ISSN: 0018-9219. DOI: `10.1109/PROC.1978.10837`.

[172] K. Küpfmüller and G. Kohn, *Theoretische Elektrotechnik und Elektronik: Eine Einführung*, 15th ed. Berlin, Heidelberg: Springer-Verlag, 2000, ISBN: 978-3-662-10425-5. DOI: `10.1007/978-3-662-10425-5`.

[173] Deutsches Institut für Normung e.V., *DIN EN ISO 12354-1:2017: Building acoustics - Estimation of acoustic performance of buildings from the performance of elements - Part 1: Airborne sound insulation between rooms*, Berlin, 2017.

[174] R. Lerch, G. Sessler, and D. Wolf, *Technische Akustik*, 1st ed. Springer Berlin Heidelberg, 2009, ISBN: 978-3-540-23430-2. DOI: `10.1007/978-3-540-49833-9`.

[175] L. L. Beranek, “Analysis of Sabine and Eyring equations and their application to concert hall audience and chair absorption”, *The Journal of the Acoustical Society of America*, vol. 120, no. 3, pp. 1399–1410, 2006. DOI: `10.1121/1.2221392`.

[176] International Organization for Standardization, *ISO 9613-1:1993: Acoustics; attenuation of sound during propagation outdoors; part 1: calculation of the absorption of sound by the atmosphere*, Berlin, 1993.

[177] R. H. C. Wenmaekers, C. C. J. M. Hak, and M. C. J. Hornikx, “The effective air absorption coefficient for predicting reverberation time in full octave bands”, *The Journal of the Acoustical Society of America*, vol. 136, no. 6, p. 3063, 2014. DOI: `10.1121/1.4901710`.

[178] Deutsches Institut für Normung e.V., *DIN EN ISO 18233:2006: Acoustics - Application of new measurement methods in building and room acoustics*, Berlin, 2006.

[179] A. Farina, “Simultaneous measurement of impulse response and distortion with a swept-sine technique”, in *Proceedings of the 108th AES Convention*, 2000.

[180] ——, “Advancements in impulse response measurements by sine sweeps”, in *Proceedings of the 122nd AES Convention*, 2007.

[181] S. Müller and P. Massarani, "Transfer-function measurement with sweeps", *Journal of the Audio Engineering Society*, vol. 49, no. 6, pp. 443–471, 2001.

[182] W. Meng, D. Sen, S. Wang, and L. Hayes, "Impulse response measurement with sine sweeps and amplitude modulation schemes", in *Proceedings of the 2nd International Conference on Signal Processing and Communication Systems*, 2008.

[183] A. Novak, P. Lotton, and L. Simon, "Synchronized Swept-Sine: Theory, Application, and Implementation", *Journal of the Audio Engineering Society*, vol. 63, no. 10, pp. 786–798, 2015, ISSN: 15494950. DOI: `10.17743/jaes.2015.0071`.

[184] Deutsches Institut für Normung e.V., *DIN EN ISO 3382-2:2008: Acoustics - Measurement of room acoustic parameters - Part2: Reverberation time in ordinary rooms*, Berlin, 2008.

[185] M. Reader-Harris, *Orifice Plates and Venturi Tubes*. Cham: Springer International Publishing, 2015, ISBN: 978-3-319-16879-1. DOI: `10.1007/978-3-319-16880-7`.

[186] Deutsches Institut für Normung e.V., *DIN EN 12114:2000: Thermal performances of buildings - Air permeability of building components and building elements - Laboratory test method*, Berlin, 2000.

[187] F. C. Tenoudji, *Analog and Digital Signal Analysis: From Basics to Applications*, 1st ed. Springer International Publishing, 2016, ISBN: 978-3-319-82565-6. DOI: `10.1007/978-3-319-42382-1`.

[188] C. Vornanen-Winqvist, K. Järvi, S. Toomla, K. Ahmed, M. A. Andersson, R. Mikkola, T. Marik, L. Kredics, H. Salonen, and J. Kurnitski, "Ventilation Positive Pressure Intervention Effect on Indoor Air Quality in a School Building with Moisture Problems", *International journal of environmental research and public health*, vol. 15, no. 2, 2018. DOI: `10.3390/ijerph15020230`.

[189] L. C. Ng, A. Musser, A. K. Persily, and S. J. Emmerich, "Multizone airflow models for calculating infiltration rates in commercial reference buildings", *Energy and Buildings*, vol. 58, pp. 11–18, 2013, ISSN: 03787788. DOI: `10.1016/j.enbuild.2012.11.035`.

[190] Afnor, *FD P50-784:2016-07-20 : Thermal performance of buildings - Implementation guide for NF EN ISO 9972*, 2016.

[191] F. R. Carrié and V. Leprince, "Model error due to steady wind in building pressurization tests", in *Proceedings of the 35th AIVC Conference*, 2014.

[192] ——, "Uncertainties in building pressurisation tests due to steady wind", *Energy and Buildings*, vol. 116, pp. 656–665, 2016, ISSN: 03787788. DOI: `10.1016/j.enbuild.2016.01.029`.

[193] A. K. Persily and Grot. R. A., “Accuracy in pressurization data analysis”, *ASHRAE Transactions*, vol. 91, no. 2, 1985.

[194] M. K. Herrlin and M. P. Modera, “Analysis of errors for a fan-pressurization technique for measuring inter-zonal air leakage”, in *Proceedings of the 9th AIVC Conference*, 1988.

[195] M. Sherman and L. Palmiter, “Uncertainties in Fan Pressurization Measurements”, in *Airflow performance of building envelopes, components, and systems*, ser. STP / ASTM, M. P. Modera, Ed., Philadelphia, Pa.: ASTM, 1995, pp. 266-266–18, ISBN: 978-0-8031-2023-5. DOI: `10.1520/STP14701S`.

[196] M. Prignon, A. Dawans, S. Altomonte, and G. van Moeseke, “A method to quantify uncertainties in airtightness measurements: Zero-flow and envelope pressure”, *Energy and Buildings*, vol. 188-189, pp. 12–24, 2019, ISSN: 03787788. DOI: `10.1016/j.enbuild.2019.02.006`.

[197] F. R. Carrié and A. Mélois, “Modelling building airtightness pressurisation tests with periodic wind and sharp-edged openings”, *Energy and Buildings*, vol. 208, p. 109 642, 2020, ISSN: 03787788.

[198] C. Delmotte and J. Laverge, “Interlaboratory tests for the determination of repeatability and reproducibility of buildings airtightness measurements”, in *Proceedings of the 32nd AIVC Conference*, 2011.

[199] H. Okuyama and Y. Onishi, “Reconsideration of parameter estimation and reliability evaluation methods for building airtightness measurement using fan pressurization”, *Building and Environment*, vol. 47, pp. 373–384, 2012, ISSN: 0360-1323.

[200] C. Delmotte, “Airtightness of buildings - considerations regarding the zero-flow pressure and the weighted line of organic correlation”, in *Proceedings of the 38th AIVC Conference*, 2017.

[201] M. Prignon, A. Dawans, and G. van Moeseke, “Uncertainties in airtightness measurements: regression methods and pressure sequences”, in *Proceedings of the 39th AIVC Conference*, 2018.

[202] M. Prignon, C. Delmotte, A. Dawans, S. Altomonte, and G. van Moeseke, “On the impact of regression technique to airtightness measurements uncertainties”, *Energy and Buildings*, vol. 215, p. 109 919, 2020, ISSN: 03787788.

[203] I. S. Walker, “Prediction of Ventilation, Heat Transfer and Moisture Transport in Attics”, Dissertation, University of Alberta, Edmonton, Alberta, 1993.

[204] M. P. Modera and D. J. Wilson, "The Effects of Wind on Residential Building Leakage Measurements", in *Air Change Rate and Airtightness in Buildings*, M. H. Sherman, Ed., 100 Barr Harbor Drive, PO Box C700, West Conshohocken, PA 19428-2959: ASTM International, 1990, pp. 132-132–14, ISBN: 978-0-8031-1451-7.

[205] S. Weisberg, *Applied Linear Regression*, 3rd ed. Hoboken, New Jersey: John Wiley & Sons, Inc, 2005, ISBN: 0-471-66379-4.

[206] C. Delmotte, "Airtightness of buildings - calculation of combined standard uncertainty", in *Proceedings of the 34th AIVC Conference*, 2013.

[207] E. Parzen, "On Estimation of a Probability Density Function and Mode", *The Annals of Mathematical Statistics*, vol. 33, no. 3, pp. 1065–1076, 1962, ISSN: 0003-4851.

[208] B. W. Silverman, *Density Estimation for Statistics and Data Analysis*. Boca Raton, Florida: CRC Press LLC, 1986.

[209] S. Węglarczyk, "Kernel density estimation and its application", *ITM Web of Conferences*, vol. 23, no. 2, 2018. DOI: `10.1051/itmconf/20182300037`.

[210] S. J. Sheather, "Density Estimation", *Statistical Science*, vol. 19, no. 4, pp. 588–597, 2004, ISSN: 0883-4237.

[211] O. D. Lampe and H. Hause, "Interactive visualization of streaming data with kernel density estimation", in *Proceedings of the IEEE Pacific Visualization Symposium (PacificVis)*, 2011, pp. 171–178, ISBN: 978-1-61284-932-4.

[212] B. C. Moore, *An Introduction to the Psychology of Hearing*, 5th ed. London, UK: Elsevier Academic Press, 2004, ISBN: 978-1-78052-038-4.

[213] J. Billingsley and R. Kinns, "The acoustic telescope", *Journal of Sound and Vibration*, vol. 48, no. 4, pp. 485–510, 1976, ISSN: 0022460X. DOI: `10.1016/0022-460X(76)90552-6`.

[214] J. D. Maynard, E. G. Williams, and Y. Lee, "Nearfield acoustic holography: I. Theory of generalized holography and the development of NAH", *The Journal of the Acoustical Society of America*, vol. 78, no. 4, pp. 1395–1413, 1985. DOI: `10.1121/1.392911`.

[215] C.-X. Bi, Y. Liu, Y.-B. Zhang, and L. Xu, "Sound field reconstruction using inverse boundary element method and sparse regularization", *The Journal of the Acoustical Society of America*, vol. 145, no. 5, pp. 3154–3162, 2019. DOI: `10.1121/1.5109393`.

[216] W. Herbordt, *Sound Capture for Human/Machine Interfaces: Practical Aspects of Microphone Array Signal Processing*. Springer Berlin Heidelberg, 2005, ISBN: 978-3-540-23954-3. DOI: `10.1007/b99807`.

[217] O. Jaeckel, “Strengths and Weaknesses of Calculating Beamforming in the Time Domain”, in *Proceedings of the BeBeC, 8th Berlin Beamforming Conference*, Gesellschaft zur Förderung Angewandter Informatik, Ed., 2006.

[218] J. Grythe, *Acoustic camera and beampattern: Norsonic: Technical Note*, Norsonic, Ed., Lier, Norway, 2015. [Online]. Available: `https://www.norsonic.de`.

[219] H. Teutsch, *Modal Array Signal Processing: Principles and Application of Acoustic Wavefield Decomposition*, ser. Lecture Notes in Control and Information Sciences. Berlin Heidelberg: Springer, 2007, vol. 348, ISBN: 3-540-40892-2.

[220] D. Döbler, G. Heilmann, and R. Schröder, “Investigation of the depth of field in acoustic maps and its relation between focal distance and array design”, in *Proceedings of the 37th International Congress and Exposition on Noise Control Engineering*, Institute of Acoustics - Chinese Academy of Sciences, Ed., 2008.

[221] GFaI, *NoiseImage, Version 4.12.2.17221*, 2020.

[222] J. Grythe, *Beamforming algorithms - beamformers: Norsonic: Technical Note*, Norsonic, Ed., Lier, Norway, 2015. [Online]. Available: `https://www.norsonic.de`.

[223] S. Neugebauer, R. Rösel, and D. Döbler, “Correlation of parallel car interior and exterior beamforming measurements in a wind tunnel”, in *Proceedings of 43rd International Congress on Noise Control Engineering*, The Australian Acoustical Society, Ed., 2014.

[224] D. Döbler and C. Puhle, “Correlation of high channel count beamforming measurement of a car in a wind tunnel using CLEAN-SC”, in *Proceedings of the 44th International Congress and Exposition on Noise Control Engineering*, Institute of Noise Control Engineering, Ed., 2015.

[225] I. Riehle, H. Tokuno, and M. Kaltenbacher, “Identification of aeroacoustic noise sources in automotive industry by microphone array measurements”, in *Proceedings of the 41st DAGA*, Deutsche Gesellschaft für Akustik, Ed., 2015, pp. 224–227.